Supramolecular Optical Chemosensors and Assays for Sensing of Bioactive Analytes in Water and Biofluids

Zur Erlangung des akademischen Grades einer

DOKTORIN DER NATURWISSENSCHAFTEN

(Dr. rer. nat.)

von der KIT-Fakultät für Chemie und Biowissenschaften

des Karlsruher Instituts für Technologie (KIT)

genehmigte

DISSERTATION

von

M. Sc. Amrutha Prabodh

1. Referent: Prof. Dr. Pavel Levkin

2. Korreferentin: Prof. Dr. Anne Ulrich

Tag der mündlichen Prüfung: 20. Juli 2022

Die vorliegende Arbeit wurde in der Zeit von 01. Oktober 2018 bis 30. April 2022 am Institut für Nanotechnologie (INT) auf dem Campus Nord des Karlsruher Instituts für Technologie (KIT) unter der Leitung von Dr. Frank Biedermann (Emmy Noether-Nachwuchsgruppenleiter) und Prof. Dr. Pavel Levkin (Professor für Organische Chemie) angefertigt. Die Arbeit wurde von dem Deutscher Akademischer Austauschdienst (DAAD) und der Deutschen Forschungsgesellschaft (DFG) gefördert.

The present work was realized between October 1, 2018 and April 30, 2022 at the Institute of Nanotechnology (INT) on the Campus North of Karlsruhe Institute of Technology (KIT) under the supervision of Dr. Frank Biedermann (Emmy Noether junior research group leader) and Prof. Dr. Pavel Levkin (Professor of Organic Chemistry). The work was funded by the German Academic Exchange Service (DAAD) and Deutsche Forschungsgesellschaft (DFG).

Declaration

I, Amrutha Prabodh, declare that this thesis entitled "*Supramolecular Optical Chemosensors and Assays for Sensing of Bioactive Analytes in Water and Biofluids*" and the work presented in it are my own, and the work was undertaken under the supervision of Dr. Frank Biedermann and Prof. Dr. Pavel Levkin at the Institute of Nanotechnology (INT), at the Karlsruhe Institute of Technology (KIT). I confirm that:

- This work was done wholly while in candidature for a research degree at KIT.
- The whole thesis was written by me, and no other sources other than the specified were used.
- The rules for ensuring good scientific practice of the Karlsruhe Institute of Technology (KIT) have been used, and the submission and archiving of the primary data in accordance with section A(6) of the rules for ensuring good scientific practice of KIT have been ensured.
- The electronic version of the work is consistent with the written version.
- Where I have consulted the published work of others, this is always clearly attributed.
- I have acknowledged all main sources of help.
- Where the thesis is based on work done by myself jointly with others, I have clarified exactly what was done by others and what I have contributed myself.
- Furthermore, I declare that I did not undertake any previous doctoral studies and that I am currently not enrolled in any other ongoing doctoral procedure.

Amrutha Prabodh

Deklaration

Ich, Amrutha Prabodh, erkläre, dass diese Arbeit mit dem Titel "*Supramolecular Optical Chemosensors and Assays for Sensing of Bioactive Analytes in Water and Biofluids* " und die darin vorgestellten Ergebnisse meine eigenen sind. Die Arbeit wurde unter der Leitung von Dr. Frank Biedermann und Prof. Dr. Pavel Levkin am Institut für Nanotechnologie (INT), am Karlsruher Institut für Technologie (KIT) angefertigt. Ich bestätige:

- Diese Arbeit wurde vollständig während der Kandidatur für ein Forschungsstudium am KIT durchgeführt.
- Die gesamte Arbeit wurde von mir verfasst und es wurden keine anderen Quellen als die angegebenen verwendet.
- Es wurden Maßnahmen zur Sicherstellung einer guten wissenschaftlichen Praxis des Karlsruher Instituts für Technologie (KIT) angewendet und die Übermittlung und Archivierung der Primärdaten gemäß Abschnitt A(6) der Regeln zur Sicherstellung einer guten wissenschaftlichen Praxis des KIT sichergestellt.
- Die elektronische Fassung des Werkes entspricht der schriftlichen Fassung.
- Im Fall, dass ich die veröffentlichten Arbeiten anderer konsultiert habe, wird dies immer eindeutig zugeordnet.
- Ich habe alle wichtigen Hilfsquellen zur Kenntnis genommen.
- Wenn die Arbeit auf Arbeiten basiert, die ich gemeinsam mit anderen geleistet habe, habe ich kenntlich gemacht, was von anderen geleistet wurde und was ich selbst beigesteuert habe.
- Des Weiteren erkläre ich, dass ich kein vorheriges Promotionsstudium absolviert habe und mich derzeit nicht in einem anderen laufenden Promotionsverfahren befinde.

Amrutha Prabodh

This work is dedicated to my family.

My parents, Meena and Prabodh, my sister, Adi,

and my grandmother, Vinodhini.

For their endless love, support and encouragement.

Table of Contents

Abstract

The recognition and detection of biologically important analytes, especially small biomolecules, is of prime relevance and has become an upsurging area of research in chemistry and biology. Consequently, the development of robust chemical molecular sensors ("chemosensors") based on artificial recognition elements with the potential to detect molecules with high sensitivity and selectivity and coupled with a sensitive signal transduction strategy continues to attract considerable attention. Optical methods based on fluorescence are highly desirable for signal transduction because of their versatility, high sensitivity, low cost with readily available instrumentation, and potential for real-time analysis. Thus, optical/fluorescent chemosensors, in combination with innovative assay protocols, find broad application potential in many disciplines, such as biochemistry and clinical and medical diagnostics. They offer a cost-efficient alternative to conventional instrumental analytical methods, such as HPLC-MS, GC-MS, and NMR, and are superior to biosensors in terms of stability, equilibration time, price, and scope for small molecule detection. However, developing chemosensors that fully meet the requirements for practical applications is still challenging. The low binding affinity or selectivity of chemosensors for most biomolecules or their metabolites in biofluids, as well as the low stability of the chemosensor's guest-host ensemble (e.g., upon dilution), are main reasons why the practical application potential of artificial chemosensors has not yet been fully realized.

In this work, artificial chemosensors based on supramolecular host-guest chemistry coupled with optical signal transduction are utilized to realize both detection and chirality sensing of biologically relevant analytes in aqueous media and complex biofluids. In addition, the various aspects of realizing their practical diagnostic applications are addressed.

The first research project involves the development of electronic circular dichroism (ECD)-based chemosensors for the detection and chirality sensing of diverse chiral organic analytes in water. Chemosensors that can detect molecular chirality are crucial due to the significance of chiral bio-relevant molecules and the influence of chirality on their related biological activity, *e.g.*, in drug production. However, only a few chirality-based chemosensors are available to date for the detection of compounds in aqueous media. My thesis utilized achiral chromophoric hosts, *i.e.,* acyclic cucurbit[*n*]urils and molecular tweezers as recognition elements in the chemosensor. The achiral chromophoric hosts were found to respond with information-rich induced ECD signals to the presence of micromolar concentrations of chiral small molecule guests, such as chiral hydrocarbons, terpenes, amino acids and their derivatives,

steroids, and drugs in water. In favorable cases, this also allowed for analyte identification and reaction monitoring.

In the second research project, fluorescence-detected circular dichroism (FDCD) spectroscopy is applied for the first time for the chiroptical analysis of supramolecular host-guest and host-protein systems and compared to the widely utilized electronic circular dichroism (ECD). The main goal was to explore the utility of FDCD to improve the sensitivity and selectivity of chiroptical supramolecular assays. The comprehensive investigations demonstrate that FDCD is an excellent choice for common supramolecular applications, *e.g.*, the detection and chirality sensing of chiral organic analytes and label-free reaction monitoring. FDCD can be conducted in favorable circumstances at much lower concentrations than ECD measurements, even in chromophoric and auto-emissive biofluids such as blood serum, overcoming the sensitivity limitation of absorbance-based chiroptical spectroscopy. Furthermore, the combined use of FDCD and ECD provided additional valuable information about the system, *e.g.*, the chemical identity of an analyte or hidden aggregation phenomena.

The third research project addresses the importance of thermodynamic and kinetic investigations to properly analyze the association and dissociation processes of supramolecular host-guest recognition interactions, which are crucial to designing host-guest systems with improved properties and advancing their practical applications. However, kinetic descriptions of supramolecular systems are scarce in the literature, mainly due to the lack of suitable experimental protocols. Thus, three novel fluorescence-based time-resolved approaches are introduced that allowed the convenient determination of kinetic rate constants of spectroscopically silent and even insoluble guests with the macrocyclic cucurbit[*n*]uril and human serum albumin as representative hosts. Furthermore, a new kinetic method is adopted to achieve selective analyte sensing even in situations of poor thermodynamic selectivity due to the host's often observed similar binding affinities for structurally similar analytes. The method allowed a selective identification and quantification of analytes without the need to modify the parent host synthetically.

The fourth research project involves the development of a novel fluorescent chemosensor for the detection of biogenic polyamines, which serve as health indicators in the human body. The fluorescent chemosensor self-assembled from sulfonated pillar[*n*]arene host in combination with suitable dicationic indicator dyes responds instantly with a fluorescence "turn-on" signal to the presence of biogenic polyamines. The photophysical and binding properties of the new fluorescent chemosensor explored in detail in both saline buffers and biologically relevant

media display their excellent functionality for polyamine sensing with no salt interferences on the sensing assay. Moreover, the chemosensor allowed the detection of biogenic polyamines down to the low micromolar concentration range in biofluids, such as urine and saliva, with good selectivity even in the presence of potential interferents present in the media. Thus, because of its simplicity, cost-effectiveness, and fast detection capabilities, the newly developed fluorescent chemosensor for polyamines will assist the future development of rapid diagnostic tests for home-use and point-of-care applications.

In summary, this doctoral thesis highlights the different strategies for developing supramolecular optical chemosensors for sensitive and selective analyte detection, which are also applicable in biologically relevant media. Future research and development of sensors with improved practical applicability will contribute significantly to the advancement of analytical chemistry and biochemical/medical research.

Zusammenfassung

Die Erkennung und der Nachweis biologisch wichtiger Analyten, insbesondere kleiner Biomoleküle, ist von größter Bedeutung und hat sich zu einem aufstrebenden Forschungsgebiet in Chemie und Biologie entwickelt. Die Entwicklung robuster chemischer Molekularsensoren ("Chemosensoren"), die auf synthetische Erkennungselemente basieren und Moleküle mit hoher Empfindlichkeit und Selektivität in Kombination mit einer empfindlichen Signaltransduktionsstrategie nachweisen können, findet daher weiterhin große Beachtung. Optische Methoden, die auf Fluoreszenz beruhen, sind wegen ihrer Vielseitigkeit, hohen Empfindlichkeit, geringen Kosten und der Möglichkeit der Echtzeitanalyse für die Signalübertragung sehr wünschenswert. Daher finden optische/fluoreszierende Chemosensoren in Kombination mit innovativen Testprotokollen ein breites Anwendungspotenzial in vielen Disziplinen wie der Biochemie und der klinischen und medizinischen Diagnostik. Sie bieten eine kosteneffiziente Alternative zu herkömmlichen instrumentellen Analysemethoden wie HPLC-MS, GC-MS und NMR und sind den Biosensoren in Bezug auf Stabilität, Äquilibrierungszeit, Preis und Möglichkeiten zum Nachweis kleiner Moleküle überlegen. Die Entwicklung von Chemosensoren, die den Anforderungen praktischer Anwendungen in vollem Umfang gerecht werden, ist jedoch nach wie vor eine Herausforderung. Die geringe Bindungsaffinität von Chemosensoren für die meisten Biomoleküle oder deren Metaboliten in Bioflüssigkeiten sowie die geringe Stabilität des Gast-Wirt-Ensembles des Chemosensors (z. B. bei Verdünnung) sind die Hauptgründe dafür, dass das praktische Anwendungspotenzial künstlicher Chemosensoren noch nicht voll ausgeschöpft wurde.

In dieser Arbeit werden künstliche Chemosensoren, die auf supramolekularer Wirt-Gast-Chemie basieren und mit optischer Signaltransduktion gekoppelt sind, eingesetzt, um sowohl den Nachweis als auch die Chiralitätsmessung biologisch relevanter Analyten in wässrigen Medien und komplexen Bioflüssigkeiten zu realisieren. Darüber hinaus werden die verschiedenen Aspekte bei der Verwirklichung ihrer praktischen diagnostischen Anwendungen behandelt.

Das erste Forschungsprojekt befasst sich mit der Entwicklung von Chemosensoren auf der Grundlage des elektronischen Zirkulardichroismus (ECD) für den Nachweis und die Chiralitätserkennung verschiedener organischer Analyten in Wasser. Chemosensoren, die die Chiralität von Molekülen nachweisen können, sind aufgrund der Bedeutung chiraler bio-relevanter Moleküle und des Einflusses der Chiralität auf deren biologische Aktivität, z. B. bei der Arzneimittelherstellung, von entscheidender Bedeutung. Bisher gibt es jedoch nur wenige

auf Chiralität basierende Chemosensoren für den Nachweis von Verbindungen in wässrigen Medien. In meiner Arbeit wurden achirale chromophore Wirte, d. h. azyklische Cucurbit[*n*]urile und molekulare Tweezer, als Erkennungselemente im Chemosensor verwendet. Es wurde festgestellt, dass die achiralen chromophoren Wirte mit informationsreichen induzierten ECD-Signalen auf die Anwesenheit mikromolarer Konzentrationen chiraler kleiner Gastmoleküle wie chiraler Kohlenwasserstoffe, Terpene, Aminosäuren und ihrer Derivate, Steroide und Drogen in Wasser reagieren. In günstigen Fällen ermöglichte dies auch die Identifizierung von Analyten und die Überwachung von Reaktionen.

Im zweiten Forschungsprojekt wird die Fluoreszenz-detektierte Zirkulardichroismus-Spektroskopie (FDCD) zum ersten Mal für die chiroptische Analyse von supramolekularen Wirt-Gast und Wirt-Protein systemen eingesetzt und mit dem weit verbreiteten elektronischen Zirkulardichroismus (ECD) verglichen. Hauptziel war die Erforschung des Nutzens von FDCD zur Verbesserung der Empfindlichkeit und Selektivität von chiroptischen supramolekularen Assays. Die umfassenden Untersuchungen zeigen, dass FDCD eine ausgezeichnete Wahl für gängige supramolekulare Anwendungen ist, z. B. für den Nachweis und die Chiralitätserkennung von chiralen organischen Analyten und die markierungsfreie Reaktionsüberwachung. FDCD kann unter günstigen Bedingungen bei viel niedrigeren Konzentrationen als ECD-Messungen durchgeführt werden, sogar in chromophoren und autoemissiven Bioflüssigkeiten wie Blutserum, wodurch die Empfindlichkeitsbeschränkung der absorbanzbasierten chiroptischen Spektroskopie überwunden wird. Darüber hinaus lieferte die kombinierte Verwendung von FDCD und ECD zusätzliche wertvolle Informationen über das System, z. B. über die chemische Identität eines Analyten oder verborgene Aggregationsphänomene.

Das dritte Forschungsprojekt umfasst thermodynamische und kinetische Studien, zur Beschreibung der Assoziations- und Dissoziationsprozesse supramolekularer Wirts-Gast-Wechselwirkungen , die für die Entwicklung von Wirts-Gast-Systemen mit verbesserten Eigenschaften und deren praktische Anwendung entscheident sind. Kinetische Beschreibungen supramolekularer Systeme sind in der Literatur jedoch kaum zu finden, was vor allem auf das Fehlen geeigneter Versuchsprotokolle zurückzuführen ist. Daher werden drei neuartige fluoreszenzbasierte, zeitaufgelöste Ansätze vorgestellt, die die einfache Bestimmung der kinetischen Geschwindigkeitskonstanten von spektroskopisch unauffälligen und sogar unlöslichen Gästen mit dem makrozyklischen Cucurbit[n]uril und menschlichem Serumalbumin ermöglichen. Darüber hinaus wird eine neue kinetische Methode angewandt, um selbst in Situationen mit geringer thermodynamischer Selektivität aufgrund der häufig

beobachteten ähnlichen Bindungsaffinitäten der Wirte für strukturell ähnliche Analyten einen selektiven Analytsensor zu erzielen. Die Methode ermöglichte eine selektive Identifizierung und Quantifizierung von Analyten, ohne dass der Ausgangswirt synthetisch verändert werden musste.

Das vierte Forschungsprojekt betrifft die Entwicklung eines neuartigen fluoreszierenden Chemosensors für den Nachweis biogener Polyamine, die als wichtige Krankheitsindikatoren dienen. Der fluoreszierende Chemosensor, der aus einem sulfonierten Pillar[*n*]aren-Wirt in Kombination mit geeigneten dikationischen Indikatorfarbstoffen aufgebaut ist, reagiert sofort mit einer Fluoreszenzsignaländerung auf die Anwesenheit von biogenen Polyaminen. Die photophysikalischen und Bindungseigenschaften des neuen fluoreszierenden Chemosensors, der sowohl in Salzpuffern als auch in biologisch relevanten Medien eingehend untersucht wurde, zeigen seine ausgezeichnete Funktionalität für die Polyamin-Sensorik, ohne dass Salz den Sensor-Assay stört. Darüber hinaus ermöglichte der Chemosensor den Nachweis von biogenen Polyaminen bis in den niedrigen mikromolaren Konzentrationsbereich in Bioflüssigkeiten wie Urin und Speichel mit guter Selektivität, selbst bei Vorhandensein von potenziellen Störfaktoren in den Medien. Aufgrund seiner Einfachheit, Kosteneffizienz und schnellen Nachweisfähigkeit wird der neu entwickelte fluoreszierende Chemosensor für Polyamine die künftige Entwicklung von diagnostischen Schnelltests für den Heimgebrauch und Point-of-Care-Anwendungen unterstützen.

Zusammenfassend zeigt diese Dissertation die verschiedenen Strategien zur Entwicklung supramolekularer optischer Chemosensoren für den empfindlichen und selektiven Nachweis von Bioanalyten auf, die auch in biologisch relevanten Medien anwendbar sind. Die künftige Forschung und Entwicklung von Sensoren mit verbesserter praktischer Anwendbarkeit werden wesentlich zum Fortschritt der analytischen Chemie und der biochemischen/medizinischen Forschung beitragen.

Chapter 1

1 General Introduction

1.1. Molecular recognition in chemical sensing

Sensitive and selective detection of biologically important analytes, especially small biomolecules, plays a vital role in biomedical studies and clinical diagnosis.[1-5] Molecular recognition in biological systems is realized by the association of two or more molecules (usually the receptor with the target analyte) *via* selective non-covalent interactions, such as, hydrogen bonding, electrostatic effects, metal coordination, hydrophobic forces, van der Waals forces, and π-π interactions.[6] This crucial phenomenon mediates several events, including antigen-antibody, protein-protein, protein-nucleic acid, and enzyme-substrate interactions in the human body.[7-10] Over the past decades, supramolecular chemistry based on molecular recognition has attracted considerable attention and has been under extensive investigation to prepare molecular recognition agents for sensing biological analytes.[11-14] Since the recognition event occurs on a molecular level, gathering and processing information poses a fundamental challenge.

A typical chemical sensor or chemosensor consists of an analyte–binding receptor (the recognition element) and a molecular signaling component that reports the binding status of the receptor (the signal transducer), Figure 1.1. A biosensor is a chemical sensor that uses a molecular recognition element that is derived from a biological system (a bioreceptor).[15]

For chemical sensors or biosensors, the input is usually the concentration of an analyte. An efficient sensor performs two crucial functions: (i) it interacts with the target species with high affinity (preferably in a highly selective manner), thereby recognizing it selectively out of a pool of co-existing species, and (ii) it reports the recognition event by providing an analytical

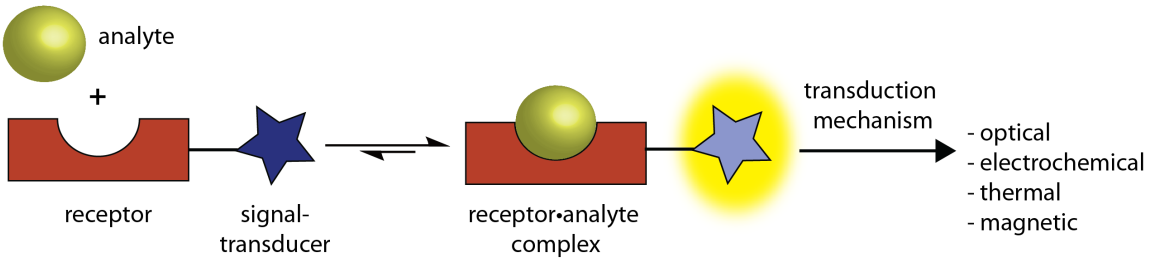

Figure 1.1: Schematic representation of a chemical sensor or biosensor consisting of an analyte-binding receptor and a signal transducer, which reports the binding event with an optical, electrochemical, thermal, or piezoelectric response, such as changes in the absorption, fluorescence, potentiometric, calorimetric or mass-spectrometry signals.

signal that can be analyzed qualitatively as well as quantitatively such as absorbance, fluorescence, reflectance, luminescence, or redox potential. In particular, fluorescent chemosensors have gained importance because of their high sensitivity (even single-molecule detection is possible), detection capabilities with high spatial and temporal resolution, low cost, and readily available instrumentations.[16]

Chemical sensors are useful and have several advantages over traditional analytical techniques for bioanalyte detection, such as high-performance liquid chromatography (HPLC) and gas chromatography. The execution of these conventional techniques is cumbersome and time-consuming, requiring expensive instrumentation and skilled operators. Thereby they are restricted to specialized diagnostic laboratories and are challenging to implement for home use and in point-of-care units. In addition, capabilities for high-throughput screening are limited. Therefore, the development of chemical sensors comprised of dynamically responding receptors with a sensitive signal transduction capability provides an invaluable method for low-cost, robust and fast responding analyte detection with real-time monitoring capabilities, offering many new diagnostic opportunities.

The following sections in this chapter review the different bioreceptors and artificial receptors used as recognition elements in sensing of biological analytes, their advantages, and current shortcomings in achieving a practical sensing assay. Later, section 1.2 addresses the different signal transduction mechanisms and sensing assay strategies, mainly based on fluorescence in chemical sensors. Finally, strategies for chirality sensing of bio-analytes based on chemical sensors are dealt with in section 1.3.

1.1.1. Bioreceptors

The bioreceptor comprises the recognition element of a biosensor towards the target analyte and is a significant feature that confers sensitivity and selectivity of the overall biosensor.[2,17] Antibodies, enzymes, and nucleic acids (DNA, RNA, or aptamers) are the common bioreceptors (see Figure 1.2) used extensively in biosensors and are primarily obtained from living organisms or synthetically engineered to mimic the functions of a natural bioreceptor.[18] They operate by either generating or consuming an analyte that can be recognized by the signal transducer (biocatalytic-based sensor) or by binding an analyte which can then be measured (affinity-based sensor).[15,17,19]

Clark and Lyons introduced the first enzyme-based biosensor aimed at the detection of glucose in blood plasma, using the enzyme glucose oxidase.[20] In principle, an enzyme-based biosensor

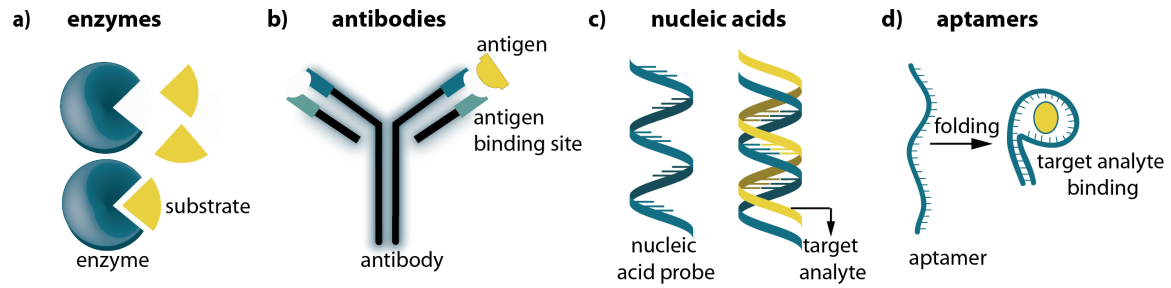

Figure 1.2: Types of bioreceptors and various analyte recognition mechanisms: (a) enzymes, (b) antibodies, (c) nucleic acids, and (d) aptamers.

(Figure 1.2a) is developed on the capability of an enzyme to selectively catalyze or inhibit a reaction involving the target analyte, and signal transduction is achieved by measuring either the amount of product formed or the amount of a substrate consumed by the enzyme-catalyzed reaction.[21] Enzymes achieve analyte specificity through binding cavities that are complementary in structure with the target analyte.[18] While there are several successful examples of this approach,[22,23] development of enzyme-based biosensors also faces several challenges. It is limited by the availability of enzymes, and the search for new highly efficient and active enzymes is difficult and costly.[24] In addition, achieving sensitivity, stability, and adaptability of the sensor to specific application scenarios is always challenging.[21]

Another class of bioreceptors are antibodies, which are naturally occurring Y-shaped 3D protein structures that possess a unique recognition pattern with high specificity and accuracy for the target analyte (Figure 1.2b).[18,25] An antibody-based biosensor is an affinity-based sensor, and the biosensor signal is dependent on the binding event that results in a stable antibody-antigen complex. The specific binding site of the antibody towards it antigen depends on their amino acid constituents.[26] Antibody-based biosensors have found many use-cases in clinical diagnostics and early analysis of diseases in the past years.[27-29] However, using antibodies as bioreceptors has its own drawbacks that limit their potential applications, such as inappropriate for small molecule detection, production challenges requiring experimentation with animals, lack of stability and batch-to-batch consistency, long assay periods, and high costs of production.[21,30]

Nucleic acid sequences are gaining importance as bioreceptors for specific diagnostic applications, where the highly specific hybridization reaction between two single-stranded DNA (ssDNA) chains to form double-stranded DNA (dsDNA) is utilized in the biosensor (Figure 1.2c).[31] An ssDNA or RNA is used as a probe in the bioreceptor in which the base sequence is complementary to the target of interest.[18,19] Hence, once the target DNA or RNA sequence has been identified, a complementary nucleic acid sequence can be generated for use

as bioreceptors in the sensor. As recognition elements, nucleic acids (DNA and RNA) are chemically more stable than antibodies.[21] However, one major drawback with nuclei acid-based biosensors involves challenges in the synthesis, purification, and characterization of nucleic acid sequences. Moreover, they are rather limited in their range of applications as their use is only optimal for biosensor applications targeting nucleic acids.[19,21]

The use of aptamer-based biorecognition elements provides a broader range of sensing capabilities and can be used to detect various bioanalytes, including amino acids, oligosaccharides, metal ions, peptides, and proteins.[18,32] Aptamers are artificial single-stranded oligonucleotides synthesized through a combinatorial selection process called Systemic Evolution of Ligands by Exponential Enrichment (SELEX).[18,33] Even though they are chemically related to nucleic acid probes, aptamers behave more like antibodies. The single-stranded nucleic acids fold into specific 3D structures and selectively bind to target molecules (Figure 1.2d).[19] Compared to antibody-based sensors, aptamers have several advantages such as small size and high stability, avoiding animal source components, and being less sophisticated, making them attractive recognition elements in biosensors.[33] However, aptamer technology is still in development, with challenges to overcome, such as the limited

Table 1.1: Summary of advantages and limitations of biorecognition elements used in biosensors.[18,19,21]

Bioreceptors	Advantages	Limitations
Enzymes	• analyte specificity and selectivity • reusability	• poor chemical, thermal and pH stability • purification is costly and time-consuming • limited substrates /analytes as targets
Antibodies	• high binding affinity • analyte specificity and selectivity	• production requires use of animals • lack of stability • batch-to-batch variations • laborious and high costs of production • long assay periods • small molecule detection (especially endogenously occurring analytes)
Nucleic acids	• stability • analyte specificity	• limited target (complementary nucleic acid) • challenges in synthesis, and purification
Aptamers	• stability • possibility to design structure • reproducibility	• non-specific binding • time-consuming procedures for aptamer modification

availability of aptamer types and chemical modifications of aptamers to reduce nonspecific binding interactions with competing analytes to improve biosensor selectivity.[18,33]

Natural biomolecules can provide as recognition elements in biosensors significant analyte selectivity and specificity combined with high binding affinities. However, they suffer from severe limitations for their practical applications, including stability issues, high cost of production and limited range of detectable analytes.[18,19,21] Table 1.1 lists the advantages and limitations associated with common bioreceptors used in biosensors. As a result, alternative sensing platforms utilizing artificial chemosensors with synthetic recognition elements prepared from low-cost starting materials that readily report or interact with biological systems attracted the attention of researchers.[1,16] The development of artificial chemosensors will aid a fast, cost-efficient, robust and non-invasive detection of bioanalytes.

1.1.2. Concepts for artificial chemosensors based on host-guest chemistry

Supramolecular chemistry based on reversible non-covalent host-guest interactions has been extensively investigated for the development of synthetic recognition elements in analyte sensing assays.[14,34,35] Artificial chemosensors based on host-guest systems consist of a host molecule, synthesized from chemically robust components as the recognition element in the sensor. The receptor host molecules contain a guest binding pocket that is formed by the convergent arrangement of functional groups to either a macrocyclic or cleft shaped scaffold (Figure 1.3).[14,35] Complementary guest molecules are encapsulated in the host cavities resulting in a host-guest inclusion complex (Figure 1.3). The internal features of the host cavities facilitate guest inclusion *via* strong driving forces such as hydrogen bonding, electrostatic interaction, and hydrophobic forces and *via* specific molecular shape or size matching.[36] The binding event can cause changes on the physical, chemical and spectroscopic properties of the host or guest.[37] The host molecular architectures are limited only by the creativity and capabilities of synthetic organic chemists, and can in principle be tailored for a wide variety of analytes of interests.[11,37,38] The optical properties, solubilities, and other characteristics of the recptor host molecule can be adjusted to meet requisite sensor specifications. As a result, synthetic host molecules as recognition elements in chemosensors have gained increasing popularity, especially for their applications in the biomedical field.[39-41]

In order to design practical applications using host-guest systems, it is essential to understand the molecular recognition of host-guest binding interactions. The association event can be characterized in terms of its thermodynamic (the extent to which association occurs) and kinetic (the rate at which it occurs) properties.

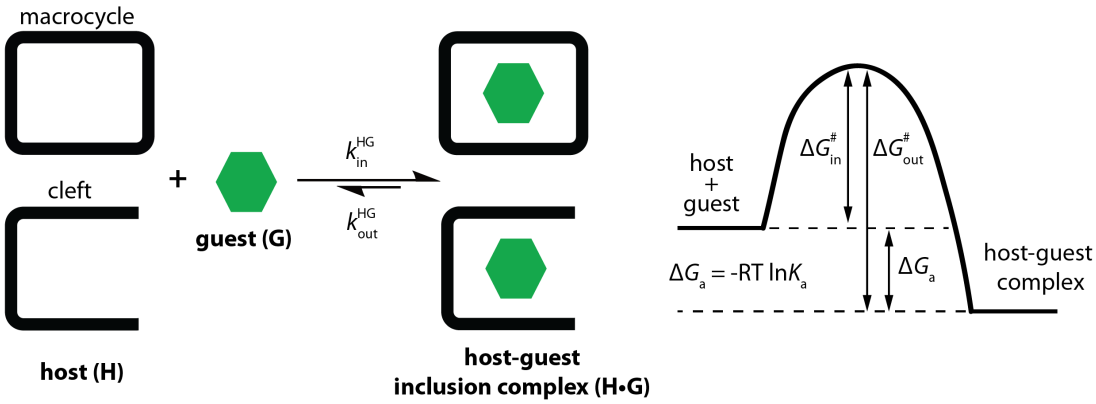

Figure 1.3: Schematic representation of the host-guest inclusion phenomenon, where the host molecule (H) possessing a macrocyclic cavity or cleft encapsulates the guest molecule (G). The energy diagram for the complexation of the host and the guest is shown on the right.

Different sensing applications have distinctive thermodynamic and kinetic requirements for optimal performance, and hence these parameters are often informative benchmark values.[42,43] The binding interaction between host, H and guest, G is reversible and may be described as:

$$\mathrm{H} + \mathrm{G} \rightleftarrows \mathrm{HG} \qquad \text{Eq. 1.1}$$

The association constant or binding constant (K_a) for this reaction can be defined as:

$$K_\mathrm{a} = \frac{[\mathrm{HG}]}{[\mathrm{H}][\mathrm{G}]} = \frac{1}{K_\mathrm{d}} \qquad \text{Eq. 1.2}$$

The larger the K_a, the more stable the respective complex.[44] The binding efficiency is also often characterized by the dissociation constant (K_d), which is the reciprocal of the association constant. Both K_a and K_d belong to the key thermodynamic parameters that describe the stability of supramolecular host-guest complexes.[44]

The thermodynamic driving force of complex formation is described in quantitative terms by the following equation:

$$\Delta G_\mathrm{a} = -\mathrm{RT} \cdot \ln K_\mathrm{a} \qquad \text{Eq. 1.3}$$

The equation describes the correlation between the association constant of the complex (K_a) and the Gibbs free energy of its formation (ΔG_a). R and T are the gas constant and temperature.

In addition to thermodynamic studies, kinetic studies are essential to understanding the supramolecular binding dynamics, which are crucial to the properties of the systems, such as in the case of guest release or transport, catalysis, etc.[43]

The kinetics of host-guest complex formation is defined as follows:

$$\mathrm{H} + \mathrm{G} \underset{k_\mathrm{out}}{\overset{k_\mathrm{in}}{\rightleftarrows}} \mathrm{HG} \qquad \text{Eq. 1.4}$$

$$\frac{\mathrm{d}[\mathrm{HG}]_t}{\mathrm{d}t} = k_{\mathrm{in}} \cdot [\mathrm{H}]_t[\mathrm{G}]_t - k_{\mathrm{out}} \cdot [\mathrm{HG}]_t \qquad \text{Eq. 1.5}$$

where k_{in} and k_{out} denote the rate constants for complexation and decomplexation.

The association constant is connected to the kinetic rate constants *via*:

$$K_{\mathrm{a}} = \frac{k_{\mathrm{in}}}{k_{\mathrm{out}}} \qquad \text{Eq. 1.6}$$

The Gibbs free energy of activation for complexation ($\Delta G_{\mathrm{in}}^{\#}$) and decomplexation ($\Delta G_{\mathrm{out}}^{\#}$), dictate the corresponding rate constants for these steps (k_{in} and k_{out}, respectively) and can be approximated using the Eyring's equation[45] as follows:

$$\Delta G_{\mathrm{in}}^{\#} = -\ln\left(\frac{k_{\mathrm{in}}}{k_B \mathrm{T}/h}\right) \cdot \mathrm{RT} \qquad \text{Eq. 1.7}$$

$$\Delta G_{\mathrm{out}}^{\#} = -\ln\left(\frac{k_{\mathrm{out}}}{k_B \mathrm{T}/h}\right) \cdot \mathrm{RT} \qquad \text{Eq. 1.8}$$

where k_B is the Boltzmann constant and h is the Planck constant.

An important goal in synthetic supramolecular chemistry is to design host molecules that are operational in water and reach the performance of natural receptors.[38,46,47] High analyte selectivity is a hallmark of biological receptors.[18] At the same time high binding affinity ensures high sensitivity for the chosen analyte of interest.[18] Achieving this finely tuned binding affinity and selectivity with supramolecular hosts is essential to fulfilling their desired applications. Thermodynamic parameters of host-guest binding such as K_{a} and ΔG_{a} determines the binding affinity. In order to assess the selectivity of a host for two guests, the thermodynamic selectivity, which is equal to the ratio of association constants for two separate guests, is often utilized.[35] In addition to thermodynamics, the kinetics of host-guest interactions can give additional molecular recognition information and is invaluable to assessing the functionality of a particular host system.[43,48] Finally, designing synthetic host molecules that are soluble in water and can still carry out their programmed binding function in the presence of salts and co-solutes is important for their biological applications, which are mainly pursued in saline buffers or biofluid with high salt contents, *e.g.*, blood serum, urine and saliva.[34] The following section gives an overview of common water-compatible host systems utilized as synthetic recognition elements in sensing assays and their typical guest binding characteristics.

1.1.3. Examples of water-compatible host systems

To design water-compatible host systems with high affinity and selectivity for the binding guests, it is often helpful to take cues from supramolecular systems in nature. For instance, the protein streptavidin exhibits one of the highest binding affinities known for small molecules (biotin) in aqueous media with K_a of 3 x 10^{13} M^{-1}.[49] This high binding affinity is achieved by burying the guest in a structurally well-defined cavity or cleft in the protein structure.[50] In addition, the binding is driven by the release of energetically frustrated water molecules from the protein binding pocket and hydrogen bonding interaction between the host and the guest.[51] These natural receptors provide inspiration for the rational design of synthetic host molecules operational in water and help to better understand the binding forces that contribute to host-guest complex formation. The key to success is to create host molecules with cavities where the guests find appropriate binding partners with favorable forces that contribute to complex formation. The entropy-driven classical hydrophobic effect is one of the most studied driving forces for host-guest complexation in aqueous solutions.[34,52,53] Noteworthy, in the case of small hosts with highly concave surfaces, the enthalpy-driven non-classical hydrophobic effect becomes dominant with emphasis on the enthalpy gain *via* release of high-energy water molecules buried inside the host cavities upon guest binding (Figure 1.4).[46,52,54] Concave, deep macrocyclic hosts, such as molecular barrels or cups, and molecular tweezers efficiently screen the cavity water molecules from contact with the bulk solution and hence maximize the hydrophobic contributions to host-guest binding.[52] In addition, electrostatic interactions and hydrogen bonding interactions between the host and guest also play a significant role in driving the complex formation.[46,52]

Chemists have demonstrated that many macrocycles can be designed that exhibit molecular recognition.[14,38,55] One of the earliest examples of such a system includes crown ethers, which

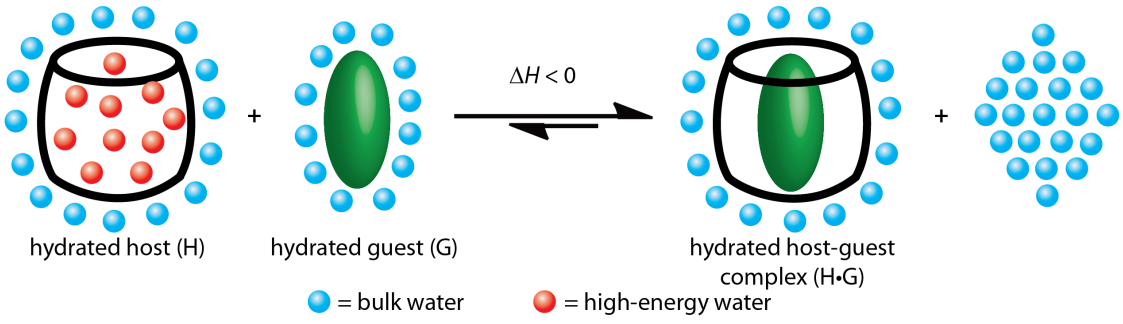

Figure 1.4: Schematic representation of the enthalpy-driven hydrophobic effect in host-guest binding interactions. Water encapsulated in small host cavities is highly constrained such that the cavity is poorly hydrated. The release of very poorly hydrogen-bonded cavity water molecules upon guest binding leads to new, favorable host-guest contacts and the formation of new hydrogen bonds, resulting in a favorable exothermic binding signature.

can selectively bind specific cations.[56] Since then, several artificial systems have been established that exhibit good binding affinities for a series of charged and neutral guests in aqueous media. Importantly, macrocyclic concave hosts and their derivatives, *e.g.*, cyclodextrins, calix[*n*]arenes, cucurbit[*n*]urils, pillar[*n*]arenes, and molecular tubes, and acyclic concave hosts, *e.g.*, clips and tweezers are prominent examples and are discussed in brief here.

Cyclodextrins (CD, see Figure 1.5a) are a popular class of water-soluble macrocyclic hosts that have attracted much attention, especially for their biological applications.[14] Cyclodextrins are cyclic oligosaccharides containing *n* 1,4-linked α-D-glucopyranoside units (α-CD, *n* = 6; β-CD, *n* = 7; γ-CD, *n* = 8), which can be produced from enzyme-triggered starch degradation.[57] They possess a truncated-cone shape with a hydrophilic external surface and a hydrophobic hollow cavity, where the hydroxyl groups of the glucose units are oriented towards the outside at the two ends of the rim, while methinic protons are located inside the cavity (Figure 1.5a).[57] Cyclodextrins and their derivatives are reported to bind a variety of guests, including small molecules,[58] charged guest[59], and proteins[60] in water, where the binding is mainly driven by the hydrophobic effect.[52] However, the binding affinity of cyclodextrin-based host-guest complexes is generally low and typically ranges from 10 to 10^5 M^{-1},[50,58] thereby requiring millimolar concentrations of the host to achieve a significant complexation of the guest molecule. Chemical modification of cyclodextrins with mono-, di- and per-substitution at the C2, C3, and C6 hydroxy groups with permanently charged cations and anions have been shown to increase binding affinities in water significantly.[61,62] One notable example is the polyanionic γ-CD derivative sugammadex (Figure 1.5b), which has been designed to bind steroidal cationic neuromuscular blocking agents in order to reverse their anesthetic effects.[63] However, the affinity do not exceed 10^6 M^{-1}. Hence, artificial binders with higher affinities and selectivities are required to eventually allow sensing at typical nanomolar concentrations of guests.

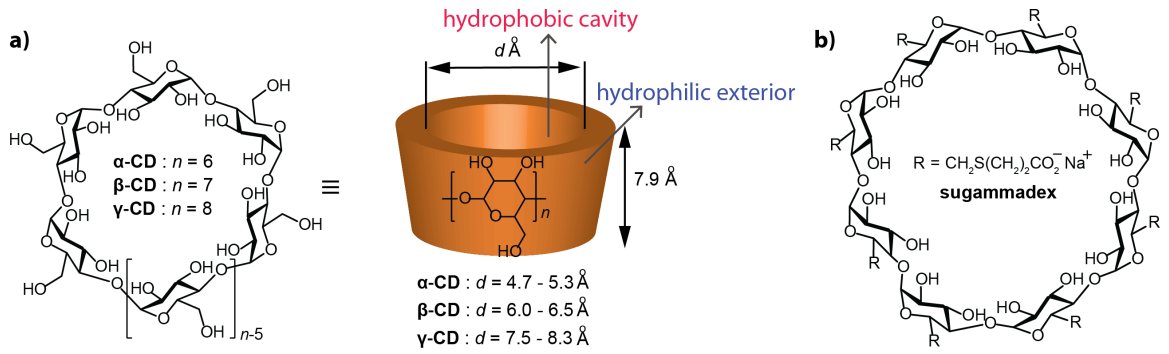

Figure 1.5: (a) Chemical structure and schematic representation of various cyclodextrins (α-CD, *n* = 6; β-CD, *n* = 7; γ-CD, *n* = 8) and the corresponding size estimations for their inner cavity diameter d and height h.[64] (b) Chemical structure of the polyanionic γ-CD derivative sugammadex that bind steroidal cationic neuromuscular blocking agents and used to reverse the effects of muscle relaxants given to patients during surgery.[63]

Another class of macrocyclic hosts is calix[*n*]arenes (CX*n*, see Figure 1.6a), formed by base-catalyzed condensation of a *p*-substituted phenol with formaldehyde, resulting in *n* number of phenol units linked by methylene bridges in the ortho position.[38] They are commercially available in different sizes (CX4, CX5, CX6, and CX8). Calix[*n*]arenes possess a vase-shaped structure with a wider upper rim and a hydrophobic cavity. A narrower lower rim features phenolic oxygen and thus has a hydrophilic property (Figure 1.6a).[14] Both the upper and lower rims can be functionalized by suitable aliphatic and aromatic groups.[65] Calix[*n*]arenes bind a range of guests, such as small organic molecules, ions, sugars, and proteins at both rims of the host, where the complexation is driven by ion-dipole interaction, the hydrophobic effect, and hydrogen bonding interaction.[65] However, compared to cyclodextrins, bare calix[*n*]arenes have poor water solubility. Sulfonation at the rims of calix[*n*]arenes is a common strategy to prepare water-soluble hosts.[66] For instance, CX5 with alkyl sulfonate substituents at the lower rim binds dopamine, tyramine, and phenethylamine in water. However, the binding affinities for the guests were found to be moderate (approx. 10^3 M^{-1}).[67,68] The anionic calix[*n*]arene derivative *p*-sulfonatocalix[4]arene (SCX4, Figure 1.6b) are highly water-soluble and exhibit low toxicity, which makes them potential hosts for diverse biomedical applications. SCX4 preferentially bind cationic guest in water ($K_a \approx 10^5$ M^{-1} for methyl viologen).[38,69] In selected cases, utilizing ion-ion interactions between the substituted calix[*n*]arene and highly charged cationic guests, affinities of the respective host-guest complex can exceed 10^9 M^{-1}.[70] The recently reported amphiphilic sulfonatocalix[5]arene (Figure 1.6c) assembly with lucigenin dye (LCG) selectively bind polycationic polyamine, spermine in aqueous buffers with binding affinities reaching 10^7 M^{-1}.[71] The self-assembled host-dye system have feasible applications for bioimaging of spermine in living cells.[71] However, the aqueous binding strength of non-charged organic guests with calix[*n*]arenes is unimpressive and does not exceed 10^3 M^{-1} as high-energy water constitutes only a minor driving force for complex formation in these widely open host cavities. The binding is driven by additional cation–π interactions in case of cationic guests.[38]

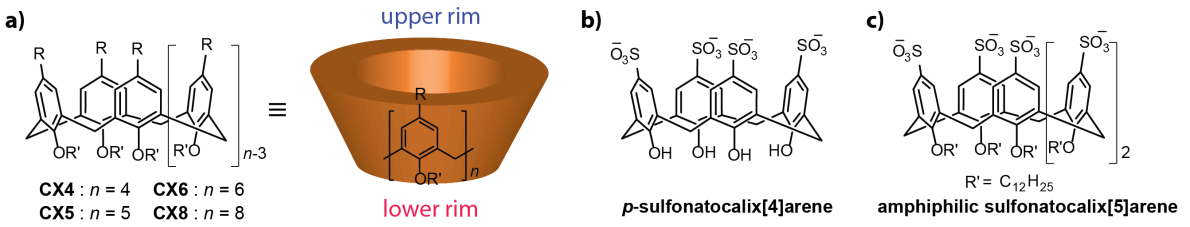

Figure 1.6: (a) Chemical structure of parent calix[*n*]arenes (CX*n*) and schematic representation of the vase-shaped structure with a wider upper rim and a narrower lower rim which both can be functionalized by suitable aliphatic and aromatic groups R and R'. (b) Water-soluble negatively charged *p*-sulfonatocalix[4]arene host that is selective for cationic guests.[69] (c) Amphiphilic sulfonatocalix[5]arene host that selectively binds polycationic polyamine, spermine in aqueous buffers.[71]

Cucurbit[*n*]urils (CB*n*, see Figure 1.7a) are macrocyclic hosts composed of *n* glycoluril units connected by methylene groups. They are obtained by acid-catalyzed condensation of glycoluril with formaldehyde.[13] CB*n* have a pumpkin-shaped structure with two hydrophilic carbonylated rims and a nonpolar and hydrophobic cavity (Figure 1.7a) that is capable of binding both neutral and positively charged guest molecules including amino acids, peptides, neurotransmitters, hormones, drugs, and toxins with binding affinities ranging from 10^3 – 10^9 M^{-1}.[13,55,72,73] The binding is mainly driven by hydrophobic effect.[52] For cationic species, the ion-dipole interactions with carbonylated portals also play a major role in host-guest binding.[52,54] Different homologs of cucurbit[*n*]urils with varying cavity and portal dimensions and different recognition properties are known, mainly CB6, CB7, and CB8. CB6 is known to strongly bind alkyl ammonium ions, while CB7 can host larger molecules such as adamantane and their derivatives. CB8 can even complex two molecules by forming 1:2 host-guest complexes.[74] Cucurbit[*n*]urils are known for their extremely high affinity towards some guest molecules.[73] For instance, CB8 binds a wide range of steroids such as testosterone and β-estradiol with K_a values exceeding 10^6 M^{-1}, stronger than any other reported water-compatible hosts, such as cyclodextrins.[75] CB7 shows one of the strongest affinities for organic molecules in water, reaching a value of 7×10^{17} M^{-1} for a diamantane derivative, exceeding even those of the streptavidin-biotin system.[76] These high binding strengths can be attributed to the strong enthalpic gain upon release of high-energy water molecules from the confined and hydrophobic host cavities into the aqueous bulk solution, where they can engage in a stronger hydrogen bonding network.[52,54]

The low water solubility of cucurbit[*n*]urils, especially CB6 and CB8, is a major limiting factor for their biomedical studies.[14] Their solubilities are enhanced in acidic conditions or in the

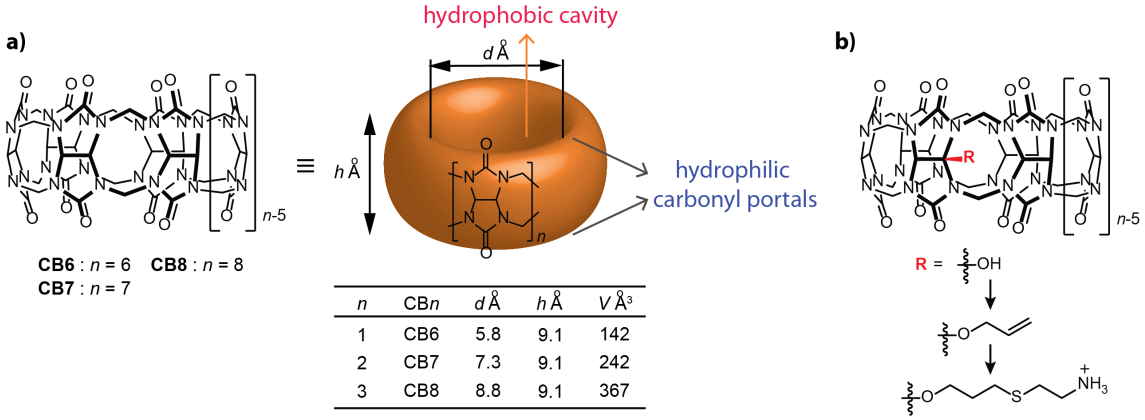

n	CB*n*	*d* Å	*h* Å	*V* Å³
1	CB6	5.8	9.1	142
2	CB7	7.3	9.1	242
3	CB8	8.8	9.1	367

Figure 1.7: (a) Chemical structure and schematic representation of various cucurbit[*n*]uril (CB*n*) and the corresponding size estimations for their inner cavity diameter *d*, height *h*, and cavity volume *V*.[38] (b) Examples of functionalized cucurbit[*n*]uril derivatives.[38]

presence of alkali metal ions. In addition, poor water solubility can be overcome by introducing functional groups onto cucurbit[*n*]urils.[14] In general, cucurbit[*n*]urils are photochemically inert. However, despite their chemical inertness, a few strategies have been established for CB*n* functionalization which include a stepwise buildup of functionalized CB*n* derivatives from tailor-made monomers or *via* controlled oxidative hydroxylation of CB*n* macrocycles.[77,78] The hydroxylated CB*n* can be further functionalized in several ways (Figure 1.7b). Cucurbit[*n*]urils are a promising class of macrocyclic hosts with versatile applications as, *e.g.*, fluorescent sensors, and as building blocks for peptide recognition, and drug delivery systems.[79-82]

Pillar[*n*]arenes (P*n*A, see Figure 1.8a), mainly pillar[5]arenes, pillar[6]arenes, and pillar[7]arenes, are a new class of reported macrocyclic hosts composed of *n* hydroquinone units connected by methylene bridges in their para positions.[83,84] Because of their facile synthesis, easy functionalization, and interesting host-guest binding properties, these host molecules are now widely used in supramolecular applications.[85-87] P*n*A possess a cylindrical-shaped cavity with symmetric openings at both ends (Figure 1.8a).[55] As the pillar[*n*]arene units are constructed from election-rich building blocks, the host cavities show a binding preference for election-deficient guests.[38,55] Furthermore, the cylindrical structure very efficiently enhances the π-electron density in the cavity.[55] While native pillar[*n*]arenes lack water solubility, they can be easily functionalized by introducing hydrophilic cationic or anionic groups on both rims to obtain water-soluble P*n*A.[55,85] In fact, water-soluble carboxylated pillar[*n*]arenes (*n* = 5 or 6, Figure 1.8b) are reported to selectively bind cationic species such as pyridinium, viologen, and ammonium salts with binding affinities in the range from 10^3 – 10^7 M^{-1}.[88-90] The binding is driven by a combination of hydrophobic effect and electrostatic interaction between the cationic guests and the carboxylate anions on the rims.[55]

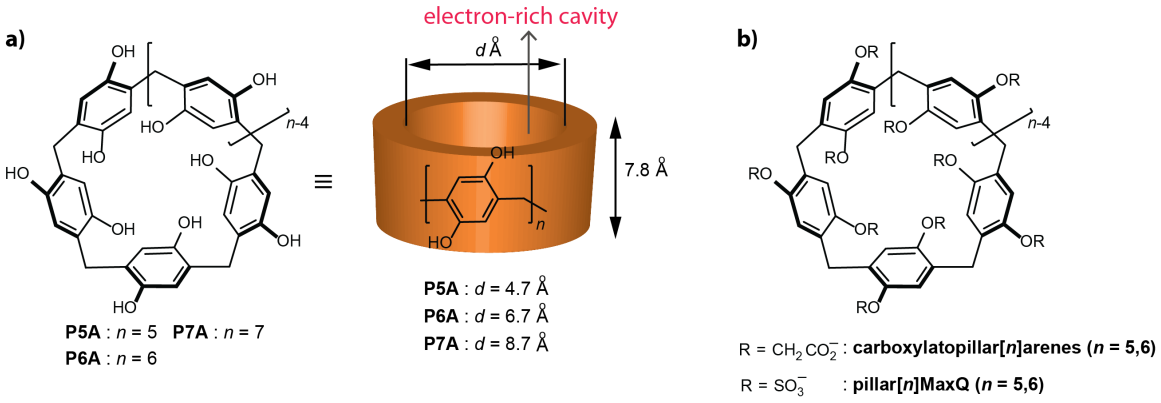

Figure 1.8: (a) Chemical structure and schematic representation of various pillar[*n*]arenes (P*n*A) and the corresponding size estimations for their inner cavity diameter d and height h.[91,92] (b) Chemical structure of the anionic water-soluble carboxylated pillar[*n*]arenes that selectively bind cationic species,[88] and the pillar[*n*]arene sulfates (Pillar[*n*]MaxQ) that possess ultratight binding towards quaternary (di)ammonium ions in aqueous solution.[90]

In addition, these host molecules are relatively nontoxic.[38] They are hence used for drug delivery and biodiagnostic applications due to their high water solubility and ability to complex drugs and biorelevant species.[93,94] The carboxylated pillar[*n*]arenes (*n* = 5 or 6, Figure 1.8b) contain CH_2-linkers between the aromatic ring and the anionic carboxylate functional groups. Removing the CH_2-linkers and changing to the highly acidic sulfate functional group would result in a higher negative charge density around the mouth of the cavity.[90] Recently reported pillar[*n*]arene sulfates (a.k.a. Pillar[*n*]MaxQ, *n* = 5 or 6, Figure 1.8b) possess high binding affinity with K_a reaching 10^{12} M^{-1} towards quaternary (di)ammonium ions in aqueous solution which makes them prime candidates for several biomedical applications.[90] The guest binding is mainly favored by sizeable electrostatic effects and due to the absence of a large hydrophobic driving force these host molecules are more selective guest binders than cyclodextrins or cucurbit[*n*]urils.[38]

The recently reported naphthalene-based molecular tubes represent a new class of macrocyclic hosts that combines a hydrophobic cavity with endo-oriented NH-amide groups as hydrogen bond donors (Figure 1.9).[95-97] The majority of the previously reported water-compatible host systems have no functional groups inside their hydrophobic cavity.[38] Hence for organic guests with both polar and nonpolar groups, these hosts either fully encapsulate them inside their hydrophobic cavity, in which case the dehydration penalty of the polar groups is not well compensated, or they only bind to the nonpolar group by exposing the polar groups to the bulk water.[98] As a result, these host systems often show poor binding affinity and selectivity to organic molecules with polar and nonpolar groups.[50] The new naphthalene-based molecular tubes (Figure 1.9) with polar binding sites in their hydrophobic pockets selectively bind highly hydrophilic molecules in water, such as 1,4-dioxane, urethane, epoxides, and carboxylic acids.[95-97,99] The binding is mainly driven by the hydrophobic effect and hydrogen bonding between the polar groups of the guests and the amide protons of the hosts, which effectively compensates for the desolvation penalty of the guest polar groups.[97,98] It has also been shown that these naphthotubes bind strongly to organic drug molecules with multiple polar groups with binding constants as high as 10^6 M^{-1} in water.[98] In contrast, other hosts, *e.g.*, β-cyclodextrin generally bind weakly to neutral drug molecules. [98] Hence, the naphthotubes are a promising class of host molecules, allowing for the selective binding of guests beyond hydrophobicity as a selection criterion with potential biomedical applications.

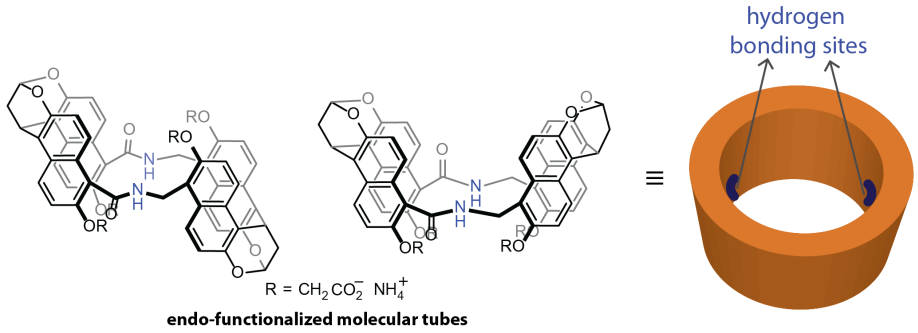

Figure 1.9: Chemical structures and schematic representations of water-soluble endo-functionalized molecular tubes that combine hydrogen bonding recognition sites in their hydrophobic pockets and selectively bind highly hydrophilic molecules in water, such as 1,4-dioxane.[95,96]

Acyclic concave hosts that contain partially enclosed cavities capable of binding guests provide unique synthetic and functional advantages than their macrocyclic counterparts.[38] Examples of such acyclic concave host systems include molecular tweezers and clips.[38] A new water-soluble molecular tweezer possessing a cavity in the form of a preorganized cleft with high electron density on its inner surface and two rotatable peripheral anionic phosphonate groups (Figure 1.10a) was reported in 2005.[100,101] The tweezer selectively bind the positively charged amino acids lysine, arginine, and their derivatives.[100,101] This selective binding is driven by a combination of size-selective interaction, electrostatics, hydrophobic effect, and dispersive interactions. Binding affinities were in the range of 10^3 – 10^4 M^{-1} when monitored in both D_2O and 25 mM phosphate buffer.[100] Even higher binding affinities with excellent selectivities for lysine and arginine were observed upon replacing the phosphonate with phosphate groups (CLR01, Figure 1.10a), with K_a values ranging from 10^4 – 10^5 $M^{-1}$when monitored in buffer solutions under physiological conditions.[102,103] Also, peptides containing sterically accessible lysine and arginine residues showed similar binding affinities.[102] The molecular tweezer CLR01 was able to bind abnormally folded peptides and proteins that possess sterically accessible lysine and arginine residues and thus ensured cell viability with promising results in animal tests as potent inhibitors of pathologic protein aggregation.[102] Moreover, CLR01 destroys enveloped viruses, including HIV, by binding the basic amino acids in amyloid-forming SEVI peptides, leading to disaggregation and neutralization of the fibrils, which lose their ability to enhance HIV-1/HIV-2 infection.[104,105] Hence molecular tweezer presents a promising class of supramolecular hosts with future medical applications. Recently introduced, acyclic cucurbit[*n*]uril-type receptors (acyclic CB*n*, see Figure 1.10b) are highly water-soluble host molecules that adopt an almost closed tweezer-type structure.[4,106,107] They display high binding affinities for aliphatic and aromatic guests, including amino acid amides, peptides, proteins, and

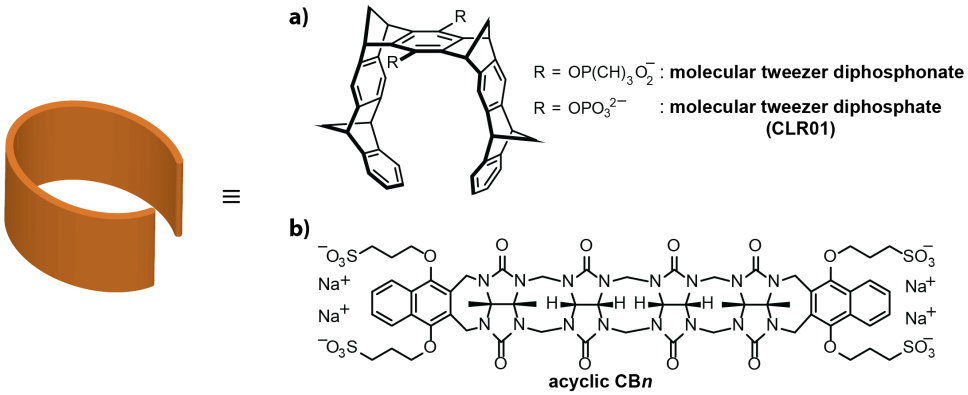

Figure 1.10: Chemical structure and schematic representation of water-soluble acyclic concave host systems. (a) Molecular tweezers bearing methanephosphonate groups or phosphate groups (CLR01) in the central benzene bridge that selectively binds lysine and arginine guests, and (b) acyclic cucurbit[*n*]uril-type receptors a general-purpose high-affinity host that binds a broad range of aliphatic and aromatic guests.

drug molecules with affinities ranging from 10^4 – 10^9 M^{-1}.[107-110] These acyclic systems shows that giving hosts small degrees of added flexibility provides specific advantages. For instance, the macrocyclic CB7 binds many ammonium ion guests very strongly. However, it does not bind morphine at all, as the structural rigidity of CB7 limits the size of drugs that can be encapsulated.[111] Conversely, acyclic cucurbit[*n*]uril host molecules bind strongly to morphine ($K_a \approx 10^5\ M^{-1}$) and a diverse range of similarly large guests.[111] These acyclic cleft-like hosts are rigid enough to exhibit strong binding but are sufficiently flexible to accommodate larger guests that cannot be bound by its cyclic counterpart.[109] Hence, acyclic cucurbit[*n*]uril functions as a more general purpose high-affinity host with modest selectivities in water.[109] They bind a broad range of hydrophobic pharmaceuticals and function as solubilizing agents for insoluble drugs for drug delivery applications.[4,107] For instance, the solubility of paclitaxel was increased 2,750 times through the formation of a soluble acyclic CB*n*–drug complex.[4]

1.2. Optical Signal Transduction

In artificial chemosensors, the generation of a signal upon analyte binding is important for sensing applications. Common detection methods employed for signal transduction include (i) optical (*e.g.*, absorbance-, fluorescence-, or chemiluminescence-based), (ii) electrochemical (*e.g.*, potentiometric-based), (iii) thermal (*e.g.*, calorimetric-based), and (iv) magnetic.[112-116] In developing an efficient chemosensor, the need for reliable and sensitive detection tools has become vitally important. In this context, optical chemosensors, particularly based on fluorescence detection techniques, have gained prominence as they are fast, highly sensitive, offers high spatial and temporal resolution, low cost with readily available instrumentation, non-invasive, applicable for high-throughput screening, and utilization in array systems to detect multiple analytes.[16,113,117,118]

The following sections give a brief introduction to fluorescence fundamentals and the different strategies employed for analyte detection in fluorescence-based sensing assays. Followingly, a few representative fluorescent chemosensors based on macrocyclic/acyclic concave hosts as recognition elements are described for analyte detection and reaction monitoring.

1.2.1. Fluorescence as a method for detection

Fluorescence, a type of luminescence, is the phenomenon of emission of light quanta or photon by a molecule or supramolecular structure in its electronically excited state after initial excitation in a light-absorption process.[119-122] The molecule in the singlet excited state upon energy relaxation transitions back to its singlet ground state, during which the excess energy is released as a photon.[119-122] Fluorescence is hence a radiative transition. However, competitive nonradiative pathways, without the emission of a photon, also exist for the relaxation of excited states.[119-122] A Jablonski diagram (see Figure 1.11a) can be used for convenient visualization of these processes and the various relaxation pathways.[119,120] The absorption and emission of photons by a molecule involves electronic transitions between quantized energy levels (see Figure 1.11a). As a result, only photons of specified energies can be absorbed or emitted. S_0 denotes the singlet electronic ground state, and S_1, S_2,.. the singlet excited states. T_1, T_2,.. denote the triplet excited states. Vibrational levels are associated with each electronic state. The irradiation of a molecule can result in the absorption (ABS) of a photon and transition from the lowest vibrational level in its electronic ground stare (S_0) to a range of vibrational levels in its electronic excited states, such as S_1 and S_2 (Figure 1.11a). This process is very fast (within 10^{-15} s) and hence occurs without any change in the atom nuclei configuration (Franck-Condon principle).[119,123] Once the molecule is in the electronic excited state, different relaxation processes starts to proceed. In most cases, the molecule relaxes quickly to its first excited electronic state (S_1) *via* internal conversion (IC, in 10^{-11} s to 10^{-9} s) and the lowest vibrational state in the given electronic state (Kasha's rule[124]) *via* vibrational relaxation (VR, in 10^{-12} s to 10^{-10} s) (see Figure 1.11a). The system can now return to its electronic ground state as the molecule relaxes from the S_1 to S_0 state *via* a radiative decay with the emission of a photon in the form of fluorescence (FL, in 10^{-10} s to 10^{-7} s) (see Figure 1.11a). This phenomenon competes with non-radiative relaxation from the S_1 to S_0 state *via* internal conversion, where the rate of the process increases exponentially with a decreasing energy gap between the excited and the ground state (energy gap law).[125,126] In addition, the molecule can also undergo a spin-forbidden transition from an excited singlet state, S_1, to the lowest excited triplet state, T_1, through nonradiative intersystem crossing (ISC, in 10^{-10} s to 10^{-8} s) (see Figure 1.11a).

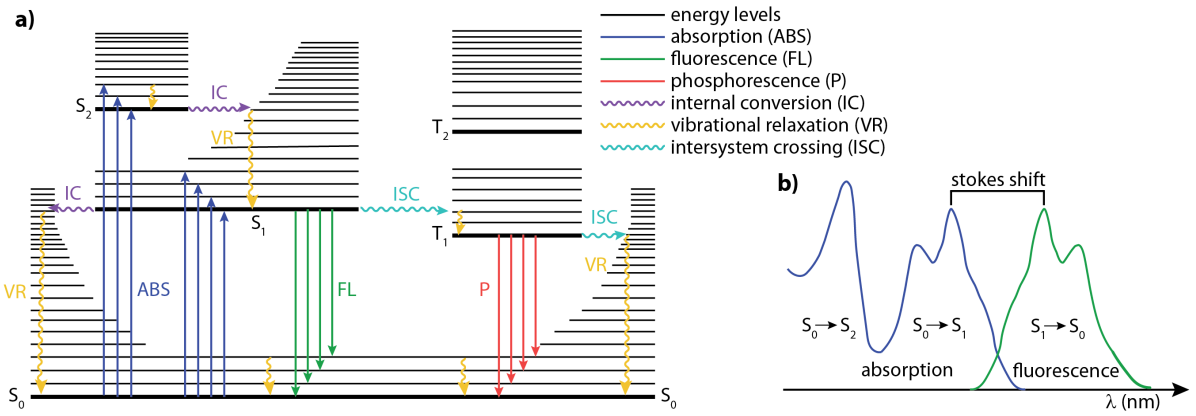

Figure 1.11: (a) Jablonski diagram summarizing the various states and photophysical processes observed following the absorption of light. (b) Typical absorption and fluorescence emission spectra; the fluorescence spectrum is located at longer wavelengths with respect to the absorption spectrum. The difference between their band maxima is demonstrated as the Stokes shift.

The molecule then relaxes from the T_1 state to the singlet ground state S_0 in a radiative pathway with the emission of a photon, which is called phosphorescence (P) (see Figure 1.11a). Due to the spin forbidden nature of phosphorescence, it is much less probable than fluorescence and proceeds on a much slower time scale (in 10^{-6} s to 1 s).

Absorption and fluorescence emission spectra can be recorded using a UV-Vis spectrometer and fluorescence spectrometer, respectively, and show a distribution of the corresponding electronic transition probabilities on their energies, where longer wavelengths correspond to lower energies (see Figure 1.11b). As is clear from the Jablonski diagram, the fluorescence emission occurs at longer wavelengths and, therefore, at lower energy than absorption (see Figure 1.11b). This is due to the loss of vibrational energy in the excited state by internal conversion. The difference between locations of the band maxima of the absorption and emission spectra of the same electronic transition is called the Stokes shift (see Figure 1.11b).[119,120] Usually, the emission spectrum is often the mirror image of the absorption spectrum since the electronic transitions are vertical (Franck–Condon principle), and the vibrational levels of the excited state are similar to the vibrational levels of the ground state.[119,120] For fluorescent sensing, a large Stokes shift is preferred as it typically results in clearer emission spectra and hence better quality data for analysis.[121]

Fluorescence-based chemosensors refer to those sensors that respond to the presence of the target analyte with a detectable change in the fluorescence signal.[16,113,127,128] Hence, fluorescent chemosensors require a component that is photophysically active in order for the target analyte to induce a measurable change in their photophysical activity, which may occur through a change in the magnitude of emission intensity, the wavelength of the emission maximum, the quantum yield, or the relative ratios of various fluorescence-emitting components.[16,113,127,128]

The following section gives an overview of different signal transduction strategies employed in fluorescence-based sensing assays with the aforementioned macrocyclic or acyclic hosts as recognition elements in the chemosensor.

1.2.2. Strategies in fluorescence-based sensing assays

To utilize artificial chemosensors based on host-guest systems in fluorescence-based sensing assays, the host-mediated complexation of an analyte has to be coupled to a signal transduction event with an easily quantifiable fluorescence signal change.[1,72,113,127] A few examples of fluorescence signal transduction strategies employed in chemosensors based on host-guest systems (see Figure 1.12) are discussed below.

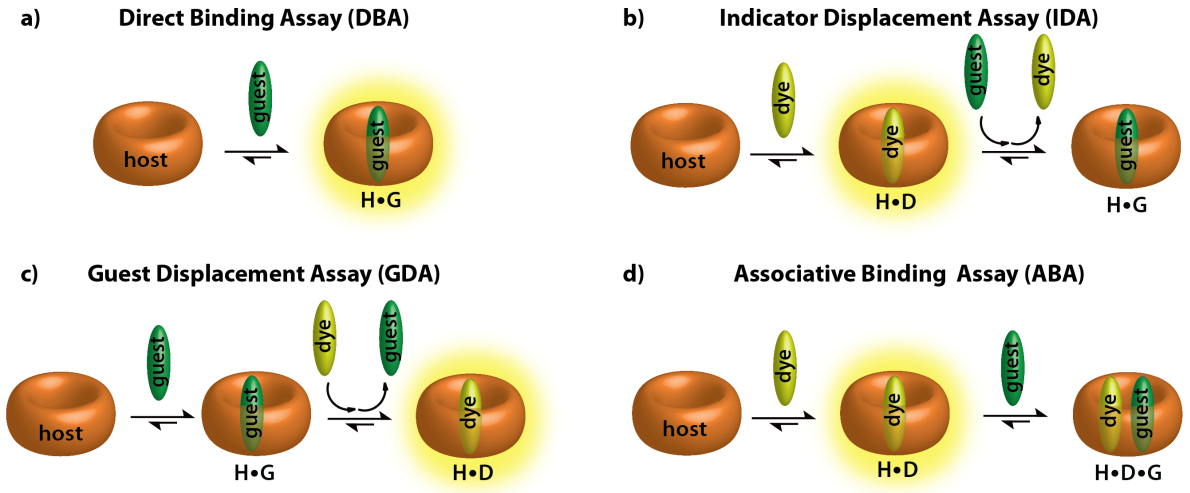

Figure 1.12: Schematic representation of (a) direct binding assay (DBA), (b) indicator displacement assay (IDA), (c) guest displacement assay (GDA), and (d) associative binding assay (ABA) involving a host (H), guest (G) and indicator dye (D). In an analytical assay, the guest refers to the analyte of interest.

In a direct binding assay (DBA, see Figure 1.12a), the interaction between the host and the guest (analyte) molecule results in a directly measurable fluorescence signal change. DBA is appropriate in the case of chromophoric/emissive host or guest molecules, such that the host-guest association interaction results in significant changes in the photophysical properties of either the host or guest.[72] If applicable, DBA is often the most straightforward and practical choice and particularly attractive when the target analyte binding provides a unique spectroscopic response that can be distinguished from the signal caused by cross-reactive analytes.[1] However, unmodified macrocyclic hosts, *e.g.*, cucurbit[*n*]urils, cyclodextrins, calix[*n*]arenes, and pillar[*n*]arenes, and acyclic concave hosts, *e.g.*, molecular tweezers, and acyclic CB*n*, either do not absorb or emit light in the practically relevant near-UV or visible wavelength region[40,41,72,128-130] or exhibit only a weak emission with a low signal response on analyte binding.[102,131] As a result, DBA sensing applications with the aforementioned

unmodified host systems are limited only to inherently spectroscopically active analytes. For instance, in the case of CB*n*•dye complexes, the complexation of the chromophoric dye in the CB*n* cavity results in significant changes in the dye emission (usually enhanced) arising from polarity differences between bulk water and the hydrophobic CB*n* interior and confinement effects by the cavity or by breaking dye aggregation due to complexation.[132-137]

Practical analyte sensing applications require signal generation in the relevant near-UV or visible wavelength region of the electromagnetic spectrum, which also allows the use of low-cost disposable plastic cuvettes and microwell plates. However, most biologically relevant analytes are either not chromophoric/emissive or absorb/emit in the practically not preferred UV range. The non-chromophoric macrocyclic or acyclic concave hosts can be functionalized with covalently linked chromophoric/emissive groups such as aromatic moieties or appended fluorescent dyes, which render them inherently emissive for detection of spectroscopically silent analytes *via* a fluorescence signal change on analyte binding.[40,79,80,129,130,138,139] A fluorescence quenching or enhancement of the chemosensor can occur, *e.g.*, either *via* photoinduced electron transfer process between the bound analyte and the host chromophore or *via* conformational changes of the fluorophore-modified host on accommodation of the analyte.[80,129,138,139] However, covalent functionalization of CB*n* or other aforementioned host systems, though possible, is often cumbersome and involves time-consuming synthetic steps.[40,79,80,129,130,138-140] Hence, new fluorescence signal transduction strategies for monitoring host-guest complex formation between spectroscopically silent hosts and guests may be preferable.

Competitive binding assays, in which a series of guests compete for a host, are well-established in supramolecular chemistry.[141-143] The reversible nature of the molecular recognition process enables differentiation of equilibrium between the host and multiple guests, leading to binding selectivity. An indicator displacement assay (IDA, see Figure 1.12b) represents an elegant class of competitive binding assay that has gained popularity in the past two decades and is extensively exploited for molecular sensing applications.[72,113,144,145] An IDA is a viable option to achieve fluorescence signal transduction in chemosensors, where the host molecule is not chromophoric/emissive or do not produce a significant signal response upon analyte binding.[72,144,145] In an IDA, an indicator dye first binds reversibly to the receptor host molecule *via* non-covalent interactions, resulting in the self-assembled host-dye complex with significant changes in the spectroscopic characteristics of the bound dye. Subsequent addition of competitive binding guest (analyte) results in the displacement of the indicator dye from the host by forming the host-guest complex and recovery of the spectroscopic properties of the unbound dye, which in turn

modulates the fluorescence signal. In general, IDA relies on the distinctly different optical properties of the free and host-bound indicator dye for signal generation. In order to have an IDA with desirable sensitivity for analyte sensing applications, the indicator dye should possess a sufficiently high binding affinity for the host, which is nearly comparable to the binding affinity of the target analyte for the host.[72,144] This helps to achieve a fine balance between a high degree of indicator dye complexation in the absence of the analyte and a sufficiently large displacement of the dye in the presence of the analyte.[72,144] The target analyte must also have a higher affinity at a particular concentration to achieve an effective displacement of the indicator dye and provide a fluorescence signal response.[72,144] The affinity here refers to the extent to which the target analyte is bound to the host relative to the indicator dye and is related to the binding constants and concentration of the host, guest, and indicator dye in the assay. Several reports have shown the utility of IDA with synthetic macrocyclic hosts for fluorescence-based detection and differentiation of diverse analytes.[145-153]

The use of competitive IDA can be limited in situations when the target analyte exhibits a low binding affinity for the host and poor aqueous solubility, prohibiting the use of excess analyte concentrations for the dye displacement. A new competitive binding assay, the guest displacement assay (GDA, Figure 1.12c), was recently introduced, which is advantageous in such situations. In a GDA, the spectroscopically silent and potentially insoluble guest (analyte) was initially complexed by the host to form the host-guest complex, where encapsulation of the guest in the host cavity results in a solubility enhancement.[154] The subsequent addition of the indicator dye results in the competitive displacement of the guest and the formation of the host-dye complex accompanied by a fluorescence signal change relative to the distinct spectroscopic properties of the free and host-bound indicator dye. As the complementary approach to IDA, the GDA method is superior for insoluble and weakly binding guests.[154]

The competitive binding assays, IDA and GDA, offer many advantages over traditional direct-sensing assays.[113,145] First, as the indicator dye is reversibly bound to the receptor host molecule *via* non-covalent interactions, the synthetic efforts to covalently attach the dye to the host molecule are avoided. Second, the reversible non-covalent interactions offer the flexibility of using different indicators with the same receptor, thereby tuning the sensitivity and selectivity of the sensing assay. Third, the technique can be easily adapted for different receptors to perform a quick analysis of the desired analyte.[113,144,145] However, in contrast to the direct signal generation approach, both IDA and GDA format does not provide analyte-specific spectroscopic fingerprints, as the displacement of the indicator dye from the host by an analyte yield always the same type of signal response, *e.g.*, a fluorescence enhancement or quenching

of the dye emission.[72] Hence, the distinction of analytes with a single host is only possible if they have sufficiently different binding constants (which is rarely the case for complicated mixtures). Nevertheless, due to the practicality of the IDA/GDA approach to multiple host systems and the ability to use different indicators, IDA/GDA sensing arrays can be employed with different chemosensing ensembles that have distinct affinity differences for the analyte of interest.[155] Hence analyte identification and differentiation can be achieved by their differential fluorescence signal response.[72,75] Several indicators dyes suitable for IDA or GDA that bind to macrocyclic hosts have been reported,[134,135] such that the preferred spectroscopic response, *e.g.*, fluorescence turn-on or off, can be adopted, and the required affinity range can be preselected depending on the analyte of interest.[72]

In selected cases, it is also feasible to establish an associative binding assay (ABA, see Figure 1.12d).[72,156] Suitable receptor host molecules for ABA are capable of simultaneously binding the dye and the analyte in their cavity.[74,156-160] In an ABA, an indicator dye is first complexed with the host molecule forming the 1:1 host-dye complex, which then allows for the subsequent associative binding of an additional aromatic guest (analyte), resulting in a 1:1:1 ternary complex coupled with a sensitive signal response. The aromatic dye and guest are held in close spatial proximity inside the host cavity in a face-to-face π-π stacking orientation, thereby giving rise to electronic coupling phenomena (*e.g.,* an emerging charge transfer band or a change in the emission spectra).[74,156-160] Hence, in an ABA sensing format, different analytes can be identified by clearly distinguishable spectroscopic fingerprints that arise from the "communication" between the dye and the analyte inside the host cavity. Therefore, the distinction between analytes based on different binding affinities as required for IDA/GDA is not necessary for ABA. In essence, the ABA resembles a DBA approach with the added advantage that the dye component, and thus signal mode, can be readily tuned.

A few examples of representative fluorescent chemosensors for analyte detection *via* the above-mentioned fluorescence signal transduction strategies are discussed in Section 1.2.3.

As discussed in section 1.1.2, it is crucial to have knowledge of the binding parameters of supramolecular host-guest complex formation to evaluate the performance of the chemosensor and for practical sensing applications with improved properties. Several reports have employed a DBA, IDA, or GDA approach with fluorescence signal transduction to elucidate the thermodynamic binding constant of the host-guest association complex.[72,113,154,161] In a DBA, a chromophoric or emissive guest solution is titrated to a spectroscopically silent host solution or vice versa, and the experimentally obtained signal titration curve is fitted following the Eq. 1.9

– Eq. 1.13 to obtain the binding constant (K_a). As the DBA is applicable only in the case of chromophoric/emissive systems, the Eq. 1.9 – Eq. 1.13 is generalized in the case of host-dye complexes, where K_a^{HD} denote the binding constant of the host-dye complex. In an IDA or GDA, the guest solution is titrated to a pre-equilibrated host-dye solution, or the indicator dye solution is titrated to a pre-equilibrated host-guest solution, respectively, and the experimentally obtained signal titration curve is fitted following the Eq. 1.14 – Eq. 1.20 to obtain the binding constant K_a^{HG} of the host-guest complex. An IDA or GDA curve fitting requires a prior determination of the K_a^{HD} value, *e.g.,* through DBA.

DBA	$H + D \rightleftarrows HD$	Eq. 1.9
	$K_a^{HD} = \frac{[HD]}{[H][D]}$	Eq. 1.10
	$[H]_0 = [HD] + [H]$	Eq. 1.11
	$[D]_0 = [HD] + [D]$	Eq. 1.12
	$I_t = I^0 + I^{HD} \cdot [HD] + I^D \cdot [D]$	Eq. 1.13
IDA or GDA	$HD + G \rightleftarrows HG + D$ (IDA) or $HG + D \rightleftarrows HD + G$ (GDA)	Eq. 1.14
	$H + D \rightleftarrows HD$ $H + G \rightleftarrows HG$	Eq. 1.15
	$K_a^{HD} = \frac{[HD]}{[H][D]}$ $K_a^{HG} = \frac{[HG]}{[H][G]}$	Eq. 1.16
	$[H]_0 = [HD] + [H] + [HG]$	Eq. 1.17
	$[D]_0 = [HD] + [D]$	Eq. 1.18
	$[G]_0 = [HG] + [G]$	Eq. 1.19
	$I_c = I^0 + I^{HD} \cdot [HD] + I^D \cdot [D]$	Eq. 1.20

Parameters for Eq. 1.9 to Eq. 1.20 were assigned as follows: [H] – host concentration at equilibrium, $[H]_0$ – initial host concentration, [D] – dye concentration at equilibrium, $[D]_0$ – initial dye concentration, [G] – guest concentration at equilibrium, $[G]_0$ – initial guest concentration, [HD] – host•dye (HD) concentration at equilibrium, [HG] – host•guest (HG) concentration at equilibrium, K_a^{HD} – binding constant of the host•dye (HD) complex, K_a^{HG} – binding constant of the host·guest (HG) complex, I^0– background signal, I^{HD} – signal from host•dye (HD) complex, I^D – signal from free dye (D), I_c – observable signal as a function of concentration.

In addition to the thermodynamic parameters, the kinetic parameters of host-guest interactions are important to obtain a full picture of the supramolecular system.[43,48,162,163] However, kinetic investigations of host-guest systems are lacking in the literature and are available only in a few cases for inherently chormophoric or emissive systems.[43,163-166] Hence new methods to elucidate the kinetic parameters of host-guest interactions for spectroscopically silent hosts and guests need to be developed (see Chapter 4 for more details).

1.2.3. Representative fluorescent chemosensors for detection of biorelevant molecules

A few examples of representative fluorescent chemosensors based on macrocyclic or acyclic concave receptor host molecules are discussed in this section.

In recent years, the IDA-based technique with synthetic receptors has gained significant attention and has been successfully employed for the detection of various biologically relevant analytes. [72,113,144,145] For instance, Nau and coworkers developed a series of IDAs for the detection of amine-containing molecules, such as biogenic amines, peptides, neurotransmitters, etc., in aqueous buffered solutions.[70,128,146,167,168] Amines are protonated at physiological pH, and the resulted ammonium cations can form strong inclusion complexes with macrocyclic hosts, such as calix[*n*]arenes and cucurbit[*n*]urils (Figure 1.13a).[70,128,146,167,168] In order to construct an IDA-based chemosensor, several fluorescent indicator dyes (Figure 1.13b) were evaluated that bind to the macrocyclic host with considerable alteration of their fluorescence behavior upon confinement in the host cavity.[128,134] Specifically, in the case of cucurbit[*n*]urils, the fluorescence of the encapsulated dye is usually enhanced due to relocation into a more hydrophobic, solvent-protected environment.[128,134] While for the electron-rich substituted calix[*n*]arenes, a charge-transfer induced quenching of the complexed fluorescent dyes generally applies. [128,134] As a result, the displacement of the dye from the host cavity in the presence of competitive binding analytes results in a fluorescence decrease in the case of CB*n* complexes and a fluorescence increase in the case of CX*n* complexes (Figure 1.13c). Hence, these systems were adopted for the fluorescence-based detection of diverse amine-containing analytes and to track their real-time changes in concentrations as they occur in enzymatic reactions or during membrane transport.[70,128,146,167,168] For example, an IDA-based approach was adopted to monitor the products of amino acid decarboxylase catalyzed reactions.[167] The macrocyclic hosts cucurbit[7]uril (CB7, see Figure 1.13a) and *p*-sulfonatocalix[4]arene (SCX4, see Figure 1.13a) that interact with two fluorescent dyes, dapoxyl (DAP, see Figure 1.13b) and aminomethyl-substituted 2,3-diazabicyclo[2.2.2]oct-2-ene (DBO, see Figure 1.13b), respectively, were used as the host-dye reporter pairs in the assay. Both CB7 and SCX4 bind weakly with the amino acid substrate (*e.g.*, lysine, arginine, histidine, ornithine) but possess a strong affinity for the corresponding amino acid decarboxylase catalyzed enzymatic product, the cationic biogenic amines (*e.g.*, cadaverine, agmatine, histamine, putrescine), in 10 mM ammonium acetate buffer at pH 6.[167] The fluorescence of dapoxyl is enhanced 200-fold upon binding to CB7. The presence of the stronger competitor, the cationic biogenic amines, results

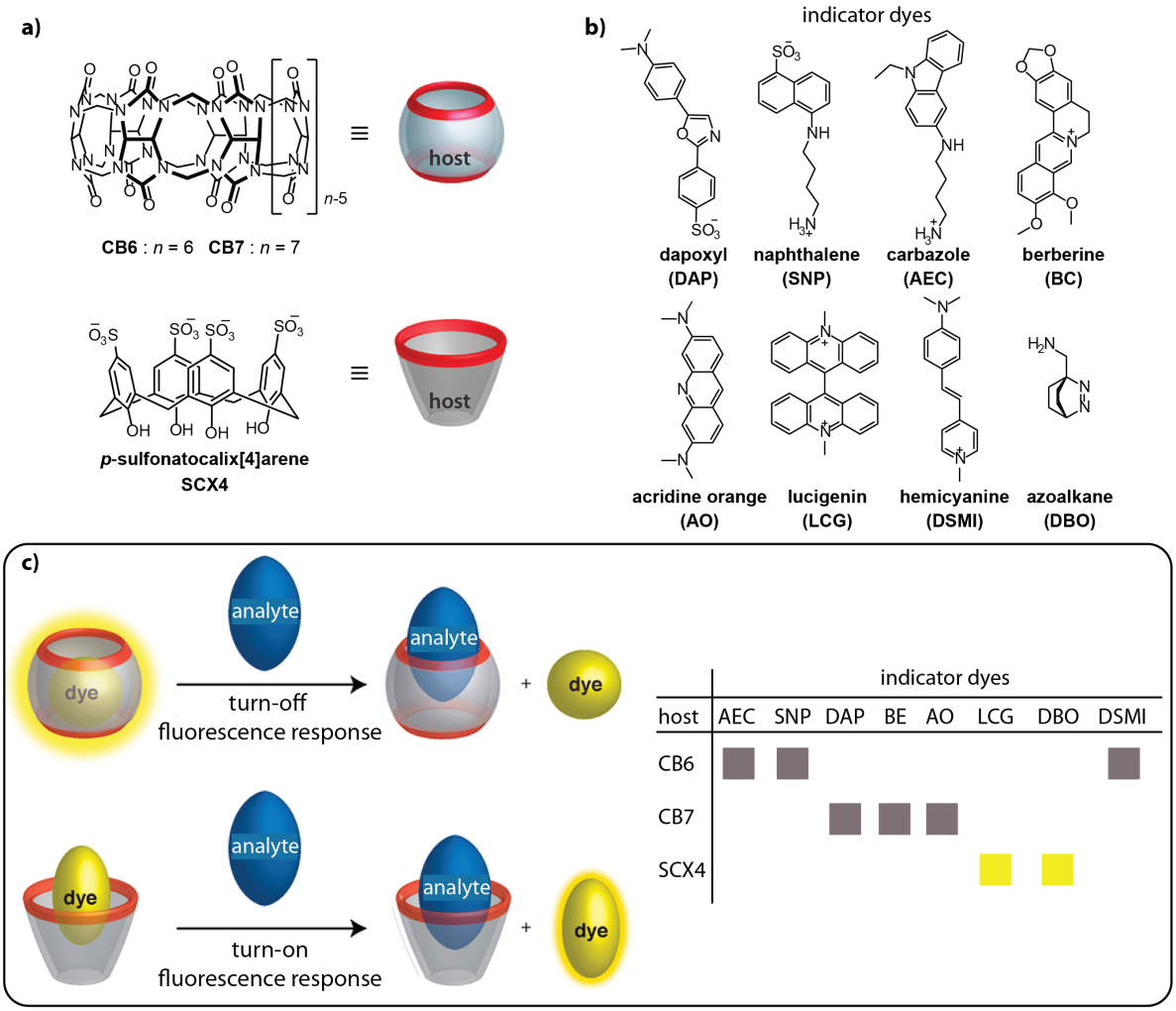

Figure 1.13: Chemical structure of (a) macrocyclic hosts CB6, CB7, and SCX4 used as synthetic receptors and (b) suitable fluorescent indicator dyes. (c) IDA for analyte sensing, where the addition of an analyte is signaled by either a fluorescence decrease or a fluorescence increase due to displacement of the dye from the host. The matrix representation shows the combination of host and dye complexes suitable as chemosensing ensembles in sensing assays indicated by a bar. The color coded in yellow and grey represents an enhancement and quenching of the fluorescence intensity, respectively, upon analyte binding. Reprinted (adapted) with permission from ref.[128] Copyright 2014 American Chemical Society.

in a displacement of the dye from the host molecule with a decrease in fluorescence (turn-off response). However, in the case of SCX4•DBO there is an enhancement in fluorescence once DBO is displaced from the host (turn-on response). The addition of the weaker competitor, the amino acids, did not interfere with the assay. Based on these IDAs, label-free and real-time monitoring of amino acid decarboxylase activity was achieved.[167] Ideally, the fluorescent indicator dye is selected such that its affinity (related to the binding constant and concentration) to the host lies in between that of the substrate and the corresponding product.

Similarly, Urbach, Nau and co-workers developed a method for the continuous monitoring of protease activity on unlabeled peptides in real-time (see Figure 1.14).[146] The macrocyclic host CB7 and the fluorescent dye acridine orange (AO) were used as

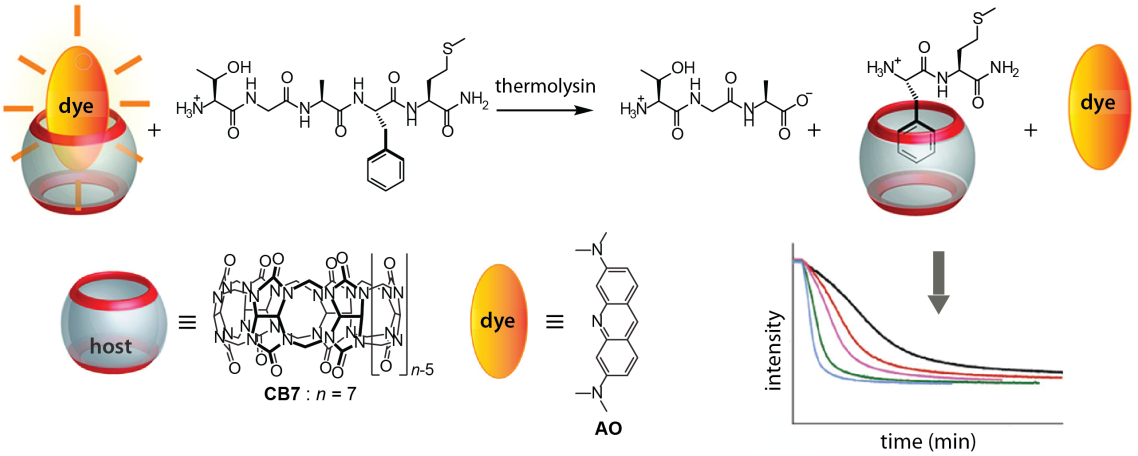

Figure 1.14: Schematic representation of a product selective fluorescence switch-off supramolecular tandem assay for monitoring the hydrolysis of the Thr-Gly-Ala-Phe-Met-NH_2 peptide by the endopeptidase thermolysin using the macrocyclic host CB7 and the fluorescent dye AO as the host-dye reporter pair in an IDA approach. The spectra show the continuous fluorescence signal intensity monitored with time upon adding thermolysin to the peptide in the presence of CB7•AO in 10 mM ammonium phosphate buffer, pH 7.2, at 37 °C. Reprinted (adapted) with permission from ref.[146] Copyright 2011 American Chemical Society.

the host-dye reporter pair in the assay (Figure 1.14). The encapsulation of acridine orange in the CB7 cavity results in an enhancement of the dye fluorescence. CB7 selectively recognizes the N-terminal phenylalanine residue that is produced during the enzymatic cleavage of enkephalin-type peptide by the metalloendopeptidase thermolysin. The affinity of the indicator dye for CB7 lies between that of the peptidic substrate, Thr-Gly-Ala-Phe-Met-NH_2, and of the produced dipeptide, Phe-Met-NH_2, in 10 mM ammonium phosphate buffer at pH 7.2.[146] Thus, during the enzymatic reaction, the indicator dye is displaced from the CB7 cavity by the stronger binding dipeptide, Phe-Met-NH_2 produced during the reaction, resulting in a turn-off fluorescence response and the process can be monitored conveniently by fluorescence spectroscopy in real-time (Figure 1.14). In another work, Nau and coworkers showed a real-time fluorescence monitoring of analyte transport through the lipid bilayer by the selective co-encapsulation of a macrocycle and a fluorescent dye inside liposomes.[70] SCX4 or CB7 (see Figure 1.13a) in combination with fluorescent indicator dyes, lucigenin (LCG, see Figure 1.13b) and berberine (BC, see Figure 1.13b), respectively, was utilized as the host-dye reporter pair in the assay. Once the competitive analyte passes through the membrane, the dye is displaced from the host cavity resulting in a fluorescence signal change. The new method allowed to observe the direct rapid translocation of protamine, an antimicrobial peptide, through the bacterial transmembrane protein OmpF.[70]

A fluorescence-based IDA was adopted inside living cells for the uptake of several bioorganic analytes such as acetylcholine, choline, and protamine .[147] The macrocyclic host SCX4 that

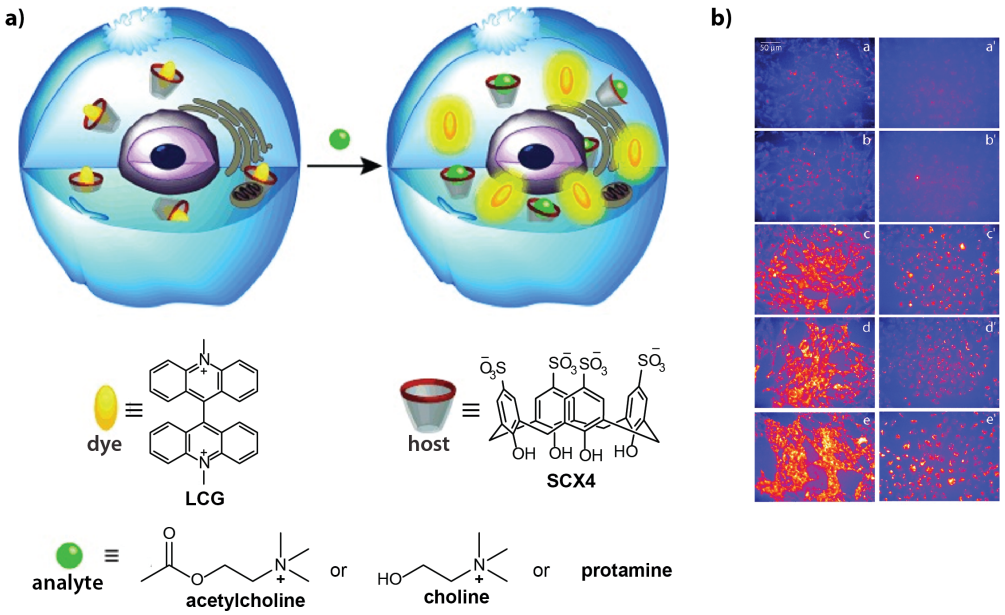

Figure 1.15: (a) Schematic representation showing an IDA inside live cells preloaded with a host-dye complex. It is used in monitoring the cellular uptake of cationic amine analytes in live V79 and CHO cells resulting in a turn-on fluorescence response. The chemical structure of the host, SCX4, dye, LCG, and the analytes tested are shown below. (b) Fluorescence imaging of V79 cells (left) and CHO cells (right) incubated with LCG (50 μM) and CX4 (250–300 μM), followed by the addition of a cationic amine. Reprinted (adapted) with permission from ref.[147] Copyright 2015 John Wiley and Sons.

bind the fluorescent indicator dye, lucigenin (LCG), resulting in a quenching of the dye fluorescence was utilized as the host-dye reporter pair in the assay (Figure **1.15**a). Spontaneous uptake of the SCX4•LCG complex was observed upon its incubation with live fibroblast cells (V79) and Chinese hamster ovary cells (CHO). The SCX4•LCG host–dye complex displayed an initial low fluorescence emission intensity. But subsequent addition of choline, acetylcholine, or protamine, which have a high affinity for SCX4, resulted in the displacement of the dye from the host cavity after entering the live cells, giving a fluorescence turn-on response (Figure 1.15).[147]

Apart from amine-containing molecules, Biedermann, Nau, and co-workers developed fluorescent chemosensors for the detection of steroids and drugs using macrocyclic CB*n* hosts in combination with fluorescent indicator dyes in an IDA format.[75] CB8 is a general steroid binder with micro- to nanomolar affinities in aqueous media.[75] The smaller host homolog, CB7, preferentially binds the small steroid nandrolone. In contrast, larger analytes such as testosterone bind (much) more weakly to CB7.[75] To construct a fluorescent chemosensor, berberine (BC)[169] and a perylene bis(diimide) derivative (PDI–OH)[137] were used as suitable indicator dyes for CB8 which forms a 1:2 and 1:1 CB8•dye complex, respectively, with an enhancement of the dye emission. For CB7, berberine (BC)[170] and methylene blue (MB)[171] were used as indicator dyes resulting in 1:1 complexes also with an enhancement in dye

emission. Hence, the presence of the stronger binding steroids resulted in the displacement of the dye accompanied by a fluorescence turn-off response in aqueous media. An IDA-based distinction of a set of steroids with a single CB*n* host was possible only if they exhibited sufficiently different binding constants, which was rarely the case for the structurally similar steroids studied.[75] Hence, an IDA sensing array using four different chemosensing ensembles, CB7•BC, CB7•MB, CB8•PDI, and CB8•$(BC)_2$, was adopted to achieve significant improvement in analyte identification through the differential fluorescence response in a microplate format.[75] Multivariate data analysis routines such as principal component analysis (PCA) or linear discriminant analysis (LDA) were employed to classify analytes by their multiple responses towards the receptors.[172] As steroids/drugs generally exhibit poor solubility in aqueous media, a GDA based sensing approach is more beneficial in such systems as the pre-complexation of the steroid/drug by CB7 or CB8 results in solubility enhancement upon complexation in the host cavity, enabling appropriate determination of their binding properties with minimal errors.[154]

Improved analyte differentiation was realized when using a set of inherently chromophoric macrocyclic and acyclic CB*n* derivatives. Isaacs, Anzenbacher Jr., and coworkers developed a fluorescent CB6 and acyclic CB*n* derivative featuring wall-integrated fluorescent naphthalene units (see Figure 1.16a and 1.16b), whose fluorescence is partly quenched by Eu^{3+} ions coordinated to C═O moieties.[79] This is due to the energy transfer from the naphthalene moieties to the Eu^{3+} ions. Both the fluorescent CB*n* derivatives show strong binding affinities (10^3 – 10^5 M^{-1}) in aqueous media for several hydrophobic/positively charged drugs, such as acetaminophen, pseudoephedrine, doxylamine, and histamine (see Figure 1.16b), which are found as mixtures in over-the-counter (OTC) cold remedies.[79] Hence, in the presence of the stronger binding analytes, the spectral properties of the host–Eu^{3+} complex is modulated upon the formation of the host–analyte complex. Whether the analytes induce quenching or intensity amplification of the chemosensor fluorescence depends on the interplay between the structure, binding mode, and analyte–receptor affinity.[79] Multivariate analysis methods with array-based sensing using cyclic and acyclic cucurbit[*n*]urils derivatives allowed for detection and distinction of different addictive OTC drugs at μM concentrations even within binary and ternary mixtures in water (pH 3.0 or pH 5.0). The analyte binding selectivity was higher for the cyclic CB6-chemosensor than for the acyclic variant (pre-organization and lock-and-key effect). Remarkably, drug identification and quantification were possible even in human urine of properly hydrated volunteers that ingested the manufacturer-recommended amount of cold medication.[79] This showcases the promising real practical utility of supramolecular IDA.

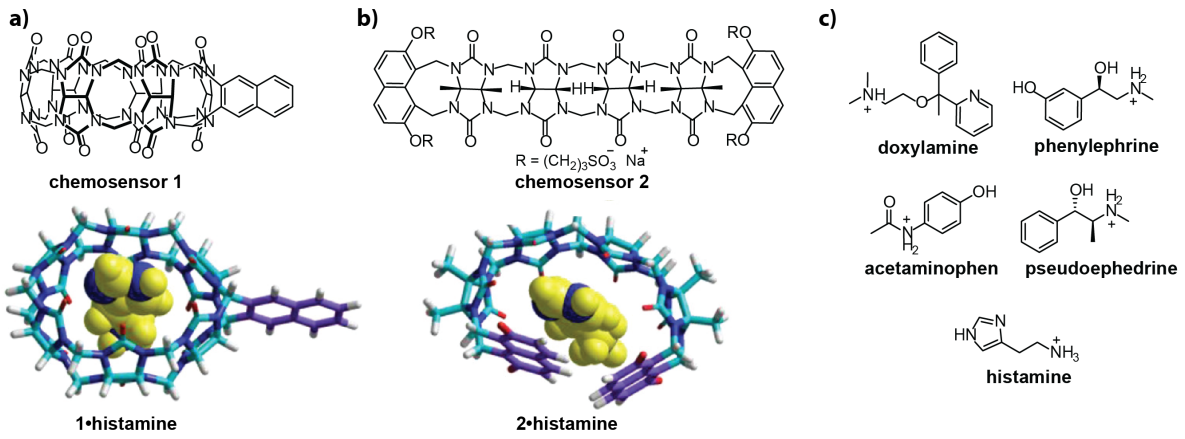

Figure 1.16: Chemical structure and 3D rendering of the (a) cyclic cucurbit[*n*]uril chemosensor and (b) acyclic cucurbit[*n*]uril chemosensors with naphthalene fluorophores used for the micromolar detection of addictive over-the-counter (OTC) drugs in water. Both probes are shown as complexes with histamine in the 3D rendering. (c) Chemical structure of the analytes tested in the study which are associated with over-the-counter cold remedies such as NyQuil. Reprinted (adapted) with permission from ref.[79] Copyright 2013 American Chemical Society.

Nevertheless, for measurements in biofluids, one must take care to avoid false-positive results in the presence of other substances excreted in the urine, *e.g.*, drugs or food components, due to the generally low binding selectivity of CB*n*-based chemosensors.

Bojtár and co-workers recently reported a carboxylated pillar[6]arene-based fluorescent indicator displacement assay for the recognition of monoamine neurotransmitters (Figure 1.17).[151] AQ stilbazolium dye (i1) and a naphthalimide derivative with positively charged 'anchor' groups (i2) were utilized as the fluorescent indicator dyes, (see Figure 1.17b). Complexation of i1 by the carboxylated pillar[6]arene (WP6, see Figure 1.17a) resulted in a strong enhancement of the dye fluorescence, arising from the confinement and restricted motion of the dye on encapsulation in the host cavity.[151] In contrast, complexation of i2 by WP6 resulted in a strong quenching of the dye fluorescence as the proximity of the negative charges on the carboxylato groups shields the positively charged tetramethylammonium anchor groups, leading to a recovery of the photoinduced electron transfer (PET) from the amino to the naphthalimide group.[151] The systems WP6•i1 and WP6•i2 were tested in indicator displacement assays for the sensing of monoamine neurotransmitters, *e.g.*, choline, acetylcholine, histamine, dopamine, serotonin, epinephrine, and norepinephrine as the analytes (see Figure 1.17c) in HEPES buffer at pH 7.4. It was shown that both the tested sensing systems WP6•i1 and WP6•i2 display opposite fluorescence responses and high selectivity for histamine over other analytes in the neurotransmitter category. The addition of histamine resulted in the displacement of the indicator dye with a fluorescence turn-off response in case of and a WP6•i1 and a fluorescence turn-on response in case of and a WP6•i2 (Figure 1.17d).[151]

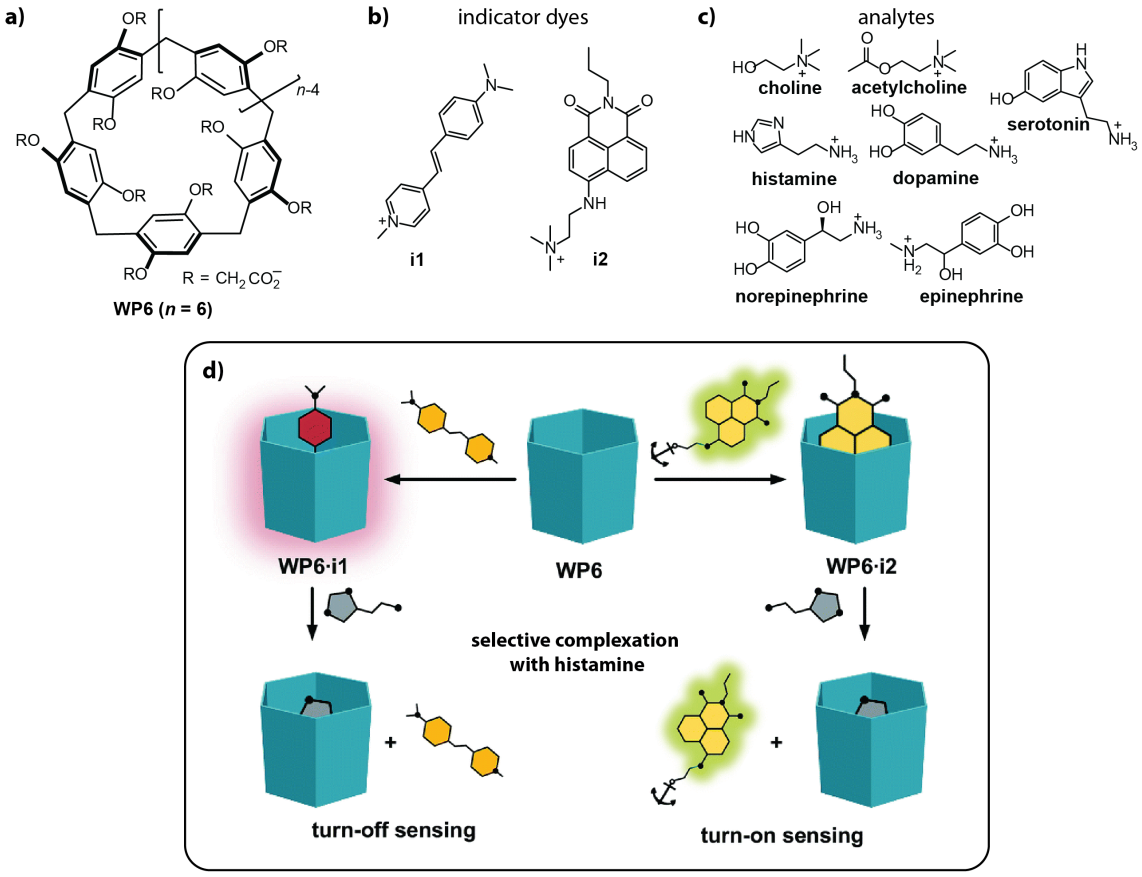

Figure 1.17: Chemical structure of (a) carboxylated pillar[6]arene (WP6) macrocyclic host, (b) suitable fluorescent indicators dyes, and (c) numerous monoamine neurotransmitters as analytes evaluated in the study. (d) A schematic representation of the fluorescence-based IDA for histamine analyte. WP6•i1 and WP6•i2 display opposite fluorescence responses and high selectivity for histamine over other analytes in the neurotransmitter category when studied in HEPES buffer at pH 7.4 Reprinted (adapted) with permission from ref.[151] Copyright 2019 Royal Society of Chemistry.

Fluorescence-based associative binding assays has been employed with CB8•dye-based chemosensors for the detection of several aromatic analytes using the unique ability of CB8 hosts to form 1:1:1 hereto-ternary complexes.[156,159,160,173,174] For instance, Scherman and coworkers showed that self-assembled 1:1 complexes of CB8 (Figure 1.18a) with perylene bisdiimide indicator dye (PDI, see Figure 1.18b) are promising fluorescent chemosensors for neurotransmitters in water and low salt buffers.[174] The encapsulation of PDI in CB8 cavity results in a simultaneous and dramatic enhancement of the dye fluorescence as a result of the breaking of the PDI π –stacks. In general, the binding of a second guest to the CB8•PDI binary complex quenches the fluorescence emission of the encapsulated PDI (Figure 1.18d). Among the studied neurotransmitters, dopamine, norepinephrine, and epinephrine (see Figure 1.18c), CB8•PDI shows high selectivity towards the ethylamine moiety of the dopamine as catechol unit alone does not show binding with CB8•PDI. The difference in the binding behavior of dopamine compared to norepinephrine or epinephrine also indicated that the alkyl components of these molecules play a major role in binding.[174] The presence of hydroxyl group on the alkyl

arm of the norepinephrine appears to hinder binding, which could result from steric hindrance and/or unfavorable interactions of the hydroxyl group with the electronegative carbonyl portals. The method allowed for the sensitive and selective detection of dopamine in aqueous media, with detection limits below 2 x 10^5 M^{-1}, even in the presence of known interferents including ascorbic acid and the catecholamines epinephrine and norepinepherine.[174] Biedermann, Nau and coworkers have later utilized a 1:1 self-assembled complex of CB8 with methylated diazaperoperylenium (MDPP)[156,173] dye that shows high binding affinities for several phenylalanine- and tryptophan-containing species with useful spectroscopic responses (emission, absorbance, CD).[156,173] For instance, the amino acid phenylalanine (Phe) and derived peptides could be spectroscopically distinguished from tryptophan (Trp) containing analytes with the CB8•MDPP chemosensor by the corresponding distinct UV/Vis and fluorescence spectra. In comparison, an IDA-type chemosensor would have given the same signal type, *e.g.*, change in the emission intensity, for both classes of peptides. The CB8-based ABA chemosensors were also employed with chiral analytes with even better analyte differentiation capabilities *via* the inducted circular dichroism (ICD) signal generation strategy[173] (see details in Section 1.3.3).

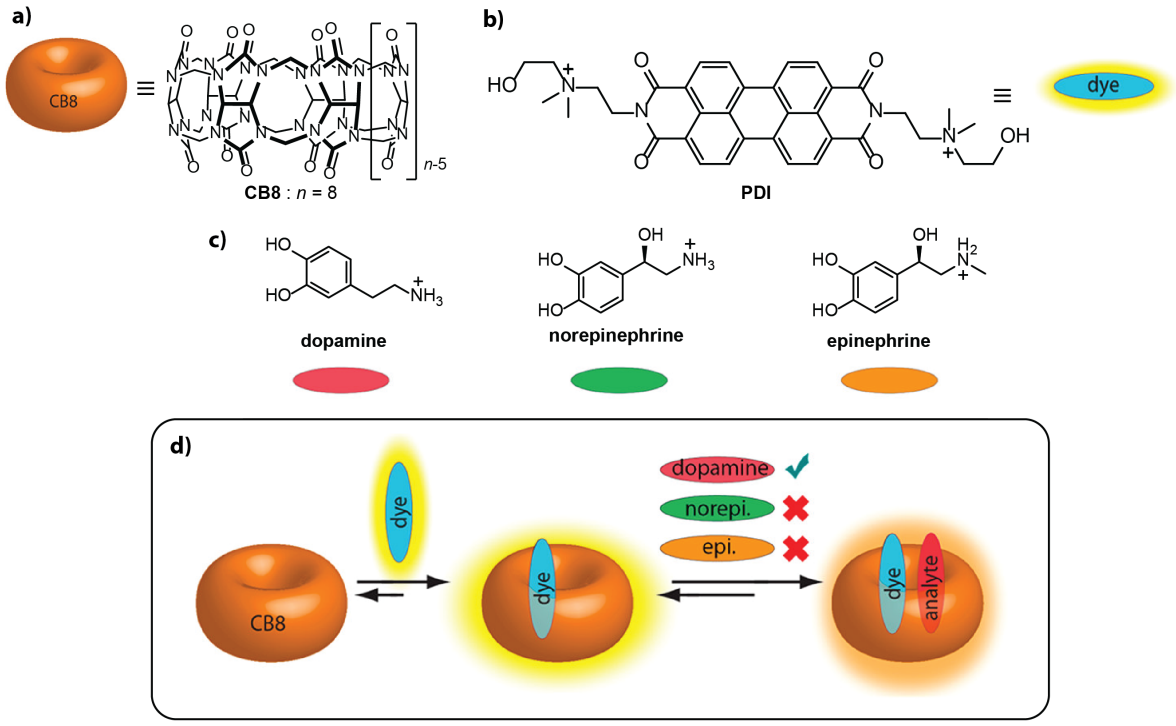

Figure 1.18: Chemical structure of (a) macrocyclic host CB8, (b) indicator dye PDI, and (c) monoamine neurotransmitters as analytes evaluated in the study. (d) Schematic representation of the fluorescence-based ABA using PDI•CB8 with selectivity towards dopamine in the presence of other catecholamine neurotransmitters, *i.e.*, epinephrine and norepinephrine, accompanied by a fluorescence quenching when studied in water. Reprinted (adapted) with permission from ref.[174] Copyright 2013 Taylor & Francis.

A large number of fluorescence-based sensing assays for the detection of various biologically-relevant analytes have become available in the past years, with excellent functionalities in aqueous and low salt buffers.[1,72,113,144,145] However, only a few have been available for practical diagnostic applications in biofluids, such as urine, blood, and saliva.[1,79,152] Both affinity and selectivity of the chemosensor for the target analyte are often the main practical limitation for their use in complex biofluids. For instance, the macrocyclic cucurbit[*n*]urils exhibit high binding affinities in water for many hydrophobic and/or positively charged guests.[76,175] However, CB*n* and other reported negatively charged receptor host molecules interact competitively with metal cations such as Na^+ and K^+ [54,176-178] which occur in millimolar concentrations in biofluids, leading in most cases to greatly reduced actual binding affinities between the host and biorelevant target analytes in saline biofluids.[179] Hence, the design of chemosensors with high binding affinity and selectivity for the analyte of interest is crucial for their performance in complex biofluids containing high millimolar salt concentrations and other potential interferents. In the present thesis, a new fluorescent chemosensor self-assembled from sulfonated pillar[*n*]arene host and dicationic indicator dye is introduced for the sensitive and selective detection of polyamines in biofluids. The strategies employed to achieve stability of the self-assembled chemosensor in biofluids and selectivity for the target analyte are discussed in chapter 5.

1.3. Chirality sensing systems

1.3.1. Importance of molecular chirality

Chirality is ubiquitous in nature. By definition, chirality (handedness) is the property of any object that is non-superimposable with its mirror image. Our right and left hands represent a familiar and convenient example of chirality. The right hand is a mirror image of the left one, and they cannot be superimposed no matter how the two hands are oriented.[180] In the case of molecules, chirality is a special form of stereoisomerism (molecules having identical chemical formulas but different spatial configurations).[181] If the stereoisomers are two non-superimposable mirror images of each other, the molecule is chiral, and the two stereoisomers are called enantiomers (see Figure 1.19a). The source of chirality in molecules can originate from different types of configurations of their atoms. The most common one is the chiral center, usually generated by an asymmetric carbon atom (sp^3) attached to four different substituents. Other types of chirality elements include chiral axis, chiral plane, and helix. Figure 1.19b-e shows examples of all four different kinds of chiral classes. The two enantiomers are generally

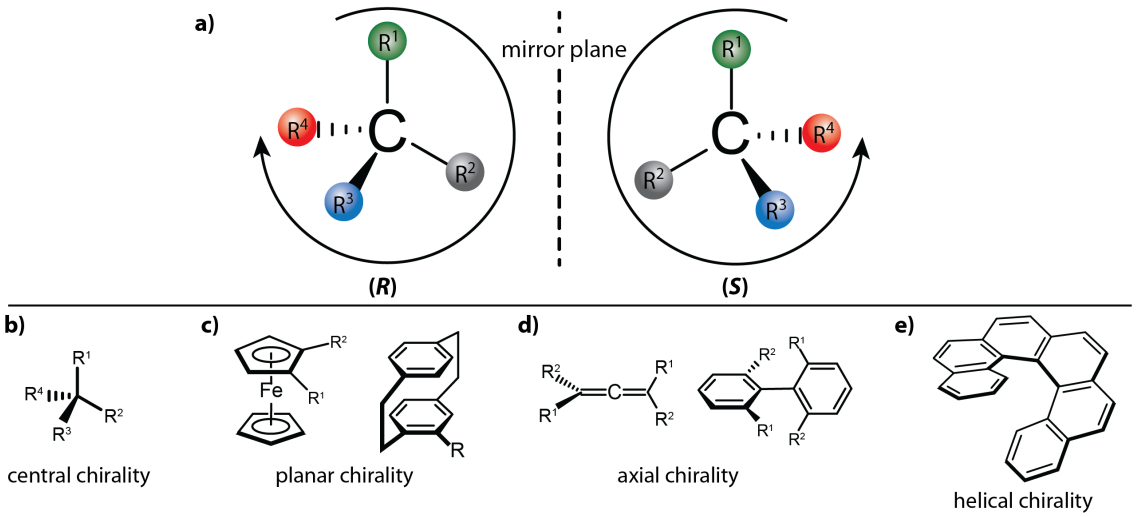

Figure 1.19: (a) Representation of (*R*)-and (*S*)-enantiomers that are non-superimposable mirror images of each other. The dashed line represents an imaginary mirror in the middle. The designation of the enantiomers as (*R*) and (*S*) is based on the Cahn-Ingold-Prelog (CIP)[182,183] nomenclature. The substituents are numbered according to their atomic number in descending order. (b-e) Examples of different types of molecular chirality: (b) Chiral center: C-atom with 4 different substituents; c) Chiral plane: ferrocene, cyclophane derivative; c) Chiral axis: allenes, biphenyls; d) Helical chirality: helicenes.

designated to have an (*R*)- or (*S*)- configuration, which indicates the clockwise and anti-clockwise turning sense, respectively, of substituents around the chiral center, axis, or plane in order of priority following the Cahn-Ingold-Prelog (CIP) convention (see Figure 1.19a).[182,183] In case of helicity, the enantiomers (*P*) or Δ designate a right-handed helix, whereas (*M*) or Λ designate a left-handed helix. [184] For amino acids and sugar, it is still common to use the older Fischer-Rosanoff convention,[184] where the enantiomers can be distinguished by the D- or L-configuration relative to the configuration of D- or L-glyceraldehyde, respectively, which is used as reference.

Molecular chirality is of profound importance in many areas of biology and chemistry. Most biomolecules, such as amino acids, proteins, sugars, and nucleic acids, are chiral in nature. Notably, the building blocks of life, *i.e.,* amino acids (those form proteins), are almost exclusively present in the chiral L form, and sugars (that constitute DNA) are present in the D form.[185] This natural selection of L-amino acids and D-sugars in life formation points out that different chiral compounds must have different biological effects on the life process and, hence, underlines many fundamental biomolecular processes such as biological recognition and catalysis. As an outcome, chirality also plays a vital role in drug-biomolecule interaction.[186] The two enantiomers of a chiral compound can exhibit significantly different pharmacological and toxicological effects. This is particularly important for medicinal chemistry. For example, in the case of the drug ethambutol, the (*S*,*S*)-enantiomer can be used to treat tuberculosis, whereas the (*R*,*R*)-enantiomer causes blindness.[187] Even if the enantiomer of a given drug is not

dangerous but simply not effective, a patient has to take a double dose of medicine if the drug exists as a racemate (a mixture of an equal amount of both enantiomers). Hence the need for enantiomerically pure drugs has become imperative. In fact, more than 50% of commercially available drugs consist of compounds of single enantiomers. The significance of chiral compounds makes chirality sensing and analysis critically important. A sensitive and rapid detection and differentiation of enantiomers in small quantities present a growing demand.

1.3.2. Chiroptical methods: Electronic Circular Dichroism

Chiroptical spectroscopies are efficient optical methods used in chirality sensing and analysis.[188-191] Electronic circular dichroism (ECD) is one of the most popular chiroptical methods and measures the difference in the absorption of left- and right-circularly polarized light by a molecule containing on or more chiral chromophores in the UV–visible spectral range (see Figure 1.20a).[190,191] Because circularly polarized light is chiral, it interacts differentially with opposing enantiomers and induces dissymmetric electronic transitions.[192] Thus, left and right circularly polarized light is absorbed differentially by an enantiomerically enriched chiral chromophore or a chromophore in an enantiomerically enriched chiral environment.[192]. Accordingly, the electronic circular dichroism is defined as:

$$\mathrm{ECD} = A_{\mathrm{L}} - A_{\mathrm{R}} \qquad \text{Eq. 1.21}$$

where A_{L} and A_{R} are the absorption of left and right circularly polarized light, respectively.

In analogy to the Beer-Lambert law, one can define a molar quantity as:

$$\Delta\varepsilon = \varepsilon_{\mathrm{L}} - \varepsilon_{\mathrm{R}} = \frac{\mathrm{ECD}}{(\mathrm{c} \times \mathrm{l})} \qquad \text{Eq. 1.22}$$

which is a concentration-independent quantify, where and c and l are the sample concentration expressed in mol L^{-1} and path length expressed in cm, respectively.

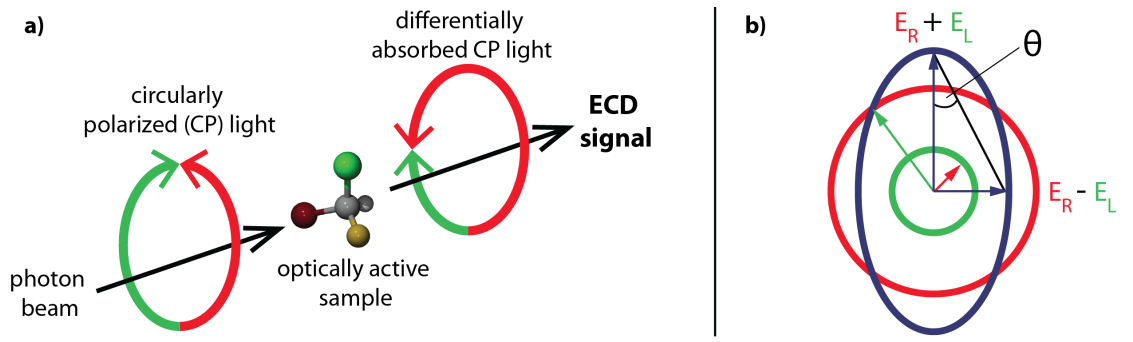

Figure 1.20: (a) The differential absorption of left-handed (green) and right-handed (red) circularly polarized light by the chiral species resulting in an ECD signal. (b) The resulting elliptical polarized light (blue) is composed of unequal contributions of right (red) and left (green) circularly polarized light. The degree of ellipticity is defined as the tangent of the ratio of the minor to major elliptical axis. E_R and E_L are the magnitudes of the electric field vectors of the right-circularly and left-circularly polarized light, respectively.

As per Eq. 1.21, ECD is measured in correspondence to absorption bands, and a dichroic peak is also called a Cotton effect or Cotton band. As ε_L maybe smaller or larger than ε_R (and consequently A_L and A_R), ECD is a signed quantity, and the spectra of two enantiomers are always exactly opposite.[190]

ECD is measured using commercial CD spectrometers operating in the UV–visible spectral region. In most commercial CD instruments and in literature reports, the ECD measurements are expressed in terms of ellipticity θ (in mdeg). The degree of ellipticity can be described in the following way. After the circularly polarized light passes through an optically active chiral sample, the left and right components will no longer have equal magnitudes of the counter-rotating electric field components. Hence, the direction of the electric field vector (E) no longer traces a circle; instead, it traces an ellipse (which means the light is elliptically polarized). The degree of ellipticity is defined as the tangent of the ratio of the minor to major elliptical axis (see Figure 1.20b).[192]

The ellipticity, θ (in mdeg), is related to ECD through:

$$\theta = 32980 \times \mathrm{ECD} \qquad \text{Eq. 1.23}$$

Hence, the experimentally recorded ellipticity values (θ in mDeg) can be converted to molar circular dichroism values ($\Delta\varepsilon$ in M^{-1} cm^{-1}) according to Eq. 1.24.

$$\Delta\varepsilon = \frac{\theta}{(32980 \times l \times c)} \qquad \text{Eq. 1.24}$$

A brief theoretical basis of circular dichroism is provided here based on the light-molecule interactions. For each electronic transition, one can define an electric and a magnetic transition dipole related to the electron cloud redistribution during the transition. A linear charge displacement leads to a non-vanishing electric transition dipole $\overrightarrow{\mu_{ij}} \neq 0$ whereas a rotation of electrons brings about a magnetic transition dipole $\overrightarrow{m_{ij}} \neq 0$.[190] In traditional absorption spectroscopy, both these situations can lead to the absorption of radiation, and the intensity of the absorption band is directly related to the oscillator strength, f_{ij}, as per Eq.1.25.[190]

$$\int \varepsilon \, d\upsilon \propto f_{ij} \approx \left|\overrightarrow{\mu_{ij}}\right|^2 + \left|\overrightarrow{m_{ij}}\right|^2 \qquad \text{Eq. 1.25}$$

Very often, the electric dipole term is much larger than the magnetic dipole.[190] And hence one generally makes a distinction between (electric-dipole) allowed and forbidden transitions based on whether $\overrightarrow{\mu_{ij}} \neq 0$ or $\overrightarrow{\mu_{ij}} = 0$, respectively.[190] Contrary, in chiroptical spectroscopy, both transition dipole moments play a crucial role. In the simplest case, a chiral electronic

displacement that gives rise to an ECD signal is along a helical path. This implies a simultaneous translation and rotation of charge, *i.e.,* a transition with $\overrightarrow{\mu_{ij}} \neq 0$ or $\overrightarrow{m_{ij}} \neq 0$ (and the two vectors are not orthogonal).[190] In analogy to Eq. 1.25, the integral of an ECD band is directly proportional to the scalar product, R_{ij} defined as rotational strength (see Eq. 1.26), which is a signed quantity.[190]

$$\int \varepsilon \, \mathrm{d}\upsilon \propto R_{ij} \approx \overrightarrow{\mu_{ij}} \cdot \overrightarrow{m_{ij}} \qquad \text{Eq. 1.26}$$

Most of the non-empirical interpretations of ECD spectra and configurational assignments are based on the evaluation of R_{ij} and its sign.[190] This is not discussed here, and the reader can refer to books and reviews available on the topic for details.[190,192]

In the case of chiral molecules containing a single, isolated chromophore, the interpretation of ECD spectra can be straightforward. However, this is not the case for chiral molecules that are complex entities containing several light-absorbing groups in the UV-visible wavelength range. In such cases, the interchromophoric interactions are important and provide the most significant contributions to the ECD spectra.[190,192] When two (or more) chromophores are located in space and have a proper (chiral) mutual orientation due to the influence of neighboring chiral groups, considerable rotational strengths can result from the interactions between their transition dipoles. Among various possibilities of mixing between electric- and magnetic-dipole allowed transitions, the most significant case arises when two (or more) chromophores with strong electric-dipole allowed transitions couple to each other. This is known as exciton coupling.[193,194] Due to the coupling between two equal chromophores, the two otherwise degenerate excited states split into two levels separated by a quantity $2V_{12}$ (Eq.1.27), called Davydov splitting (see Figure 1.21a).[190]

$$V_{12} = \frac{\mu_1 \mu_2}{r_{12}^3} \left[\overrightarrow{e_1} \cdot \overrightarrow{e_2} - 3(\overrightarrow{e_1} \cdot \overrightarrow{e_{12}})(\overrightarrow{e_2} \cdot \overrightarrow{e_{12}})\right] \qquad \text{Eq. 1.27}$$

μ_1, μ_2 and r_{12} are the intensities and mutual distance of the two transition dipoles, and $\overrightarrow{e_i}$ are the corresponding unit vectors.

The excited state splitting reflects in a split or broadened absorption band, centered around the wavelength transition of the isolated chromophore (λ_0). A bisignate ECD couplet is generated around λ_0 and associated with two opposite non-vanishing rotational strengths as defined in Eq. 1.28 (see Figure 1.21c and 1.21d).[193,194]

$$R_{12} \propto \pm \overrightarrow{r_{12}} \cdot \overrightarrow{\mu_1} \times \overrightarrow{\mu_2} \qquad \text{Eq. 1.28}$$

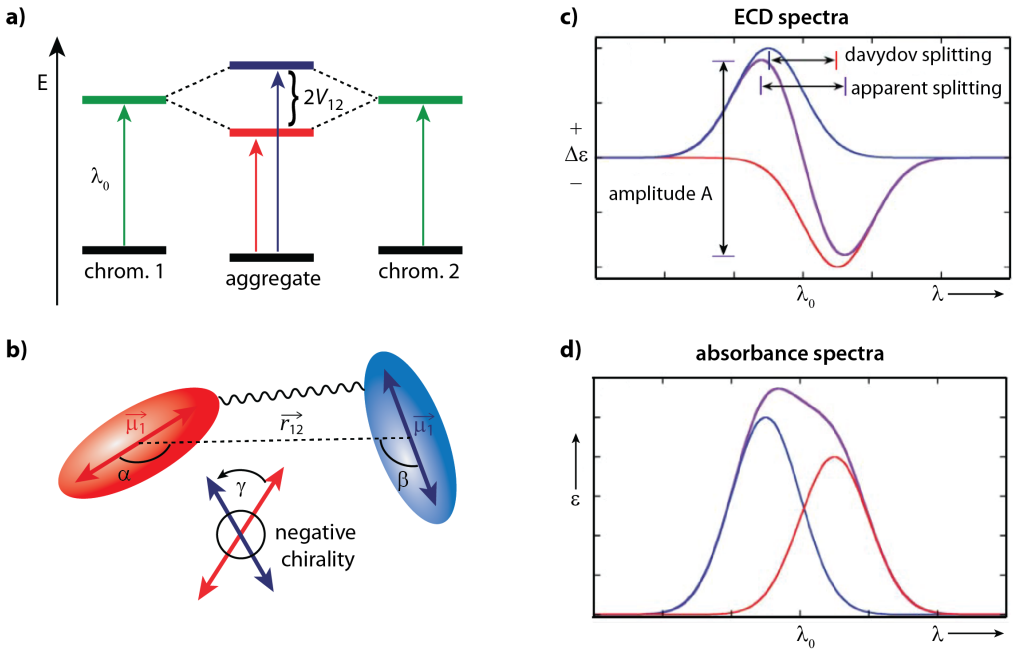

Figure 1.21: (a) Splitting of the excited states of two degenerate exciton-coupled chromophores linked by a chiral spacer. (b) The orientation of the two chromophores and depiction of the geometrical parameters necessary for predicting ECD sign and intensity through Eq. 1.29. Expected (c) ECD and (d) absorption spectra in case of exciton splitting as shown in (a): the blue and red lines represent the spectra of chromophore 1 and 2 individually, and the violet line represents the spectra of the complex after exciton coupling. The distance between the peak and the trough of the split CD curve is called amplitude or A. Reprinted (adapted) with permission from ref.[190] Copyright 2007 Royal Society of Chemistry.

Taking the band-shapes and the mutual cancellation between the two oppositely signed bands into account, the resulting ECD couplet is determined by the expression given in Eq. 1.28.[190]

$$\Delta\varepsilon(\lambda) \propto \pm\Gamma(\lambda,\lambda_0)V_{12}\,\overrightarrow{r_{12}}\cdot\overrightarrow{\mu_1}\times\overrightarrow{\mu_2} \propto \pm\Gamma(\lambda,\lambda_0)\,\frac{\mu_1^2\mu_2^2}{r_{12}^2}\,\Omega(\alpha,\beta,\gamma) \qquad \text{Eq. 1.29}$$

The factor Γ accounts for the dispersive couplet shape. The three angles, α,β,γ are depicted in Figure 1.21b. The ECD depends on the quadruple product $V_{12}\,\overrightarrow{r_{12}}\cdot\overrightarrow{\mu_1}\times\overrightarrow{\mu_2}$, which can be factorized into a module and a geometric term Ω.[190] This shows that the intensity of the ECD couplet is directly proportional to the fourth power of the dipole strength and inversely proportional to the square of the interchromophoric distance. Most often we have two different chromophores in the systesm. In the case of non-degenerate coupling between two different chromophores, R is also inversely proportional to the transition frequency separation.[190] Hence, in essence, strongly absorbing chromophores situated near in space and close in energy are expected to give rise to very intense ECD couplets.[193,194] The sign of the couplet (defined by the sign of its longer wavelength component) is also related to the orientation expressed by Ω, which again depends on the molecular configuration and conformation.[190]

Apart from absorbance-based ECD, fluorescence-based chiroptical methods have promising potential for sensitive and selective detection of chiral biomolecules.[195] For *e.g.*, fluorescence-detected circular dichroism (FDCD) measures the differential fluorescence intensity that results from excitation with left-handed and right-handed circularly polarized light by probing the differences in the excitation spectrum.[196-198] In essence, the information derived is essentially the ECD of the ground state of the fluorophore. However, fluorescence detection leads to several advantages over conventional ECD. Given the high specificity and sensitivity of fluorescence, FDCD can be more sensitive and selective than ECD by probing only the fluorescent chromophores in a macromolecule or a solution mixture at concentrations much lower than those required for ECD.[196-199] Even though FDCD was introduced, many years ago, the application of FDCD (and other chiroptical techniques based on fluorescence) in chirality sensing studies are still lacking in the literature and not so frequently employed compared to the widely used ECD.[195]. However, given the interest for sensitive and selective detection of biologically relevant analytes for practical sensing applications in complex media such as biofluids, FDCD may find future applications in the field (refer to Chapter 3 for details).

1.3.3. Molecular recognition-based chirality sensing

Most biologically relevant analytes of interest lack a strong chromophoric group. Hence, they do not produce ECD signals in the practically preferable near UV or visible wavelength region or are even completely ECD silent.[200,201] Thus, ECD spectroscopy is of limited use for the detection and identification of small biomolecules such as metabolites, hormones, and peptides. Many classic chirality analysis methods are based on the chemical derivatization of the chiral analyte by introducing one or two chromophoric groups that engage in exciton coupling and produce ECD signals in the preferred near UV or visible range.[190,199,202-204] In order to avoid additional synthesis and isolation, molecular recognition based approaches were introduced in the past years for the chirality sensing of small molecules by ECD spectroscopy.[113,200,205,206] Thus, chromophoric probes and chemosensors were developed which engage in covalent or non-covalent interactions with the chiral analyte giving rise to induced chiroptical signals in the relevant near UV or visible wavelength range.[96,173,207-210] Typically, metal coordination[209,211-213] or dynamic covalent bonds[214-217] were harnessed to bind the analyte to the sensor and achieve chirality transfer. Even though these methods were quite successful in the determination of absolute configuration and *ee* values, they also suffer from several limitations. For instance, chiral analytes should contain reactive functional groups to engage in coordination or covalent bonds, and the chiral center should be in close proximity to the functional group.[200] Additionally, long reaction times are usually required to reach equilibrium, making real-time

analyte detection and reaction monitoring difficult.[200] Artificial chemosensor based on non-covalent host-guest interactions has attracted a lot of attention in the past few years for chiroptical sensing.[200] They often exhibit fast equilibrium kinetics and are not sensitive to functional groups of guests.[96,173] Importantly, water-soluble macrocyclic and acyclic concave hosts are particularly attractive to achieve chirality-sensors operational in aqueous media and for their application potential in Life Sciences and diagnostics.

In order to generate induced ECD signals, the host molecule should possess one or more chromophores, and effective chirality transfer should occur between the chiral analyte and the host upon binding.[200,218] The host involved can be either inherently chromophoric or self-assembled hosts in combination with indicator dyes. Exciton coupling is one of the most common mechanisms for generating induced ECD signals.[190,200] The influence of the chiral group of the guest on the orientation of the chromophores of the host is vital for effective chirality transfer. The possible mechanisms for chirality transfer from the chiral analyte to the achiral host are shown in Figure 1.22 and further described below.

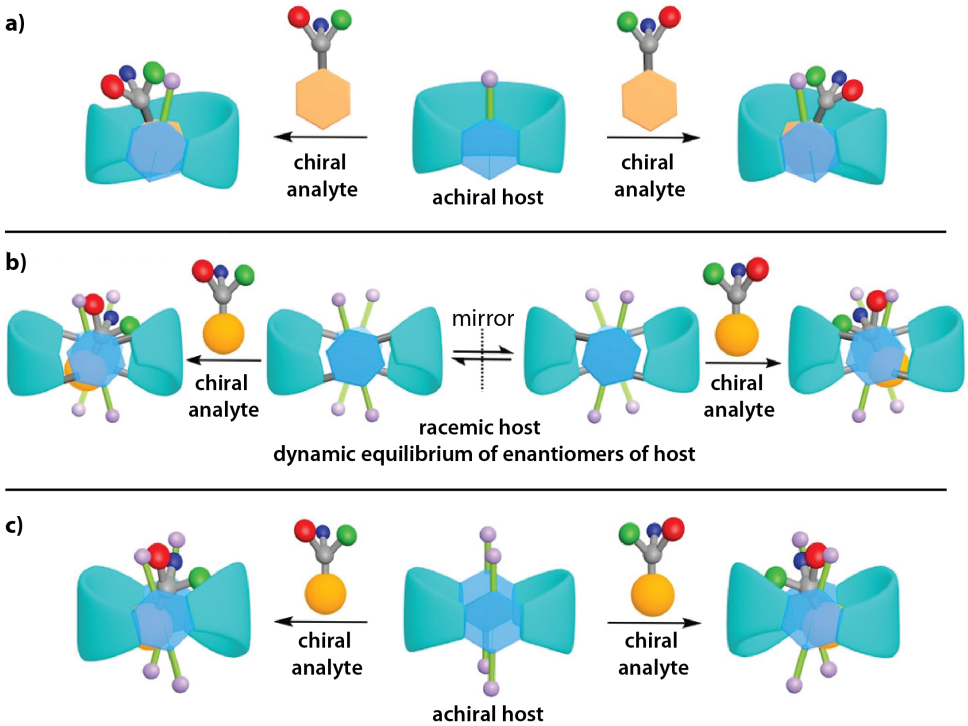

Figure 1.22: Schematic representation of the different possible mechanisms for chirality transfer between chiral analytes (the two enantiomers are shown) and achiral chromophoric host. (a) The complexation of a chiral chromophoric analyte by an achiral chromophoric host can rise to exciton coupling, generating induced ECD signals. (b) The chiral (non)chromophoric analyte has a binding preference for one of the two enantiomers of the racemic chromophoric host and hence induce one predominant enantiomer giving rise to ECD signals. (c) The complexation of a chiral (non)chromophoric analyte by an achiral chromophoric host can induce a chiral conformation of the host, giving rise to induced ECD signals.

When both the host and the guest possess a chromophoric group, host-guest complexation will bring the two chromophores in close proximity, and the chiral group of the guest forces the two chromophores to be arranged in a chiral orientation (see Figure 1.22a).[173] This ensures exciton coupling, generating induced ECD signals with split ECD bands. As a result, analyte-specific spectroscopic signals are usually obtained, which can be used to differentiate different analytes. However, this approach requires the analyte to possess at least one chromophoric group, thereby limiting the range of substrates that can be detected. The detection of non-chromophoric analytes can be achieved with host molecules that possess two or more chromophoric groups, for instance the aromatic side walls defining the binding cavity of the host (Figure 1.22b and 1.22c). Close contact between the chiral groups of the analyte and the chromophoric groups of the host upon host-guest binding can result in effective chirality transfer with induced ECD signals *via* the following mechanisms. In one case, if the host is racemic and exists as two interconvertible enantiomers, the chiral analyte may have a binding preference for one of the two enantiomers through a conformational selection mechanism (Figure 1.22b).[200,219,220] As a result, in the presence of the chiral analyte, the balance between the two enantiomers may be broken, and one predominant enantiomer is induced by binding the chiral guest.[200,221,222] The underlying mechanism and the magnitude of the ECD signals thus depend on the differential binding affinity of the two host enantiomers to the same chiral guest. In another case, the binding of the chiral guest can induce a chiral conformation of the relatively rigid host, which is not detectable in the free state, through an induced-fit mechanism,[223] thereby giving rise to induced ECD signals (Figure 1.22c).[200,224] In the latter two cases, the induced ECD signals are located in the same wavelength range for different analytes, and analyte-specific spectroscopic fingerprints are absent. Thereby they are more of a general approach for detecting a diverse range of analytes. Nevertheless, if the analytes carry a chormophoric group, exciton coupling between the host and guest chromophores may still occur, giving rise to analyte–specific fingerprints together with the induced ECD signals from the chromophores of the host alone.

A few examples of molecular recognition-based chirality sensing utilizing macrocyclic concave hosts in water are described below. Biedermann, Nau, and coworkers realized chiroptical sensing utilizing the self-assembled CB8•dye receptor that forms ternary complexes with chiral aromatic analytes in water (see Figure 1.23).[173] A constrained face-to-face arrangement of the analyte and reporter dye in the rigid CB8 cavity results in a constructive orbital overlap, which ensures exciton coupling and a conformationally confined interaction geometry.[173] Consequently, analyte indicative induced ECD signals were observed for a diverse range of

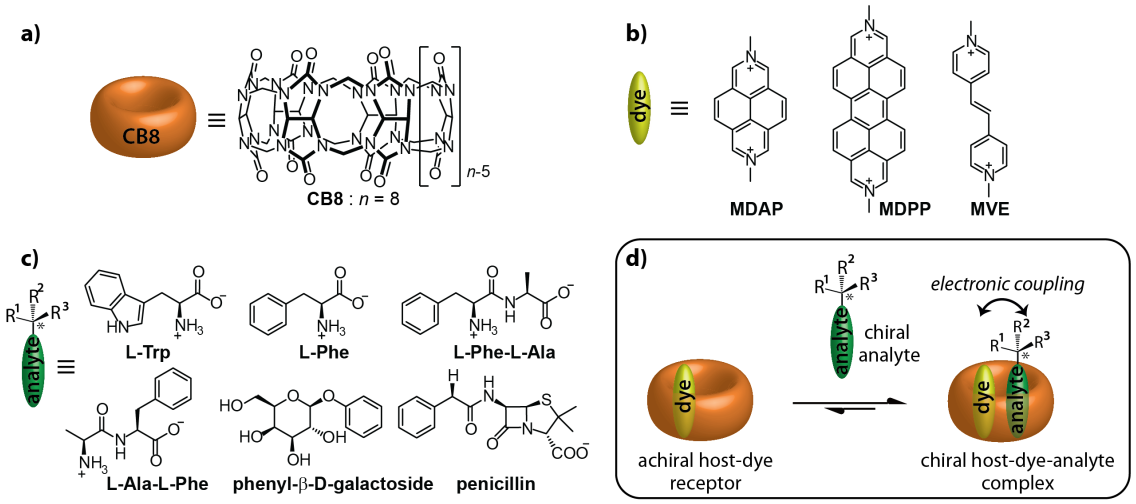

Figure 1.23: Chemical structure of (a) macrocyclic host CB8, (b) indicator dyes, and (c) a few representative chiral analytes tested in the study. (d) Schematic representation of the complexation of chiral analyte by the self-assembled, achiral CB8•dye receptor leading to induced ECD signal generation *via* electronic–coupling between chromophoric receptor and analyte. Reprinted (adapted) with permission from ref.[173] Copyright 2014 John Wiley and Sons.

analytes tested, including amino acids, peptides, proteins (human insulin and somatostatin), and drug molecules. By using the ECD spectral fingerprints generated upon chiral analyte binding to CB8•MDAP and CB8•MDPP chemosensors (see Figure 1.23a and 1.23b), it was possible to distinguish Phe-containing from Trp-containing analytes. Furthermore, N-terminal Phe containing dipeptides can be distinguished from the C-terminal Phe variants. Also, penicillin-type antibiotics and the protein insulin are detected in low salinity buffers.

Wang and coworkers recently showed that the chirality sensing of amino acid esters were achieved using a chromophoric water-soluble carboxylated pillar[*5*]arene host (WP5, see Figure 1.24a).[221,222] Pillar[*n*]arene hosts exhibit peculiar dynamically racemic planar chirality (*p*R or *p*S) in solution, where *p*R and *p*S enantiomers of pillar[*n*]arene are interconvertible by rotation of the repeating hydroquinone units (see Figure 1.24a). [221,222] Hence, the two enantiomers may show different binding affinities for the same chiral guest and can therefore be utilized as chirality sensors. Interestingly, only L-arginine ethyl ester induces the *p*R conformation of WP5, whereas 18 other L-amino acid esters induce the *p*S conformation (Figure 1.24), resulting in strong ECD bands in the positive and negative direction, respectively. The binding preference can be attributed to the different binding modes. It was demonstrated that the competition between the α-positioned side-chain moiety or ethyl ester moiety of amino acids to bind the cavity of the WP5 host induces the *p*R or *p*S conformation of the dynamically racemic WP5. Furthermore, D-alanine ethyl ester and D-arginine ethyl ester induce the *p*R and *p*S conformation, respectively (Figure 3), which is opposite to that observed for their "L" enantiomers.

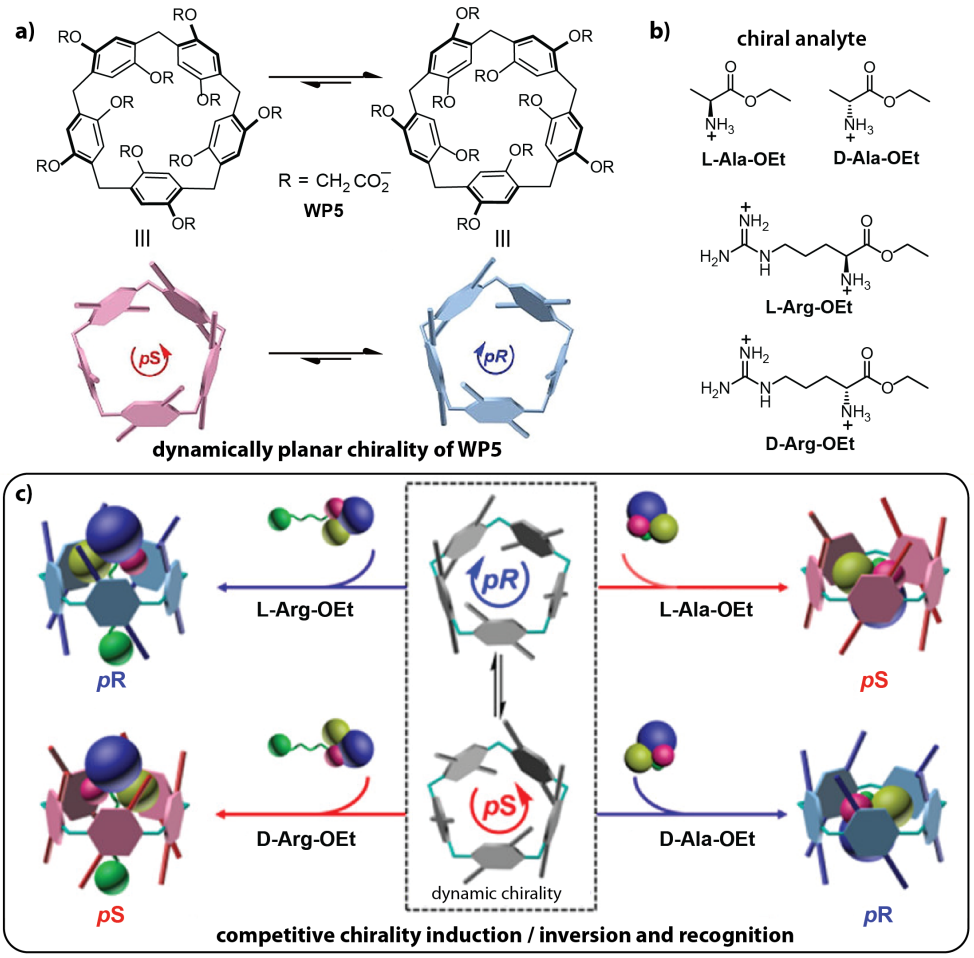

Figure 1.24: Chemical structure of (a) WP5 host and the dynamically planar chirality of WP5 (*p*R and *p*S enantiomers), and (b) a few representative chiral analytes tested in the study. (c) Competitive conformation chirality of WP5 induced in the presence of chiral amino acid alkyl ester hydrochloride. Reprinted (adapted) with permission from ref.[221] Copyright 2020 American Chemical Society.

Jiang and co-workers employed the endo-functionalized amide naphthotubes for the chirality sensing of a wide range of organic molecules, including common products in asymmetric catalysis, natural products, drug molecules, and biological building blocks in water (see Figure 1.25).[96,224] The amide naphthotubes are relatively rigid hosts with only limited flexibility in the bisnaphthalene cleft. The binding of a chiral guest induces a chiral conformation of the host resulting in induced ECD signals being generated. Figure 1.25c shows the DFT calculated structures of the complexes of amide naphthotubes with 1-phenylethanol. It can be seen that the two enantiomers of the guest induce an opposite helical arrangement of the naphthalenes, which is responsible for the mirror-imaged ECD spectra of the two complexes.[224] The amide naphthotubes have a rather wide substrate scope in terms of chiroptical sensing. They are not limited to common functional groups addressed by other chemosensor assays, and chiral molecules with epoxide, ester, ether, acetal, or sulfinamide can also be detected.

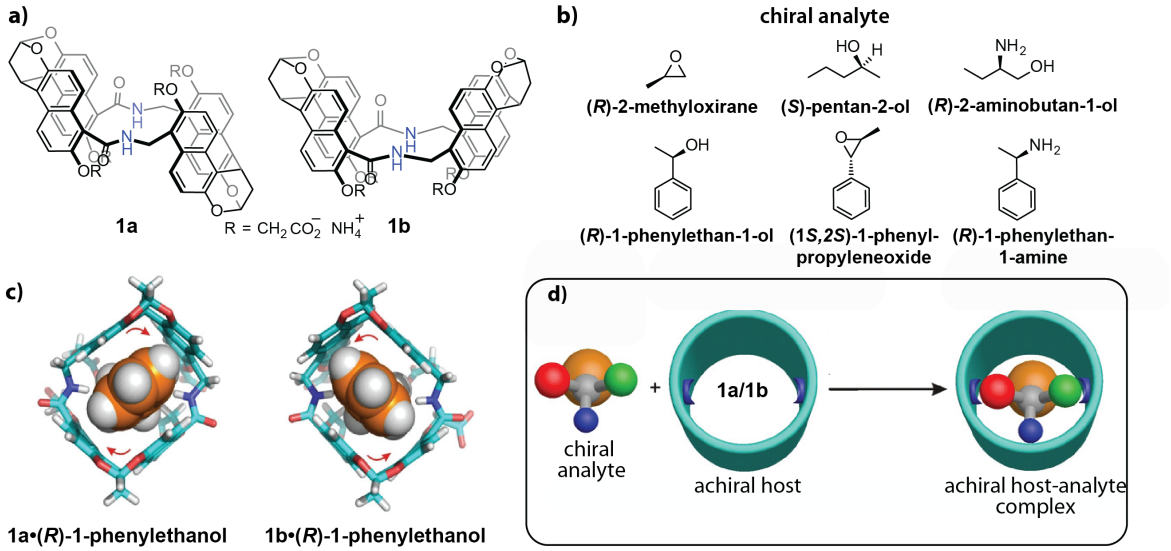

Figure 1.25: Chemical structures of (a) amide naphthotubes (1a and 1b), and (b) a few representative chiral analytes tested in the study, (c) DFT calculated structures of 1a in the presence of (*R*)-1-phenylethanol or (*S*)-1-phenylethanol. The red arrows indicate the twist directions of the bis-naphthalene clefts. d) Schematic representation of chiroptical sensing of chiral organic molecules through biomimetic recognition of the amide naphthotubes in water. Reprinted (adapted) with permission from ref.[224] Copyright 2020 John Wiley and Sons.

Despite the wide range of synthetic receptors reported for the recognition of biologically relevant analytes, only a few chirality-based chemosensors are available to date for the detection of compounds in aqueous media. Hence, in the present thesis, new chirality sensors have been explored with functionality in aqueous media. Chapter 2 discusses the chiroptical sensing applications utilizing the chromophoric acyclic concave hosts for the detection of a diverse range of chiral analytes in water and the different binding models to achieve chirality transfer.

Further research towards the development of synthetic chirality sensors with improved practical utility, enantioselective recognition ability, and enhanced chiroptical response during chiral induction can help realize the future real-world applications of chiroptical sensing.

Aim of the Thesis

Artificial chemosensors based on supramolecular host-guest systems have gained increasing popularity in the past years. Chemosensors used in combination with innovative assay protocols for optical signal transduction have promising application potential in molecular diagnostics and biochemical/medical research. As a result, significant progress has been made in the development of synthetic receptor host molecules that can serve as recognition elements in the chemosensor, and their guest binding properties have been extensively investigated. They have been employed in several optical fluorescence-based or ECD-based sensing assays, and an evaluation of their practical applicability for analyte detection and chirality sensing has been explored. However, developing chemosensors that fully meet the requirements for practical applications is still challenging. Consequently, the real-world sensing applications of optical chemosensors have not yet been fully realized. The main goal of my thesis was to achieve chemosensors operational in aqueous media and complex biofluids, such as urine, saliva, or blood, with a sensitive and selective signal response towards the presence of the target analyte, thereby selectively detecting it from a pool of other interferents in the media.

In this present work, several aspects in the advancement of artificial chemosensors have been addressed to realize their practical diagnostic applications.

- In chapter 2, electronic circular dichroism detected chirality sensing is investigated with acyclic cucubit[*n*]urils and molecular tweezer as achiral chromophoric hosts for chiral (non)-chromophoric small molecule guests, such as chiral hydrocarbons, terpenes, amino acids and their derivatives, steroids, and drugs in aqueous media. The binding mechanism for chirality transfer and the potential utility of the chemosensor for chirality sensing, analyte identification, and reaction monitoring applications are evaluated. The promising results of the ECD-based chemosensor can hence enhance the library of available chirality sensors operational in water, where, to date, only a few systems are available.
- For practical application in real biological media, where the analytes are mostly present in the low micromolar to nanomolar concentration regime, the widely utilized ECD, an absorbance-based chiroptical method, suffers from low sensitivity impeding the investigation of biological analytes at their clinically relevant concentration levels. Furthermore, real biological media that contain a range of chromophoric chiral substances gives rise to strong signal backgrounds in the ECD spectra, making the analysis practicality difficult In chapter 3, fluorescence-detected circular dichroism (FDCD) spectroscopy is explored for the first time for the chiroptical analysis of supramolecular host-guest and host-

protein systems in an effort to improve the sensitivity and selectivity of chiroptical supramolecular assays. FDCD combines the advantages of both chiroptical and fluorescence techniques and possesses additional merit for sensing applications in complex biofluids as only compounds that are both chiral and fluorescent are expected to give rise to an FDCD signal. The sensitivity of FDCD over ECD measurements for chiral analyte detection at clinically relevant concentrations is assessed. In addition, the combined use of FDCD and ECD is evaluated to obtain additional valuable information about the system, such as analyte identification and hidden supramolecular processes. The work also looks into FDCD measurements for label-free reaction monitoring, both in an endpoint assay version and for continuous reaction monitoring even in the presence of other chromophoric compounds, as found in biofluids such as human blood serum.

- A detailed understanding of the supramolecular host-guest recognition interaction is vital for designing chemosensors based on host-guest systems with improved properties. Both thermodynamic and kinetic insights can provide a proper analysis of the association and dissociation processes of host-guest interactions. However, kinetic investigations of supramolecular systems are scarce in the literature, often due to a lack of suitable experimental protocols. In Chapter 4, novel approaches to unravel the kinetic features of supramolecular host-guest complexes through fluorescence-based assays are explored. Three competitive time-resolved methods for the kinetic description of host-guest systems were designed and applied for the determination of kinetic rate constants of spectroscopically silent guests with macrocyclic cucurbit[*n*]uril and human serum albumin as representative hosts. A correlation between the available kinetic and thermodynamic data is made to get detailed insights into the host-guest binding event. In addition, a new kinetic method to achieve selective analyte sensing, even in situations of poor thermodynamic selectivity caused by similar binding affinities of the host for different bioorganic analytes, is assessed to further demonstrate the importance of kinetic investigation in supramolecule sensing assays.
- Chapter 5 involves the design and development of a novel fluorescent chemosensor for the detection of polyamines in biofluids. Polyamines are an interesting group of biomarkers that serve as health indicators in the human body. Thus, the development of robust, low-cost, and fast-responding sensors for polyamines that are applicable in biofluids (urine, blood, and saliva) could aid early disease detection and personalized medicine strategies. A self-assembled host-dye fluorescent chemosensor is investigated using a sulfonated pillar[*n*]arene host, in combination with dicationic diazapyrenium-based indicator dyes. The

photophysical and host-dye binding properties of the new fluorescent chemosensors have been explored in detail, and their stability is evaluated in saline buffers and biologically relevant media. Following this, an in-depth analysis of the binding characteristics (affinities and selectivity) of the pillar[*n*]arene-based fluorescent chemosensors with biogenic polyamines is carried out in saline buffers and biologically relevant media through fluorescence-based thermodynamic assays. Based on the results obtained, a general design concept for pillar[*n*]arene-based fluorescent chemosensors for the selective monitoring of individual polyamines and combined polyamine levels in biofluids is adopted through indicator dye modifications in the chemosensor and tuning the chemosensor selectivity. Ultimately, the practical applicability of the new chemosensor is evaluated in human urine and saliva samples at practically relevant polyamine levels.

Chapter 2

2 Chirality sensing of bioactive analytes in aqueous media with acyclic concave hosts

The results described in this chapter have been published as "Chirality sensing of terpenes, steroids, amino acids, peptides, and drugs with acyclic cucurbit[n]urils and molecular tweezers" in Chemical Communications, 2020.[201] The experimental data collection and analysis were carried out by me under the supervision of Dr. F. Biedermann. The manuscript was organized and written by me under the guidance of Dr. F Biedermann. The co-authors contributed by synthesizing materials for analysis (C1, C2: D. Bauer; CLR01: P. Rebmann; (R/S)-trinorbornane: L. Delarue Bizzini), providing valuable discussions and reviewing the article draft. Sections in this chapter have been reproduced from the published work[201] with permission from the Royal Society of Chemistry.

2.1. Introduction

Chirality is an intrinsic property of many compounds of biological origin, including amino acids, peptides, and proteins, but also widely present in synthetic molecules such as drugs.[201] Electronic Circular Dichroism (ECD) spectroscopy, which measures the difference in the absorption of left and right circularly polarized light, has been extensively used to study chiral, light-absorbing molecules.[190,191,210,225-227] However, most bioactive small molecules lack a strong chromophoric group and hence, absorb outside the practical, convenient near UV and visible wavelength region or are even entirely ECD silent. This has prompted several groups to develop supramolecular chromophoric probes and chemosensors that interact with the chiral analyte *via* covalent or non-covalent interactions, thereby giving rise to spectroscopic responses in the near UV or visible region.[96,173,207,209,210,228-230] In the simplest case, the complexation of a chiral analyte by an achiral chromophoric host can give rise to induced chiroptical signals, as the chromophore is then situated in a chiral environment.[210] Essentially, suitably strong emerging ECD signals are usually obtained if an electronic-coupling between the chromophoric host and the chiral analyte occurs (see Figure 2.1a).[173,207,208] In favorable cases, analyte-specific induced circular dichroism (ICD) bands occur, which can be utilized for analyte identification and differentiation.[173,201,231] The systems frequently use hydrogen bonding,[232-234] metal coordination,[209,211-213] or dynamic covalent bonds[214-217] as directional bonding motifs, leading to well-defined binding conformations.[234] However, for detecting compounds in aqueous media, only a few chirality-based chemosensors are available to date,[96,173,235-237] as the directional, polar non-covalent interactions are screened by the solvent. Furthermore, the hydrophobic effect as the most important driving force for binding in water,[52,238] lacks directionality and thus generally leads to ensembles of supramolecular complex conformations

with overall low ECD signals. This severely limits their biological applications, which requires the systems to be functional in water and hence the range of biorelevant molecules that can be detected. To achieve chirality sensing in water, concave hosts can be adopted that provide both strong hydrophobic binding forces and restrict the number of host-guest conformations.[52] For instance, the noncovalent chemosensing ensembles composed of the macrocycle cucurbit[8]uril (CB8) and dicationic reporter dyes respond with induced, analyte-indicative ECD signals in water to the presence of biorelevant chiral aromatic metabolites.[173]

In my investigations, I extended the concept of "chirality transfer" to a chromophoric achiral and concave host to acyclic cucurbit[*n*]urils and molecular tweezers. These acyclic concave hosts display sizeable binding constants for small bioactive molecules in aqueous media and engulf their guests inside their concave cavity. Acyclic cucurbit[*n*]urils bind a broad range of bioactive molecules, *e.g.*, amino acids, drugs, and hormones.[4,107,108] Molecular tweezers are more selective binders, for instance, for lysine, arginine, and their derivatives.[100-103] They also selectively recognize peptides and proteins with sterically accessible lysine and arginine residues.[102] This chapter focuses on systematic investigations into ECD-detected chirality sensing with acyclic cucurbit[*n*]urils or molecular tweezers as hosts for chiral analytes in water. Figure 2.1 and Figure 2.2 shows the different binding mechanisms in ECD signal generation and the chemical structures of the hosts and analytes tested in the study, respectively.

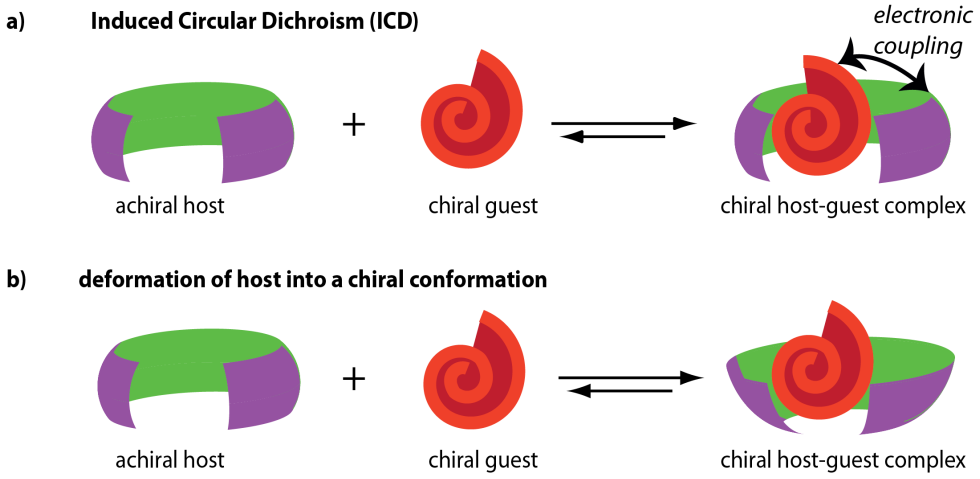

Figure 2.1: (a-b) Schematic representation of the two major mechanisms for complexation of chiral guests by achiral hosts, leading to ECD signal generation *via* (a) induced circular dichroism (ICD) through electronic-coupling between chromophoric host and guest, or (b) adoption of a chiral host conformation.

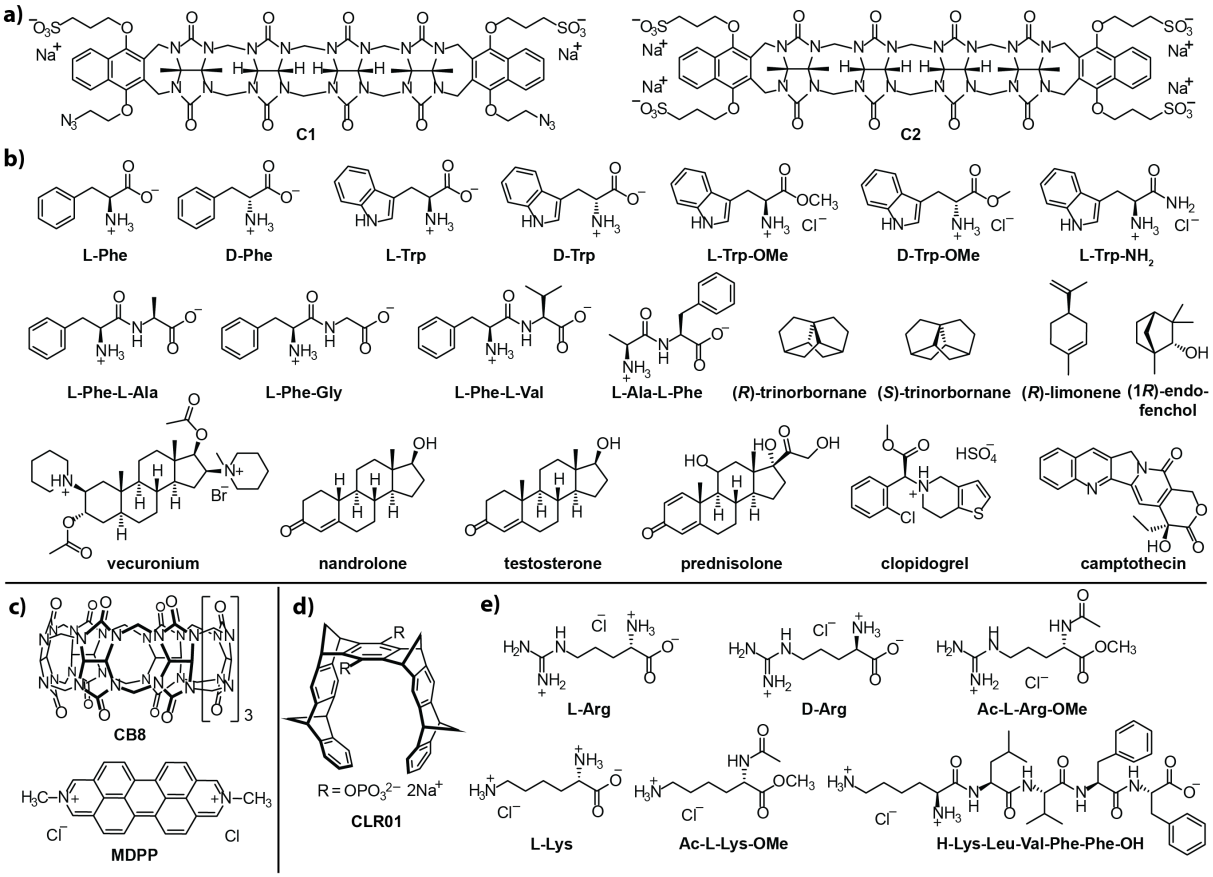

Figure 2.2: Chemical structures of (a) acyclicCB*n* hosts and (b) their chiral guests. (c) Chemical structure of the CB8•MDPP chemosensing ensemble that was used for comparison. Chemical structure of (d) the molecular tweezer and (e) its chiral guests. All compounds are shown in their native charge state in water.

2.2. Results and Discussion

2.2.1. Chirality sensing with acyclic cucurbit[*n*]urils

In this investigations, two different acyclic CB*n* (C1 and C2) (see Figure 2.2a), obtained *via* a stepwise oligomerization procedure[4,239] were utilized as the receptor host molecules. C1 and C2 differ in their charge, *i.e.,* C1 is a dianion and C2 a tetraanion, and the functional groups appended to their terminal aromatic units. Both C1 and C2 exhibit good water solubility.[239]

2.2.1.1. Detection of amino acids and dipeptides

To assess the utility of acyclic CB*n* for chirality sensing, the chiral aromatic amino acids L-Phe and L-Trp were added to aqueous solutions of the host C1 and the ECD spectra were recorded (Figure 2.3). A strong positive ECD band at 292 nm and a weaker one at 326 nm was observed for the supramolecular complex of C1 with either L-Phe or L-Trp. Their enantiomers D-Phe and D-Trp gave the expected mirrored ECD spectra upon complexation with host C1 (Figure 2.3). Similar results were obtained upon using several phenylalanine and tryptophan derivatives as guests (Figure 2.4a - 2.4b).

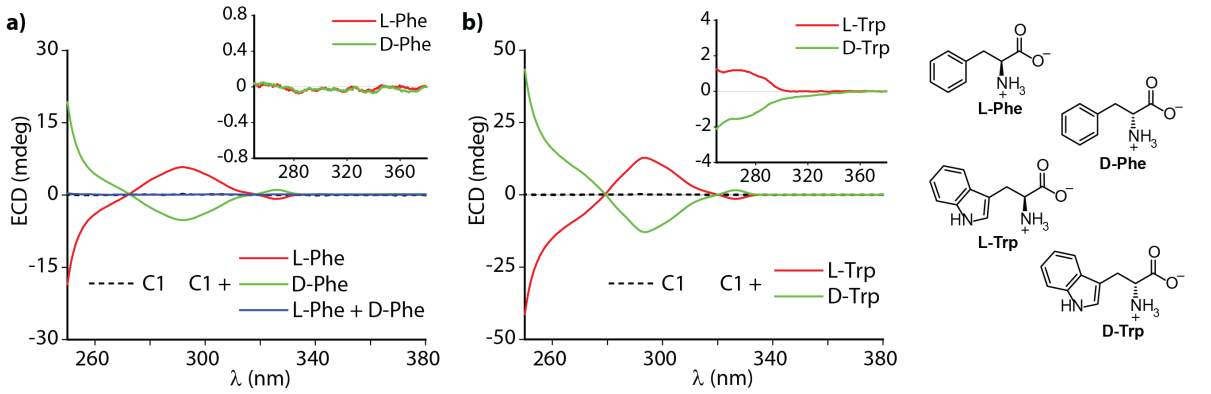

Figure 2.3: ECD spectra in water of host C1 (100 µM) and C1 (100 µM) in the presence of (a) L-Phe (100 µM), D-Phe (100 µM), and a racemic mixture composed of L-Phe and D-Phe (each at 100 µM), and (b) L-Trp (100 µM) and D-Trp (100 µM). The insets show the ECD spectra of the guests alone in water; the phenylalanine analytes do not show any ECD signals. The tryptophan analytes show weak ECD signals in the region examined when compared to the signals observed in the presence of C1.

In order to gain better insights into the "chirality transfer" recognition mechanism, the ECD signals arising on the addition of the chiral analytes to achiral acyclic C1 were compared to that of achiral CB8•MDPP[173](see Figure 2.2c) receptor. The complexation of phenylalanine and tryptophan derivatives by the CB8•MDPP chemosensing ensemble resulted in a completely different type of ECD spectra than observed for Phe- or Trp-species bound by the host C1 (Figure 2.4). In the case of acyclic CB*n*•guest complexes, the ECD band position and shapes (*e.g.,* a stronger band at 292 nm and a weaker one at 326 nm) coincide with the absorbance band maxima of the free host (Figure 2.4a – 2.4b and see Figure 2.13a in Section 2.5 - Additional Information for C1 absorbance spectrum). Furthermore, the ECD spectra of C1 complexes with different chiral guests did not give rise to unique ECD spectral bands but rather differed only in the signal magnitude. On the contrary, the ECD spectra of the CB8•MDPP chemosensing ensemble displayed analyte indicative spectral fingerprints for different phenylalanine and tryptophan derivatives (Figure 2.4c – 2.4d). In addition, the band shape in the ECD spectrum clearly differed from that in the absorbance spectrum of the CB8•MDPP chemosensing ensemble (Figure 2.4c – 2.4d and see Figure 2.13d in Section 2.5 - Additional Information for CB8•MDPP absorbance spectrum).

Two different mechanisms may therefore be at work: i) In the case of acyclicCB*n*•guest complexes, the host deforms into a chiral conformation upon binding the chiral analyte (Figure 2.1b). Different chiral analytes can result in a different degree of host deformation and are thus characterized by different signal magnitudes in the ECD spectra. Indeed, reported crystal structures of acyclicCB*n* and acyclicCB*n*•guest complexes show substantial conformational deformations upon guest binding.[4,109] However, there is no substantial contribution of a

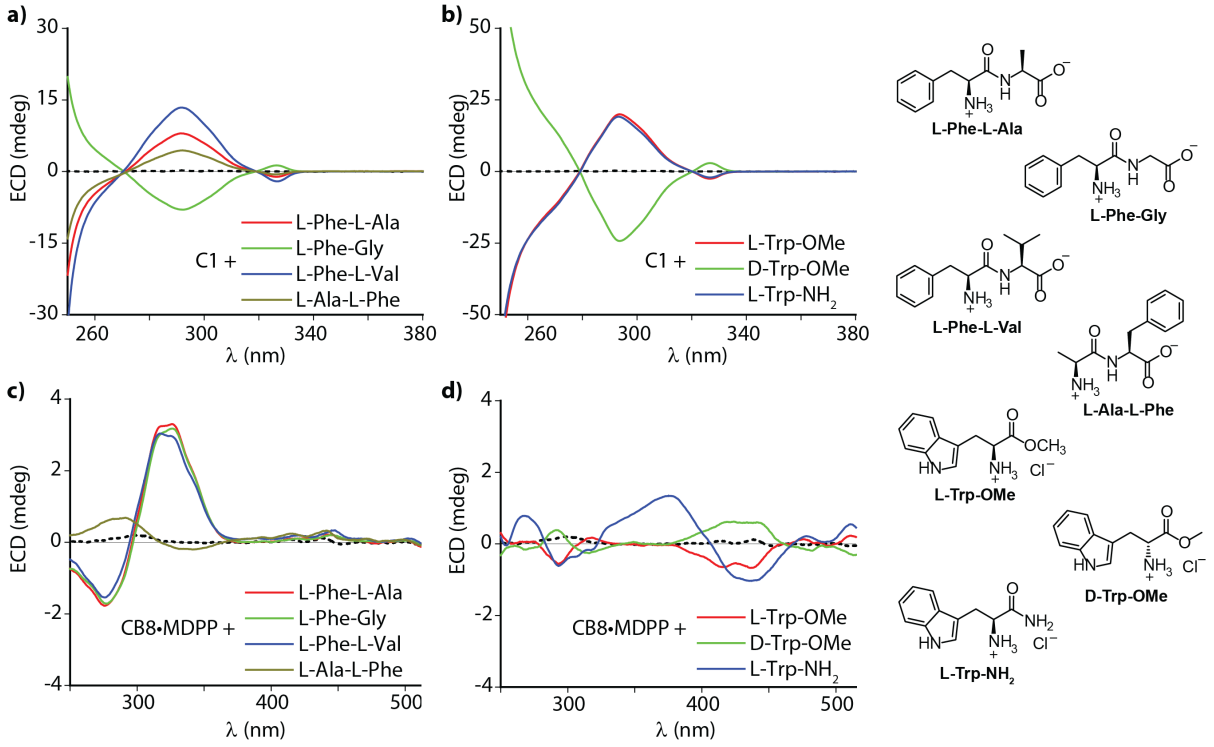

Figure 2.4: ECD spectra in water of host C1 (100 μM) in the presence of (a) L-Phe-L-Ala, L-Phe-Gly, L-Phe-L-Val, and L-Ala-L-Phe (each at 100 μM) and (b) L-Trp-OMe, D-Trp-OMe and L-Trp-NH_2 (each at 100 μM). ECD spectra in water of host CB8•MDPP (20 μM) in the presence of (c) L-Phe-L-Ala, L-Phe-Gly, L-Phe-L-Val, and L-Ala-L-Phe (each at 50 μM) and (d) L-Trp-OMe, D-Trp-OMe and L-Trp-NH_2 (each at 50 μM). In each case, the dashed black line represents the ECD signals from the receptor host molecule alone.

transition dipole coupling between the naphthol-type chromophores of the host and any chromophoric unit of the chiral guest. Therefore, the ECD spectrum of acyclicCB*n*•guest complexes closely resembles the absorbance spectrum of the host. ii) For complexes of aromatic chiral guests with CB8•MDPP, there is a significant contribution of a transition dipole coupling between the dicationic MDPP chromophore and the aryl moiety of the guest, leading to guest-indicative induced circular dichroism (ICD) bands. Similarly, upon changing the chromophore to MDAP,[173] completely new ICD bands and trends were observed for the same series of chiral guests (see Figure 2.14 in Section 2.5 - Additional Information), as is expected for an ICD effect. Because both CB8 and MDPP (or MDAP) are relatively rigid,[73] there is likely no significant contribution of chiral deformation of the host upon analyte binding.

The different ECD signal generation mechanisms in the case of C1 and CB8•MDPP hosts upon binding chiral analytes can be used complementarily in specific sensing assays. For instance, host C1 can be used to distinguish the dipeptides L-Phe-Gly, L-Phe-L-Ala, L-Phe-L-Val, and L-Ala-L-Phe from each other by ECD spectroscopy (Figure 2.4a). At the same time, with the CB8•MDPP chemosensing ensemble, only L-Ala-L-Phe can be differentiated from the other dipeptides (Figure 2.4c).

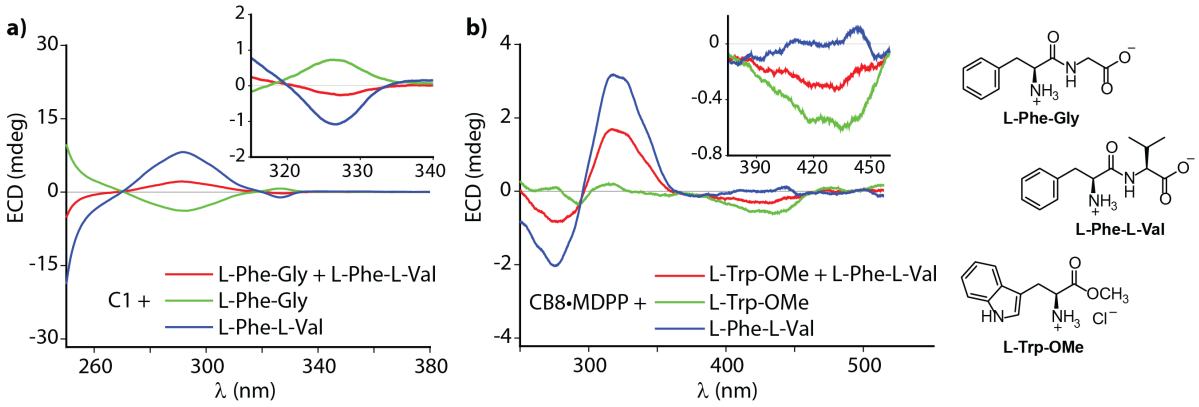

Figure 2.5: (a) ECD spectra in water of host C1 (100 µM) in the presence of L-Phe-Gly (50 µM), L-Phe-L-Val (50 µM), and a 1:1 mixture of L-Phe-Gly and L-Phe-L-Val (each at 50 µM). The inset shows the magnified spectrum between 315-340 nm. (b) ECD spectra in water of host CB8•MDPP (20 µM) in the presence of L-Trp-OMe (50 µM), L-Phe-L-Val (50 µM), and a 1:1 mixture of L-Trp-OMe and L-Phe-L-Val (each at 50 µM). The inset shows the magnified spectrum between 375-460 nm.

In addition, simple mixtures of peptides, *e.g.*, L-Phe-Gly and L-Phe-L-Val can be deconvoluted by using the emerging ECD signals in the presence of host C1 (see Figure 2.5a). While the CB8•MDPP chemosensing ensemble is particularly useful for analyzing mixtures of Phe- and Trp-species (Figure 2.5b).

The molar ellipticity and molar circular dichroism values for C1 and CB8•MDPP complexes with the studied chiral analytes are shown in Table 2.2 and Table 2.3 in Section 2.5 - Additional Information.

2.2.1.2. Racemization reaction monitoring of amino acids and dipeptides

In addition to chirality sensing, the emerging ECD signals in C1 in the presence of amino acids can be utilized for monitoring their racemization reaction. Under alkaline conditions, several neutral free amino acids such as L-Phe undergo serious racemization and decomposition in polar organic solvents such as DMF and ethylene glycol. At the same time, this phenomenon is largely decreased in water under the same alkaline conditions.[240] However, in order to monitor the racemization event, reported studies adopt a rather lengthy derivatization procedure before the samples were analyzed by HPLC.[240] In my investigation, I monitored the base-catalyzed racemization of L-Phe and the peptide L-Phe-Gly in organic solvents (DMF, ethylene glycol) and water by ECD spectroscopy. L-Phe and L-Phe-Gly were heated in separate reaction vials in the presence of 1.2 eq. of K_2CO_3 in DMF, ethylene glycol, and water at 130°C for 2 h. A control reaction was carried out at 25°C in DMF under the same conditions for 24 h. Aliquots of the reaction mixture were added before and at the end of the reaction to the aqueous C1 host solution at 25°C. The resulting racemization was evaluated by monitoring the emerging ECD signal intensities.

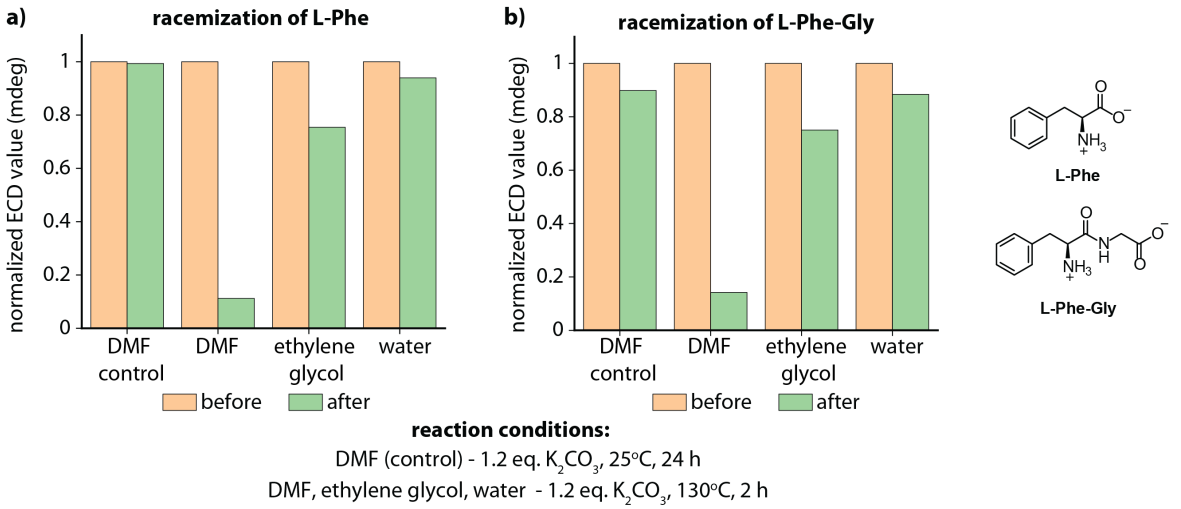

Figure 2.6: Monitoring the racemization of (a) L-Phe and (b) L-Phe-Gly in the presence of C1 before and after completion of the reaction in DMF, ethylene glycol and water using single wavelength ECD measurements (λ_{obs} = 292 nm, Data Pitch = 10 s, D.I.T = 16 s, $t_{measure}$ = 6 min). The ECD signals were monitored in water at a concentration of C1 of 100 µM in the presence of an excess of L-Phe and L-Phe-Gly (≈200 µM) from the reaction mixture. The DMF (control) shows the control reaction in DMF when the reaction mixture was kept at room temperature instead of heating to 130 °C.

In accordance with the literature,[240] I found that water suppressed racemization that is occurring in DMF at increased temperature, which was characterized by the diminished ECD signals (Figure 2.6). This chemosensor-based monitoring approach is faster than the established chromatography-based method,[240] and thus allows for screening of reaction conditions.

2.2.1.3. Detection of water-insoluble terpenes

As acyclic CB*n* binds a wide range of hydrophobic molecules, and because no ICD signal generation is required for acyclic CB*n*, these hosts can be used for chirality sensing of analyte classes beyond the scope of previously reported chemosensing ensembles. For instance, the water-insoluble terpenes, limonene, and fenchol do not show ECD signals above 250 nm (Figure 2.7a). However, the addition of both (*R*)-limonene and (1*R*)-*endo*-(+)-fenchol to an aqueous solution of host C1 enhances their solubility on host-guest complexation and clearly displayed bands in the ECD spectrum up to 340 nm (Figure 2.7a). The ECD signals can be attributed to the chiral induction upon supramolecular complex formation. Similarly, the complexation of the chiral bridged-alkane trinorbornane[241,242] by host C2 gave rise to clear ECD signals despite the completely non-chromophoric nature of the hydrocarbon guest (Figure 2.7b).

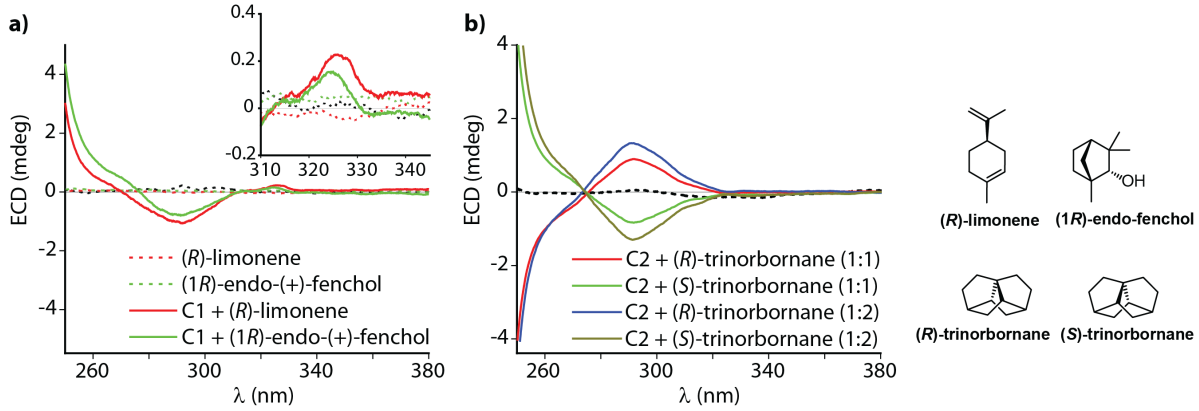

Figure 2.7: ECD spectra of C1 (100 μM) in the presence of (*R*)-limonene (100 μM) and (1*R*)-endo-fenchol (100 μM) in water (with ≤ 5 vol% ethanol). The dashed red and green line represents the ECD spectra of the guests alone. (b) ECD spectra of C2 (100 μM) in the presence of the enantiomers, (*R*)- or (*S*)-trinorbornane (99 μM), and excess of the analyte (197 μM) in water (with ≤ 1.2 vol% ACN). In each case, the dashed black line represents the ECD signals from the receptor host molecule alone.

2.2.1.4. Detection of water-insoluble and partially soluble drugs

The acyclic CB*n* type molecular containers are known to bind and enhance the solubility and bioactivity of a wide range of poorly soluble pharmaceuticals.[4] Hence, the utility of acyclic CB*n* for ECD-based detection of chiral drugs was evaluated. The steroidal drugs vecuronium, nandrolone, and prednisolone were added to aqueous solutions of the host C1 and C2, and the resulting ECD signals were monitored. In presence of host C1 and C2, vecuronium show emerging ECD signals in the 250 - 350 nm region upon complex formation, while the steroid alone does not show any ECD signals in this region (Figure 2.8a – 2.8b). The chromophoric steroids, nandrolone, and prednisolone possess ECD signals on their own but binding to C1 or C2 caused characteristic shifts and increase in the signal intensities in the ECD spectra (Figure 2.8a – 2.8b). Besides, the different host variants C1 and C2 gave rise to different induced ECD spectra with these steroids, which may be useful for pattern-recognition-based[75] steroid identification. In principle, it was also possible to deconvolute steroid mixtures using the host-guest binding induced circular dichroism signals (Figure 2.8c – 2.8d). The addition of C1 to a mixture of nandrolone and vecuronium showed ECD bands characteristic of both guests.

Likewise, strong ECD signals were observed when the water-insoluble chiral chromophoric drugs, testosterone, camptothecin, and clopidogrel were solubilized in water through binding with acyclic CB*n*,[4], *i.e.,* by both C1 and C2 (Figure 2.9). The host•drug complex for the measurement was obtained by stirring solutions containing a known concentration of C1 or C2 with an excess of the solid drug in water at room temperature for 12 hrs. The excess insoluble drug was removed by centrifugation, and the supernatant containing the complex collected for the measurement. All the three steroids tested solubilized in water upon complexation by C1

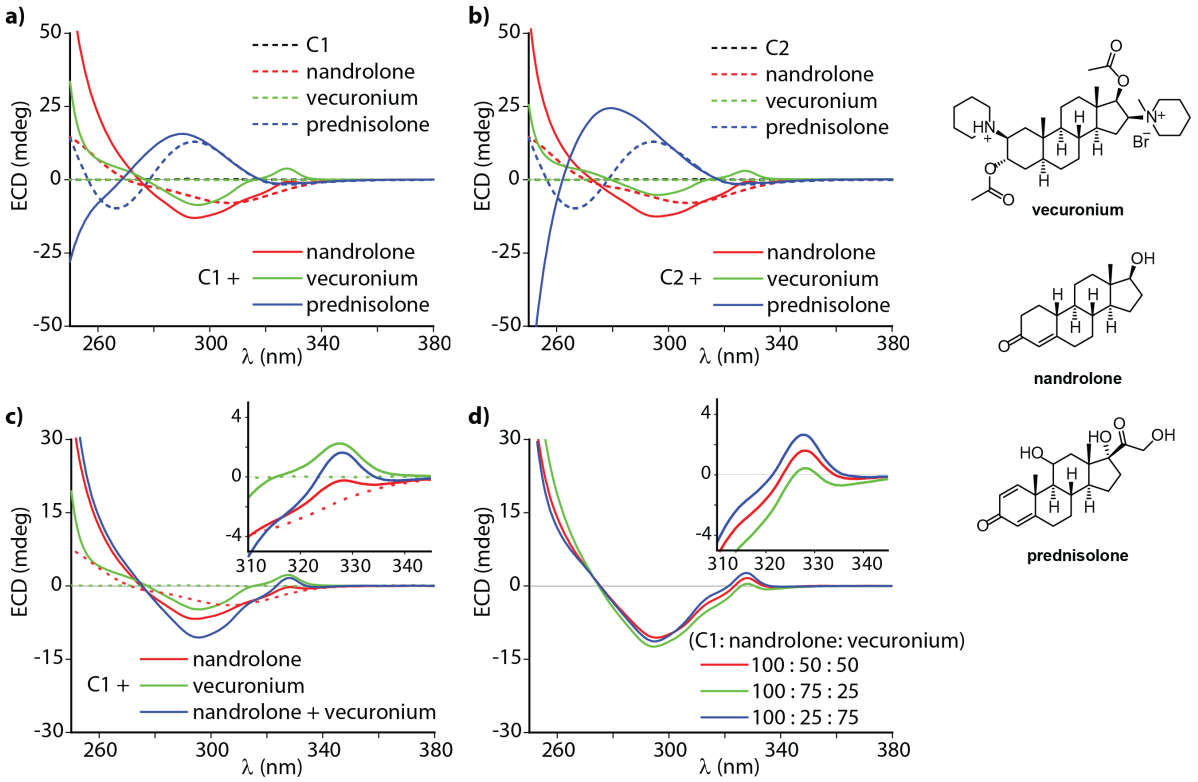

Figure 2.8: ECD spectra in water of the steroids nandrolone, vecuronium, and prednisolone (each at 100 μM) in the absence and presence of host (a) C1 (100 μM) and (b) C2 (100 μM). (c) ECD spectra in water of C1 (100 μM) in the presence of nandrolone (50 μM), vecuronium (50 μM), and a 1:1 mixture of nandrolone and vecuronium (each at 50 μM). The dashed red and green line represents the ECD spectra of the guests alone. (d) ECD spectra of C1 (100 μM) in the presence of varying ratios of nandrolone and vecuronium in the mixture (C1: nandrolone: vecuronium).

or C2 and showed distinct induced ECD signals (Figure 2.9). Figure 2.9a inset shows the control experiment for the ECD spectra of the drugs alone measured in ethanol. Again, the binding of the chiral chromophoric guests by the achiral chromophoric host caused characteristic changes in the ECD spectrum.

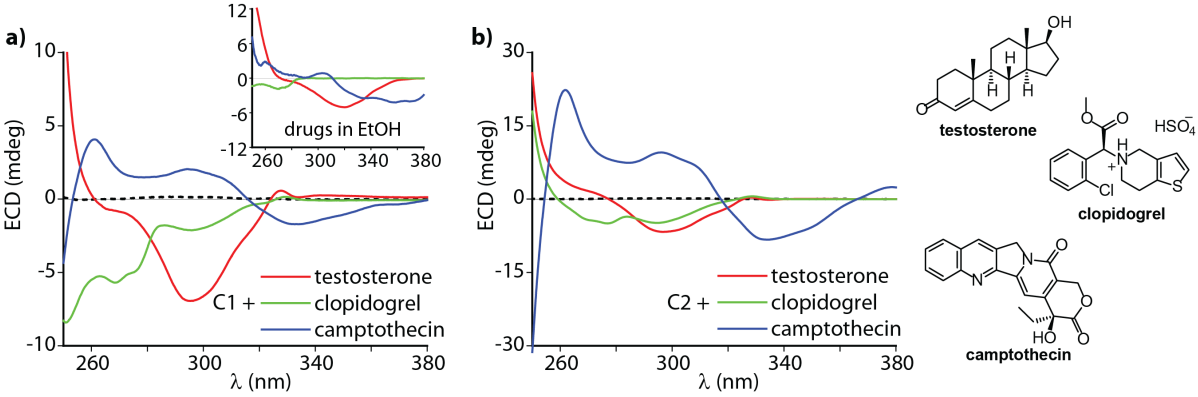

Figure 2.9: ECD spectra in water of host (a) C1 (100 μM) and (b) C2 (100 μM) in the presence of excess of testosterone, clopidogrel and camptothecin. The inset in (a) shows the ECD spectra of testosterone, clopidogrel, and camptothecin (each at 100 μM) in ethanol.

2.2.2. Chirality sensing with molecular tweezer

In this investigations a water-soluble molecular tweezer, CLR01 (see Figure 2.2d) with a phosphate group on either side of the tweezer's central benzene bridge was utilized.

2.2.2.1. Detection of lysine and arginine based amino acids and peptides

The molecular tweezer, CLR01 (see Figure 2.2d), selectively complex lysine and arginine derivatives and reject all other amino acids. Unlike the previously used acyclic CB*n* molecular tweezer, CLR01 is a rigid host[102,103]. Thus, it is unlikely that a substantial chiral twist of the host structure occurs upon the inclusion of a chiral guest. Nevertheless, the addition of chiral amino acids, Arg, Lys, and their derivatives to an aqueous solution of the host CLR01 showed distinguishable analyte-specific ECD fingerprints in their recorded spectra upon complexation by CLR01 (Figure 2.10 and Figure 2.11). This ICD effect can be explained through the coupling of the transition dipole of the host with that of the chromophores of the Lys/Arg derivatives (*e.g.*, the amide groups).

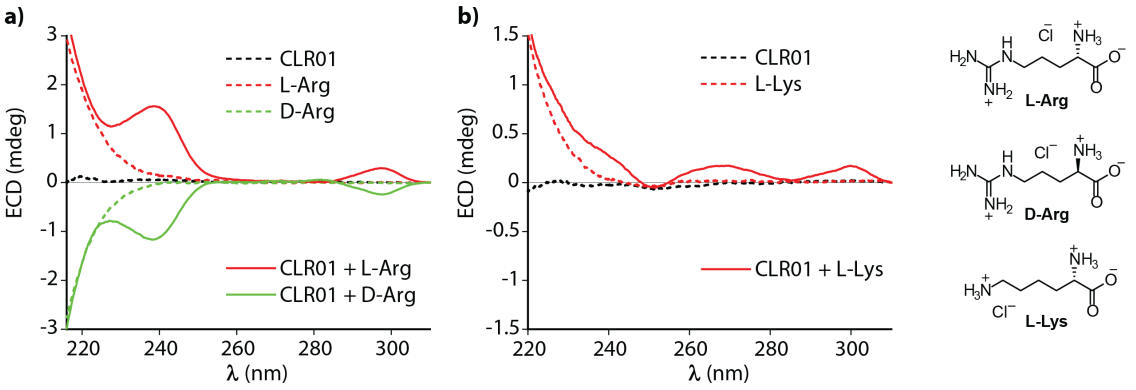

Figure 2.10: ECD spectra in water of host CLR01 (20 µM) in the presence of (a) L-Arg (200 µM) and D-Arg (200 µM) and (b) L-Lys (200 µM). The dashed lines represent the ECD spectra of the guests and host alone.

The amino acids and their derivatives possess ECD signals on their own below 250 nm; however, complexation with CLR01 resulted in induced ECD signals up to 310 nm. In addition to amino acids, even peptides containing lysine units gave clearly distinguishable ECD bands in the presence of host CLR01 (Figure 2.11c). In analogy to the aforementioned examples, an ECD-based sensing protocol can, in principle, be established with host CLR01 to deconvolute mixtures of Lys- and Arg-derivatives. The addition of CLR01 to a 1:1 mixture of L-Arg and L-Lys in water showed ICD bands characteristic of both guests in the spectra (Figure 2.12).

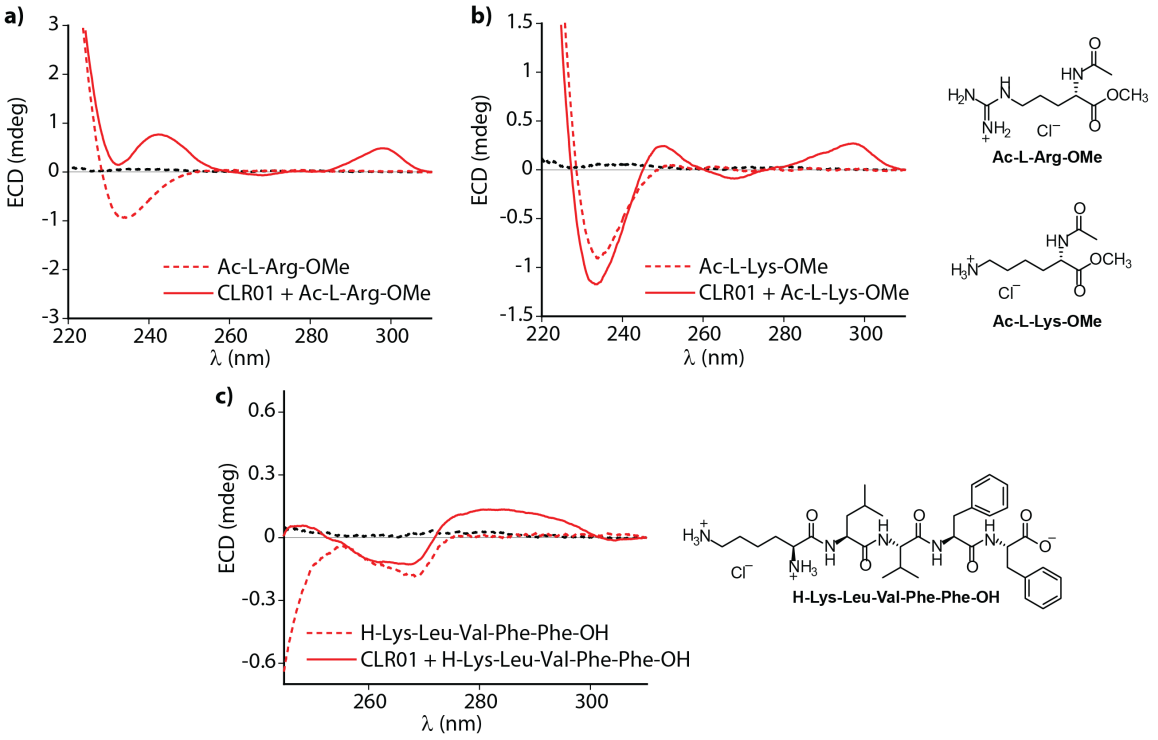

Figure 2.11: ECD spectra in water of host CLR01 (20 μM) in the presence of (a) Ac-L-Arg-OMe (200 μM), (b) Ac-L-Lys-OMe (200 μM), and (c) H-Lys-Leu-Val-Phe-Phe-OH (200 μM). The dashed red line represents the ECD spectra of the guests alone. The dashed black line in each case represents the ECD signals from the receptor host molecule alone.

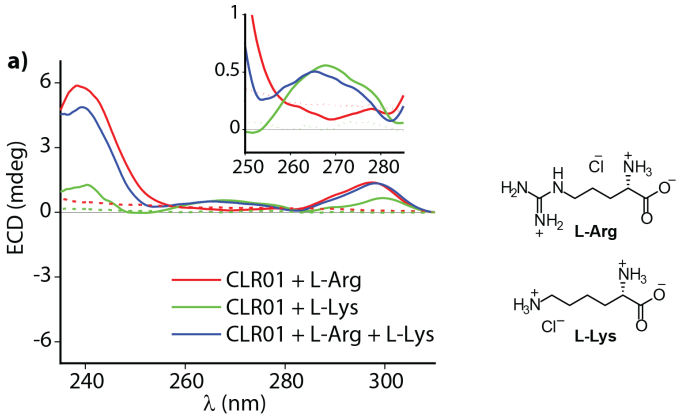

Figure 2.12: ECD spectra in water of host CLR01 (20 μM) in the presence of (a) L-Arg (70 μM), (b) L-Lys (70 μM), and a 1:1 mixture of L-Arg and L-Lys (each at 70 μM). The dashed red and green line represents the ECD spectra of the guests alone.

Surprisingly, the ICD for arginine is much larger than that for lysine (Figure 2.12), although CLR01 binds Lys tighter.[103] Possibly of more practical relevance, this may be used to differentiate the tweezer binding motif in structurally complex, simultaneously Lys- and Arg-containing peptides and proteins. To date, structural information about the preferred tweezer binding sites on peptides and proteins must be derived from 2D/3D NMR spectra and crystal structures.[243]

2.3. Conclusion

In conclusion, acyclic concave hosts, namely a molecular tweezer CLR01 and acyclic cucurbit[*n*]uril derivatives, C1 and C2, were successfully utilized for the Electronic Circular Dichroism-detected chirality sensing of small bioactive molecules in aqueous media. The formation of the chiral supramolecular host-guest complex self-assembled from the achiral, chromophoric host and chiral (non-)chromophoric small molecule guest gave information-rich ECD spectra with potential utility for chirality sensing, analyte identification, and reaction monitoring applications. The findings suggest two tentative host design principles for chirality sensing: 1) if a host should provide analyte-indicative induced circular dichroism fingerprints, then the use of rigid host structures is recommended. 2) General binders for chiral guests should possess a flexible and adaptable host structure that adopts a chiral, twisted conformation upon binding the chiral analyte. Such hosts are then also applicable for chirality sensing of non-chromophoric guests. These supramolecular chirality sensing systems show promising potential due to their advantages for high-throughput and fast chirality detection. They may find routine applications in the laboratory praxis in the near future.

2.4. Experimental details

2.4.1. Materials

All solvents were used as received from Aldrich or Fluka without further purification. All chemicals were purchased and used as received unless stated otherwise. The acyclic CB*n* molecular container C1[239] and C2[239] were synthesized according to the literature procedures. Daniel Bauer from the research group of Prof. Stefan Kubik carried out the synthesis of C1 and C2. The molecular tweezer CLR01 were synthesized according to the literature procedures.[103] Philipp Rebmann from the research group of Prof. Thomas Schrader carried out the synthesis of CLR01. The chiral tetracyclic hydrocarbon analytes, (*R*)-trinorbornane and (*S*)-trinorbornane were synthesized according to the literature procedures.[241,242] Lorenzo Delarue Bizzini from the research group of Prof. Marcel Mayor carried out the synthesis of (*R*)-trinorbornane and (*S*)-trinorbornane. CB8 was synthesized according to literature procedures[244] but was also purchased from Strem or Sigma. MDPP[245] was synthesized from 1,3,8,10 tetrahydro-2,9-dimethyl-2,9-diazadibenzoperylene, according to literature procedures.[245] Likewise, MDAP[159] was synthesized from 1,3,6,8-tetrahydro-2,7-dimethyl-2,7-diazapyrene, according to the literature procedure.[246,247] Dr. Laura Grimm from the research group of Dr. Frank Biedermann carried out the synthesis of MDAP.

2.4.2. Instrumentation

Absorption spectra were measured on a Jasco V-730 double-beam UV–VIS spectrophotometer and baseline corrected. ECD spectra were recorded on a Jasco J-1500 CD spectrometer equipped with a Peltier-thermostated cell holder and an emission optical kit, including a collecting lens and a filter holder. The spectrometer contains two PMT detectors: a standard detector (for ECD) and a dedicated FDCD detector. The HT Voltage applied to the PMT of the ECD detector was kept in auto mode. The second FDCD detector was not utilized here for the measurements. All ECD spectra reported were baseline corrected for the appropriate solvent system used. All the spectral measurements were conducted at 25°C unless stated otherwise. For measurements conducted in water, deionized water was used in all cases. Blank measurements of water or buffer provided no induced ECD effects in the regions examined. For spectroscopy analysis in quartz cuvettes, suprasil (type 111-QS) emission cuvettes with a light path of 10 mm and dimensions of 10x10 mm from Hellma-Analytics were utilized.

2.4.3. Sample Preparation

The stock solutions of water-soluble molecules were prepared in water and kept in the fridge at +8 °C for storage, except for CLR01, Ac-L-Lys-OMe, and H-Lys-Leu-Val-Phe-Phe-OH, which were stored in the freezer at −20°C. For water-insoluble molecules such as (*R*)-limonene, (1*R*)-endo-(+)-fenchol, clopidogrel, testosterone, and camptothecin, the stock solutions were prepared in ethanol and then diluted in the host-containing water solution for the ECD measurements. For the water-insoluble chiral bridged-alkane trinorbornanes studied, the stock solutions were prepared in acetonitrile and then diluted in the host-containing water solution for the ECD measurements. All the stock solutions prepared in ethanol and acetonitrile were stored in the freezer at -20°C. Nandrolone and prednisolone have a solubility of 810 μM[75] and 483 μM[75], respectively, in water. Hence, their stock solutions were prepared in water.

The concentration of the dyes and the analyte stock solutions were determined by UV-Vis absorption titration measurements unless stated otherwise. The molar extinction coefficients of the samples used to determine the concentration of their stock solutions by UV-Vis absorption titration are given in Table 2.1.

Table 2.1: Absorption maxima (λ_{max}) and molar extinction coefficients ($\varepsilon_{\lambda max}$) of the dyes and analytes used for the determination of the concentration of their stock solutions by UV-Vis absorption titration measurements.

Sample	λ_{max} (nm)	$\varepsilon_{\lambda max}$ ($M^{-1}cm^{-1}$)
C1	290	12161
C2	290	8610
CLR01	285	8425
MDPP	413	26000
MDAP	393	7800
CB8•MDPP	443	55000
CB8•MDAP	419	7600
D-Phe	257.6	1952[248]
L-Phe	257.6	195[248]
L-Trp	278	5579[248]
D-Trp	278	5579[248]
L-Trp-NH_2	278	5579[248]
L-Trp-OMe	278	5579[248]
D-Trp-OMe	278	5579[248]
L-Phe-L-Ala	257.6	195[248]
L-Phe-Gly	257.6	195[248]
L-Phe-L-Val	257.6	195[248]
L-Ala-L-Phe	257.6	195[248]

For samples whose molar extinction coefficient could not be found in the literature, the stock solutions were prepared by appropriately weighing in the required amount of the pure sample to attain the desired concentration for the determination of the molar extinction coefficient. The concentration of the stock solution of the host CB8 was determined by fluorescence titration against the high-affinity MPCP dye[152] by exciting the sample at 368 nm and collecting the emission intensity at 531 nm.

2.5. Additional Information

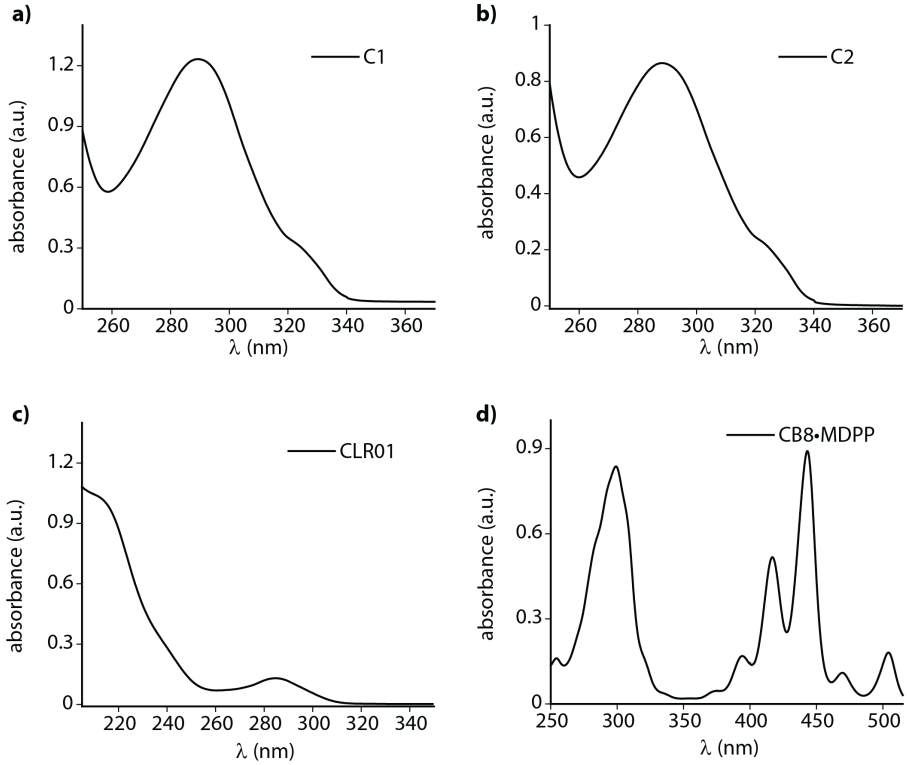

Figure 2.13: Absorbance spectra in water of (a) C1 (100 µM), (b) C2 (100 µM) and (c) CLR01 (20 µM). Absorbance spectra in water of the chemosensing ensemble (d) CB8•MDPP (20 µM) used for comparison.

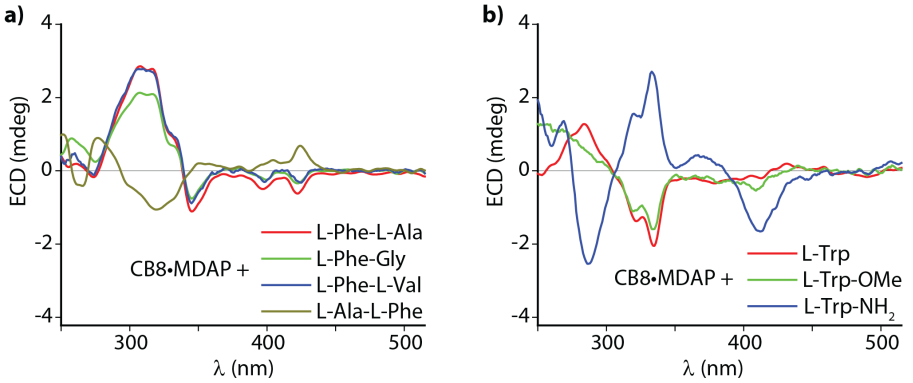

Figure 2.14: ECD spectra in water of host CB8•MDAP (100 µM) in the presence of (a) L-Phe-L-Ala (400 µM), L-Phe-Gly (350 µM), L-Phe-L-Val (350 µM), and L-Ala-L-Phe (1800 µM) and (d) L-Trp (176 µM), L-Trp-OMe (200µM) and L-Trp-NH_2 (176 µM).

Experimentally recorded ellipticity values (θ in mDeg) were converted into molar ellipticity ([θ]) values according to [θ] = θ/(10*L*C), with the pathlength L in cm and the concentration C of the receptor in mol/L. The molar circular dichroism (Δε) was obtained *via* Δε = [θ] /3298.

Table 2.2: Molar ellipticity and molar circular dichroism data for complexes of C1 (100 μM) with chiral analytes in water at 25 °C.

Chiral analyte	λ_{max} (nm)	[θ] x 10^3 (deg M^{-1} m^{-1})	Δε (M^{-1} cm^{-1})
L-Phe	292	5.80	1.76
	326	−1.09	−0.33
D-Phe	292	−5.22	−1.58
	326	1.08	0.33
L-Phe-L-Ala	292	7.98	2.42
	326	−1.09	−0.33
L-Phe-Gly	292	−7.99	−2.42
	326	1.26	0.38
L-Phe-L-Val	292	13.39	4.06
	326	−2.02	−0.61
L-Ala-Phe	292	4.43	1.34
	326	−0.60	−0.18
L-Trp	293	12.79	3.88
	326	−1.38	−0.41
D-Trp	293	−12.86	−3.40
	326	1.59	0.48
L-Trp-OMe	293	19.88	6.03
	326	−2.47	−0.75
D-Trp-OMe	293	−24.18	−7.33
	326	2.85	0.86
L-Trp-NH_2	293	19.10	5.79
	326	−2.06	−0.62
vecuronium	296	−8.75	−2.65
	328	3.94	1.19
(*R*)-limonene[a]	291	−1.03	−0.31
	326	0.23	0.07
((1*R*)-endo-(+)-fenchol[a]	291	−0.79	−0.24
	324	0.15	0.05
(*R*)-trinorbornane[b]	291	1.34	0.40
(*S*)-trinorbornane[b]	291	−1.30	−0.39

[a] with ≤ 5 vol% ethanol in DI-water
[b] with ≤ 1.2 vol% ACN in DI-water

Table 2.3: Molar ellipticity and molar circular dichroism data for complexes of CB8•MDPP (20 μM) with chiral analytes in water at 25 °C.

Chiral analyte	λ_{max} (nm)	[θ] x 10^3 (deg M^{-1} m^{-1})	Δε (M^{-1} cm^{-1})
L-Phe	280	−10.91	−3.31
	330	8.02	2.43
D-Phe	280	11.48	3.41
	330	−7.89	−2.39
L-Phe-L-Ala	276	−8.86	−2.69
	322	16.29	4.94
L-Phe-Gly	276	−8.53	−2.55
	322	15.55	4.72
L-Phe-L-Val	276	−7.69	−2.33
	322	14.90	4.52
L-Ala-Phe	286	3.27	0.99
	326	−0.95	−0.29
L-Trp	293	−2.19	−0.66
	439	−2.50	−0.76
D-Trp	293	2.30	0.70
	439	2.42	0.73
L-Trp-OMe	287	−1.88	−0.57
	418	−3.20	−0.97
D-Trp-OMe	287	1.52	0.46
	418	3.04	0.92
L-Trp-NH_2	375	6.68	2.03
	435	−5.16	−1.56

Chapter 3

3 Fluorescence detected circular dichroism (FDCD) for supramolecular host-guest complexes: Improved signal generation strategies

The results described in this chapter have been published as "Fluorescence detected circular dichroism (FDCD) for supramolecular host–guest complexes" in Chemical Science, 2021.[249] The experimental design, investigation, and data analysis were carried out by me under the supervision of Dr. S. Sinn and Dr. F. Biedermann. The manuscript was organized and written by me under the guidance of Dr. F Biedermann. The co-authors contributed by synthesizing materials for analysis ((S_p)- and (R_p)-MPCP: Dr. E. Spuling; (S_p)-MVCP: Y. Wang; MT: L. P. Yang), providing additional supporting data (LD, LB, FDLD, and fluorescence anisotropy measurements and analysis: C. Spies, P. Albertini; DOSY NMR measurements for MT aggregation study: L. P. Yang) along with valuable discussions and reviewing the article draft. Sections in this chapter have been reproduced from the published work[249] with permission from the Royal Society of Chemistry.

3.1. Introduction

Investigations into the chirality of biological and synthetic compounds and monitoring of chiral transformations have always been of prime importance. Such investigations provide valuable lessons for the design of drugs and functional materials and enrich the general understanding of molecular recognition principles.[201,205,250,251] Among the chirality detection methods, supramolecular chemosensors and probes based on molecular recognition have made significant progress in the recent years for the optical chirality sensing of small bioactive and synthetic molecules by ECD spectroscopy.[201,209,210,228-230] The complexation of a chiral analyte (guest) by an achiral chromophoric host can give rise to induced ECD signals (Figure 3.1).[173,207,208] The induction of chirality can occur either by an electronic-coupling between the chromophoric host and the chiral guest in case of rigid host molecules or by the deformation of the host into a chiral conformation upon guest binding in case of flexible host molecules.[201] Such supramolecular ECD-based chemosensors and probes have been used by Berova,[207,211] Wolf,[213-215,231] Borhan,[252-254] Anslyn,[255-257] Biedermann,[173,201] Canary,[257-259] Jiang,[96] and others[260-262] for the analysis of chiral compounds in organic or aqueous media. Chirality-sensors that operate in aqueous media are of the widest practical relevance.[96,173,236] For instance, endo-functionalized molecular tube MT, see Figure 3.2a, shows strong induced ECD signals above 300 nm upon binding to chiral epoxides in water (concentration of host and guest ≥100 μM), while the chiral guests alone do not absorb in this wavelength region.[96] For chemosensors that were modularly assembled of the large macrocycle cucurbit[8]uril (CB8, see Figure 3.2a) and dicationic reporter dyes, these induced ECD signals were present in the wavelength region up

to 600 nm, allowing for the facile distinction of structurally similar tryptophan-containing peptides and biorelevant chiral aromatic metabolites at concentrations as low as 20 μM.[173] However, the concentration range where ECD measurements can be applied is relatively narrow, as it depends on the intensity of dichroic absorption.[263,264] Thus, the ECD detection limit is set by the molar extinction coefficient of the chromophoric host (or guest), which rarely reaches 10^5 M^{-1} cm^{-1}. As a result, receptor and analyte concentrations ≥10 μM, oftentimes even >100 μM, are required in most cases for generating meaningful ECD signals.[96,173,228] This can be challenging for sensing in real biological media, where many diagnostically relevant analytes are only present in the low micromolar-to-nanomolar concentration regime and thus escape ECD-based detection protocols. Moreover, most biomolecules and artificial supramolecular systems are prone to aggregate in aqueous environments and need to be measured at low concentrations.

An attempt to improve the sensitivity of chiroptical supramolecular assays is the use of a fluorescence-based instead of an absorbance-based chiroptical method. Both fluorescence-detected circular dichroism (FDCD) spectroscopy[198,199,265] and circularly polarized luminescence (CPL) spectroscopy[266-269] are promising techniques, with the latter receiving a revival in recent years.[266-269] In principle, CPL measures the circularly polarized emission from a chiral emitter,[270] while FDCD is probing differences in the excitation spectrum when the sample is irradiated with circularly polarized light, see Figure 3.1.[196,197] In addition to a sensitivity enhancement, FDCD and CPL possess additional merit for sensing applications in

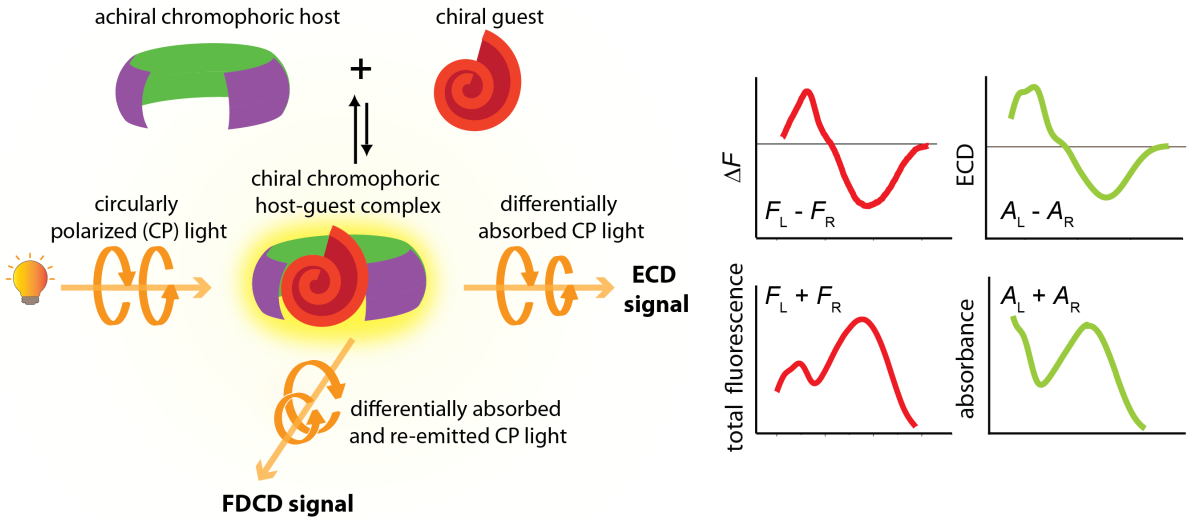

Figure 3.1: Complexation of a chiral guest by an achiral chromophoric and emissive host can give rise to induced ECD and FDCD signals. The ECD signal measures the difference in absorption of left-handed and right-handed circularly polarized light by the chiral species, whereas the FDCD (or ΔF) signal measures the differential fluorescence intensity that results from excitation with left-handed and right-handed circularly polarized light.

(complex) biofluids by reducing the chiroptical background of non-fluorescent matrix components, as only compounds that are both chiral and fluorescent give rise to an emission-based chiroptical signal.[271-273] Practicably, FDCD has an edge over CPL for the chirality sensing of analytes and differentiation by spectroscopic fingerprints. Firstly, in excitation, a variety of electronic transitions ($S_0 \rightarrow S_n$, $n \geq 1$) can be observed, giving rise to well-structured spectra (= spectroscopic fingerprints), while molecular luminescence generally occurs only from the lowest excited state ($S_1 \rightarrow S_0$ or $T_1 \rightarrow S_0$, following Kasha's rule), and are typically featureless.[274,275] Secondly, FDCD measurements can be readily obtained, even simultaneously to ECD, by upgrading commercial ECD spectrometers with an FDCD set-up,[195,275] while CPL measurements are often difficult to carry out as they require the purchase of a high-cost stand-alone CPL equipment or specialized expertise to construct home-build CPL accessories,[195,276,277] thereby restricting their use mainly to a few expert groups.

Despite these above-stated potential advantages, only very few studies have focused on the use of FDCD for chiroptical applications and were mostly performed on chiral chromophores,[278,279] protein-ligand[280-282], and nucleobase systems.[283,284] For instance, a review of the available literature revealed that less than 70 studies had mentioned the term 'fluorescence-detected circular dichroism' in the abstract, while more than 2,600 studies have referred to the term 'electronic circular dichroism' and more than 60,000 have mentioned 'circular dichroism', which is often used as a synonym for ECD.[285] One of the first reports on FDCD dates back to 1974, when the chiral fluorophore tryptophan was selectively detected in a mixture containing the chiral non-fluorescent chromophore cysteine.[196,199] Later on, exciton coupled FDCD measurements were performed to detect structural changes in the tertiary structure of proteins, which the exciton-coupled ECD measurement could not.[282] Moreover, the selectivity advantage of FDCD measurements was exploited for investigating DNA bichromophore assemblies.[286] Exciton-coupled FDCD has also been utilized for the stereochemical analysis of steroids covalently tethered to a porphyrin center.[199]

In this contribution, fluorescence-detected circular dichroism (FDCD) spectroscopy has been applied for the first time to (synthetic) supramolecular complexes for the chirality sensing of analytes in aqueous media. The chapter focuses on systematic investigations into FDCD measurements for representative supramolecular host-guest systems, provides generalizable recommendations for the set-up of experiments, and presents a case study for the combined use of FDCD and ECD spectroscopy for characterizing fluorescent supramolecular chiral systems.

3.2. Results and Discussion

In this study, self-assembled CB8•MDPP chemosensor and endo-functionalized molecular tube (MT) were utilized as achiral chromophoric and emissive hosts, and CB8 was used as a non-chromophoric achiral host for comparison (see Figure 3.2a-b for the chemical structures). Planar-chiral paracyclophane dyes, (R_p)-MPCP, (S_p)-MPCP, and (S_p)-MVCP (see Figure 3.2b), were introduced as chiral indicators. A wide range of biorelevant chiral compounds, shown in Figure 3.2c was used as guests, including amino acids (*e.g.*, Phe, Trp), amino acid derivatives, peptides, and synthetic intermediates (chiral epoxides). The protein insulin that binds to the host CB8•MDPP was also investigated.

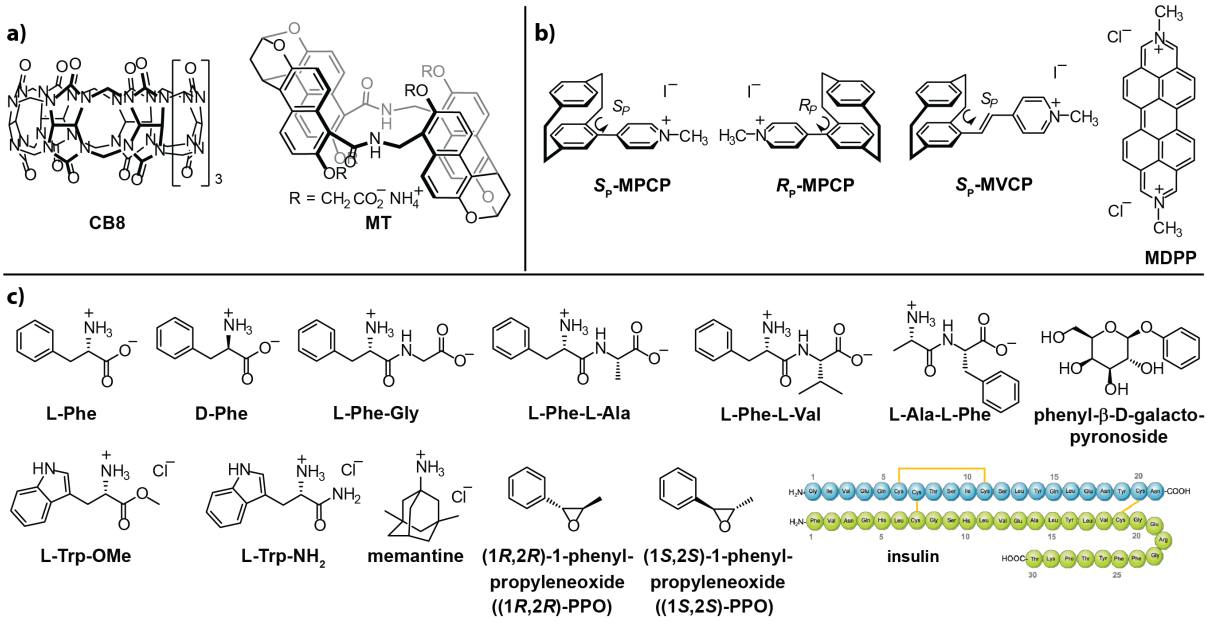

Figure 3.2: Chemical structure of (a) host, (b) dye molecules, and (c) investigated chiral analytes and the achiral drug memantine utilized in this study. Their protonation state represents their occurrence under the measurement conditions.

3.2.1. General protocol for FDCD measurements

In contrast to ECD spectroscopy, FDCD has not yet been widely used, possibly because FDCD is less known. As a result, measurement protocols for FDCD measurements on supramolecular systems were lacking prior to this work, which was particularly hindering because FDCD can be more complex and artifact-prone than ECD measurements.[199] Hence as a first step, I optimized the measurement parameters for FDCD (procedures, parameters, conditions), providing a general and transferable FDCD measurement protocol, which will be of utility even beyond supramolecular systems (see below and *FDCD characteristics* in Section 3.5 - Additional Information for further details).

It is widely known that ECD measurements should be conducted on samples with an absorbance value between 0.4. to 1 (theoretically, a value of 0.87 is optimal for ECD measurements).[263,264] In general, ECD measurements are taken at a fixed direct current (DC) voltage and by automatically varying the high tension (HT) voltage on the photomultiplier (PM) tube of the ECD detector. The ECD signal thus obtained is proportional to the concentration of the chiral analyte. As the measurements are conducted at a fixed DC voltage, a direct comparison of the different measured spectra is possible.

FDCD measurements can be performed simultaneously along with ECD on a CD spectrometer that is equipped with an FDCD accessory, where a long-pass filter (LP-Filter) and lenses are installed at 90-degree geometry to the excitation light source, directing the fluorescence light towards an additional detector, *e.g.,* a PM tube.[275] Appropriate long-pass filters should be used in FDCD measurements to avoid the scattered light from excitation wavelength, which could contaminate the observed emission, and to maximize the emitted light signal. Contrary to ECD, FDCD measurements are taken at a varying DC voltage by fixing the HT Voltage on the PM tube of the FDCD detector. In practical terms, the HT Voltage should be set at a value giving proper intensity (2 – 3 V) of the fluorescence signal and avoiding any signal saturation. Hence, two different fluorescence-based chiroptical parameters can be obtained from FDCD spectroscopy. (i) Under the set conditions, the instrument initially outputs the "differential circularly polarized fluorescence excitation" (often termed as (ΔF), defined as the fluorescence intensity difference resulting from excitation with left (F_{L}) and right (F_{R}) circularly polarized light, see Eq. 3.1. The ΔF value is dependent on the concentration of the chiral analyte and the applied HT Voltage, and can be considered as the analogue to the ECD value (also known as the ellipticity, θ), even though both quantities have different units. (ii) The ΔF value is then normalized by the total fluorescence of the sample ($F_{\mathrm{L}} + F_{\mathrm{R}}$), which is measured as the DC component, to arrive at a concentration-independent quantity, see Eq. 3.2. This parameter is typically referred to as the FDCD value. Although the derivation is mathematically more complex, the FDCD value can be considered the fluorescence-based chiroptical analogue of the concentration-independent molar circular dichroism ($\Delta\varepsilon$). See also *FDCD characteristics* in Section 3.5 - Additional Information for further details.

$$\Delta F = F_{\mathrm{L}} - F_{\mathrm{R}} \qquad \text{Eq. 3.1}$$

$$\mathrm{FDCD} = \frac{\Delta F}{\mathrm{DC}} = \frac{F_{\mathrm{L}} - F_{\mathrm{R}}}{F_{\mathrm{L}} + F_{\mathrm{R}}} \qquad \text{Eq. 3.2}$$

In a typical FDCD measurement set-up, both the Δ*F* signal and the DC voltage (= total fluorescence) should be collected in two separate channels, and these measurements should be performed for both the sample and the solvent ("blank") used. The FDCD spectra can then be obtained by first subtracting the blank-solvent spectra from the sample spectra, arriving at baseline-corrected Δ*F* and DC spectra. Subsequently, dividing the baseline-corrected Δ*F* spectra by the corrected DC voltage results in the normalized FDCD spectra.

Unlike in ECD measurements, recording Δ*F* in FDCD measurements offers the user additional variability in choosing the measurement parameters. For instance, the HT Voltage and the bandwidth (BW) can be tuned independently, through which the signal intensity can be adjusted, and thereby a wider measurement range can be accessed than available for ECD measurements – examples are shown in the following sections. Few studies have also focused on the use of Δ*F* component of the FDCD data directly for sensing applications.[195,287] Therefore, the measurement parameters for the Δ*F* signal were optimized with respect to the bandwidth and the HT Voltage. The recommended measurement options and empirical correlation curves between signal intensity, HT Voltage, and bandwidth are discussed under *FDCD characteristics* in Section 3.5 - Additional Information.

In principle, FDCD spectra provide analyte-concentration-independent and HT-voltage independent spectra that are particularly useful for comparing different spectroscopic fingerprints between different samples of possibly very different emission quantum yields. Moreover, FDCD data is useful when comparing systems that were measured at different HT Voltages or on different spectrometers. The Δ*F* data is preferred when comparing systems measured at the same HT Voltage on the same spectrometer and for sensing studies where a change in the fluorescence (or concentration) of the system needs to be monitored. In general, both Δ*F* and FDCD spectra should be considered for data analysis and interpretation. A step-by-step user guide formulated for FDCD measurements can be found under *FDCD characteristics* in Section 3.5 - Additional Information.

3.2.2. Comparison of sensitivity for FDCD and ECD measurements

As a fluorescence-based chiroptical method, FDCD may therefore be, in principle, more sensitive than absorbance-based ECD.[196,197,265] To assess the sensitivity of FDCD measurements over ECD for supramolecular systems, a simple 1:1 host-dye complex of a chiral chromophoric dye with an achiral non-chromophoric host was initially investigated (see Figure 3.3a). CB8 (see Figure 3.2a) was used as the achiral non-chromophoric host and enantiomers of the paracyclophane-derived dye MPCP, *i.e.*, (S_P)- and (R_P)-MPCP (see Figure 3.2b), were

utilized as chiral chromophoric indicator dyes. On account of their rigid planar-chiral structure, both (S_P)- and (R_P)-MPCP displayed strong ECD bands (Figure 3.3b). Recent reports from our group have shown that the racemic dye MPCP forms a highly stable inclusion complex with CB8 in water, with K_a = 3.89 (±0.99) x 10^{12} M^{-1}.[152] The rather high binding constant associated with the host-guest complex formation rendered the CB8•MPCP inclusion complex fully intact even upon dilution to the nanomolar (10^{-9} M) concentration regime, which was verified by fluorescence titration experiments.[152] The CB8•MPCP supramolecular system, extended here with chiral MPCP dyes, therefore provided an ideal starting point to verify if the fluorescence-based quantity ΔF can also be under practical conditions more sensitive than ECD.

At micromolar concentrations, both (S_P)- and (R_P)-MPCP displayed clearly defined signals in the ECD and ΔF spectra with signal maxima at 264 nm and 333 nm in water (Figure 3.3b and 3.3c). Addition of CB8 to the dye solutions resulted in a bathochromic shift in both the ECD and ΔF signals upon host-dye complex formation with the maxima at 275 nm and 340 nm for the bound dye (Figure 3.3b and 3.3c). This was further accompanied by a strong enhancement in the dye fluorescence on CB8 binding, which was also reflected in the ΔF spectra (Figure 3.3c and 3.3d). Both the ECD and ΔF spectra of the enantiomers are mirror images of each other, exhibiting opposite signs, as theoretically predicted for enantiomeric complexes.[190] It has to be noted that strong signal differences were observed in the ΔF than in ECD between the CB-bound and free MPCP, indicating that host-guest binding commonly leads to more pronounced changes in the emission than in the absorbance spectra. As a result, one can generally expect to find larger signal differences in ΔF than in ECD. This feature can be particularly advantageous for sensing applications that rely on signal differences, for *e.g.*, the ΔF-based quantification of the drug memantine using the CB8•MPCP reporter pair in blood serum, see further below.

Analysis of the ΔF component of the FDCD value of the CB8•MPCP system is more practical for the sensitivity assessment studies described below, as the FDCD component normalizes the signal against the total fluorescence. However, to compare the spectra obtained at different concentrations and measurement settings, the conversion of the ΔF spectra into the concentration-independent FDCD spectra is useful; see Figure 3.3e. The FDCD spectra hence obtained can be related to the measured ECD spectra by converting them into their molar circular dichroism ($\Delta\varepsilon$) values (see Eq. 3.5 and Eq. 3.7 under FDCD characteristics in Section 3.5 - Additional Information). Clearly, the FDCD and ECD data conversion for the CB8•MPCP reporter pair yielded very similar $\Delta\varepsilon$-spectra (Figure 3.4), as is theoretically expected.[196,197,199]

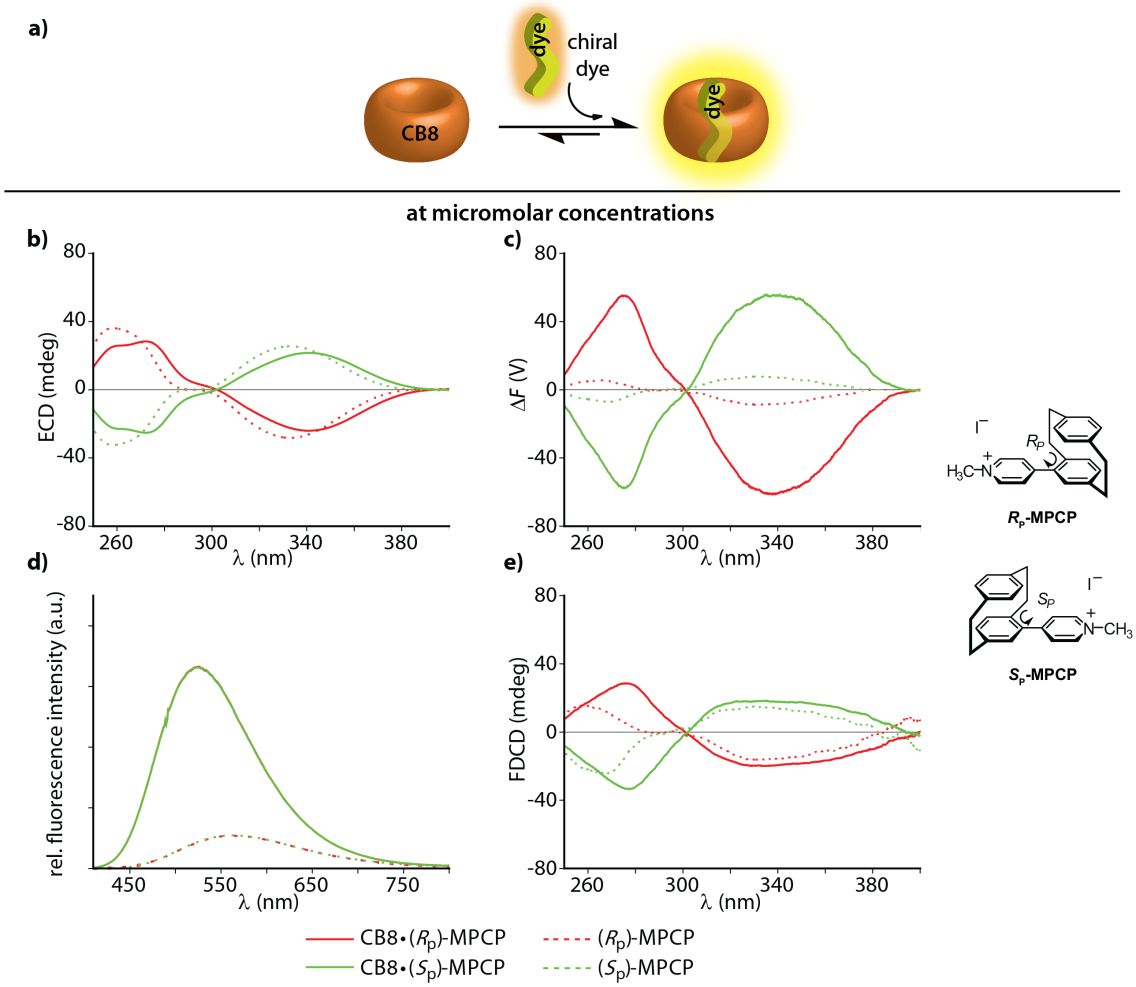

Figure 3.3: (a) Schematic representation of a 1 : 1 host–dye complex formation between the chiral chromophoric MPCP dye and the non-chromophoric host CB8. (b) ECD and (c) ΔF spectra of the MPCP dye enantiomers (R_p)-MPCP (45 µM) and (S_p)-MPCP (45 µM) in the absence and presence of CB8 (45 µM) in water. Parameters used: HT = 650 V, BW = 4 nm, Acc = 20, LP-Filter = 420 nm. (d) Enhancement in the fluorescence intensity of (R_p)-MPCP (45 µM) and (S_p)-MPCP (45 µM) upon addition of CB8 (45 µM) in water, λ_{exc} = 350 nm. (d) FDCD spectra of (R_p)-MPCP (45 µM) and (S_p)-MPCP (45 µM) in the absence and presence of CB8 (45 µM) in water.

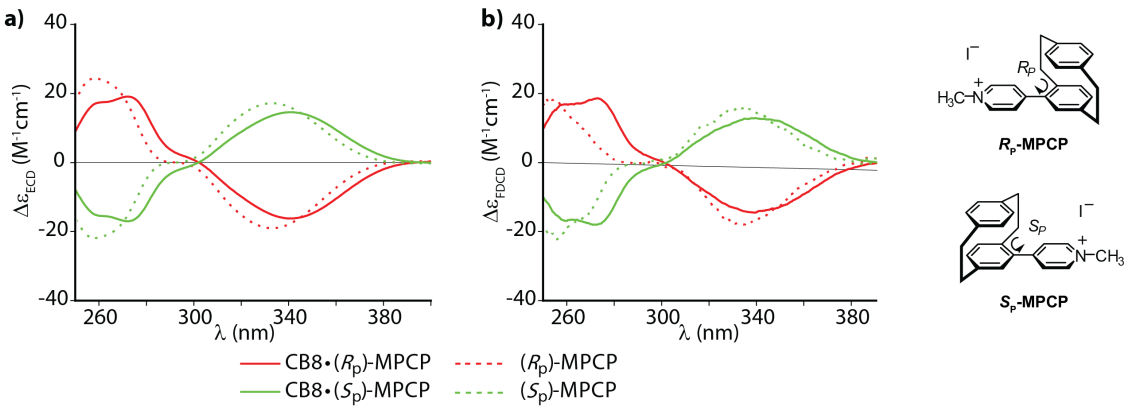

Figure 3.4: (a) $\Delta\varepsilon_{ECD}$ and (b) $\Delta\varepsilon_{FDCD}$ spectra of the MPCP dye enantiomers (R_p)-MPCP (45 µM) and (S_p)-MPCP (45 µM) in the absence and presence of CB8 (45 µM) in water calculated from ECD and FDCD ellipticity values using Eq. 3.5 and Eq. 3.7.

To assess the sensitivity of FDCD over ECD measurements, the ECD and Δ*F* spectra of the enantiomers (*S*P)- and (*R*P)-MPCP in the presence of CB8 were measured by diluting the samples down to 100 nM. The comparison of the resulting Δ*F* and ECD spectra at the submicromolar concentration range was striking. It was not possible to detect clear ECD signals for the CB8•MPCP complex at low concentrations (<1 μM, although complex formation is ensured with logK_a = 12.6). Conversely, the Δ*F* signals are clearly measurable even at 100 nM (Figure 3.5), indicating at least an order of magnitude higher sensitivity of FDCD over ECD measurements. The Δ*F* and FDCD spectra of the CB8•MPCP complex showed a more "noisy" character than ECD spectra, which also holds true for the other systems investigated in this work and reported in the literature.[195,199] This obstacle was overcome by either increasing the number of accumulations in the measurement or using single-wavelength time course Δ*F* measurements instead of measuring the whole spectrum. The ECD and Δ*F* signals for the CB8•(*S*P)-MPCP complex measured at 20 and 100 accumulations (Figure 3.27 in Section 3.5 - Additional Information) showed that the spectrum is reproducible and the signal to noise ratio improves with increasing accumulations, at the cost of longer measurement times. Faster experiments can be performed through single wavelength measurements. For *e.g.*, the single-wavelength Δ*F* measurements of the CB8•(*S*P)-MPCP and CB8•(*R*P)-MPCP complexes upon dilution to 50 nM provided Δ*F* values that were reproducible and consistent with the ones obtained from the whole spectral recording. The FDCD values obtained in all cases show – within error – the concentration independence of this value, as is expected, ruling out photophysical or other artefacts. Conversely, no meaningful ECD signal was reproducibly obtained in the nanomolar concentration range (see Table 3.1).

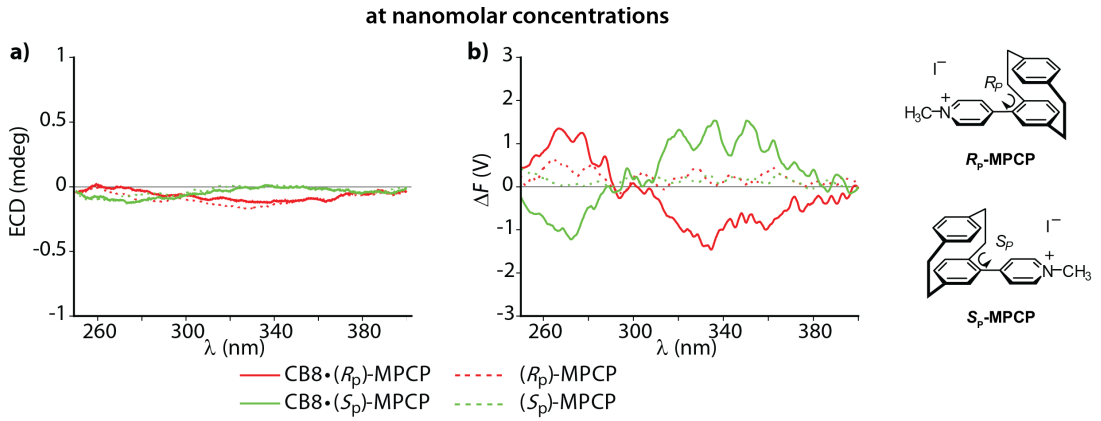

Figure 3.5: (a) ECD and (b) Δ*F* spectra of MPCP dye enantiomers (R_p)-MPCP (100 nM) and (S_p)-MPCP (100 nM) in the absence and presence of CB8 (100 nM) in water. Parameters used: HT = 800 V, BW = 4 nm, Acc = 20, LP-Filter = 420 nm.

Table 3.1: Single-wavelength ECD and ΔF measurements of CB8•(R_p)-MPCP and CB8•(S_p)-MPCP complex at low concentrations of 100 nM and 50 nM. The parameters are kept constant for each individual set of measurements.

Sample[a]	ECD (mdeg)	ΔF[b] (V)	FDCD[c] (mdeg)
CB8•(R_p)-MPCP 100 nM	-0.11	-1.34	-36.3
CB8•(R_p)-MPCP 50 nM	-0.01	-0.82	-40.0
CB8•(S_p)-MPCP 100 nM	0.09	1.13	29.9
CB8•(S_p)-MPCP 50 nM	-0.05	0.55	29.0

[a] Measured at λ_{obs} = 335 nm, BW = 4 nm, Data Pitch = 30 s, D.I.T = 30 s, $t_{measure}$ = 10 min. [b] HT = 800 V, LP-Filter = 420 nm. [c] Obtained by dividing the ΔF value with the DC voltage (total fluorescence).

The difference in the ΔF and FDCD values (not exact mirror images) for the enantiomeric CB8•(R_P)-MPCP and CB8•(S_P)-MPCP complexes in Table 3.1 maybe caused by the higher %*ee* for (R_P)-MPCP dye compared to (S_P)-MPCP (refer to synthetic details in publishedwork[249]).

The sensitivity of FDCD over ECD measurements was also assessed for the self-assembled CB8•MDPP chemosensor (see Figure 3.2a and 3.2b), which bind chiral aromatic analytes, such as Phe containing amino acids and peptides (see section below for measurement details).[173] The results obtained further confirmed the higher sensitivity of FDCD over ECD measurements.

3.2.3. Combined use of FDCD and ECD for detection of chiral analytes and label-free endpoint and continuous reaction monitoring

The combination of FDCD and ECD measurements is potentially more informative and can provide additional, and useful chiroptical information about the analyte present than when using the individual methods on their own. This was evaluated for the achiral chemosensing ensemble composed of the macrocyclic CB8 and the dicationic racemic dye MDPP (see Figure 3.2a and 3.2b), which are known to subsequently bind chiral aromatic analytes such as amino acids, peptides, and proteins, resulting in 1:1:1 hetero-ternary complexes (Figure 3.6a).[173] Hence, the ECD and FDCD signals arising on the addition of achiral CB8•MDPP chemosensor to aqueous solutions with chiral Phe- and Trp-containing species were monitored, see Figure 3.6.

In ECD measurements, as observed in previous reports,[173] an analyte-indicative induced chiroptical signal was observed for all the chiral analytes studied (Figure 3.6b). At the same time, FDCD was far more selective, where only the combination of CB8•MDPP with Phe but not with Trp species gave rise to induced chiroptical FDCD effects (Figure 3.6c and 3.6e). This can be explained by the strong quenching in the fluorescence intensity of CB8•MDPP

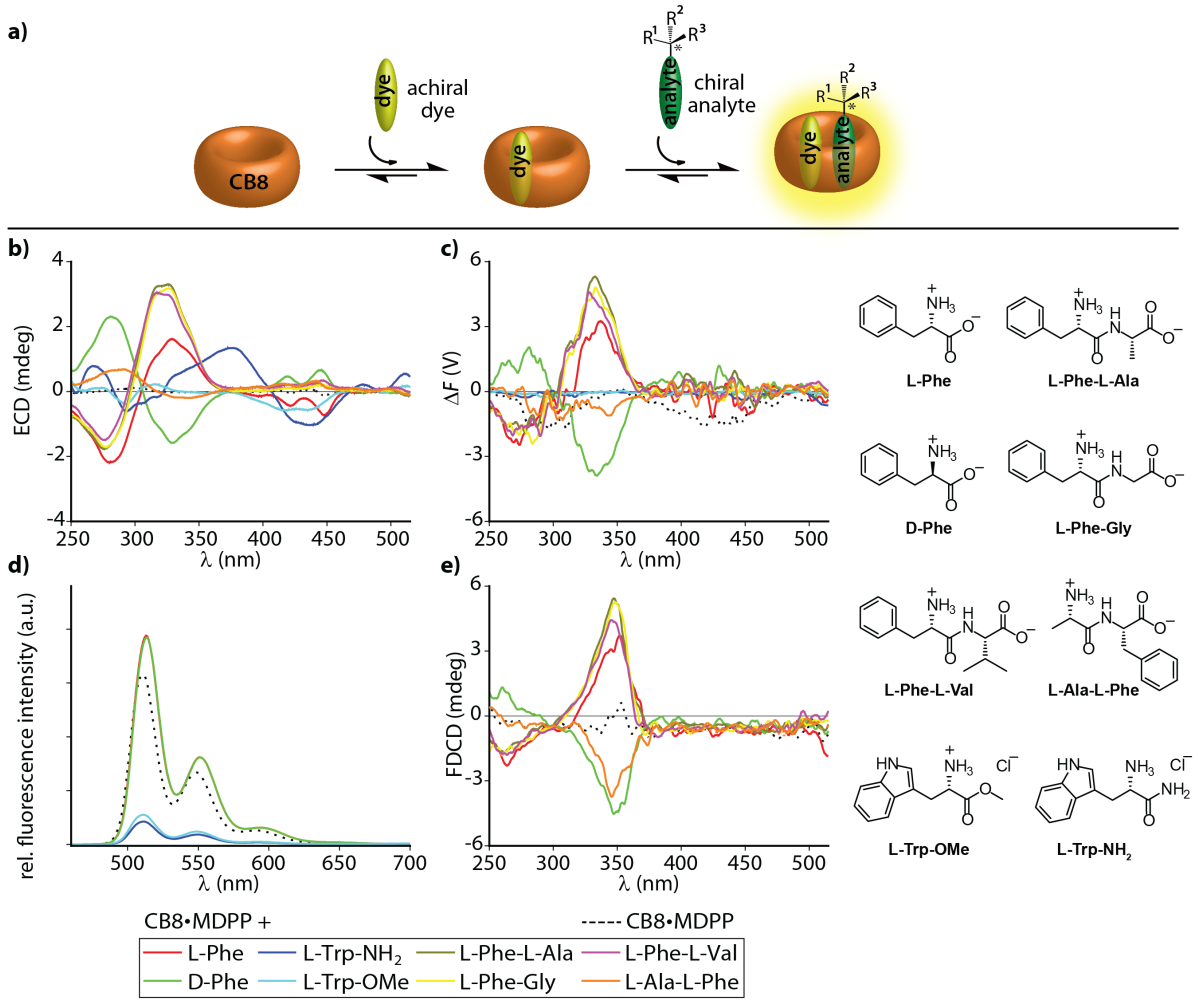

Figure 3.6: (a) Schematic representation of a 1 : 1 : 1 ternary complex formation between the achiral chromophoric CB8•MDPP receptor and the chiral analyte. (b) ECD and (c) Δ*F* spectra of CB8•MDPP receptor (20 µM) in the absence (dashed lines) and presence (solid lines) of several amino acids, amino acid derivatives, and dipeptides (50 µM) in water. Parameters used: HT = 520 V and 510 V (for dipeptides), BW = 4 nm, Acc = 20, LP-Filter = 515 nm. (d) Enhancement in the fluorescence of CB8•MDPP receptor (20 µM) upon addition of L-Phe and D-Phe (50 µM) and quenching in the fluorescence of CB8•MDPP receptor (20 µM) upon addition of L-Trp-NH_2 and L-Trp-OMe (50 µM) in water, λ_{exc} = 450 nm. (e) FDCD spectra of CB8•MDPP (20 µM) in the absence and presence of several amino acids and dipeptides (50 µM) in water.

chemosensor by Trp-species, while Phe binding leads to a slight bathochromic shift and emission increase (Figure 3.6d). Moreover, the N-terminal Phe containing dipeptides were distinguished from C-terminal Phe variants by both FDCD and ECD, see Figure 3.6. However, different Phe–X dipeptides remained indistinguishable by both techniques utilizing CB8•MDPP as the host. In these examples, both the FDCD and the Δ*F* signals were informative and useful. However, when using the Δ*F* spectra, signal artefacts arising from the CB8•MDPP receptor alone (see Figure 3.6c) must be considered and corrected (see *Photoselection artefacts in FDCD* and *Correction of signal artefacts in FDCD* in Section 3.5 - Additional Information for further details). FDCD values can only be presented for systems with a measurable Δ*F* spectrum (and thus, for instance, not in the case of the CB8•MDPP complexes with Trp-

species). The combined information obtained from both the FDCD and ECD measurements for this system was, for instance, useful for verifying that the CB8•MDPP receptor targets phenylalanine and not the multiple tyrosine residues present in the protein insulin (see Figure 3.2c for the amino acid sequence), because binding to tyrosine would have resulted in no FDCD signals due to emission quenching,[156] see further below. This finding agrees well with the binding geometry concluded from the crystal structure of the host CB7 with insulin.[81]

The sensitivity of FDCD versus ECD measurements was also assessed for this supramolecular system by monitoring the single-wavelength ΔF and ECD signals for CB8•MDPP receptor at varying analyte concentrations. Table 3.2 depicts the data for the CB8•MDPP receptor complex with the peptidic guest L-Phe-L-Ala. For this concentration-dependent study, an excess of the chiral guest over the host was used to ensure a sufficient degree of complexation of the chromophoric and emissive host (the ratio of CB8•MDPP receptor to analyte was always kept at 1:2.5). Again, the results evidenced a remarkably higher sensitivity of ΔF over ECD. No reliable ECD signals was obtained at the low micromolar concentration regime (<5 μM of the analyte), while ΔF signals were still present even at a concentration of 0.50 μM of analyte (Table 3.2). Because the binding constant of the complex (K_a = 9.80 (±0.98) x·10^5 M^{-1})[173] is limiting the concentration range where the complex remains stable; it was not feasible to dilute the solution further. The ECD and ΔF values obtained were consistent in the concentration range studied. The standard deviation for the measurements was calculated in each case from three independent measurements by varying the measurement parameters in each set (Table 3.3). In ΔF measurements, it is convenient to increase the HT Voltage on the FDCD detector to increase the signal intensity when measuring at low concentrations; in fact, this option is not available for ECD measurements. However, a direct comparison between the measured ΔF values is not possible for measurements conducted at different HT Voltages! Instead, a correction function was developed that relates the HT Voltage and the measured ΔF signal, which can be used to obtain the value of HT Voltage-corrected ΔF signal (ΔF_{corr}), see Table 3.2 and also *FDCD characteristics* in Section 3.5 - Additional Information for details. The FDCD values calculated again show the concentration independence of this value (Table 3.2). The sensitivity assessments were also conducted for the dipeptides, L-Phe-Gly, and L-Phe-L-Val, as guests with CB8•MDPP receptor, further demonstrating at least an order of magnitude higher sensitivity of ΔF over ECD (see Table 3.5 and Table 3.6 in Section 3.5-Additional Information).

One factor limiting the sensitivity of supramolecular assays is the degree of complexation, which is a function of the binding affinity and the receptor and analyte concentrations. A common strategy to enhance the degree of complexation in spectroscopic assays is to increase

Table 3.2: Single-wavelength ECD and Δ*F* measurements of CB8•MDPP receptor in the presence of varying concentrations of L-Phe-L-Ala analyte. The parameters were kept constant for each individual set of measurements.

Sample[a]	Δ*F* (V)	HT[b] (V)	ΔF_{corr}[c] (V)	FDCD[d] (mdeg)	ECD (mdeg)
CB8•MDPP 20 µM + L-Phe-L-Ala 50 µM	6.29	520	174.45	3.45	3.27
CB8•MDPP 10 µM + L-Phe-L-Ala 25 µM	4.64	540	95.17	3.75	1.53
CB8•MDPP 2 µM + L-Phe-L-Ala 5 µM	2.80	620	18.30	3.52	0.35
CB8•MDPP 0.4 µM + L-Phe-L-Ala 1 µM	2.18	760	3.51	3.91	0.03
CB8•MDPP 0.2 µM + L-Phe-L-Ala 0.5 µM	1.02	800	1.02	3.00	0.01

[a] Measured at BW = 4 nm, λ_{obs} = 333 nm, Data Pitch = 30 s, D.I.T = 30 s, $t_{measure}$ = 10 min, LP-Filter = 515 nm; [b] HT Voltage applied to the PMT of the FDCD detector. Hence this is only influencing the Δ*F* value, not the ECD value (different detectors); [c] Corrected Δ*F* value at HT = 800 V; [d] Obtained by dividing the Δ*F* value with the DC voltage (total fluorescence).

Table 3.3: Standard deviation for the single-wavelength ECD and Δ*F* measurements of CB8•MDPP receptor in the presence of varying concentrations of L-Phe-L-Ala analyte. The standard deviation was obtained from three measurements by varying the measurement parameters in each individual set.

Sample	Δ*F* (V)	S.D[a] (V)	ECD (mdeg)	S.D[a] (mdeg)
CB8•MDPP 20 µM + L-Phe-L-Ala 50 µM	6.29	0.29	3.27	0.04
CB8•MDPP 10 µM + L-Phe-L-Ala 25 µM	4.64	0.20	1.53	0.02
CB8•MDPP 2 µM + L-Phe-L-Ala 5 µM	2.80	0.15	0.35	0.04
CB8•MDPP 0.4 µM + L-Phe-L-Ala 1 µM	2.18	0.52	0.03	0.005

[a] Standard deviation obtained from three measurements by varying the measurement parameters in each individual set.

the concentration of the spectroscopically silent component, mostly the analyte. However, this strategy is flawed in some cases, for *e.g.*, if the spectroscopically silent component shows solubility limitations[75] or undesirable aggregation tendencies (see below), is expensive or is present in very low concentrations in the analytical sample.[152,201] In ECD and FDCD analysis, the degree of analyte complexation can be enhanced by using an excess of the achiral chromophoric/emissive host, as they do not contribute to the chiroptical signals. For *e.g.*, see the ECD and Δ*F* signals monitored on titration of CB8•MDPP receptor to L-Phe-Gly analyte in water (Figure 3.7). An enhancement in the ECD and Δ*F* signals was observed upon increasing the receptor concentration until the degree of complexation reached unity, beyond which the ECD and Δ*F* signals saturated. This desirable behavior is a consequence of the chiroptical response that only originates from the host-guest complex. On the other hand, in conventional absorbance- or emission-based assays, such an approach is generally infeasible as

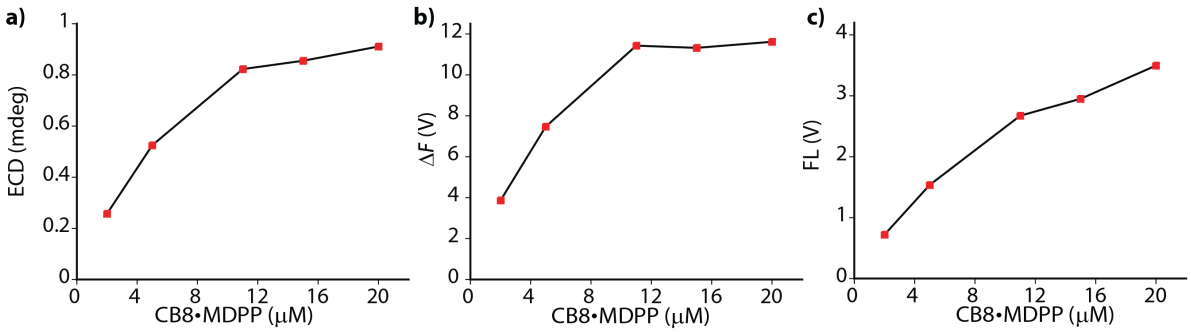

Figure 3.7: Variation in the (a) ECD, (b) Δ*F,* and (c) total fluorescence (FL) (or DC voltage) signal on titration of CB8•MDPP receptor to a solution containing L-Phe-Gly (5μM) in water when monitored at 333 nm by single-wavelength measurements. Parameters used: HT = 640 V, BW = 4 nm, λ_{obs} = 333 nm, Data Pitch = 30 s, D.I.T = 30 s, $t_{measure}$ = 10 min, LP-Filter = 515 nm.

it causes an undesirable signal increase proportional to the concentration of the unbound emissive host. For *e.g.*, the fluorescence intensity showed a steady increase on titrating CB8•MDPP receptor to L-Phe-Gly (Figure 3.7c). Thus, ECD and FDCD measurements can be a convenient choice for studying the interaction of chromophoric receptors with biomolecules or proteins at low analyte concentrations.

In addition to the chirality sensing of analytes, the combination of FDCD and ECD measurements can be practically useful for a sensitive and selective endpoint and label-free continuous reaction monitoring of (bio)chemical and (bio)physical processes in real-time. Examples for both purposes, utilizing synthetic supramolecular receptors, for *e.g.*, cucurbit[*n*]urils,[167,288,289] molecular tubes,[96,290] calix[*n*]arenes[167,168] and CB8•dye chemosensors[156,173], reported so far are based on absorbance, emission or ECD spectroscopy for analyte reaction monitoring. In this chapter, the utility of FDCD measurements in combination with supramolecular hosts has been demonstrated for (i) endpoint and (ii) continuous reaction monitoring of chiral analytes with representative examples.

(i) The racemization of amino acids is an important obstacle under synthetic conditions in organic solvents.[240] A common strategy to monitor amino acid racemization is the use of chiral HPLC, which requires time-consuming sample extraction, amino acid derivatization, and HPLC measurements, leading to several hours of assaying time.[240] In the previous chapter, the base-catalyzed racemization of both L-Phe and L-Phe-Gly in water, DMF and ethylene glycol at elevated temperatures were monitored using acyclic CB*n* supramolecular receptor *via* ECD spectroscopy (see Figure 2.6). Herein, the induced Δ*F* and ECD signals in the CB8•MDPP reporter pair to the presence of L-Phe and L-Phe-Gly were utilized for the endpoint monitoring of racemisation of these amino acids. In practice, L-Phe and L-Phe-Gly were heated in the presence of 1.2eq. of K_2CO_3 at 130 °C for 2 h in DMF, ethylene glycol and water and the

resulting racemization was evaluated by measuring the induced Δ*F* and ECD signals at 338 nm (for L-Phe) and 333 nm (for L-Phe–Gly) arising on adding aliquots of the reaction mixture to an aqueous solution of the CB8•MDPP chemosensor, before and after the chemical reaction (Figure 3.8 and Figure 3.9). Pleasingly, both the Δ*F* and ECD signals monitored provided information on the influence of the reaction conditions on the racemization of amino acids, which were in full agreement with the more cumbersome HPLC-based literature procedure.[240] For reactions conducted in DMF and ethylene glycol, a reduction in both the Δ*F* and ECD signals were observed after the completion of the reaction. In contrast, reactions conducted in water showed no significant signal changes before and after the reaction, indicating water suppresses the racemization of L-Phe and L-Phe–Gly. In contrast, DMF and ethylene glycol as solvents lead to a fast loss of chirality (Figure 3.8 and Figure 3.9). Both Δ*F* and ECD signals were equally suitable for the analysis under the conditions tested. However, Δ*F* has the additional advantage of its higher sensitivity for detection at lower concentration ranges.

(ii) A real-time monitoring of chemical reactions can be achieved using supramolecular chemosensors by adding them directly to the reaction mixture and recording a continuous signal readout, provided the chemosensors are compatible with the reaction conditions (solvent, pH, additives, temperature, etc.). This has been demonstrated here using the CB8•MDPP chemosensor for the real-time monitoring of hydrolysis of chiral epoxides using ECD and FDCD spectroscopy. Chiral epoxides can be converted into many functional groups and are important intermediates in chemistry[291,292] and biology.[293] The CB8•MDPP receptor showed induced ECD and Δ*F* signals upon binding aromatic chiral epoxides, *e.g.*, (1*R*,2*R*)-1-phenylpropylene oxide ((1*R*,2*R*)-PPO) in water (Figure 3.10a and 3.10b). The hydrolysis of chiral epoxides under different reaction conditions was monitored *in situ* by adding 20 μM of CB8•MDPP receptor to 100 μM (1*R*,2*R*)-PPO in deionized water (pH 7), 50 mM acetate buffer (pH 4.5), and 50 mM carbonate buffer (pH 10) and recording the ECD and Δ*F* signals at 350 nm (Figure 3.10c and 3.10d). Both time course Δ*F* and ECD spectral measurements revealed that complete hydrolysis and racemization occurred in an acidic environment after 4 h and under neutral conditions after 12 h. At the same time, the epoxide did not hydrolyze under basic conditions, see Figure 3.10c and 3.10d. This observation was in agreement with expectations for secondary-carbon containing epoxides that likely follow an H^+-catalyzed S_N1 type reaction mechanism (see Figure 3.10e).[294,295]

The chemosensing ensemble CB8•MDPP also showed useful induced ECD and Δ*F* signals in the presence of phenyl-β-D-galactopyranoside (Figure 3.28a and 3.28b in Section 3.5 - Additional Information). Phenyl-β-D-galactopyranoside is used as a substrate for

detecting β-galactosidase enzymatic activity.[296,297] The hydrolysis of phenyl-β-D-galactopyranoside by β-galactosidase was monitored with the help of CB8•MDPP receptor by Δ*F* and ECD recordings. The reaction was monitored at 25°C in 10 mM phosphate buffer at pH 5 at 50 μM concentration of phenyl-β-D-galactopyranoside in the presence of 10 μM of CB8•MDPP receptor. The enzyme β-galactosidase was present at a concentration of 43 μg/ml in the assay.

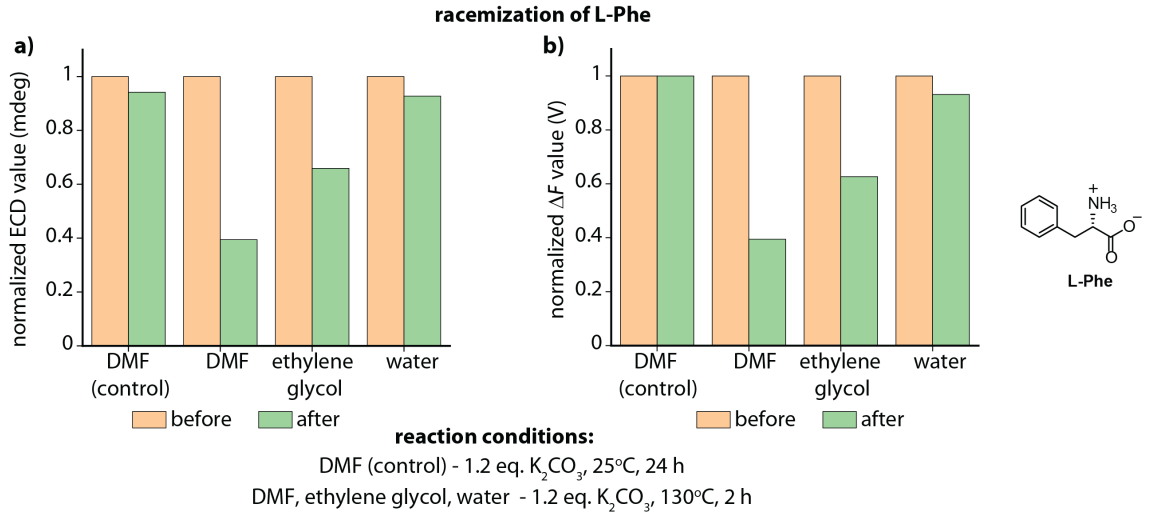

Figure 3.8: Monitoring the racemization of L-Phe in the presence of CB8•MDPP before and after the reaction in DMF, ethylene glycol, and water using single-wavelength (a) ECD and (b) Δ*F* measurements. Parameters used: HT = 520 V, BW = 4 nm, λ_{obs} = 338 nm, Data Pitch = 30 s, D.I.T = 30 s, $t_{measure}$ = 10 min, LP-Filter = 515 nm. The signals are monitored in water at a CB8•MDPP concentration of 20 μM in the presence of an excess of L-Phe (≈100 μM) from the reaction mixture. The DMF (control) shows the control reaction in DMF when the reaction mixture was kept at room temperature instead of heating to 130 °C.

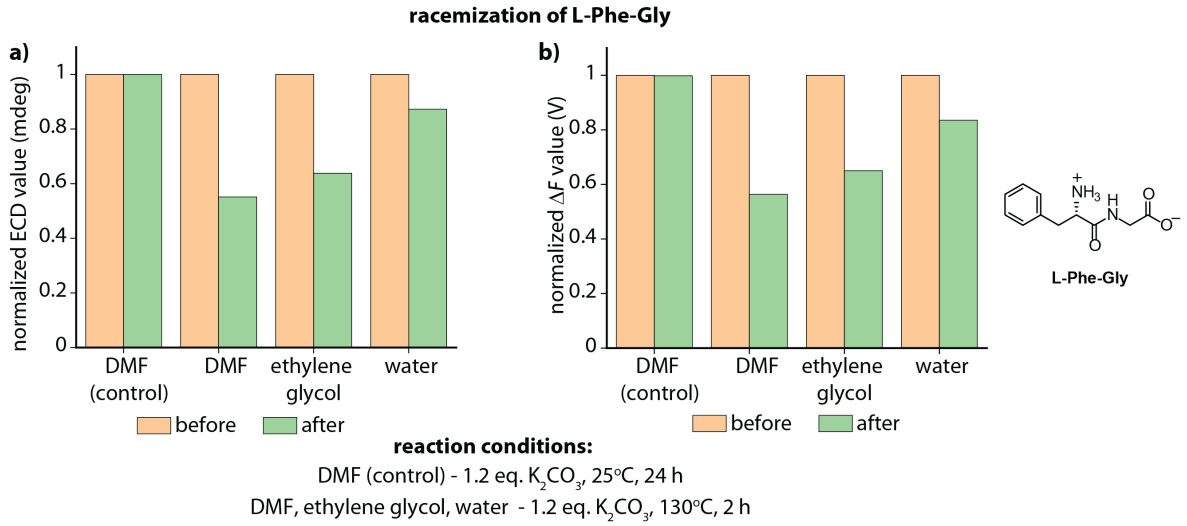

Figure 3.9: Monitoring the racemization of L-Phe-Gly in the presence of CB8•MDPP before and after the reaction in DMF, ethylene glycol, and water using single-wavelength (a) ECD and (b) Δ*F* measurements. Parameters used: HT = 520 V, BW = 4 nm, λ_{obs} = 333 nm, Data Pitch = 30 s, D.I.T = 30 s, $t_{measure}$ = 10 min, LP-Filter = 515 nm. The signals are monitored in water at a CB8•MDPP concentration of 20 μM in the presence of an excess of L-Phe-Gly (≈100 μM) from the reaction mixture. The DMF (control) shows the control reaction in DMF when the reaction mixture was kept at room temperature instead of heating to 130 °C.

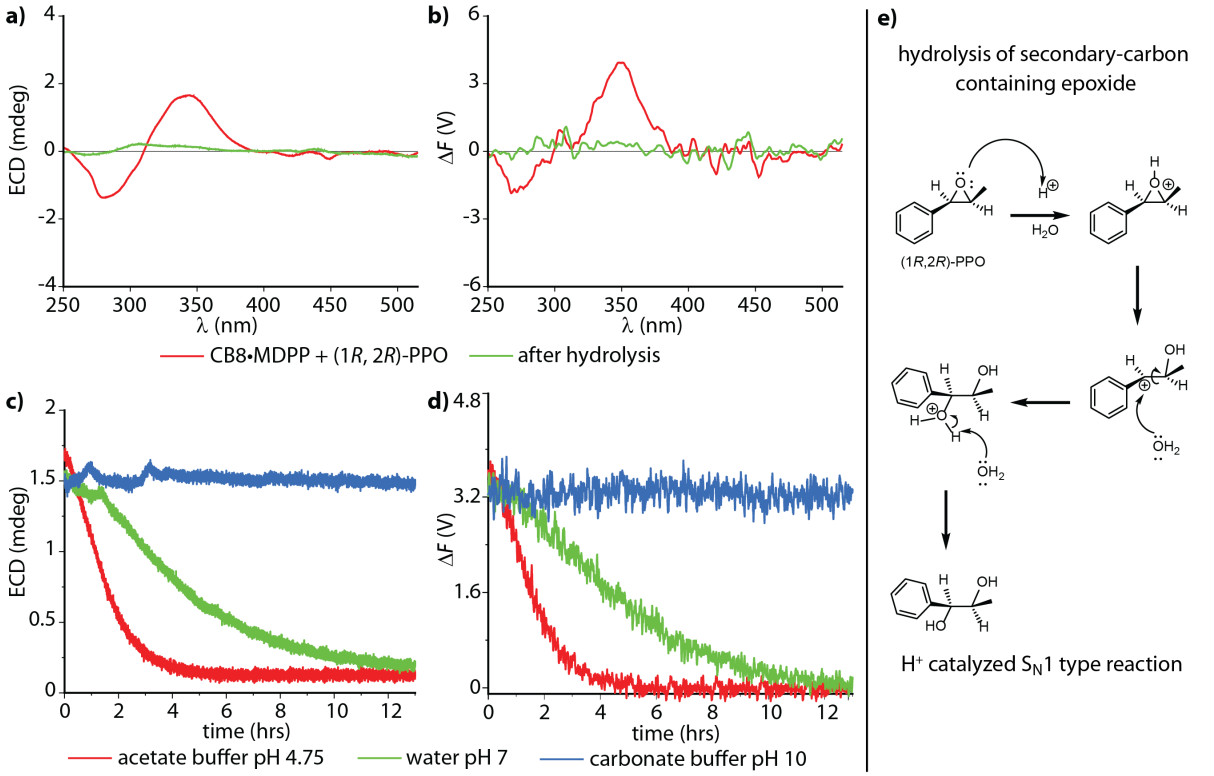

Figure 3.10: (a) ECD and (b) ΔF spectra of CB8•MDPP (20 µM) in the presence of the chiral epoxide, (1*R*,2*R*)-1-phenylpropylene-oxide (100 µM) (red line) in water and the spectra after hydrolysis of the epoxide measured after 12 hrs (green line). Single-wavelength time course (c) ECD, and (d) ΔF measurements of CB8•MDPP (20 µM) in the presence of (1*R*,2*R*)-1-phenylpropylene oxide (100 µM) in different solvent systems: 50 mM acetate buffer at pH 4.75 (black), water at pH 7 (red) and 50 mM carbonate buffer at pH 10 (blue). Parameters used: HT = 520 V, BW = 4 nm, Acc = 20, LP-Filter = 515 nm, λ_{obs} = 350 nm, Data Pitch = 5 s, D.I.T = 8 s, $t_{measure}$ = 14 h. (e) Schematic representation of the hydrolysis of secondary carbon-containing epoxide ((1*R*,2*R*)-PPO) following an S_N1 type reaction mechanism. Note that racemization can occur in the carbocation intermediate through rotation along the C-C bond of the opened epoxide.

The time course ΔF and ECD measurements showed a gradual decrease in the intensity of both induced ΔF and ECD signals upon the addition of β-galactosidase, allowing real-time monitoring of the enzymatic conversion (Figure 3.28c and 3.28d in Section 3.5 - Additional Information).

The representative examples depicted here demonstrate that combining FDCD and ECD measurements clearly provides additional useful chiroptical information about the analyte present and, in addition, is practical for sensitive, fast, and label-free reaction monitoring.

3.2.4. Uncovering of hidden aggregation phenomena by FDCD

The combined information gathered from FDCD and ECD measurements could provide a detailed description and understanding of complex supramolecular host-guest systems. This has been evaluated here when studying the host-guest binding interactions of the achiral emissive endo-functionalized molecular tube, MT (see Figure 3.2a), with chiral analytes. The MT receptor is known to selectively bind polar guests with hydrogen-bond accepting capacities,

such as dioxane, esters, and epoxides in aqueous media with K_a up to 10^5 M^{-1}.[95,96,298] For instance, the chiral aromatic epoxides, (1*R*,2*R*)-1-phenylpropylene oxide ((1*R*,2*R*)-PPO) and its enantiomer (1*S*,2*S*)-1-phenylpropylene oxide ((1*S*,2*S*)-PPO), are strongly complexed by MT in water with $K_a = 8.97\ (\pm 0.9) \times 10^4\ M^{-1}$ resulting in a 1:1 host-guest complex (see Figure 3.11a).[96] This interaction is reported to give rise to a strong induced ECD signal, *e.g.,* approx. ±89 mdeg at 254 nm when monitored at 100 µM and 500 µM of the host and guest concentrations, respectively.[96] In my investigation, I employed FDCD measurements to the system, which gave rise to an induced negative Δ*F* and FDCD signal on the addition of (1*R*,2*R*)-PPO and a positive signal on the addition of (1*S*,2*S*)-PPO to an aqueous solution of MT receptor (Figure 3.11c and 3.11e). The binding was also accompanied by an enhancement in the fluorescence intensity of MT receptor (Figure 3.11d). However, compared to the induced ECD signals, the FDCD signals

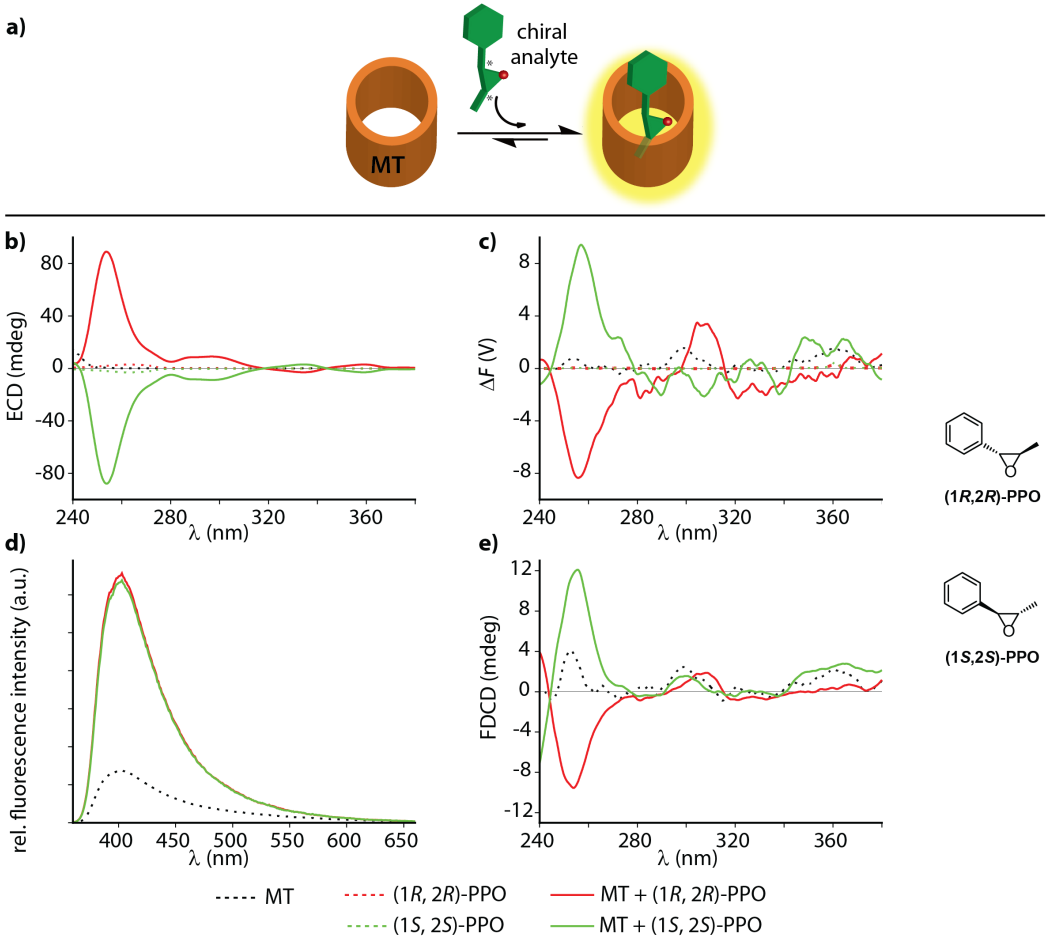

Figure 3.11: (a) Schematic representation of the complex formation between the achiral chromophoric host MT and the chiral epoxide guest. (b) ECD and (c) Δ*F* spectra of freshly prepared MT receptor (100 µM) in the absence (dashed lines) and presence (solid lines) of (1*R*,2*R*)-PPO (500 µM) and (1*S*,2*S*)-PPO (500 µM) in water. Parameters used: HT = 630 V, BW = 4 nm, Acc = 20, LP-Filter = 380 nm. (d) Enhancement in the fluorescence intensity of freshly prepared MT receptor (100 µM) upon addition of (1*R*,2*R*)-PPO (500 µM) and (1*S*,2*S*)-PPO (500 µM) in water, $\lambda_{exc} = 340$ nm. (e) FDCD spectra of freshly prepared MT receptor (100 µM) in the absence (dashed lines) and presence (solid lines) of (1*R*,2*R*)-PPO (500 µM) and (1*S*,2*S*)-PPO (500 µM) in water.

were markedly weaker, approx. ±10 mdeg at 254 nm at the same concentrations studied. Moreover, the Δ*F* and FDCD spectra showed pronounced signals in the excitation peak region for the achiral MT receptor alone (see Figure 3.11c and 3.11e), which – of course – do not reflect chiroptical properties, but must arise from anisotropic excitation, also known as photoselection, and from instrument-related artefacts.[199,299,300] Essentially, the larger the emissive compound, *e.g.,* the macrocyclic host, and the higher the viscosity of the medium, the larger photoselection artefacts will be observed due to restricted rotation of the emitter[199,301] (for further details and suggested artefact-subtraction procedures, refer to *Photoselection artefacts in FDCD* and *Correction of signal artefacts in FDCD* in Section 3.5 - Additional Information).

Striking changes to the FDCD and ECD spectra were observed upon dilution of the system. On probing lower analyte concentrations, the ECD spectra showed a strong reduction in the signal intensity corresponding to the decrease in host-guest concentration, while a completely unexpected inversion in the direction of Δ*F* and FDCD signal (positive FDCD signal on the addition of (1*R*,2*R*)-PPO and negative FDCD signal on the addition of (1*S*,2*S*)-PPO) was observed in the recorded spectra (Figure 3.12). An excess of the epoxide to the receptor was present in all the cases studied, and the degree of complexation of the MT receptor at MT : epoxide concentrations of 100 : 500 μM, 2.5 : 10 μM, and 1.25 : 5 μM varied from 97.3% to 44.4% and 29.4%, respectively upon dilution. However, even though the amount of MT receptor complexed decreased upon dilution, an inversion in the Δ*F* and FDCD signal direction was still not expected. Moreover, the FDCD signal should be concentration-independent, which holds true for the spectra measured at lower concentrations (MT : epoxide concentrations of 2.5 : 10 μM and 1.25 : 5 μM), while the inversion in the FDCD signal direction at higher concentrations indicates the influence of other effects.

In order to evaluate the influence of photoselection artefacts or anisotropy of the system in the measured ECD and FDCD spectra at higher concentrations, the linear polarization components, *i.e.*, linear dichroism (LD)[302,303]and linear birefringence (LB)[303,304] in case of ECD, and fluorescence-detected linear dichroism (FDLD)[199,305] in case of FDCD, were investigated for the achiral MT receptor and MT•epoxide complex at receptor and analyte concentrations of 100 μM and 500 μM, respectively (Figure 3.13a – 3.13c). In the absence of photoselection artefacts both LD and FDLD spectra should not give any signal. For the LB measurements, simulations conducted by the instrument manufacturer indicated that artefacts induced in the ECD spectra from the LB components have an intensity ratio of 1/100 with respect to the

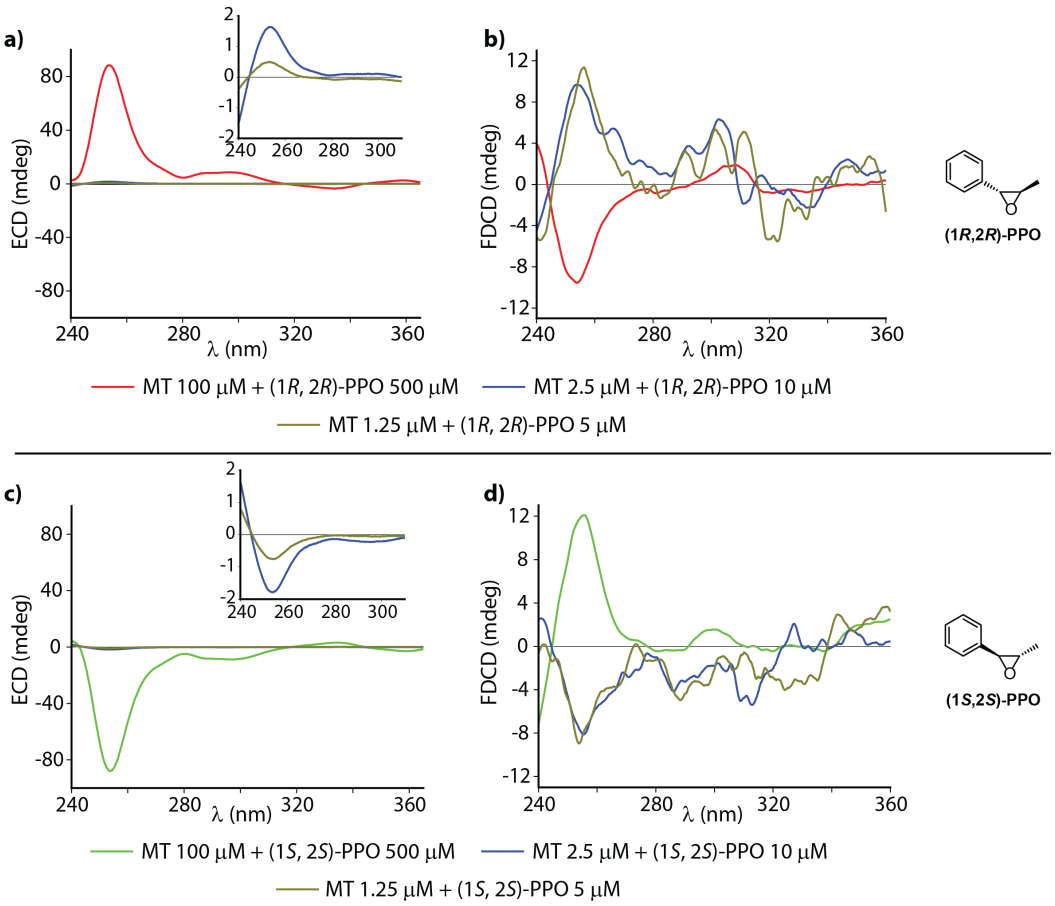

Figure 3.12: Concentration-dependent ECD and FDCD spectra of freshly prepared MT receptor in the presence of (a-b) (1*R*,2*R*)-PPO and (c-d) (1*S*,2*S*)-PPO in water. The inset in the ECD spectra shows the zoomed-in signals in the 240 nm to 310 nm region. Parameters used: HT = 630 V (MT : epoxide = 100 : 500 µM), 800V (MT : epoxide = 2.5 : 10 µM and 1.25 : 5 µM), BW = 4 nm, Acc = 20, LP-Filter = 380 nm. The parameters were kept constant for each individual set of measurements. An inversion in the direction of the FDCD signal was observed at lower concentrations.

measured LB values (thus, a signal strength of 200 mdeg measured on the LB spectra corresponds to an artefact of 1 mdeg in the ECD spectra). Furthermore, the fluorescence excitation anisotropy of the system was measured to obtain supplementary information about the sample's properties (Figure 3.13d). As shown in Figures 3.13a and 3.13b, the measured LD and LB values were only modest in magnitude, indicating that the observed induced ECD signals in the system reflect a direct measure of its chiroptical properties. The LD and LB signals observed below 250 nm were due to the high sample absorbance in the lower wavelength region and did not seem to coincide with the ECD signal peak. In contrast, the measured FDLD spectra showed strong signals in the region where the FDCD bands were observed from the achiral MT receptor (Figure 3.13c), indicating a strong influence of fluorescence anisotropy. Hence, the observed induced FDCD signals in this system should be considered as apparent values, which do not directly report on chiroptical properties but also contain other contributions indicative of fluorophore orientation. Additionally, the measured

excitation fluorescence anisotropy spectra also revealed the presence of strong fluorescence anisotropy in the system (Figure 3.13d). Thus, the FDCD and ECD measurements for the MT•(1*R*,2*R*)-PPO complex were also conducted on an artefact-free FDCD spectrometer set-up utilizing an ellipsoidal mirror (measured at JASCO, Japan),[306] at receptor and analyte concentration of 100 µM and 500 µM, respectively (Figure 3.14). The FDCD spectrum obtained in this case at high micromolar concentrations of the receptor and the analyte resembled the spectrum collected at lower concentrations on the standard ECD spectrometer with the FDCD setup utilized in this study (see Figure 3.14 and Figure 3.12a-3.12b). Hence, it was concluded that something unusual occurs at higher receptor and analyte concentrations, that was previously undetected by ECD, absorbance, fluorescence, and NMR measurements.[96]

Based on the available data, I hypothesized that the MT and MT•PPO complexes form supramolecular self-aggregating structures at higher micromolar concentrations (see Figure 3.15), which resulted in an enhanced ECD signal and sizeable FDLD contributions in the measured FDCD signal.

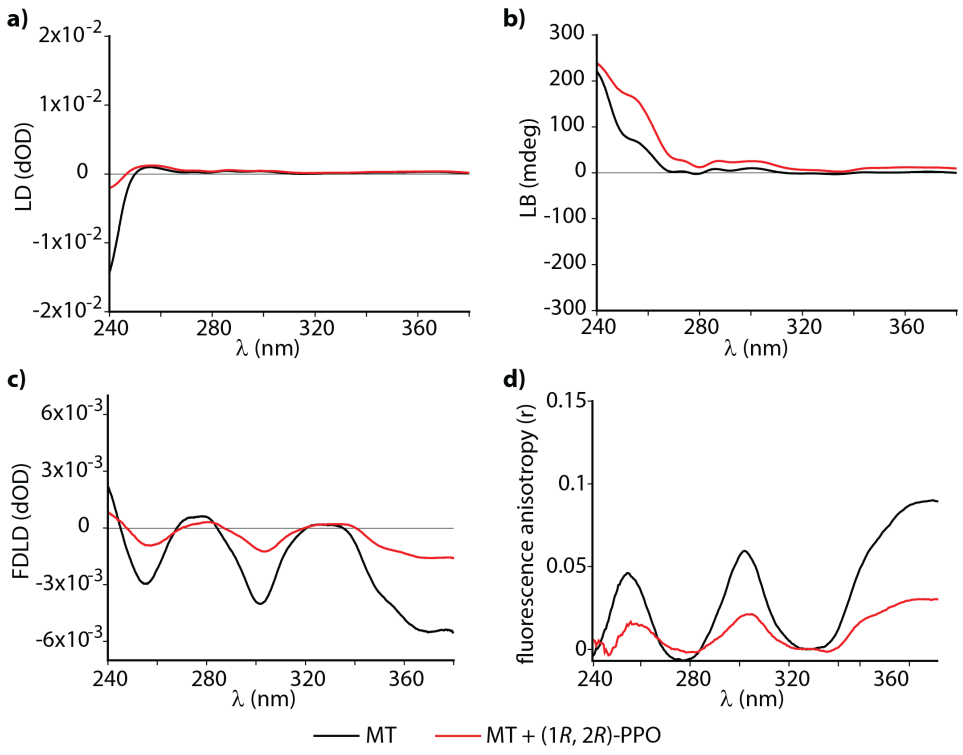

Figure 3.13: (a) LD and (b) LB, and (c) FDLD spectra of MT receptor (100 µM) in the absence and presence of (1*R*,2*R*)-PPO (500 µM) in water. Parameters used: HT = 570 V, BW = 4 nm, Acc = 20, LP-Filter = 380 nm. The LB spectra were measured on a JASCO J-1500 CD spectrometer at a JASCO facility in Pfungstadt by placing a Glan-Taylor polarizer behind the sample at 45° into the beam path. (d) Fluorescence excitation anisotropy spectra of MT receptor (100 µM) in the absence and presence of (1*R*,2*R*)-PPO (500 µM) in water, λ_{ems} = 450 nm.

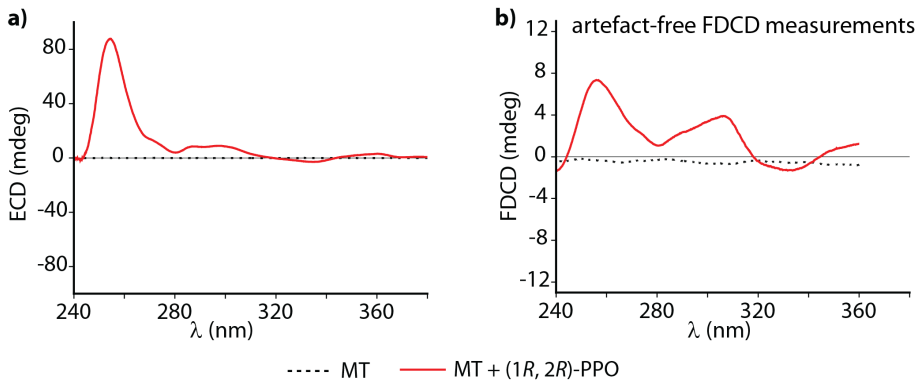

Figure 3.14: (a) ECD and (b) FDCD spectra of MT receptor (100 µM) in the absence and presence (1*R*,2*R*)-PPO (500 µM) in water using artefact-free 551-FDCD spectrometer, measured in Japan. Parameters used: HT = 350 V (for MT receptor) and 300 V (for MT + (1*R*,2*R*)-PPO), BW = 4 nm, Acc = 20, LP-Filter = 380 nm, 2.5 mm balancing mask was used for preventing the influence from fluorescence anisotropy.

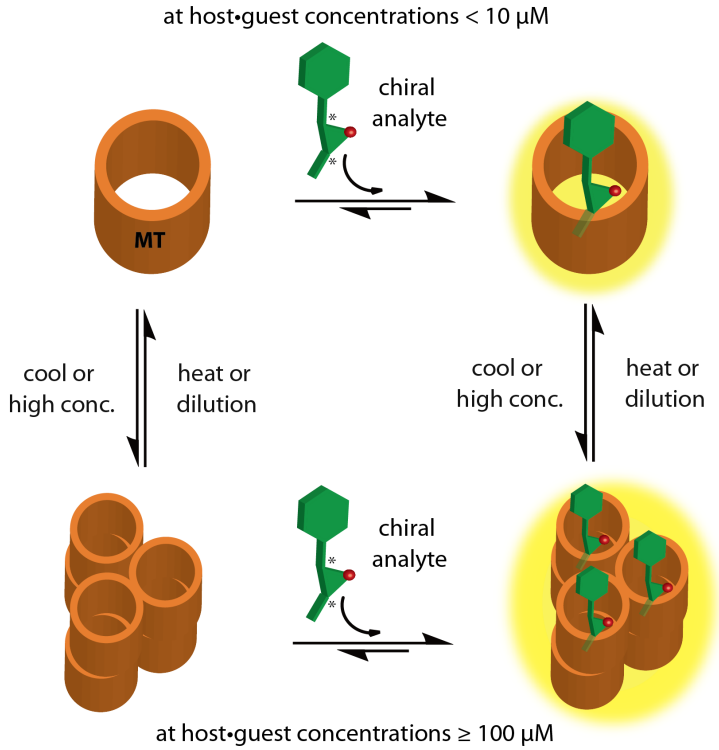

Figure 3.15: Schematic representation showing the complex formation between the achiral chromophoric MT host and the chiral epoxides in their non-aggregated state at low concentrations and upon aggregation at higher concentrations and lower temperature.

Additional experiments were conducted to support the aggregation hypothesis. For instance, the aggregation properties of the achiral MT receptor were evaluated by monitoring the FDCD spectrum at longer time intervals (Figure 3.16a). In practice, a 1 mM stock solution of the MT receptor in water was freshly prepared, and the FDCD spectrum of a 100 µM solution prepared by diluting this freshly prepared stock solution was measured at 25°C. The 1 mM stock solution was then kept aside in a sealed vial and stored in the refrigerator for 1 day. Following this, the FDCD spectrum of a 100 µM solution prepared from the one-day-old 1.0 mM stock solution

was also measured at 25°C. The spectra collected showed an "aging phenomenon" of the achiral MT receptor with an emerging FDCD band at 300 nm and 360 nm with time (Figure 3.16a). This indicated the receptor is undergoing aggregation over time in the 1.0 mM stock solution, which is still present at a concentration of 100 µM, resulting in strong photoselection artefacts in the measured FDCD spectra. Subsequently, the temperature effects on the FDCD signal at 300 nm for the aged solution of MT receptor at 100 µM were monitored by increasing the temperature from 5°C to 60°C followed by cooling the solution back from 60°C to 5°C. This showed a strong decrease in the FDCD signal with increasing temperature (Figure 3.16b), implying the MT receptor aggregates dissociated when going to higher temperatures. The aggregation/deaggregation process was reversible, as seen by the enhancement in the FDCD signal and returning to the initial value when cooling the solution back from 60°C to 5°C (Figure 3.16b). It should be noted that the photoselection artefacts/fluorescence anisotropy also decreases with an increase in temperature, as the viscosity of the media decreases with an increase in temperature and *vice versa*. [307] This effect was also seen here in the temperature-dependent graph (Figure 3.16b).

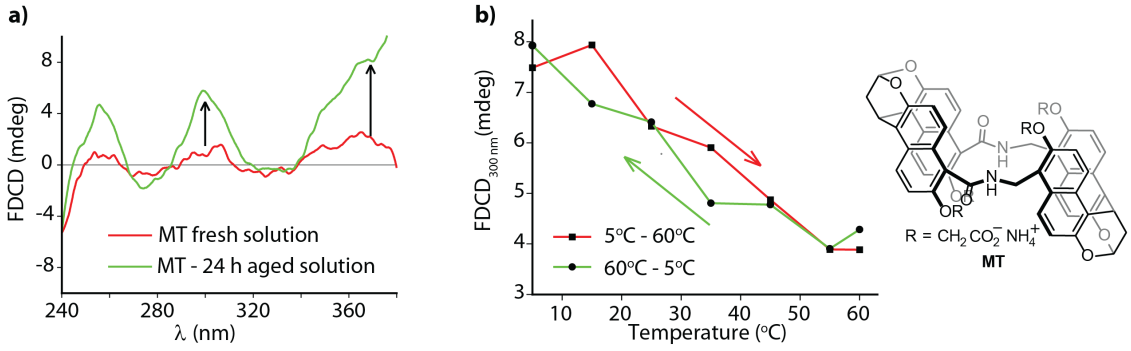

Figure 3.16: (a) FDCD spectra of a 100 µM MT receptor solution prepared from a freshly prepared 1.0 mM stock solution in water (red line) and after keeping the 1.0 mM stock solution for 24 h (green line). (b) FDCD signal at 300 nm of the MT receptor (100 µM) in water on increasing the temperature from 5°C to 60°C (red line) and on cooling the solution back from 60°C to 5°C (green line). Parameters used: HT = 630 V, BW = 4 nm, Acc = 20, LP-Filter = 380 nm.

In addition, the possibility of aggregation at higher concentrations was also evaluated by collecting the emission intensity of the MT receptor at 404 nm on increasing the receptor concentration from 1.56 µM to 100 µM (Figure 3.17a). The excitation wavelength was chosen accordingly such that the absorbance of the 100 µM MT solution is less than 0.1 at the exciting wavelength, thereby excluding any inner filter effects.[119] According to theory, under these conditions tested, the fluorescence intensity should display a straight line with increasing concentration of the fluorophore, provided it remains in its fully dissolved, non-aggregated state.[119] However, a deviation from linearity was observed for the MT receptor at higher

concentrations, which further suggested the formation of aggregates at higher concentrations (Figure 3.17a). Moreover, concentration-dependent DOSY NMR spectra (which is more sensitive to aggregation properties than ^{1}H NMR) of the MT receptor in D_2O, displayed a slower diffusion rate of MT at higher concentrations, which also supported the aggregation hypothesis (Figure 3.18). Dynamic Light Scattering (DLS)[308] experiments were performed to characterize the size of the aggregates. An MT receptor solution at 100 µM in water was filtered using a polyethersulfone membrane with a pore size of 0.43 µm prior to the measurement. Figure 3.17b displays the acquired data as intensity size distribution, which showed a prominent peak with

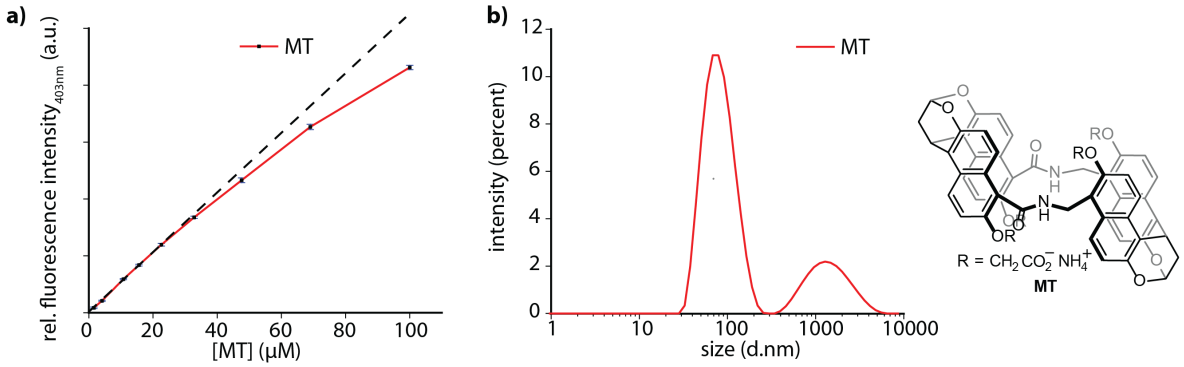

Figure 3.17: (a) Emission intensity collected at 403 nm upon increasing the concentration of MT receptor from 1.56 µM to 100 µM in water, λ_{exc} = 383 nm. The vertical error bars for the fluorescence intensity values are depicted in blue in the graph. (b) DLS measurements showing the intensity distribution versus particle diameter of MT receptor solution (100 µM) in water. Parameters used: material RI = 1.45, dispersant RI = 1.330, viscosity = 0.8872 cP, measurement position = 4.65 mm, attenuator = 11.

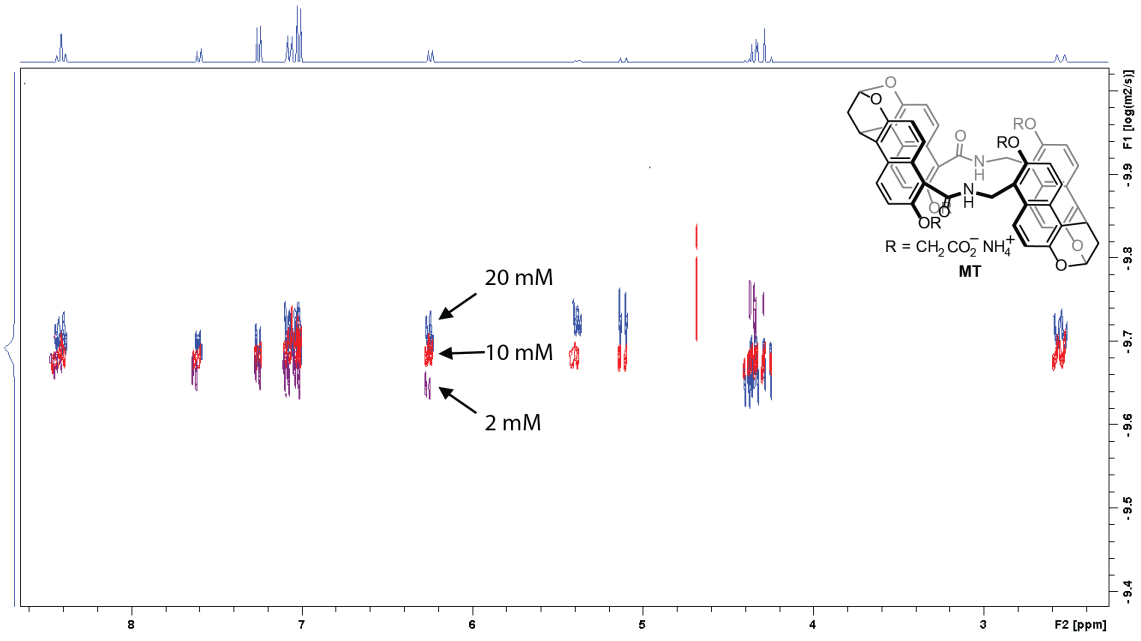

Figure 3.18: DOSY NMR spectrum of MT receptor at 2 mM, 10 mM, and 20 mM in D_2O

a hydrodynamic diameter of ~60 nm and a minor peak with a hydrodynamic diameter of 1752 nm corresponding to some bigger aggregates. The peak at ~60 nm has a polydispersity index (PDI)[309] of 0.165. Given that the size of MT receptor is on the order of 1 nm, it is clear that the peak at ~60 nm corresponds to aggregates. On comparing the DLS results to the DOSY NMR measurements, it appeared that higher concentrations are needed to influence the DOSY signal. This can be because NMR operates on a different time scale and generally yields an averaged diffusion coefficient among the fast exchanging aggregates of different sizes.[310] Hence, it may well be that the aggregates formed at ~100 μM of MT receptor are still fleeting in nature and diffuse relatively freely. At the same time, optically-probed properties (*e.g.*, ECD, FDCD, fluorescence) and DLS provide the instant snapshot and hence display several distinct species according to the aggregate size.[310]

This study clearly demonstrates that FDCD-based investigations can uncover interesting supramolecular phenomena that were invisible to ECD and other spectroscopic techniques alone.

3.2.5. FDCD measurements for background reduction in complex systems and chromophoric biofluids

The FDCD technique, being sensitive to only chiral and fluorescent molecules, can provide background-reduced signals compared to ECD and standard absorbance or fluorescence measurements. This is particularly important when a chiral analyte should be detected in the presence of other chiral (and chromophoric) substances, *e.g.,* proteins, DNA, etc., or in complex media such as biofluids that exhibit strong ECD, absorbance, and emission signals. Hence, I investigated two supramolecular host-guest systems in this work as representative examples.

(i) The CB8•MDPP chemosensing ensemble is known to bind the protein insulin resulting in strong induced ECD signals in the 250-350 nm region upon complex formation.[173] Nevertheless, one finds a substantial contribution from the ECD signal of the insulin backbone at <310 nm in the measured ECD spectrum (see Figure 3.19a). FDCD measurements were applied to this system, where strong induced FDCD signals were observed on the addition of CB8•MDPP receptor to insulin in 10 mM phosphate buffer at pH 2.7. However, in FDCD, a chiroptical signal contribution from the protein insulin was completely absent upon utilizing a 515 nm long-pass filter (Figure 3.19b). The FDCD spectrum selectively showed the induced FDCD signal from the CB8•MDPP complex bound to and located in the chiral protein environment (see Figure 3.19c).

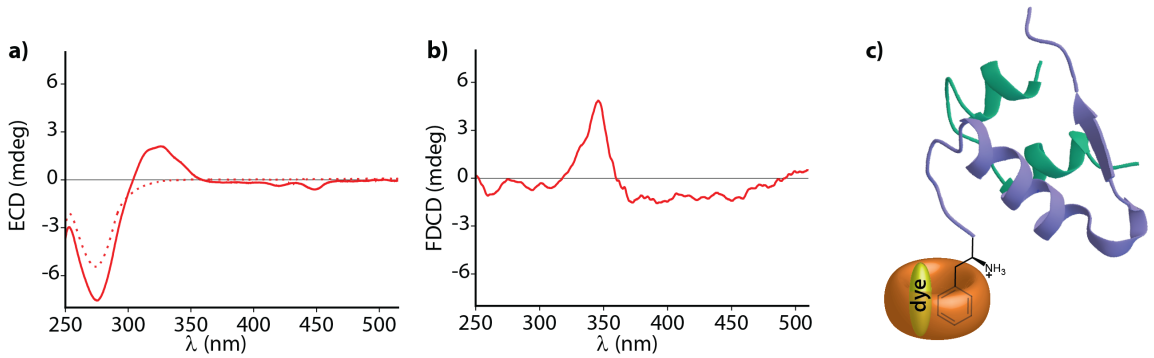

Figure 3.19: (a) ECD, (b) FDCD spectra of CB8•MDPP (20 µM) in the presence of insulin (50 µM) (red line) in 10 mM phosphate buffer at pH 2.7. The red dashed line represents the ECD signals arising from insulin (50 µM) alone. No Δ*F* signals were observed from insulin alone. Parameters used: HT = 510 V, BW = 4 nm, Acc = 20, LP-Filter = 515 nm. (c) Representative diagram showing CB8•MDPP complex bound to the N-terminal phenylalanine (Phe) residue of insulin.

(ii) The advantage of FDCD-based detection schemes was also portrayed for selective analyte detection in human blood serum (HS), a strongly chromophoric and autoemissive biofluid containing many chiral components. An emission-based supramolecular assay for detecting Alzheimer's drug memantine in human blood serum was recently developed by our group using the CB8•MPCP chemosensor.[152] However, variations in the total fluorescence background signal due to sample to sample differences can complicate the assay analysis in the fluorescence-based assay. To obtain background-reduced signals in the sensing assay, the FDCD technique, which selectively reports only on chiral and emissive species, was adopted to detect memantine in human blood serum using CB8•MPCP chemosensor with chiral MPCP enantiomers as indicator dyes. As shown in the previous section, the chiral MPCP dye enantiomers, (R_p)-MPCP and (S_p)-MPCP, showed strong ECD and Δ*F* signals in water (see Figure 3.3). The addition of CB8 to the dye solution resulted in a strong enhancement in the Δ*F* signal, accompanied by a bathochromic shift in both ECD and Δ*F* signal upon host-dye complex formation (Figure 3.3). Hence, in the sensing assay, the presence of stronger binding analyte memantine in HS will result in the displacement of chiral emissive MPCP from the CB8 cavity and is expected to give rise to strong signal changes in the Δ*F* spectra (see Figure 3.20a). Experimental investigations were conducted to evaluate the performance of the assay. The HS sample was filtered using a polyethersulfone membrane with a pore size of 0.22 µm prior to the measurements. The spectrum of HS alone showed a strong positive ECD and Δ*F* background signal (Figure 3.20b – 3.20e). The addition of 20 µM CB8•(R_p)-MPCP or CB8•(S_p)-MPCP host-dye reporter pair to the HS sample resulted in changes in both the ECD and Δ*F* spectra. The ECD and Δ*F* signal became more negative in the case of CB8•(R_p)-MPCP and more positive in the case of CB8•(S_p)-MPCP) (Figure 3.20b – 3.20e).

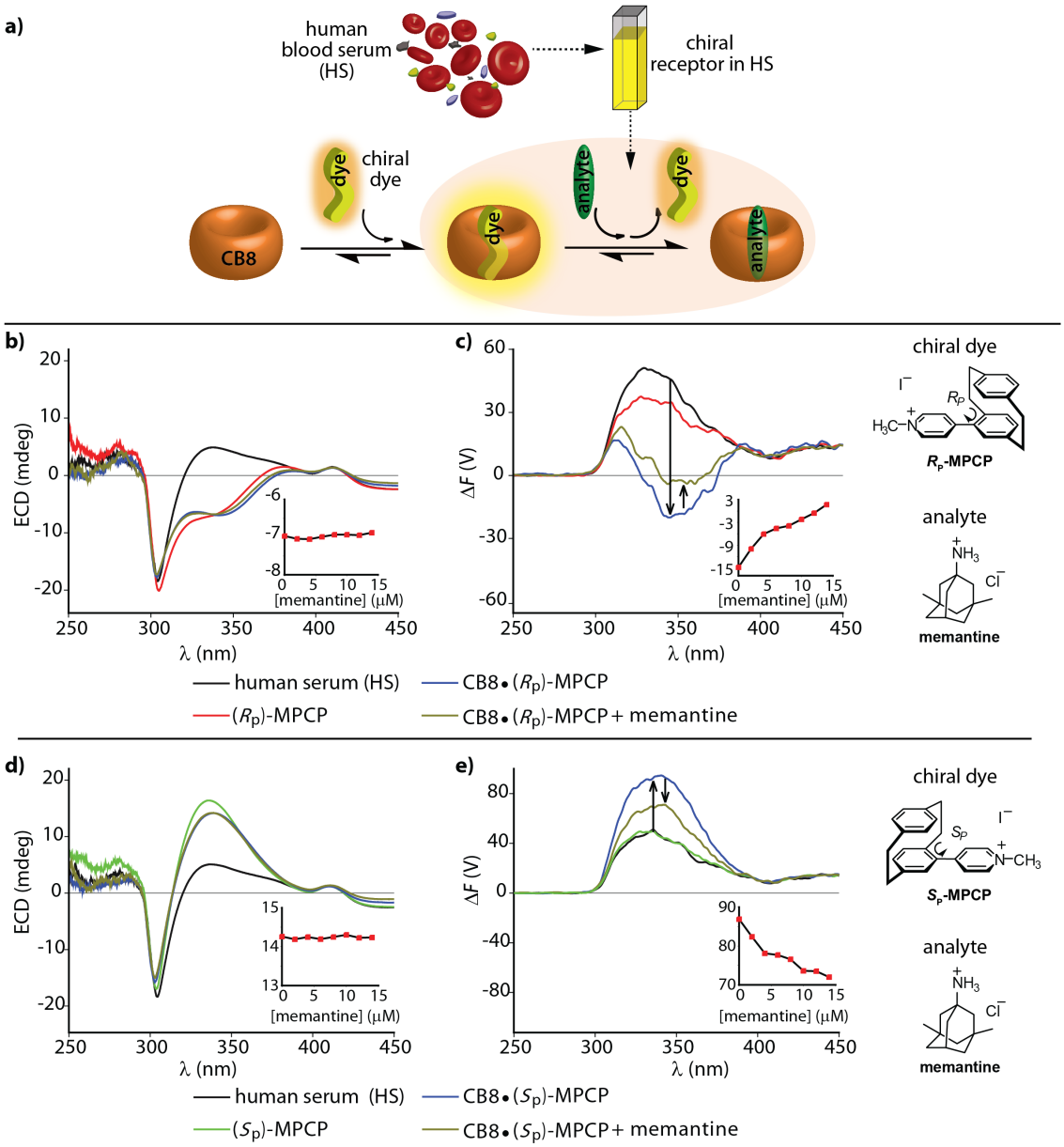

Figure 3.20: (a) Schematic representation depicting the formation of a 1 : 1 CB8•MPCP complex, followed by the displacement of MPCP from the host cavity upon addition of a higher binding analyte, *e.g.*, memantine. ECD and Δ*F* spectra of (b-c) CB8•(R_p)-MPCP (20 μM) and (d-e) CB8•(S_p)-MPCP (20 μM) in human blood serum before and after addition of memantine (20 μM). Parameters used: HT = 800 V, BW = 4 nm, Acc = 20, LP-filter = 515 nm. The insets show the ECD and Δ*F* signal variation at 340 nm on the stepwise addition of memantine.

Following this, the achiral drug memantine was added stepwise to the chemosensor sample in HS with a 15 minutes of equilibration time between each addition. The variation in both the ECD and Δ*F* signal was monitored at 340 nm with the help of single-wavelength ECD and Δ*F* measurements (Figure 3.20b – 3.20e, insets). As shown in Figure 3.20b – 3.20e, the background was expectedly much lower in FDCD than for conventional emission or ECD spectroscopy. As a matter of fact, only by Δ*F* and not by ECD was it possible to quantitatively detect memantine in human blood serum in the low micromolar concentration range. For instance, the addition of 15 μM of memantine to a solution of CB8•(R_p)-MPCP or CB8•(S_p)-MPCP (reporter pair at

20 µM) in HS led to a Δ*F* signal change by +16 V or −15 V, respectively. In contrast, the ECD signals did not show any significant change (Figure 3.20b – 3.20d, insets). Notably, using the enantiomeric indicator dyes (R_p)-MPCP and (S_p)-MPCP in the sensing assay, the behavior was similar but not identical (see the ECD and Δ*F* spectra and titration curves in Figure 3.20b – 3.20e). These differences may be originating from the diastereomeric interaction of the chiral indicator dye with the chiral components in HS, *e.g.,* human serum albumin and other chiral proteins with large binding pockets. Hence, while developing practical assays in biofluids containing chiral compounds, it is advisable to access both enantiomers of the dye or host, as the combined chiroptical information obtained by using both chiral forms can enrich the understanding of the system and help to identify artefacts.

The ECD and Δ*F* signals of the CB8•(R_p)-MPCP and CB8•(S_p)-MPCP complex lie in the same region as the background ECD and Δ*F* signals arising from HS alone and are hence not ideally suited for sensing applications in HS. Therefore, a new chiral paracyclophane dye ((S_p)-MVCP) was prepared by the Bräse group with a longer excitation wavelength. The obtained (S_p)-MVCP dye, see Figure 3.2b for its chemical structure, showed absorption bands in the 350 -450 nm region, which is by 46 nm red-shifted compared to the MPCP dye (Figure 3.21a and 3.21b). Similar to MPCP, at micromolar concentrations, (S_p)-MVCP displayed clearly defined signals in the ECD and Δ*F* spectra with signal maxima at 285 nm and 363 nm in water (Figure 3.21a and 3.21b). The addition of CB8 to the dye solutions resulted in an enhancement in the Δ*F* signal accompanied by a bathochromic shift in both ECD and Δ*F* signals with maxima at 299 nm and 386 nm for the bound dye (Figure 3.21a and 3.21b).

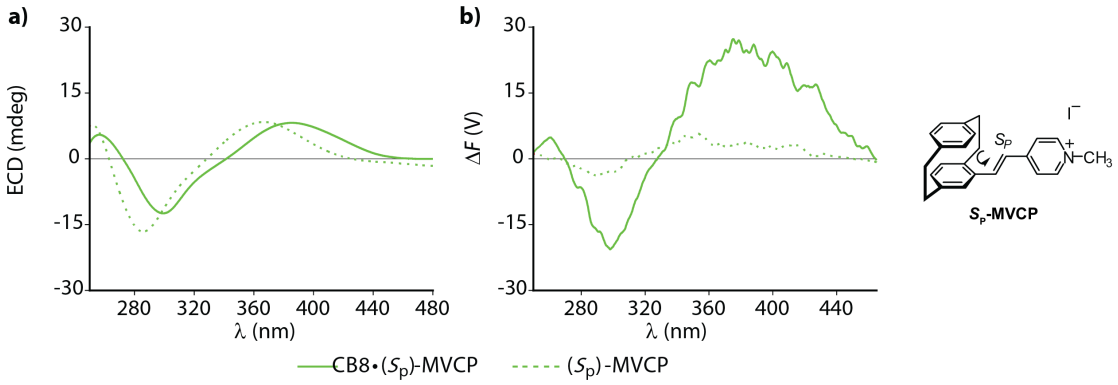

Figure 3.21: (a) ECD and (b) Δ*F* spectra of (S_p)-MVCP (45 µM) in the absence and presence of CB8 (45 µM) in water. Parameters used: HT = 800 V, BW = 4 nm, Acc = 20, LP-Filter = 480 nm. (c) ECD and (d) Δ*F* spectra of CB8•(S_p)-MVCP (20 µM) in human blood serum before and after addition of memantine (20 µM). Graph (e) shows the zoomed-in Δ*F* signal in the 380 – 440 nm region. Parameters used: HT = 800 V, BW = 4 nm, Acc = 20, LP-filter = 515 nm. The insets show the variation in ECD and Δ*F* signal at 407 nm on stepwise addition of memantine.

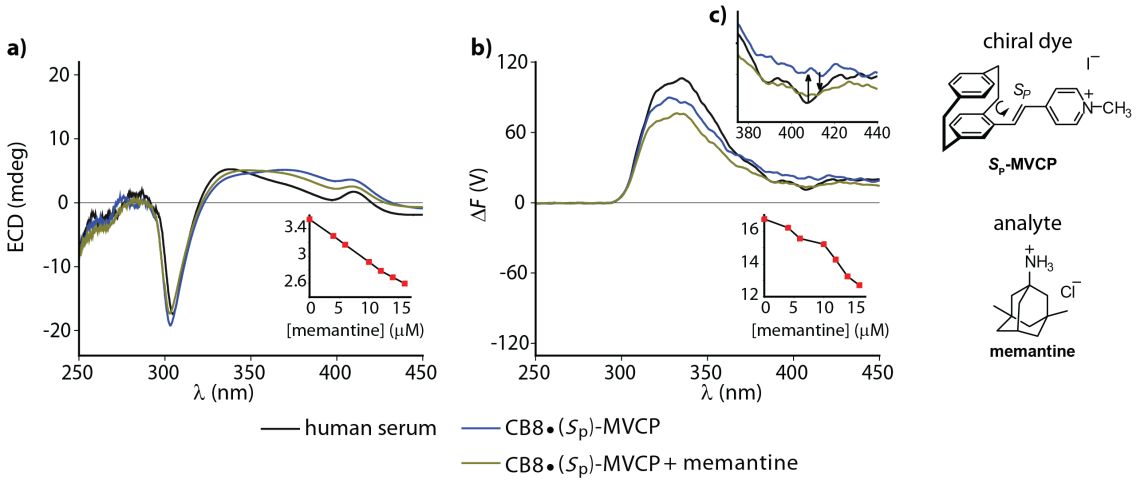

Figure 3.22: (a) ECD and (b) Δ*F* spectra of CB8•(S_p)-MVCP (20 μM) in human blood serum before and after addition of memantine (20 μM). Graph (c) shows the zoomed-in Δ*F* signal in the 380 – 440 nm region. Parameters used: HT = 800 V, BW = 4 nm, Acc = 20, LPfilter = 515 nm. The insets show the variation in ECD and Δ*F* signal at 407 nm on stepwise addition of memantine.

The CB8•(S_p)-MVCP reporter pair is therefore an interesting candidate for sensing studies in human blood serum. The addition of 20 μM CB8•(S_p)-MVCP to HS resulted in changes in both the ECD and Δ*F* spectra of HS, with positive signals arising in the 380 – 440 nm region, which appeared slightly sifted from the main HS background ECD and Δ*F* signals (Figure 3.22a and 3.22b). Subsequently, the addition of the achiral drug memantine to the solution of CB8•(S_p)-MVCP in HS resulted in a Δ*F* signal change by −4 V at 407 nm monitoring wavelength (Figure 3.22a and 3.22b). Interestingly, upon using CB8•(S_p)-MVCP instead of CB8•MPCP reporter pair, ECD-based detection of memantine was also feasible with a signal change of −0.9 mdeg at 407 nm, see Figure 3.22a and 3.22b (however, stronger signal differences were observed when using the Δ*F* measurements).

These examples demonstrate that Δ*F* measurements can be superior to ECD recordings for sensing applications in complex systems and chromophoric biofluids.

3.3. Conclusion

In conclusion, FDCD measurements were applied for the first time on (synthetic) supramolecular complexes in aqueous media and is shown to be a promising chiroptical technique for sensing applications. It was demonstrated that at least an order of magnitude higher sensitivity can be achieved with FDCD compared to ECD measurements, and even the nanomolar sensitivity can be reached by FDCD in favorable circumstances, which is beyond the scope of most other techniques used for characterization of supramolecular systems. The high sensitivity of FDCD will be advantageous for sensing applications in real biological media, where the analytes mainly occur in the low micromolar to nanomolar concentration regime.

In addition to a sensitivity enhancement, the combined use of FDCD and ECD was demonstrated to provide a detailed description and understanding of (complex) supramolecular host-guest systems. For instance, the hidden aggregation phenomenon was uncovered by comparing FDCD to ECD spectra, which were not identified by the single-handed use of other spectroscopic tools alone. Moreover, FDCD and ECD provided complementary information that was useful for distinguishing chiral analytes from each other, through which the target binding sites of the host were identified, *e.g.*, Phe- from Trp residues in proteins. FDCD spectra can be informative, but it is crucial to monitor the influence of anisotropic excitation/photoselection and instrument-related artefacts in the measured spectra that can produce apparent FDCD signals unless a dedicated artefact-free FDCD setup is utilized. This chapter also established FDCD measurements for label-free reaction monitoring, both in an endpoint assay version and continuous reaction monitoring, which can provide faster and more facile analysis of chemical or enzymatic transformations compared to other established methods such as HPLC-MS.

FDCD was also shown to be a highly selective spectroscopic method that is ideally suited for the selective monitoring of a target analyte that forms a host-guest complex in the presence of other chromophoric compounds. In ECD, strong influences from the matrix components can often complicate the picture, while no FDCD signal is generated from most biorelevant chiral molecules (*e.g.*, drugs, metabolites) because they are non- or only weakly emissive. For instance, FDCD measurements were carried out for the first time in the complex chromophoric biofluid, human blood serum, to detect the Alzheimer's drug memantine using a supramolecular indicator displacement assay. In addition, specific approaches were exploited to improve the performance of chiroptical assays, *i.e.,* both ECD and FDCD in biofluids through the design of novel chiral indicator dyes, *e.g.*, MVCP, with large Stokes shift and red-shifted absorbance spectra. Likewise, the design of protein- and analyte-binding emissive hosts with improved photophysical properties will increase the scope of FDCD-based supramolecular applications in biorelevant media.

To conclude, my investigations not only established the use of FDCD (and ECD) for a wide range of host-guest and host-protein complexes, but also provides a comprehensive user guide and recommendation for the most effective and general use of FDCD spectroscopy. I believe that the combined use of FDCD and ECD will become the new standard in chiroptical research.

3.4. Experimental details

3.4.1. Materials

All solvents were used as received from Aldrich or Fluka without further purification. All chemicals were purchased and used as received unless stated otherwise. CB8 was synthesized according to literature procedures[244] and was also purchased from Strem or Sigma. The molecular tube MT was synthesized according to literature procedures.[95] Liu-Pan Yang from the research group of Prof. Wei Jiang carried out the synthesis of the molecular tube, MT. The MPCP dye enantiomers, (R_p)-MPCP and (S_p)-MPCP, and the (S_p)-MVCP dye were prepared according to the synthetic route shown in Scheme 3.1 and Scheme 3.2 in Section 3.5-Additional Information.[249] Dr. Eduard Spuling and Yichuan Wang from the research group of Prof. Stefan Bräse, carried out the synthesis of the MPCP dye enantiomers, (R_p)-MPCP and (S_p)-MPCP, and the (S_p)-MVCP dye, respectively. The synthesis details of the chiral paracyclophane type indicator dyes are available at Chemotion at https://dx.doi.org/10.14272/reaction/SA-FUHFF-UHFFFADPSC-BAIBHOHKSY-UHFFFADPSC-NUHFF-NUHFF-NUHFF-ZZZ.3 and https://dx.doi.org/10.14272/reaction/SA-FUHFF-UHFFFADPSC-GRWXNDHDQX-UHFFFADPSC-NUHFF-MABGN-NUHFF-ZZZ. MDPP was synthesized according to literature procedures from 1,3,8,10-tetrahydro-2,9-dimethyl-2,9-diazadibenzoperylene.[245]

3.4.2. Instrumentation

Absorption spectra were measured on a Jasco V-730 double-beam UV–VIS spectrophotometer and baseline corrected. Steady-state emission spectra were recorded on a Jasco FP-8300 fluorescence spectrometer equipped with a 150 W xenon arc lamp, single-grating excitation, and emission monochromators. Emission and excitation spectra were corrected for source intensity (lamp and grating) and the emission spectral response (detector and grating) by standard correction curves. ECD, LD, FDCD, and FDLD spectra were recorded on a Jasco J-1500 CD spectrometer equipped with a Peltier-thermostated cell holder and an emission optical kit including a collecting lens and a filter holder. The spectrometer contains two PMT detectors: a standard detector and a dedicated FDCD detector, which allows the simultaneous measurement of ECD/LD and FDCD/FDLD signals. Appropriate long pass filters were used for the FDCD/FDLD measurements to avoid the scattered light from excitation wavelength, which could contaminate the observed emission, and to maximize the emitted light signal. The HT Voltage applied to the PMT of the ECD detector (standard detector) was kept in auto mode (fixed DC voltage and by automatically varying the HT Voltage), and the HT Voltage applied to the PMT of the FDCD detector was kept in manual mode (fixed HT Voltage and varying DC

voltage) and adjusted accordingly so that a fluorescence signal saturation is not reached in each set of measurements. The applied HT Voltage is reported for all experiments. The ECD/LD and FDCD/FDLD spectra reported were baseline corrected for the appropriate solvent system used. As the FDCD measurements were conducted in manual mode (varying DC voltage by fixing HT Voltage on PMT of FDCD detector), the instrument initially outputs the fluorescence intensity difference for the two circularly polarized excitations ($F_L - F_R = \Delta F$) which is then corrected for the total fluorescence ($F_L + F_R$ = DC voltage). The FDCD spectrum was hence obtained by dividing the baseline-corrected ΔF signal with the baseline-corrected DC voltage (= total fluorescence collected from the sample) for each measurement. The ΔF spectra were corrected for the signal artefacts, arising from the achiral host or dye molecule alone when the artefacts overlapped with the induced chiroptical bands for the host-guest complexes. Similarly, for the FDLD measurements conducted in manual mode (varying DC voltage by fixing HT Voltage on PMT of FDCD detector), the instrument initially outputs the fluorescence intensity difference for the two linearly polarized excitations ($F_{\parallel} - F_{\perp}$), which was then baseline corrected and divided by the baseline-corrected DC voltage (= total fluorescence collected from the sample) to obtain the FDLD spectrum. The LB spectra were measured on a JASCO J-1500 CD spectrometer at a JASCO facility in Pfungstadt by placing a Glan-Taylor polarizer behind the sample at 45° into the beam path. The fluorescence anisotropy spectra were recorded on a JASCO FP-8500 fluorescence spectrometer using FDP-837 automatic excitation and emission polarizers at the JASCO facility in Pfungstadt. All the spectral measurements were conducted at 25°C unless stated otherwise. For measurements conducted in water, deionized water was used in all cases. Blank measurements of water or buffer provided no induced ECD/LD and FDCD/FDLD effects in the regions examined. For spectroscopy analysis in quartz cuvettes, suprasil (type 111-QS) emission cuvettes with a light path of 10 mm and dimensions of 10x10 mm from Hellma-Analytics were utilized. Dynamic Light Scattering (DLS) experiments were carried out on a Malvern Zetasizer Nano ZS in disposable polystyrene cuvettes with a light path of 10 mm and dimensions of 10x10 mm at 25°C.

The DOSY NMR spectra was recorded on a Bruker Ascend TM 400 NMR spectrometer at 25°C.

3.4.3. Sample Preparation

The stock solutions were prepared in water and kept in the fridge at +8 °C for storage. The insulin stock solution was prepared in 10 mM phosphate buffer acidified with HCL to pH 2.7 and kept in the freezer at -20°C for storage. The phenyl-β-D-galactopyranoside and

β-galactosidase stock solutions were prepared in 10 mM phosphate buffer using phosphoric acid and basified with NaOH to pH 5 and kept in the freezer at −20ºC for storage. The concentration of the stock solutions of the dyes and the analytes were determined by UV- Vis absorption titration measurements unless stated otherwise. The molar extinction coefficient of the samples used to determine the concentration of their stock solutions by UV-Vis absorption titration is given in Table 3.4.

For compounds featuring unreported molar extinction coefficient, the stock solutions were prepared by weighing in the required amount of the pure sample to attain the desired concentration. The concentration of the stock solution of the host CB8 was determined by fluorescence titration against MPCP dye by exciting the sample at 368 nm and collecting the emission intensity at 531 nm. The concentration of the memantine stock solution was determined by a fluorescence-based indicator displacement assay using CB8⊃BC_2 as the chemosensor by exciting the sample at 445 nm and collecting the emission intensity at 520 nm.[152]

Table 3.4: Absorption maxima (λ_{max}) and molar extinction coefficients ($\varepsilon_{\lambda max}$) of the dyes and analytes used for the determination of the concentration of their stock solutions by UV-Vis absorption titration measurements.

Sample	λ_{max} (nm)	$\varepsilon_{\lambda max}$ ($M^{-1}cm^{-1}$)
(R_p)-MPCP	335	7,110[152]
(S_p)-MPCP	335	7,110[152]
(S_p)-MVCP	402	11,218
MDPP	413	26,000[201]
CB8•MDPP	443	55000[173]
MT	340	10830
D-Phe	257.6	195[248]
L-Phe	257.6	195[248]
L-Trp-NH_2	278	5,580[248]
L-Trp-OMe	278	5,580[248]
L-Phe-L-Ala	257.6	195[248]
L-Phe-Gly	257.6	195[248]
L-Phe-L-Val	257.6	195[248]
L-Ala-L-Phe	257.6	195[248]
insulin	276	6,020[311]
rhodamine 6G	529.8	116,000[248]

The MT receptor and the epoxides, (1*R*,2*R*)-1-phenylpropylene oxide and (1*S*,2*S*)-1-phenylpropylene oxide stock solutions were freshly prepared each time before the start of the measurements to avoid any aggregation of the receptor molecule and the hydrolysis of the epoxides, unless stated otherwise. For the ECD and FDCD measurements, the host and guest concentrations required to form the host-guest complex were chosen such that a sufficient degree of complexation of either the host or guest (preferably ≥ 50%) is achieved.

3.5. Additional Information

Synthesis of chiral dyes

- **Synthesis of (S_p)-MPCP and (R_p)-MPCP**

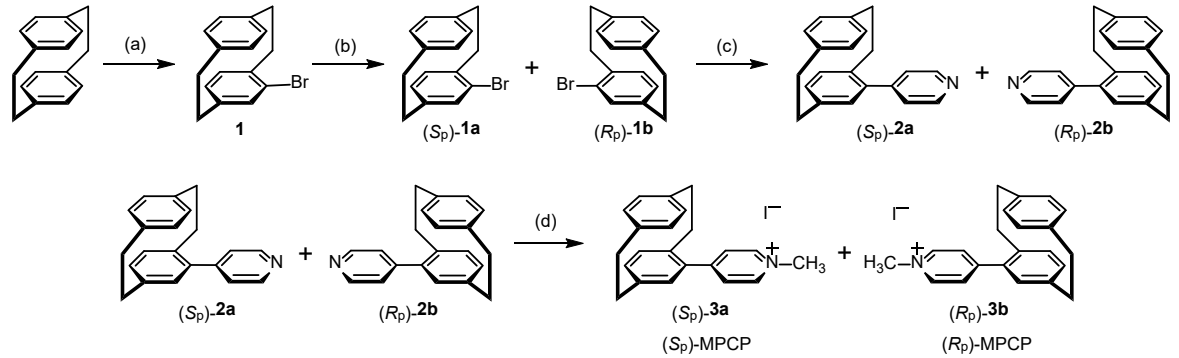

Scheme 3.1: Synthetic route of (S_p)-MPCP.and (R_p)-MPCP. (a) Br_2, Fe_{cat}, DCM, r.t., 3 days, 98%. (b) chiral HPLC. (c) 4-pyridylboronic acid, $Pd(PPh_3)_4$, K_3PO_4, dioxane/H_2O (2/1), 110°C, 24 h, 79%. (d) methyl iodide, DCM, r.t.,3 days, 55%. This synthesis was carried out by Dr. Eduard Spuling from the research group of Prof. Stefan Bräse.

- **Synthesis of (S_p)-MVCP**

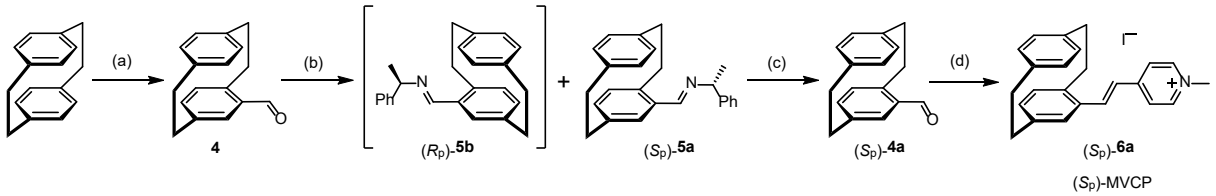

Scheme 3.2: Synthetic route of (S_p)-MVCP. (a) $TiCl_4$, dichloromethoxymethane, DCM, 0°C, 6 h, 94%. (b) *R*-(+)-phenylethylamine, toluene, 86°C, 5 h, 27%. (c) SiO_2, DCM, on-column hydrolysis, 98%. (d) piperidine, 1,4-dimethylpyridinium iodide, MeOH, 65°C, 2 h, 22%. This synthesis was carried out by Yichuan Wang from the research group of Prof. Stefan Bräse.

FDCD characteristics

- **User guide for FDCD measurements**

The FDCD measurement of any sample can be conducted by following the steps below:

1. The samples for FDCD measurements are prepared such that the absorbance value does not exceed 1 (to avoid signal saturation) and if possible, in a low viscosity solvent to avoid photoselection artefacts (see section below – Photoselection artefacts in FDCD).
2. FDCD spectra are inherently chiral excitation spectra. Hence, prior to the measurement, both the excitation and emission spectra of the sample are collected on a separate fluorescence spectrometer to choose the appropriate long-pass filter (LP-Filter) for the measurement. If the excitation and emission spectra do not overlap, the LP-Filter is chosen at the longer wavelength where the excitation spectra ends. However, in cases where the scatter of the excitation wavelengths overlapped with the emission range, it was of primary concern to adjust the LP-Filter to a longer wavelength to eliminate the scattered excitation light.
3. After selection of the LP-Filter, the HT Voltage on PMT of the FDCD detector (in manual mode) can be adjusted for the measurement at a value giving proper intensity of the fluorescence signal by simultaneously avoiding signal saturation (maximum DC $\leq$ 3 V). The HT Voltage on PMT of the ECD detector is kept in auto mode. If possible, all the measurements corresponding to one host-guest system (host-guest spectra, host alone, guest alone, baseline, etc.) should be conducted at this fixed HT Voltage. If it is impossible to select one common HT Voltage, *e.g.,* because of strong differences in emission intensity, the FDCD spectra obtained can be used for comparison instead of ΔF spectra, or the HT Voltage-corrected ΔF spectra explained in the section below can be applied.
4. The ΔF signal and the DC voltage (or total fluorescence) are then collected in two separate channels along with the ECD spectra for both the sample and the baseline solvent used.
5. The FDCD spectra are then obtained by subtracting the baseline from the sample signals to get baseline-corrected ΔF and DC spectra, and finally dividing the baseline-corrected ΔF signal by the DC voltage to get the FDCD result. The FDCD data was only obtained in cases where a measurable ΔF signal was present.

- **Comparison of Δ*F* signal collected at varying HT Voltage and bandwidth and correction function for HT Voltage-corrected Δ*F* signal**

The Δ*F* signals were optimized with respect to the HT Voltage applied to the photomultiplier tube (PMT) of the FDCD detector and bandwidth using ammonium d-10-camphorsulfonic acid (d-10-ACS) as a reference molecule (see Figure 3.23).

The results depicted in Figure 3.23 showed that it is preferable to fix the HT Voltage (if possible) and bandwidth in each measurement series and to compare only absolute Δ*F* signals for the same measurement parameters.

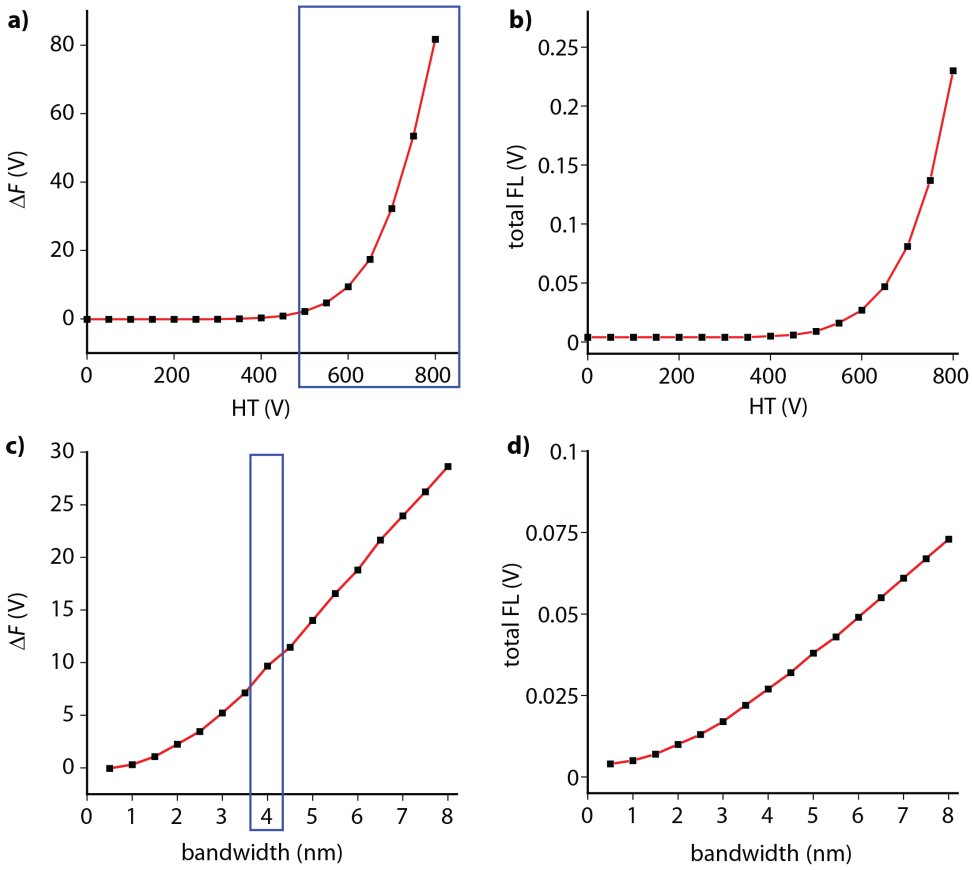

Figure 3.23: Variation of (a) Δ*F* and (b) total fluorescence (or DC voltage) with respect to HT Voltage (0-800 V) applied to the PMT of the FDCD detector in case of ammonium d-10-camphorsulfonic acid (d-10-ACS) as a reference molecule. The signal is monitored at 294 nm at a fixed bandwidth of 4 nm. Variation of (c) Δ*F* and (d) total fluorescence (or DC voltage) with respect to bandwidth (0.5–8 nm) in case of ammonium d-10-camphorsulfonic acid (d-10-ACS) as a reference molecule. The signal is monitored at 294 nm at a fixed HT Voltage of 600 V applied to the PMT of the FDCD detector.

When measuring an analyte concentration-dependent data or sensing studies where a change in concentration or fluorescence is monitored, the Δ*F* data needs to be used, as the FDCD value is concentration-independent and normalizes the value against the total fluorescence. However, when considering the Δ*F* signals, a direct comparison between two measurements is possible only when measured at the same HT Voltage, and the other measurement parameters like

bandwidth, accumulations, data pitch and D.I.T are kept constant. Herein, a function that correlates the ΔF signal and HT Voltage was developed to compare measurements taken at different HT Voltages. The ΔF signal and fluorescence intensity increase with HT Voltage and have a maximum at HT = 800 V (Figure 3.23a and 3.23b). However, when utilizing higher sample concentrations, it is not possible to measure the ΔF signal at HT = 800 V (or higher HT Voltages) due to fluorescence saturation. Hence for each sample measurement, the HT Voltage needs to be set to a value so that the fluorescence DC voltage does not exceed 4 V. In order to compare the ΔF signal obtained at different HT Voltages, a correction function was introduced, which correlates the HT Voltage and gives us the factor that needs to be multiplied to the measured ΔF signal to obtain the value of the HT Voltage-corrected ΔF signal ($\Delta F_{corr.}$) when measured at an HT Voltage of 800 V. The correction function approximated by an exponential decay function with time constant parameter (see Figure 3.24) and is given below,

$$y = A_1 \times e^{-x/t_1} + y_0 \qquad \text{Eq. 3.3}$$

where,

y = factor multiplied to the measured ΔF signal to obtain the value of the HT Voltage-corrected ΔF signal ($\Delta F_{corr.}$) at HT = 800 V, x = HT Voltage used for the measurement, t_1 = time constant = 63.49548, y_0 = offset = 1

Now,

$$\Delta F_{corr.} = y \times \text{measured } \Delta F \text{ signal} \qquad \text{Eq. 3.4}$$

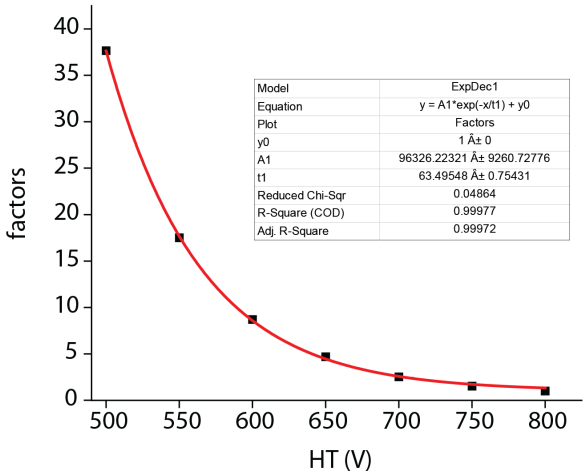

Figure 3.24: Plot of the correction function with respect to HT Voltage.

- **Conversion of ECD and FDCD ellipticity values to molar circular dichroism values**

The experimentally recorded ECD ellipticity values (θ in mDeg) can be converted to molar circular dichroism values ($\Delta\varepsilon$ in M^{-1} cm^{-1}) according to Eq. 3.5.

$$\Delta\varepsilon = \frac{\theta}{(32980 \times \mathrm{l} \times \mathrm{c})} \qquad \text{Eq. 3.5}$$

where c is the concentration of the sample in mol L^{-1} and l is the path length of the cell in cm.

The experimentally recorded FDCD values can be corrected for absorbance and converted to $\Delta\varepsilon$ by following Eq. 3.6.[196,197,199]

$$\Delta\varepsilon = \varepsilon_{\mathrm{L}} - \varepsilon_{\mathrm{R}} = \frac{2 \times \mathrm{S} \times (1 - 10^{-A})}{(\mathrm{c} \times \mathrm{l} \times 10^{-A} \times \ln 10)}; \quad S = k\left(\frac{F_{\mathrm{L}} - F_{\mathrm{R}}}{F_{\mathrm{L}} + F_{R}}\right) \qquad \text{Eq. 3.6}$$

where k is the instrument proportionality constant, F_{L} and F_{R} are the fluorescence with left and right circularly polarized excitation, A is the absorbance of the sample, c is the concentration of the sample in mol L^{-1} and l is the path length of the cell in cm.

As the k value is a conversion constant specific for each machine, it was initially determined at the standard ECD spectrometer with the FDCD setup at INT laboratory using 0.0024 M ammonium d-10-camphorsulfonic acid (d-10-ACS) as the reference. For a non-viscous solution of a single chiral and fluorophore molecule such as d-10-ACS, the molar circular dichroism calculated from both ECD and FDCD ellipticity values should arrive at the same spectra (see Figure 3.25). Taking this into account, the k value was determined to be 5.934 x 10^{-5}. Hence the Eq. 3.6 can be written as follows:

$$\Delta\varepsilon = \varepsilon_{\mathrm{L}} - \varepsilon_{\mathrm{R}} = \frac{(5.154 \times 10^{-5}) \times (1 - 10^{-A}) \times (F_{\mathrm{L}} - F_{\mathrm{R}})}{(\mathrm{c} \times \mathrm{l} \times 10^{-A}) \times (F_{\mathrm{L}} + F_{\mathrm{R}})} \qquad \text{Eq. 3.7}$$

The $\Delta\varepsilon$ values obtained from ECD and FDCD ellipticity values were termed as $\Delta\varepsilon_{\mathrm{ECD}}$ and $\Delta\varepsilon_{\mathrm{FDCD}}$, respectively. Figure 3.25d depicts the $\Delta\varepsilon_{\mathrm{ECD}}$ and $\Delta\varepsilon_{\mathrm{FDCD}}$ values obtained from the ECD and FDCD ellipticity values in the case of 0.0024 M d-10-ACS.

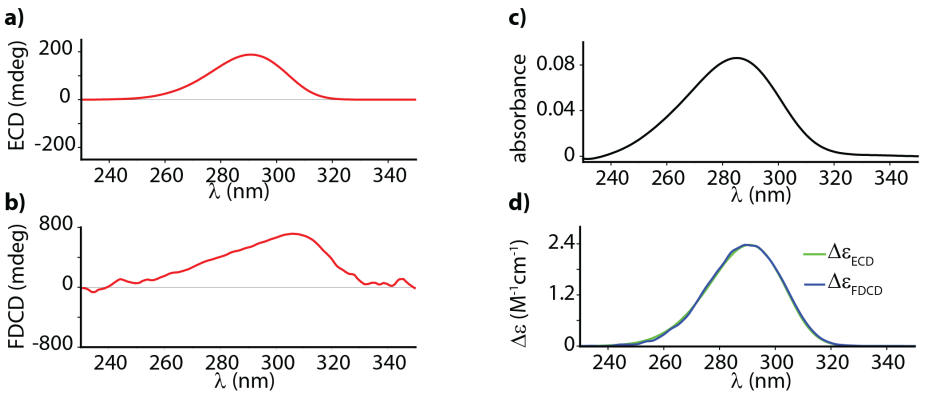

Figure 3.25: (a) ECD, (b) FDCD and (c) absorbance spectra of 0.0024M d-10-ACS in water. Parameters used: HT = 970 V, BW = 4 nm, Acc = 20, LP-Filter = 380 nm. (d) $\Delta\varepsilon_{\mathrm{ECD}}$ (green) and $\Delta\varepsilon_{\mathrm{FDCD}}$ (blue) spectra of 0.0024M d-10-ACS calculated from ECD and FDCD ellipticity values according to Eq. 3.5 and Eq. 3.7 respectively.

- **Photoselection artefacts in FDCD**

Care needs to be taken when performing FDCD measurements, especially when the system of interest exhibits a strongly polarized fluorescence, resulting in photoselection artefacts occurring from the anisotropic excitation of the emitted light.[299,300] When the rotatory Brownian motion is restricted within the fluorescence lifetime of the chromophore used (especially for larger molecules and in viscous solvents), the electronic dipole transition moments of the absorption and emission bands may not be parallel or perpendicular to each other. Hence, in the presence of photoselection, the observed fluorescence will be polarized, *i.e.*, the fluorescence intensities of the vertical and horizontal components $F_{\parallel}$ and $F_{\perp}$ differ, and the ratio $P_F = (F_{\parallel} - F_{\perp})/(F_{\parallel} + F_{\perp})$, known as fluorescence polarization, is non-vanishing. Thereby the observed differential emission upon excitation with a circularly polarized (CP) light source will not reflect the differential absorption of the CP light in a straightforward manner. From a practical viewpoint, however, the polarization of emitted light can also arise from unwanted artefacts in the FDCD instrument. This can introduce additional artefacts in FDCD due to the linear polarization present in the CP light produced by imperfect optical components in commercial ECD instruments. If the left-CP/right-CP excitation beams contain some residual linear polarization, a difference in the fluorescence signal will be detected not arising from the sample's optical activity.[199,271,312,313]

Photoselection artefacts can be eliminated by using an artefact-free FDCD unit (as shown before in Figure 3.14), which uses a unique design that includes a sandwiched elliptical cylinder mirror with two plane mirrors so that all fluorescence light emitted in a circumferential direction from the cell is collected.[306,314]The artefact-free FDCD unit not only eliminates artefacts due to fluorescence polarization, but also increases the signal-to-noise ratio (S/N) by collecting a large fraction of emitted radiation.[306,314] The artefacts can also be reduced by using a polarizer at 85° in the emission path, but this decreases the S/N as fewer photons are detected.[199]

To check for the presence of photoselection artefacts in FDCD measurements, it is advisable to measure the fluorescence-detected linear dichroism (FDLD) spectrum that can be obtained in addition to FDCD and ECD spectra (see Figure 3.13c). In the absence of signal artefacts, the FDLD spectrum should not give any signal. Furthermore, measurement of the excitation anisotropy of the system by using either the ECD or a fluorometer equipped with polarizers can give supplementary information about the sample's properties and check the influence of photoselection artefacts in FDCD measurements (see Figure 3.13d). Because photoselection is

independent of the chirality, it can in general, be also identified by using enantiomeric pairs of the host or guest.

- **Correction of signal artefacts in FDCD**

(i) In most of the representative supramolecular host-guest systems, the photoselection artefacts, if any, present for the achiral receptor molecules, arise mainly near the excitation peak maxima of the fluorophore and are often clearly distinct from the induced chiroptical peaks that are observed in the presence of the chiral analyte. Besides, they are independent of the chirality of the guest or host. Hence the photoselection artefacts do not pose any obstacle for FDCD sensing applications.

(ii) However, in cases where the signal artefacts arising from the achiral receptor molecule alone overlap with the induced chiroptical peaks that are observed in the presence of the chiral analyte (for *e.g.*, in the case of the Δ*F* signals from CB8•MDPP receptor), the signals were corrected by subtracting the signal artefacts arising from the receptor alone in all the cases. This is verified in case of the example below.

The racemization reaction between D-Phe and L-Phe in the presence of CB8•MDPP receptor was studied using both ECD and Δ*F*. An addition of a 1:1 equivalent of D-Phe and L-Phe to the CB8•MDPP receptor results in a racemic mixture and hence should exhibit no ECD and Δ*F* signals. However, the racemic mixture still showed the signal artefacts in the Δ*F* spectrum similar to the spectrum of the receptor alone (Figure 3.26b). Hence the corrected Δ*F* spectrum is obtained by subtracting the signal artefacts arising from the receptor alone (Figure 3.26c). Overall, photoselection artefacts do not strongly interfere with the FDCD signals when accounted for properly.

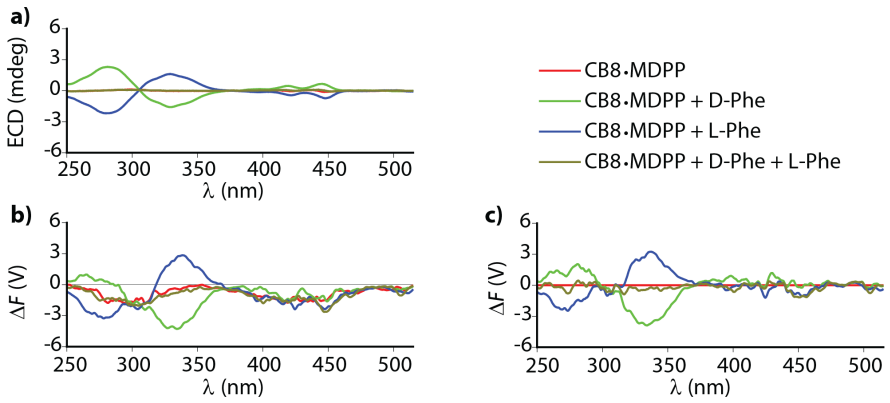

Figure 3.26: (a) ECD and (b) Δ*F* spectra (not corrected for the signal artefacts arising from the receptor alone) of CB8•MDPP (20 μM) in the presence of D-Phe (50 μM), L-Phe (50 μM) and a 1:1 mixture of D-Phe and L-Phe (50 μM) in water. The red line represents the Δ*F* signals arising from the CB8•MDPP (20 μM) alone. (c) The corrected Δ*F* spectra obtained after subtracting the signal artefacts arising from the receptor alone. Parameters used: HT = 520 V, BW = 4 nm, Acc = 20, LP-Filter = 515 nm.

Additional data

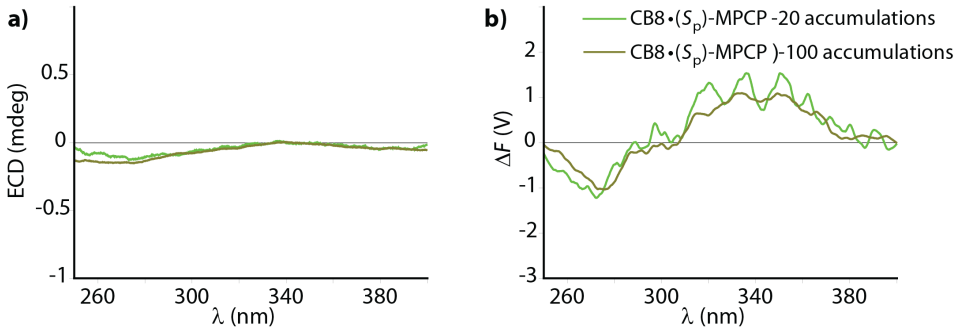

Figure 3.27: (c) ECD and (d) Δ*F* spectra of (*S*$_p$)-MPCP (100 nM) in the presence of CB8 (100 nM) in Water at 20 accumulations (green line) and at 100 accumulations (dark yellow line). Parameters used: HT = 800 V, BW = 4 nm, LP-Filter = 420 nm.

Table 3.5: Single-wavelength ECD and Δ*F* measurements of CB8•MDPP receptor in the presence of varying concentrations of L-Phe-Gly analyte. The parameters were kept constant for each individual set of measurements.

Sample[a]	Δ*F* (V)	HT[b] (V)	ΔF$_{corr}$[c] (V)	ECD (mdeg)
CB8•MDPP 20 µM + L-Phe-Gly 50 µM	6.79	520	188.31	3.17
CB8•MDPP 10 µM + L-Phe-Gly 25 µM	4.95	540	101.53	1.40
CB8•MDPP 2 µM + L-Phe-Gly 5 µM	3.35	620	21.89	0.38
CB8•MDPP 0.4 µM + L-Phe-Gly 1 µM	1.78	760	2.87	-0.05

[a] Measured at BW = 4 nm, λ_{obs} = 333 nm, Data Pitch = 30 s, D.I.T = 30 s, $t_{measure}$ = 10 min, LP-Filter = 515 nm; [b] HT Voltage applied to the PMT of the FDCD detector. Hence this is only influencing the Δ*F* value, not the ECD value (different detectors); [c] Corrected Δ*F* value at HT = 800 V

Table 3.6: Single-wavelength ECD and Δ*F* measurements of CB8•MDPP receptor in the presence of varying concentrations of L-Phe-L-Val analyte. The parameters were kept constant for each individual set of measurements.

Sample[a]	Δ*F* (V)	HT[b] (V)	ΔF$_{corr}$[c] (V)	ECD (mdeg)
CB8•MDPP 20 µM + L-Phe-L-Val 50 µM	5.22	520	144.77	2.62
CB8•MDPP 10 µM + L-Phe-L-Val 25 µM	4.01	540	82.25	1.20
CB8•MDPP 2 µM + L-Phe-L-Val 5 µM	2.22	620	14.51	0.21
CB8•MDPP 0.4 µM + L-Phe-L-Val 1 µM	1.25	760	2.01	0.02

[a] Measured at BW = 4 nm, λ_{obs} = 333 nm, Data Pitch = 30 s, D.I.T = 30 s, $t_{measure}$ = 10 min, LP-Filter = 515 nm; [b] HT Voltage applied to the PMT of the FDCD detector. Hence this is only influencing the Δ*F* value, not the ECD value (different detectors); [c] Corrected Δ*F* value at HT = 800 V

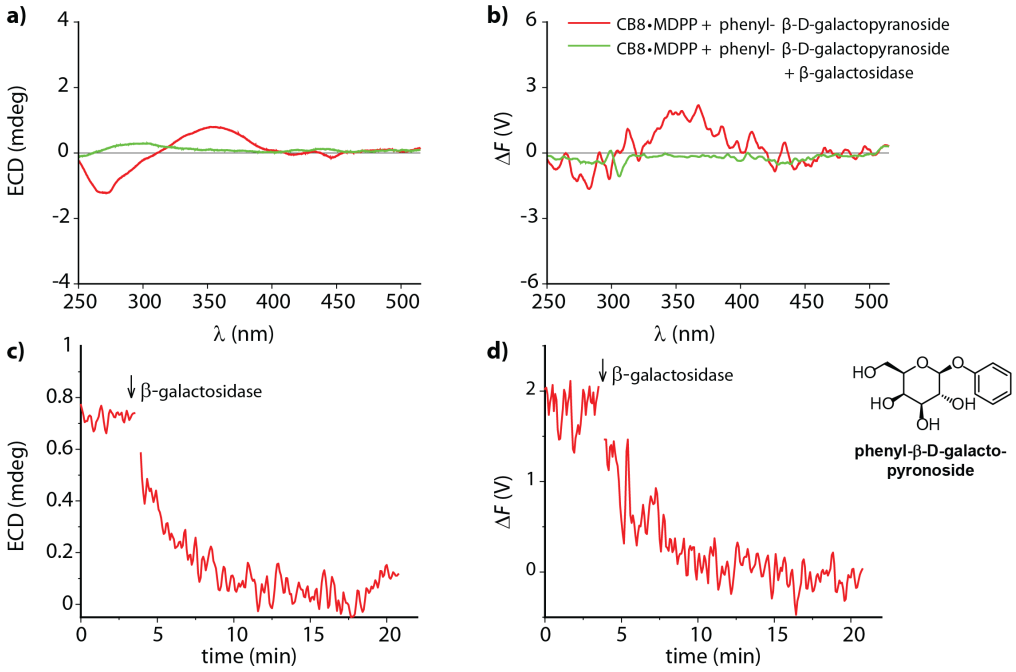

Figure 3.28: (a) ECD and (b) Δ*F* spectra of CB8•MDPP (10 µM) in the presence of phenyl-β-D-galactopyranoside (50 µM) (red line) in 10 mM phosphate buffer at pH 5 and the spectra after hydrolysis of phenyl-β-D-galactopyranoside by β-galactosidase (43 µg/ml) (green line). Single-wavelength time course (c) ECD and (d) Δ*F* measurements of CB8•MDPP (10 µM) in the presence of phenyl-β-D-galactopyranoside (50 µM) in 10 mM phosphate buffer at pH 5 upon addition of β-galactosidase (43 µg/ml). Parameters used: HT = 550V, BW = 4nm, Acc = 20, LP-Filter = 515 nm, λ_{obs} = 350 nm, Data Pitch = 5s, D.I.T = 8s, $t_{measure}$ = 21 min.

Chapter 4

4 Development of new fluorescence-based kinetic assays for detailed insights into host-guest binding dynamics and analyte identification and quantification

The results described in sections 4.2.1 and 4.2.2 of this chapter have been published as "Teaching indicators to unravel the kinetic features of host–guest inclusion complexes" in Chemical Communications, 2020.[201] The experimental design, investigation, and data analysis were carried out by me under the supervision of Dr. S. Sinn and Dr. F. Biedermann. The manuscript was organized and written under the guidance of Dr. F Biedermann. The co-authors contributed by providing materials for analysis (MPCP: from the group of Dr. S. Bräse, MDAP: Dr. L. Grimm), additional supporting data (CB7•AdOH, CB8•AdOG, and CB8•FeCp$_2$OH binding constants by ITC: Dr. L. Grimm) along with valuable discussions and reviewing the article draft. Sections in this chapter have been reproduced from the published work[201] with permission from the Royal Society of Chemistry.

4.1. Introduction

Supramolecular systems based on dynamic host-guest interactions are of significant interest in analytical chemistry, sensing, and drug delivery applications.[16,34,315,316] A detailed understanding of the molecular recognition event of host-guest binding is crucial to advance their practical applications, such as in sensing assays and stimuli-responsive/self-healing materials.[14,42,72,317-319] Both thermodynamic (*e.g.,* binding affinities) and kinetic (*e.g.,* complexation and decomplexation rates) parameters are needed for a proper analysis of the association and dissociation processes of host-guest interactions and to characterize the molecular recognition event.[14,42,72,317-319] However, to date, the binding affinity, K_a is often used as a first characterizer in the physico-chemical description of supramolecular host-guest complexes and is frequently employed to test and develop binding models and assess the sensitivity and selectivity requirements of analyte sensing assays.[161,320-326] Binding affinities of host-guest complexes have been obtained for a wide range of hosts and guests[55,72,327,328] by several different techniques, such as through absorbance or NMR titrations and calorimetric measurements (ITC) in representative direct binding assays,[113,161,329] or competitive-binding assays such as the indicator displacement assay (IDA)[72,113] and the lately by our group introduced guest displacement assay (GDA)[154] (see General Introduction - Section 1.2.2 for the assay descriptions).

In recent times, it has become clear that knowledge of kinetic parameters is also required to obtain a complete picture of supramolecular systems.[43,48,162,163] For instance, the kinetic rate constants of supramolecular complexes are critical parameters for understanding catalysis,[73]

stimuli-responsive materials,[319,330] protein-ligand binding mechanisms[331-334] and drug delivery systems.[335-338] In addition, the design of out-of-equilibrium systems also requires knowledge of both K_a values and rate constants.[339-341] However, to date, except for CEST-active[48] or slowly equilibrating systems that can be monitored by NMR (*e.g.*, DOSY, EXSY, inversion recovery),[162,342-347] kinetic rate constants of supramolecular systems are experimentally mostly only available for chromophoric or emissive systems.[43,163-166] These experiments are typically conducted as time-resolved direct host-guest binding titration assays, herein abbreviated as *kin*DBA (see Figure 4.1a). However, most water-compatible macrocyclic hosts or analytes (guests) of interest are spectroscopically silent, and their kinetic parameters cannot be accessed through a *kin*DBA. Subsequently, there is a strong mismatch between the number of reported binding affinities and kinetic parameters for any class of host-guest complexes. For instance, the macrocyclic cucurbit[*n*]urils (CB*n*) (see Figure 4.2a) are a promising class of water-soluble hosts that bind a wide range of guests, including amino acids, peptides, proteins, steroids, drugs, dyes, etc., with high binding affinities in aqueous media.[13,72,348,349] However, a survey for the cucurbit[*n*]uril macrocyclic hosts on the supramolecular repository "SupraBank.org" revealed that only 3% of all entries for CB*n*-guest complexes also included kinetic rate constants, in agreement with the much larger number of K_a values *versus* kinetic parameters tabulated in reviews. Hence, new methods for the determination of kinetic parameters of host-guest interactions are needed.

Furthermore, in view of developing practical sensing assays, a thermodynamic analysis of host-guest systems alone is often insufficient for achieving the desired selectivity requirements of the assay. As an example, several reports have exhibited the performance of CB*n*s and their chromophoric CB*n*•dye complexes for the detection of analytes, label-free reaction monitoring, and chirality sensing through absorbance, fluorescence, circular dichroism, and NMR measurements.[76,81,167,173,201] However, despite these advancements, it remains challenging to apply CB*n*-type chemosensors for selective sensing applications.[350,351] One major limiting factor of CB*n* – and many other macrocyclic hosts – for sensing applications is their promiscuous binding behavior and similar binding affinities for many bioorganic compounds, corresponding to a low thermodynamic selectivity (see Figure 4.12a in Section 4.2.3). For instance, while CB8 has been used for capturing and solubilizing steroids with nanomolar binding affinities, its immediate utility for sensing applications in complex biofluids appears very limited because atleast 20 different steroids are bound with somewhat similar binding affinities, mainly in the range of 10^6-10^8 M^{-1}.[75,352] Kinetic insights into the host-guest binding interactions can help gain additional mechanistic information for the selectivity assessment of

supramolecular sensing assays.[43,48,162,163] However, thermodynamic values are still emblematic of the field[113,154,161], and reports on kinetic insights to gain selectivity are still lacking in the literature.

In my investigations, I developed three novel competitive approaches through which the kinetic rate constants of host-guest complexes, can be accessed for spectroscopically silent hosts and guests. The chapter firstly focuses on the assay descriptions, followed by the determination of kinetic rate constants for several host-guest and protein-ligand complexes as representative examples. Furthermore, a new kinetic method is described for selective analyte sensing even in situations of poor thermodynamic binding selectivity to enable a selective identification and quantification of analytes without the need to synthetically modify the parent host.

4.2. Results and Discussion

4.2.1. Novel approaches for unraveling the kinetic features of supramolecular host-guest systems

Three novel competitive approaches were introduced here for acquiring the kinetic parameters of spectroscopically silent host-guest complexes through a fluorescence-based assay. A competitive binding network consists of a host (H), guest (G), and a competitor/indicator dye (D) (see Figure 4.1b-4.1c) and can be described both by thermodynamic (see General Introduction - Section 1.2.2)[154] and by kinetic equations (see Eq.4.6-Eq.4.14). The binding affinities of the host-dye (H•D) and host-guest (H•G) complex are denoted here as $K_a^{HD}$and K_a^{HG}, respectively. The complexation and decomplexation rate constants of the H•D and H•G complexes are symbolized by k_{in}^{HD} & k_{out}^{HD} and k_{in}^{HG} & k_{out}^{HG} respectively.

The first competitive method introduced here is the time-resolved guest displacement assay, *kin*GDA. In a *kin*GDA, an indicator dye solution is mixed with a spectroscopically silent pre-equilibrated host-guest solution, and the direct fluorescence signal change upon displacement of the guest from the host by the dye is monitored with time (see Figure 4.1b). The mathematical expression for the background-corrected observable signal intensity, I_t at time *t*, is given by Eq. 4.14, assuming that both the host and the guest are spectroscopically silent. The complexation (k_{in}^{HG}) and decomplexation (k_{out}^{HG}) rate constants of the host-guest complex can be obtained by fitting the experimentally obtained signal-time curve of the non-equilibrated competitive binding network following the equations, Eq. 4.6-Eq. 4.14 Note that the kinetic equations imply an "S_N1"-type, *i.e.*, purely dissociative mechanism for the decomplexation step of the H•G and H•D complexes. The detectable kinetic rates depend on the following factors: (i) the

concentrations of the host, guest, and indicator dye, (ii) the kinetic rate constants of the dye, k_{in}^{HD} and k_{out}^{HD}, which can be determined by a kinetic direct binding assay (*kin*DBA, see Eq. 4.1-Eq. 4.5), and (iii) the unknown kinetic rate constants k_{in}^{HG} and k_{out}^{HG} of the spectroscopically silent guest, which can be extracted from the time-resolved *kin*GDA curves through a mathematical fitting. The thermodynamic and kinetic parameters, *i.e.*, affinity and rate constants, are coupled to each other through $K_a^{HG} = k_{in}^{HG} / k_{out}^{HG}$ and the goodness of the fit improves when this is used as an input parameter. Hence, the K_a^{HG} values were determined prior to the measurement, *e.g.*, through competitive binding titrations such as GDA or IDA or direct binding assays (DBA) (see General Introduction - Section 1.2.2 for the thermodynamic assay descriptions).

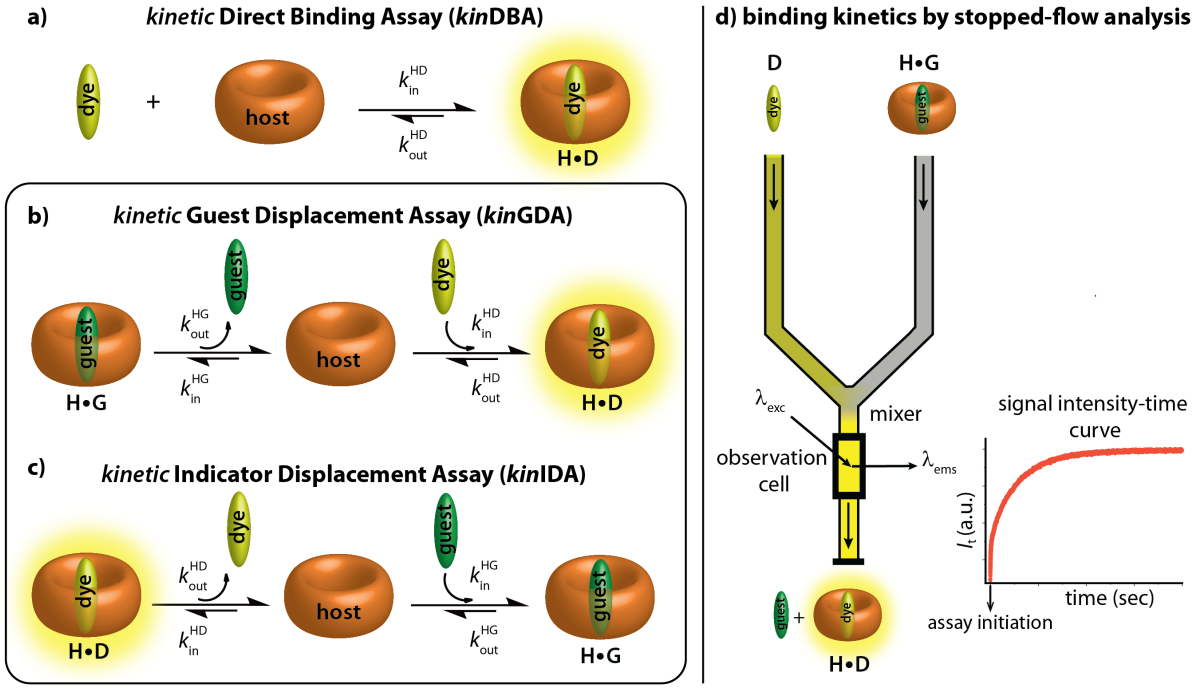

Figure 4.1: Working principles of supramolecular assays consisting of the host (H), guest(G), and indicator dye (D) for the determination of complexation (k_{in}^{HG}) and decomplexation (k_{out}^{HG}) rate constants of host-guest (H•G) complexes. k_{in}^{HD} and k_{out}^{HD} indicate the complexation and decomplexation rates of host-dye (H•D) complex (a) The known kinetic direct binding assay (*kin*DBA) that is limited to spectroscopically active host or guests. (b) and (c) Herein introduced competitive kinetic guest displacement assay (*kin*GDA) and kinetic indicator displacement assay (*kin*IDA) that are also applicable to spectroscopically silent guests. (d) A typical stopped-flow setup in combination with fluorescence measurements used to monitor the kinetic traces, represented here in case of a *kin*GDA.

	$\mathrm{H} + \mathrm{D} \underset{k_{\mathrm{out}}^{\mathrm{HD}}}{\overset{k_{\mathrm{in}}^{\mathrm{HD}}}{\rightleftarrows}} \mathrm{HD}$	Eq. 4.1
*kin*DBA	$\frac{\mathrm{d}[\mathrm{HD}]_t}{\mathrm{d}t} = k_{\mathrm{in}}^{\mathrm{HD}} \cdot [\mathrm{H}]_t[\mathrm{D}]_t - k_{\mathrm{out}}^{\mathrm{HD}} \cdot [\mathrm{HD}]_t$	Eq. 4.2
	$\frac{\mathrm{d}[\mathrm{D}]_t}{\mathrm{d}t} = -k_{\mathrm{in}}^{\mathrm{HD}} \cdot [\mathrm{H}]_t[\mathrm{D}]_t + k_{\mathrm{out}}^{\mathrm{HD}} \cdot [\mathrm{HD}]_t$	Eq. 4.3
	$\frac{\mathrm{d}[\mathrm{H}]_t}{\mathrm{d}t} = -k_{\mathrm{in}}^{\mathrm{HD}} \cdot [\mathrm{H}]_t[\mathrm{D}]_t + k_{\mathrm{out}}^{\mathrm{HD}} \cdot [\mathrm{HD}]_t$	Eq. 4.4
	$I_t = I^0 + I^{\mathrm{HD}} \cdot [\mathrm{HD}]_t + I^{\mathrm{D}} \cdot [\mathrm{D}]_t$	Eq. 4.5
	$\mathrm{HG} + \mathrm{D} \rightleftarrows \mathrm{HD} + \mathrm{G}$ (*kin*GDA) or $\mathrm{HD} + \mathrm{G} \rightleftarrows \mathrm{HG} + \mathrm{D}$ (*kin*IDA)	Eq. 4.6
	$\mathrm{H} + \mathrm{G} \underset{k_{\mathrm{out}}^{\mathrm{HG}}}{\overset{k_{\mathrm{in}}^{\mathrm{HG}}}{\rightleftarrows}} \mathrm{HG}$	Eq. 4.7
	$\mathrm{H} + \mathrm{D} \underset{k_{\mathrm{out}}^{\mathrm{HD}}}{\overset{k_{\mathrm{in}}^{\mathrm{HD}}}{\rightleftarrows}} \mathrm{HD}$	Eq. 4.8
*kin*GDA or *kin*IDA	$\frac{\mathrm{d}[\mathrm{HD}]_t}{\mathrm{d}t} = k_{\mathrm{in}}^{\mathrm{HD}} \cdot [\mathrm{H}]_t[\mathrm{D}]_t - k_{\mathrm{out}}^{\mathrm{HD}} \cdot [\mathrm{HD}]_t$	Eq. 4.9
	$\frac{\mathrm{d}[\mathrm{D}]_t}{\mathrm{d}t} = -k_{\mathrm{in}}^{\mathrm{HD}} \cdot [\mathrm{H}]_t[\mathrm{D}]_t + k_{\mathrm{out}}^{\mathrm{HD}} \cdot [\mathrm{HD}]_t$	Eq. 4.10
	$\frac{\mathrm{d}[\mathrm{HG}]_t}{\mathrm{d}t} = k_{\mathrm{in}}^{\mathrm{HG}} \cdot [\mathrm{H}]_t[\mathrm{G}]_t - k_{\mathrm{out}}^{\mathrm{HG}} \cdot [\mathrm{HG}]_t$	Eq. 4.11
	$\frac{\mathrm{d}[\mathrm{G}]_t}{\mathrm{d}t} = -k_{\mathrm{in}}^{\mathrm{HG}} \cdot [\mathrm{H}]_t[\mathrm{G}]_t + k_{\mathrm{out}}^{\mathrm{HG}} \cdot [\mathrm{HG}]_t$	Eq. 4.12
	$\frac{\mathrm{d}[\mathrm{H}]_t}{\mathrm{d}t} = -k_{\mathrm{in}}^{\mathrm{HD}} \cdot [\mathrm{H}]_t[\mathrm{D}]_t + k_{\mathrm{out}}^{\mathrm{HD}} \cdot [\mathrm{HD}]_t - k_{\mathrm{in}}^{\mathrm{HG}} \cdot [\mathrm{H}]_t[\mathrm{G}]_t + k_{\mathrm{out}}^{\mathrm{HG}} \cdot [\mathrm{HG}]_t$	Eq. 4.13
	$I_t = I^0 + I^{\mathrm{HD}} \cdot [\mathrm{HD}]_t + I^{\mathrm{D}} \cdot [\mathrm{D}]_t$	Eq. 4.14

Parameters for Eq. 4.1 to Eq. 4.14 were assigned as follows: $[\mathrm{H}]_t$ – host concentration at time *t*, $[\mathrm{D}]_t$ – dye concentration at time *t*, $[\mathrm{G}]_t$ – guest concentration at time *t*, $[\mathrm{HD}]_t$ – host-dye concentration at time *t*, $[\mathrm{HG}]_t$ – host•guest concentration at time *t*, $k_{\mathrm{in}}^{\mathrm{HD}}$ – rate constant for the association of the host-dye (HD) complex (complexation), $k_{\mathrm{out}}^{\mathrm{HD}}$ – rate constant for the dissociation of the host-dye (HD) complex (decomplexation), $k_{\mathrm{in}}^{\mathrm{HG}}$ – rate constant for the association of the host-guest (HG) complex (complexation), $k_{\mathrm{out}}^{\mathrm{HG}}$ – rate constant for the dissociation of the host-guest(HG) complex (decomplexation), I^0– background signal, I^{HD}– constant proportional to the fluorescence efficiency of host-dye (HD) complex at the monitoring wavelength, I^{D}– constant proportional to the fluorescence efficiency of free dye (D) at the monitoring wavelength, I_t – observable signal as a function of time.

The second competitive kinetic method introduced here is the pseudo-first order *kin*GDA (*kin*GDA^{PFO}), which has a close analogy to some literature reports.[344,353] In a *kin*GDA^{PFO}, the k_{out}^{HG} values can be obtained without explicit knowledge of the kinetic rate constants of the indicator dye. Firstly, the host-guest solution is pre-equilibrated, followed by the spiked addition of an excess of a high-affinity dye. The fluorescence signal change upon guest displacement from the host by the dye is monitored with time. The use of an excess of the indicator dye allowed for decoupling the guest and dye rate constants for (de)complexation through a pseudo-first order approximation (see Eq. 4.15 – Eq. 4.22). The recorded kinetic trace is then fitted by a simple exponential decay function (Eq. 4.22) to yield the kinetic decomplexation rate constant k_{out}^{HG} of interest. The k_{in}^{HG}value is then obtained from $k_{in}^{HG} = k_{out}^{HG} \times K_a^{HG}$. The knowledge of the exact concentrations of the involved partners is not needed in a *kin*GDA^{PFO}, thereby making them a more practical choice. However, it is essential to note that the applicability of *kin*GDA^{PFO} is restricted because the condition, $k_{in}^{HG}[G]_0 \ll k_{in}^{HD}[D]_0$ should be fulfilled. Ideally, in *kin*GDA^{PFO}, the recorded traces should overlay upon varying the dye concentration, excluding any concentration-induced changes in the binding mechanisms.

$$k_{in}^{HG}\,[G]_0 \ll k_{in}^{HD}\,[D]_0 \qquad \text{Eq. 4.15}$$

$$HG + D \xrightarrow{k_{out}^{HG}} H + G + D \xrightarrow{k_{in}^{HD}} HD + G \qquad \text{Eq. 4.16}$$

$$k_{out}^{HG} \ll k_{in}^{HD}[D]_0 \qquad \text{Eq. 4.17}$$

$$HG + D \xrightarrow{k_{out}^{HG}} HD + G \qquad \text{Eq. 4.18}$$

*kin*GDA^{PFO}

$$\frac{d[HD]_t}{dt} = -\frac{d[HG]_t}{dt} = k_{out}^{HG} \cdot [HG]_t \qquad \text{Eq. 4.19}$$

$$\frac{d[HG]_t}{[HG]_t} = -k_{out}^{HG} \cdot dt \qquad \int_{[HG]_0}^{[HG]_t} \frac{d[HG]_t}{[HG]_t} = \int_0^t -k_{out}^{HG} \cdot dt \qquad \text{Eq. 4.20}$$

$$\ln[HG]_t = \ln[HG]_0 - k_{out}^{HG} \cdot t \quad [HG]_t = [HG]_0\, e^{-k_{out}^{HG} \cdot t} \qquad \text{Eq. 4.21}$$

$$I_t = I^{eq.} + Ae^{-k_{out}^{HG} \cdot t} \qquad \text{Eq. 4.22}$$

Parameters for Eq. 4.15 to Eq. 4.22 were assigned as follows: $[D]_t$ – dye concentration at time *t*, $[D]_0$ – dye concentration at time 0 (initial dye concentration), $[G]_t$ – guest concentration at time *t*, $[G]_0$ – guest concentration at time 0 (initial guest concentration), $[HD]_t$ – host•dye concentration at time *t*, $[HG]_t$ – host•guest concentration at time *t*, $[HG]_0$ – host•guest concentration at time 0 (preequilibrated host•guest complex), k_{in}^{HD} – rate constant for the association of the host•dye (HD) complex (complexation), k_{out}^{HD} – rate constant for the dissociation of the host•dye (HD) complex (decomplexation), k_{in}^{HG} – rate constant for the association of the host•guest (HG) complex (complexation), k_{out}^{HG} – rate constant for the dissociation of the host•guest(HG) complex (decomplexation), $I^{eq.}$– signal offset (at equilibration of HD), *A*– amplitude, I_t – observable signal as a function of time.

Lastly, a third competitive method, the time-resolved indicator displacement assay (*kin*IDA), is introduced, which can be employed to obtain the kinetic rate constants of spectroscopically silent host-guest complexes. In *kin*IDA, a pre-equilibrated host-dye solution is mixed with the guest solution, and the direct fluorescence change upon displacement of the dye by the guest in the host cavity is monitored (see Figure 4.1c). The *kin*IDA method can be compared to the analogous *kin*GDA method (see below), and the complexation ($k_{\mathrm{in}}^{\mathrm{HG}}$) and decomplexation ($k_{\mathrm{out}}^{\mathrm{HG}}$) rate constants of the host-guest complex can be obtained by fitting the recorded kinetic trace following the equations, Eq. 4.6-Eq. 4.14.

The three introduced competitive approaches, *kin*GDA, *kin*GDA$^{\mathrm{PFO}}$, and *kin*IDA are in the following section employed to obtain the kinetic parameters of several host-guest pairs.

In general, a stopped-flow setup in combination with fluorescence measurements was used to monitor the kinetic traces. Stopped-flow is a powerful technique used to study reaction kinetics on a millisecond to minute timescale.[354,355] In a typical stopped-flow setup (see Figure 4.1d), the two syringes are loaded, for *e.g.*, in a *kin*GDA, with the indicator dye solution and the pre-equilibrated host-guest solution, respectively. On initiation of the measurement, both syringes are automatically and simultaneously engaged to release the same amount (150 µL) of each of the two different solutions, which then passes through the mixer into an observational cell with a quartz window. This results in a twofold dilution of the initial stock solutions and rapid mixing. After an initial period when the mixing is presumed to occur (typically 1–3 ms and often referred to as the "dead time"), the flow is stopped, and the fluorescence signal is recorded as a function of time (see Figure 4.1d). Once the signal-time response has been obtained, the data from the stopped-flow experiment is fitted to the appropriate kinetic assay shown in Figure 4.1 to obtain rate constants for the desired interaction.

4.2.2. Determination of kinetic parameters of several host-guest and protein-ligand complexes

The three introduced competitive approaches were employed to determine kinetic rate constants of spectroscopically silent or even insoluble guests with macrocyclic cucurbit[*n*]uril family and the protein human serum albumin (HSA) as representative hosts. Cucurbit[*n*]urils (CB6, CB7, and CB8) that bind a wide range of guests[72,75] were ideal hosts to evaluate the applicability of the developed methods. As indicator dyes, DSMI[128,356] was utilized in the case of CB6, BC[45] and MDAP[357] in the case of CB7, and MPCP[152] in the case of CB8. To check if the method can be extended to protein-ligand systems, the binding interaction of human serum albumin (HSA), a biologically important carrier protein[358,359], and anti- inflammatory drug phenylbutazone[359]

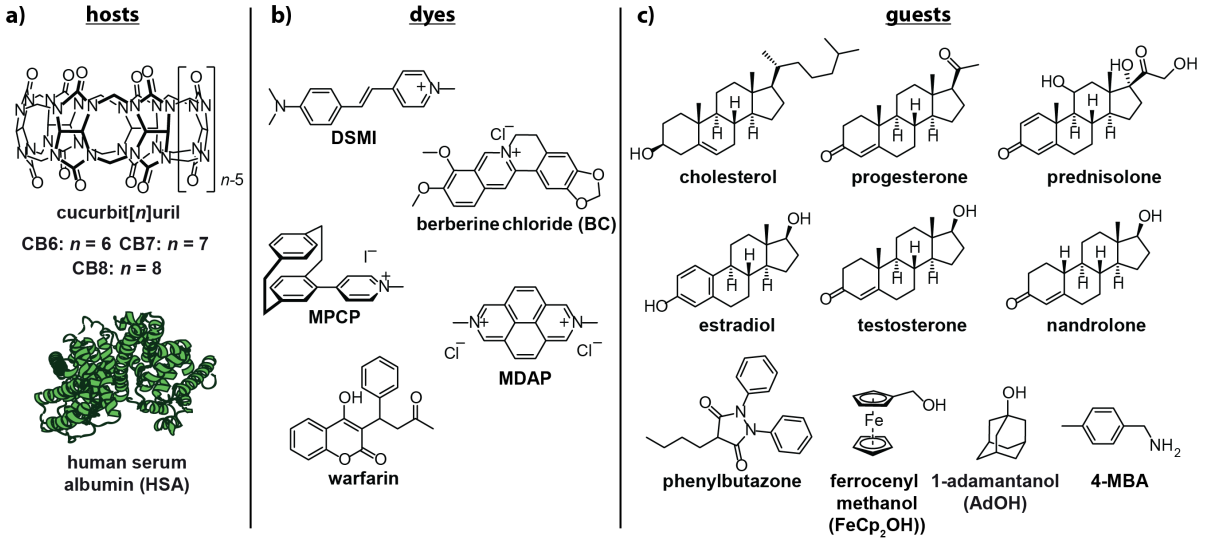

Figure 4.2: Chemical structures of (a) hosts, (b) fluorescent indicator dyes, and (c) guests utilized in this study.

was evaluated. Warfarin[359,360] that binds HSA was utilized as the indicator dye. The chemical structures of all the hosts, guests, and dyes used in this study can be found in Figure 4.2.

Prior to conducting the kinetic investigations of host-guest systems through the competitive approaches, the kinetic rate constants for the indicator dye and host binding interactions were obtained through a *kin*DBA approach (see Figure 4.3).

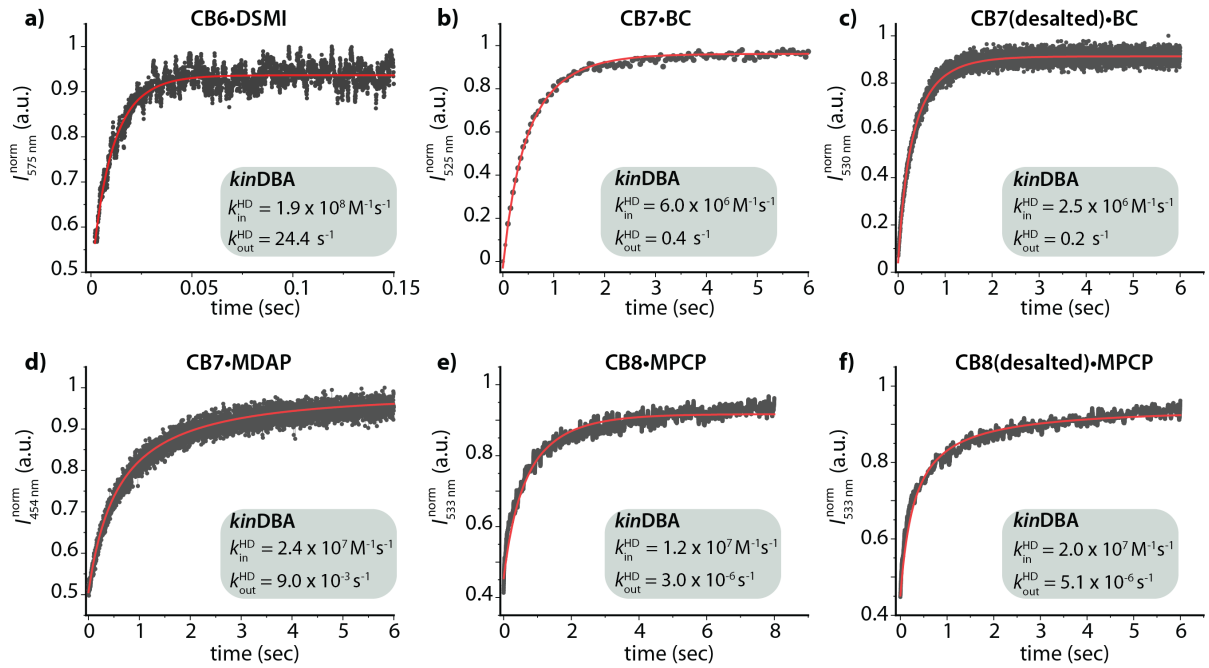

Figure 4.3: Representative *kin*DBA curve determined by fluorescence intensity variations of (a) DSMI (0.27 µM) and CB6 (0.28 µM) (λ_{exc} = 450 nm, λ_{ems} = 575 nm), (b) BC (0.2 µM) and CB7 (0.3 µM) (λ_{exc} = 465 nm, λ_{ems} = 525 nm), (c) BC (1.2 µM) and desalted CB7 (1.0 µM) (λ_{exc} = 430 nm, λ_{ems} = 530 nm), (d) MDAP (71 nM), and CB7 (72 nM) (λ_{exc} = 339 nm, λ_{ems} = 454 nm), (e) MPCP (0.2 µM) and CB8 (0.1 µM) (λ_{exc} = 366 nm, λ_{ems} = 533 nm) and (f) MPCP (0.2 µM) and desalted CB8 (0.21 µM) (λ_{exc} = 366 nm, λ_{ems} = 533 nm) in water at 25°C. Acquired data is depicted as gray dots and fitted data following the direct binding model (Eq.4.5) as red line.

The obtained k_{in}^{HD} and k_{out}^{HD} values are given in Table 4.1 and were utilized as input parameters for fitting the respective kinetic traces obtained *via* the competitive binding model for different host-guest systems. The binding affinity K_a^{HD}, were taken from the available literature data, orif not reported were obtained through thermodynamic DBA assays (see Figure 4.18 in Section 4.5 - Additional Information).

Table 4.1: Kinetic rate constants (k_{in}^{HD} and k_{out}^{HD}) for host-dye complexes determined by *kin*DBA in water.

dye	host	k_{in}^{HD} [a] / M^{-1} s^{-1}	k_{out}^{HD} [a] / s^{-1}	method	logK_a^{HD}
DSMI	CB6	$(1.9 \pm 0.8) \times 10^8$	24.4 ± 0.4	*kin*DBA	6.90[b]
BC	CB7	$(6.0 \pm 1.5) \times 10^6$	0.4 ± 0.1	*kin*DBA	7.23[c]
BC	CB7[d]	$(2.5 \pm 0.3) \times 10^6$	0.2 ± 0.03	*kin*DBA	7.03[e]
MDAP	CB7	$(2.4 \pm 0.5) \times 10^7$	$(9.0 \pm 1.8) \times 10^{-3}$	*kin*DBA	9.43[c]
MPCP	CB8	$(1.2 \pm 0.6) \times 10^7$	$(3.0 \pm 1.6) \times 10^{-6}$	*kin*DBA	12.59 [f]
MPCP	CB8[d]	$(2.0 \pm 1.0) \times 10^7$	$(5.1 \pm 1.6) \times 10^{-6}$	*kin*DBA	12.59 [f]

If not stated differently, all experiments have been conducted in deionized water at 25 °C. [a] mean and standard deviation in parenthesis of at least 3 independent measurements. Minor to no differences in dye binding kinetics have been found for non-desalted and desalted hosts. [b] See Figure 4.18a in Section 4.5 - Additional Information for binding isotherm. [c] ref.[154] [d] desalted CB7/CB8 was used. [e] See Figure 4.18b in Section 4.5 - Additional Information for binding isotherm. [f] ref.[152].

4.2.2.1. CB*n*•guest complexes

Based on the number of glycoluril units (*n*), CB6, CB7, and CB8 hosts have varying cavity diameter and portal sizes (see Figure 4.4).[13] In addition, the portal diameter is generally smaller than that of the cavity (see Figure 4.4), which means the portal is a kinetic barrier to guest ingression and egression.[13,361] The kinetics of CB*n*•guest complexes are hence, primarily expected to depend on the portal size of the host, the molecular size of the guest, and the preferred conformation adopted by the guest inside the CB*n* cavity.[162] For instance, the cavity of CB6 and its portals is too small to include large/bulky guest molecules.[162] CB6 complexes generally undergo a slow exchange of the guest. The tight portals of the host regulate access to the inner cavity and lead to constrictive binding.[162] This means the ingression of the guest into the cavity requires a substantial activation barrier, which is due to the required widening of the tight portals of the host for guest inclusion.[162] While, for the larger hosts, CB7 and CB8, the kinetic rate constants are expected to be much faster than CB6 complexes for similar guests, in analogy with the CB7 and CB8 portals being more flexible than CB6.[164,165,318,362-364] As a result, the thermodynamics of complexation may not be directly related to the kinetics in the intuitively expected manner. The thermodynamics reports on the stabilization inside the cavity, while the kinetics reports on steric interactions with the portals during ingression.[162]

a)

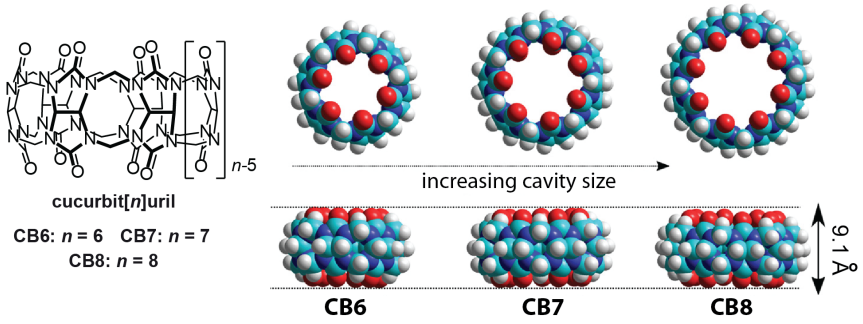

b)

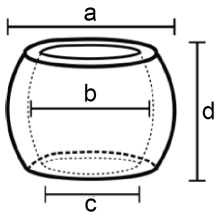

dimensions		CB6	CB7	CB8
outer diameter	a	14.4	16.0	17.5
cavity diameter (Å)	b	5.8	7.3	8.8
portal diameter (Å)	c	3.9	5.4	6.9
height (Å)	d	9.1	9.1	9.1
cavity volume (Å^3)	-	164	280	480

Figure 4.4: (a) Chemical structures and the 3D representation (space-filling model) of CB*n*. Reprinted with permission from ref.[13] Copyright 2015 Americal Chemical Society. (b) Structural parameters for the hosts CB6 , CB7, and CB8.[74] Reprinted with permission from ref.[13] Copyright 2015 Americal Chemical Society.

There are still many unanswered questions about the binding mechanisms of CB*n*•guest complexes. Different mechanisms can occur depending on the characteristics of the guest. In my investigations, I employed the newly introduced time-resolved competitive approaches to determine the kinetic parameters of several CB*n*•guest complexes. In addition, the available kinetic and thermodynamic data were correlated to get detailed insights into the host-guest binding event.

CB7 and CB8 are known to bind several structurally similar steroids with high binding affinities in water.[75] Thus, as a first example, the kinetic features of several steroids binding to both CB7 and CB8 are evaluated.

A *kin*GDA approach was used to obtain the kinetic rate constants of the steroidal drug nandrolone binding to host CB7 using BC as the indicator dye. Figure 4.5a shows the kinetic traces obtained when BC was mixed with a solution of spectroscopically silent CB7•nandrolone complex in water, resulting in a displacement of nandrolone from the CB7 cavity for the inclusion of the indicator dye. Comparable results were obtained when a *kin*IDA approach was utilized for the same system (see Figure 4.5b). In addition, a *kin*GDA^{PFO} method was utilized, where an excess of the indicator dye BC or MDAP was added to the solution of CB7•nandrolone complex in water, and the k_{out}^{HG} values obtained by fitting the kinetic traces to a simple exponential decay function (see Figure 4.6a and 4.6b). The *kin*GDA^{PFO} method was applicable for BC as the indicator dye, and the obtained kinetic parameters were in good agreement with the *kin*GDA approach (see Figure 4.6a and Figure 4.5a).

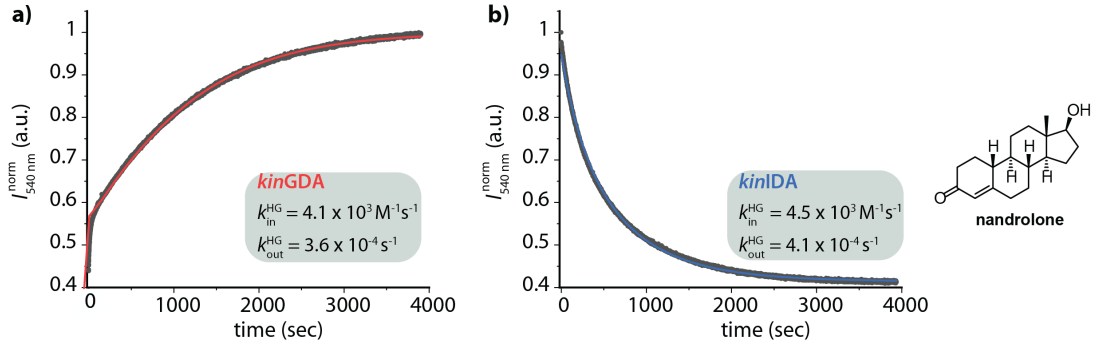

Figure 4.5: Representative (a) *kin*GDA and (b) *kin*IDA curve determined by fluorescence intensity variations (λ_{exc} = 462 nm, λ_{em} = 540 nm) of BC (2 µM), nandrolone (2 µM) and CB7 (2 µM) in water at 25 °C. Acquired data are depicted as gray dots and fitted data following the competitive binding model (Eq. 4.14) as red line in *kin*GDA and blue line in case of *kin*IDA.

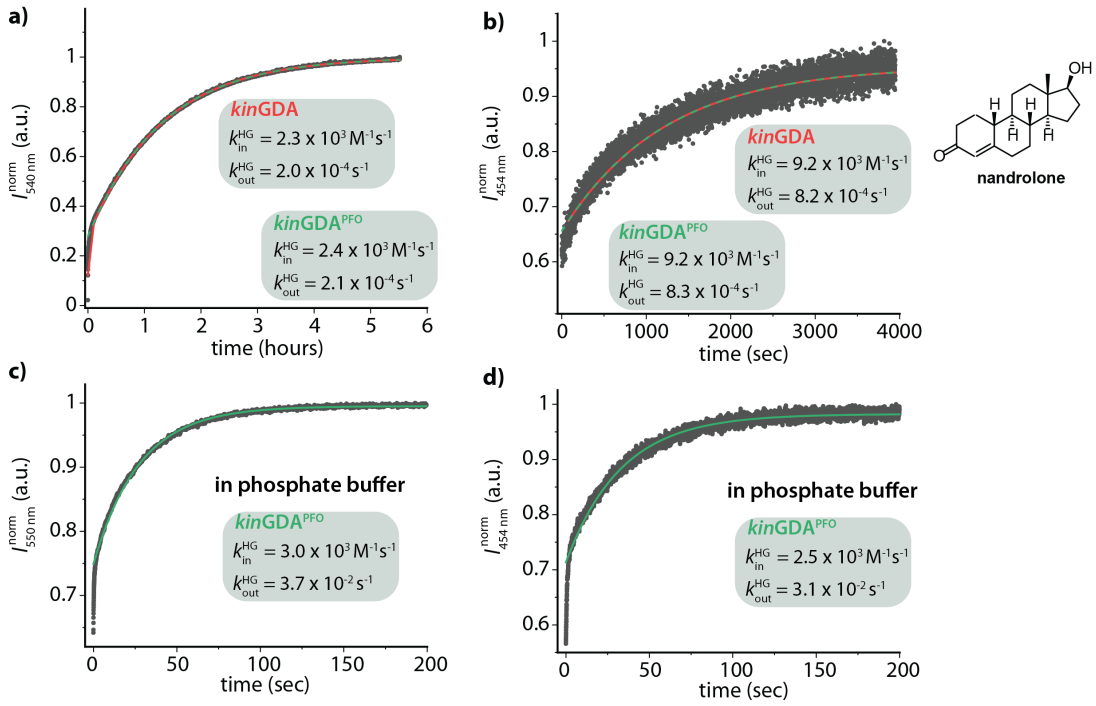

Figure 4.6: Representative *kin*GDA curve determined by fluorescence intensity variations of (a) BC (50 µM), nandrolone (2 µM), and CB7 (2 µM) (λ_{exc} = 462 nm, λ_{ems} = 540 nm) and (b) MDAP (40 µM), nandrolone (2 µM) and CB7 (2 µM) (λ_{exc} = 343 nm, λ_{ems} = 454 nm) in water at 25 °C. Representative *kin*GDA curve determined by fluorescence intensity variations of (c) BC (50 µM), nandrolone (2 µM) and CB7 (2 µM) (λ_{exc} = 462 nm, λ_{ems} = 550 nm) and (d) MDAP (25 µM), nandrolone (2 µM) and CB7 (2 µM) (λ_{exc} = 343 nm, λ_{ems} = 454 nm) in sodium phosphate buffer (50 mM) at 25 °C. Acquired data is depicted as gray dots and fitted data following the competitive binding model (Eq. 4.14) as red line and following the pseudo-first order model (Eq. 4.22) as green line.

However, the high dye concentrations for *kin*GDA^{PFO} can sometimes cause undesirable associative-binding contributions to H•G decomplexation mechanism. For example, upon using MDAP as the indicator dye, at higher concentrations, the dicationic dye may form a (transient) ternary complex with charge-neutral CB7•nandrolone in deionized water, causing an apparent increase in k_{out}^{HG} values (see Figure 4.6b). This scenario is plausible because the decomplexation rate of CB7•nandrolone was strongly increased in phosphate buffer (Figure 4.6c and 4.6d),

which implies the formation of ternary M^{n+}•CB7•nandrolone complexes. (see ref.[364-366] for the existence of M^{n+}•CB*n*•G complexes). Thus, ternary dye•CB7•guest complexes are likely not present in buffered or saline aqueous media, and the high dye concentration needed for the *kin*GDA^{PFO} method is of no concern (see Figure 4.6 and Table 4.2).

Similarly, kinetic parameters were obtained for several other steroids, such as cholesterol and estradiol binding to CB7 *via kin*GDA and *kin*GDA^{PFO} approaches using BC as the indicator dye (see Figure 4.7a and 4.7b). The kinetic rate constants obtained from both methods were in good agreement. Note that the *kin*GDA method is extendable for determining the decomplexation rates of insoluble guests such as estradiol[75] through precomplexation with the water-soluble host. The applicability of *kin*GDA to insoluble guests is an asset it shares with the thermodynamic GDA method.[154]

The kinetic parameters obtained for the CB7•steroid complexes studied reveal significant differences in their kinetic behavior. The ingression of nandrolone into the CB7 cavity shows the lowest complexation rate constants in water, followed by estradiol and cholesterol (Figure 4.6a and Figure 4.7). This could arise from the different binding geometries adopted by structurally similar steroids in the CB7 host cavity, which depends on their peculiar size or shape.[75] In addition, due to the smaller cavity and portal size of CB7 in comparison with larger homologs like CB8, the guest molecules are in a more constrained environment in CB7 complexes and hence result in a tight inclusion of the guest in the CB7 cavity.[75] As a result, significant changes in the kinetic parameters can arise even from small structural varaions in the steroid molecules. In addition, for the eggression of steroids from the CB7 cavity, cholesterol shows the fastest decomplexation rate constants, followed by estradiol and

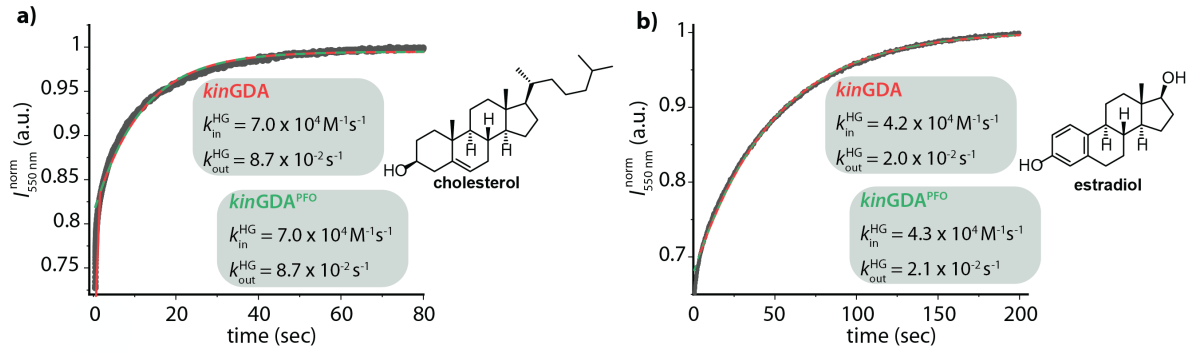

Figure 4.7: Representative *kin*GDA curve determined by fluorescence intensity variations (λ_{exc} = 462 nm, λ_{ems} = 550 nm) of (a) BC (50 µM), cholesterol (2.45 µM), and CB7 (2.22 µM) in water/ethanol (99.9/0.1, v/v) mixture and (b) BC (50 µM), estradiol (3.9 µM) and CB7 (3.9 µM) in water at 25 °C. Acquired data is depicted as gray dots and fitted data following the competitive binding model (Eq.4.14) as red line and following the pseudo-first order model (Eq. 4.22) as green line.

nandrolone, which is in accordance with the higher K_a^{HG} values of CB7 for nandrolone, followed by estradiol and cholesterol.[75,154]

The kinetic rate constants of several steroids, such as nandrolone, testosterone, and prednisolone binding to the host CB8, were investigated using both *kin*GDA and *kin*GDA^{PFO} approaches and MPCP as indicator dye. Figure 4.8 shows the *kin*GDA traces obtained when the ultra-high-affinity dye MPCP was mixed with a spectroscopically silent CB8•steroid complex solution in water. During the re-equilibration, the steroid guest leaves the CB8 cavity, making room for the inclusion of indicator dye MPCP, the stronger binding guest. Again, the kinetic rate constants obtained from both *kin*GDA and *kin*GDA^{PFO} approaches were in good agreement. For the CB8•steroid complexes, the complexation rate constants for the different steroids studied, *i.e.*, nandrolone, testosterone, and prednisolone, were nearly similar (Figure 4.8). This observation can be attributed to the larger cavity and portal size of CB8 than the CB7 host. Hence, the given guest will have more room in the CB8 cavity, and the ingression of the guest into the cavity is not limited by constrained interactions.[75] However, the decomplexation rates constants of the CB8•steroid complexes were significantly lower for CB8•testosterone, compared to CB8•nanrolone and CB8•prednisolone (Figure 4.8), which is in accordance with higher K_a^{HG} values of CB8 for testosterone, followed by nandrolone and prednisolone.[75]

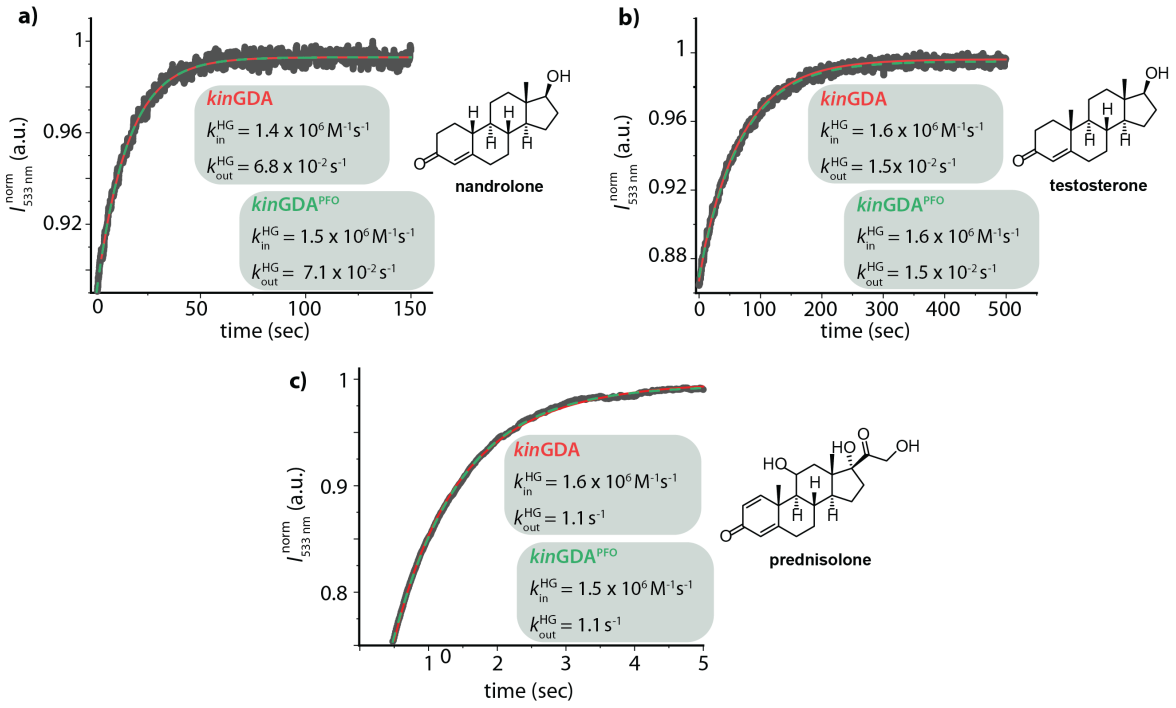

Figure 4.8: Representative *kin*GDA curve determined by fluorescence intensity variations (λ_{exc} = 366 nm, λ_{ems} = 533 nm) of (a) MPCP (50 µM), nandrolone (1 µM) and CB8 (1 µM), (b) MPCP (50 µM), testosterone (1 µM) and CB8 (1 µM), and (c) MPCP (50 µM), prednisolone (5 µM) and CB8 (5 µM) in water at 25 °C. Acquired data is depicted as gray dots and fitted data following the competitive binding model (Eq. 4.14) as red line and following the pseudo-first order model (Eq. 4.22) as green line.

The CB8•nandrolone complex shows a complexation rate constant, which is considerably larger than that found for its CB7 complex. This observation is again due to the smaller portal and cavity size of CB7 compared to CB8, which can affect the guest entry.

In addition to steroids as guests, the kinetic rate constants for a high-affinity guest, 1-adamantanol (AdOH) with CB7, were determined by the *kin*IDA model using BC as the indicator dye (Figure 4.9a). A *kin*IDA method is utilized in such situations when the guest studied has a much higher binding affinity for the host than the utilized indicator dyes. In addition, the kinetic parameters of 1-adamantanol (AdOH) with CB8 were also obtained *via* both *kin*GDA and *kin*GDA^{PFO} (Figure 4.9b). AdOH shows a very high binding affinity for CB7 compared to the CB8 complex.[367] CB7 allow a more tight inclusion of the adamantane guests inside their cavity.[367,368] However, the complexation rate constant is considerably lower for the CB7•AdOH complex than observed for its CB8 complex (Figure 4.9). The low k_{in}^{HG} value of CB7•AdOH compared to CB8•AdOH can be attributed to the smaller portal and cavity size of CB7 compared to CB8, which can act as a kinetic barrier to guest entry. In addition, the kinetic parameters reflect a very low decomplexation rate constant of the CB7•AdOH complex compared to the CB8 complex, which is in accordance with the high binding affinity of AdOH for CB7 compared to CB8 as well as the portal effects on guest eggression.

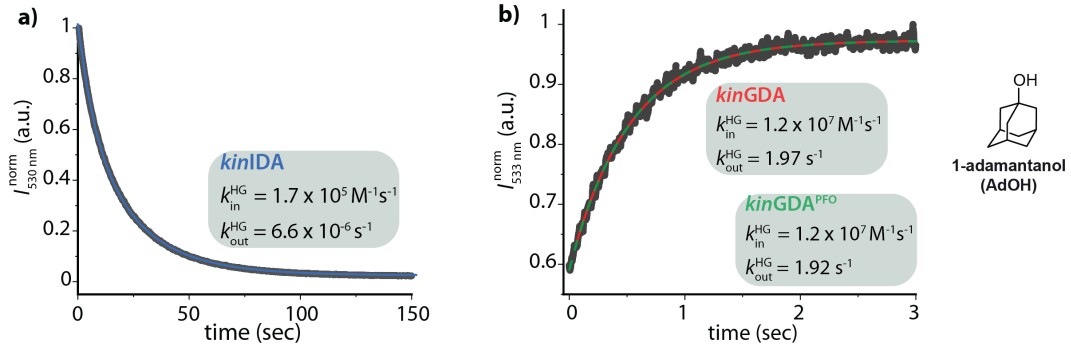

Figure 4.9: (a) Representative *kin*IDA binding curve determined by fluorescence intensity variations (λ_{exc} = 430 nm and λ_{ems} = 530 nm) of BC (1.2 µM), CB7 (1 µM), and adamantanol (5 µM) in water at 25 °C. Acquired data is depicted as gray dots and fitted data following the competitive binding model (Eq. 4.14) as blue line. (b)Representative *kin*GDA curve determined by fluorescence intensity variations (λ_{exc} = 366 nm, λ_{ems} = 533 nm) of MPCP (10 µM), adamantanol (1.43 µM), and desalted CB8 (1 µM) in water at 25 °C. Acquired data is depicted as gray dots and fitted data following the competitive binding model (Eq. 4.14) as red line and following the pseudo-first order model (Eq. 4.22) as green line.

4.2.2.2. Protein•ligand complexes

The binding interaction of the anti-inflammatory drug phenylbutazone[359] to human serum albumin (HSA)[358,359] was investigated as a representative example of host-protein systems. Before conducting the kinetic investigation of the protein-ligand interaction through the competitive approach, the kinetic rate constants for the indicator dye, warfarin[359,360] binding to

HSA in PBS, were obtained through the *kin*DBA method (Figure 4.10a). Figure 4.10b demonstrates the determination of kinetic rate constants for the binding of phenylbutazone to HSA by *kin*GDA in PBS.

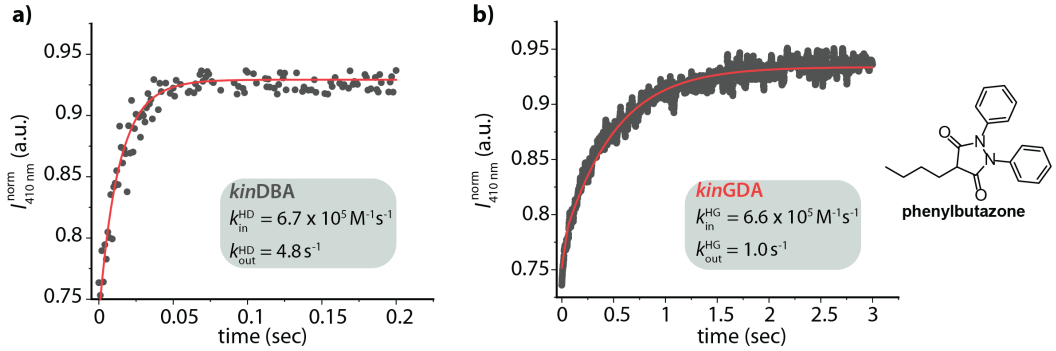

Figure 4.10: (a) Representative *kin*DBA curve determined by fluorescence intensity variations (λ_{exc} = 335 nm, λ_{ems} = 410 nm) of warfarin (100 µM) and HSA (20 µM) in PBS at 25 °C. Acquired data are depicted as gray dots and fitted data following the direct binding model (Eq. 4.5) as red line. (b) Representative *kin*GDA curve determined by fluorescence intensity variations (λ_{exc} = 335 nm, λ_{ems} = 410 nm) of warfarin (100 µM), PBZ (40 µM), and HSA (20 µM) in PBS at 25 °C. Acquired data are depicted as gray dots and fitted data following the competitive binding model (Eq. 4.14) as red line.

The new kinetic methods, *kin*GDA, *kin*GDA^{PFO}, and *kin*IDA, introduced in this investigation were applicable to all the host-guest, and protein-ligand pairs studied and allowed the convenient determinations of their kinetic rate constants. Table 4.2 shows the summarized data for all the systems studied. It needs to be noted that, in order to obtain meaningful rate constants through these methods, the host-guest and host-dye displacement step should follow a strictly dissociative and not an additional, occasionally observed[353] associative mechanism. To confirm the dissociative mechanism, several tests can be adopted. (i) *kin*GDA can be conducted at different dye concentrations and should provide similar k_{in}^{HG} and k_{out}^{HG} values. The *kin*GDA method can be compared to the analogous *kin*IDA method and should arrive at similar rate constants for the systems studied, see above.

In several cases, utilizing the competitive approaches for kinetic investigations can circumvent the need for a stopped-flow setup, as the equilibration times in a competitive assay are much longer than when using a *kin*DBA method. As a result, kinetic characterizations of several CB*n*•guest complexes can now also be performed in laboratories that do not have access to specialized stopped-flow equipment. For example, the kinetic rate constants of CB7•steroid and CB8•steroid complexes can be determined in a cuvette equipped with a magnetic stirrer on a standard fluorescence spectrometer. However, in the case of β-cyclodextrin complexes with high-affinity guests such as adamantanol, the competitive *kin*GDA and *kin*IDA experiments resulted in equilibration times that were even too fast (<100 ms at 25°C) for our stopped-flow setup. Thus, in the studied CB*n* complexes and the protein-ligand complex, the *kin*GDA,

*kin*GDA^{PFO}, and *kin*IDA investigations yielded reliable fits for guest egression rates $k_{out}^{HG} \leq 10\ s^{-1}$.

Table 4.2: Kinetic rate constants (k_{in}^{HG} and k_{out}^{HG}) for host-guest and protein-ligand complexes determined by *kin*GDA, *kin*IDA, and *kin*GDA^{PFO} in aqueous media.

guest[a]	**host**[a]	k_{in}^{HG} / $M^{-1}\ s^{-1}$	k_{out}^{HG} / s^{-1}	**method**[b]	$\log K_a^{HG}$
4-MBA	CB6[c]	$(3.3 \pm 0.03) \times 10^4$	$(6.5 \pm 0.05) \times 10^{-4}$	*kin*IDA[d]	7.7[e]
cholesterol	CB7[f]	$(7.0 \pm 0.1) \times 10^4$	$(8.7 \pm 0.1) \times 10^{-2}$	*kin*GDA[g]	5.9[h]
		$(7.0 \pm 0.1) \times 10^4$	$(8.7 \pm 0.1) \times 10^{-2}$	*kin*GDA^{PFO} [g]	
estradiol	CB7	$(4.2 \pm 0.1) \times 10^4$	$(2.0 \pm 0.1) \times 10^{-2}$	*kin*GDA[g]	6.3[h]
		$(4.3 \pm 0.1) \times 10^4$	$(2.1 \pm 0.1) \times 10^{-2}$	*kin*GDA^{PFO}[g]	
adamantanol	CB7[i]	$(1.7 \pm 0.1) \times 10^5$	$(6.6 \pm 0.4) \times 10^{-6}$	*kin*IDA[g]	10.4[k]
	CB8[i]	$(1.2 \pm 0.03) \times 10^7$	1.97 ± 0.06	*kin*GDA[j]	6.8[l]
		$(1.2 \pm 0.02) \times 10^7$	1.92 ± 0.02	*kin*GDA^{PFO}[j]	
nandrolone[m]	CB7[n]	$(4.1 \pm 0.4) \times 10^3$	$(3.6 \pm 0.2) \times 10^{-4}$	*kin*GDA[g]	7.1[o]
		$(4.5 \pm 0.3) \times 10^3$	$(4.1 \pm 0.2) \times 10^{-4}$	*kin*IDA[g]	
	CB7[p]	$(2.3 \pm 0.4) \times 10^3$	$(2.0 \pm 0.2) \times 10^{-4}$	*kin*GDA[g]	7.1[o]
		$(2.4 \pm 0.5) \times 10^3$	$(2.1 \pm 0.2) \times 10^{-4}$	*kin*GDA^{PFO}[g]	
	CB7[q]	$((9 \pm 0.2) \times 10^3)$	$((8 \pm 0.8) \times 10^{-4})$	*kin*GDA[s]	7.1[o]
		$((9\pm 0.2) \times 10^3)$	$((8 \pm 0.8) \times 10^{-4})$	*kin*GDA^{PFO}[s]	
	CB7[r]	$(3.0(\pm 0.2) \times 10^3$	$(3.7 \pm 0.1) \times 10^{-2}$	*kin*GDA^{PFO}[g]	5.2[t]
		$(2.5(\pm 0.1) \times 10^3$	$(3.1 \pm 0.1) \times 10^{-2}$	*kin*GDA^{PFO}[s]	
	CB8	$(1.4 \pm 0.1) \times 10^6$	$(6.8 \pm 0.4) \times 10^{-2}$	*kin*GDA[j]	7.3[o]
		$(1.5 \pm 0.1) \times 10^6$	$(7.1 \pm 0.2) \times 10^{-2}$	*kin*GDA^{PFO}[j]	
prednisolone	CB8	$(1.6 \pm 0.2) \times 10^6$	1.1 ± 0.1	*kin*GDA[j]	6.2[o]
		$(1.5 \pm 0.2) \times 10^6$	1.1 ± 0.1	*kin*GDA^{PFO}[j]	
testosterone	CB8	$(1.6 \pm 0.1) \times 10^6$	$(1.5 \pm 0.1) \times 10^{-2}$	*kin*GDA[j]	8.0[o]
		$(1.6 \pm 0.1) \times 10^6$	$(1.5 \pm 0.1) \times 10^{-2}$	*kin*GDA^{PFO}[j]	
ferrocenyl methanol	CB8[i]	$(2.1 \pm 0.1) \times 10^7$	5.8 ± 0.4	*kin*GDA[j]	6.6[l]
		$(2.0 \pm 0.2) \times 10^7$	5.7 ± 0.2	*kin*GDA^{PFO}[j]	6.6[l]
phenylbutazone	HSA[u]	$(6.6 \pm 0.6) \times 10^5$	1.0 ± 0.1	*kin*GDA[v]	5.8[h]

Errors (StDev) from triplicate measurements are ≤30% in k_{in}^{HG} and k_{out}^{HG} (also, taking into account estimated errors in k_{in}^{HD} and k_{out}^{HD} values used for fitting in the competitive binding model). If not stated otherwise, experiments were conducted in deionized water at 25 °C. Minor to no differences in guest binding kinetics have been found for non-desalted and desalted hosts. [a] See Figure 4.2 for chemical structures. [b] see Table 4.1 for indicator kinetics [c] in deionized water with 8.23 µM HCl. [d] DSMI as dye. [e] see Figure 4.19a in Section 4.5 - Additional Information for details. [f] H_2O/ethanol (99.9/0.1; v/v) mixture. [g] BC as dye. [h] see ref.[154] [i] desalted CB7/CB8. [j] MPCP as dye. [k] see Figure 4.19b in Section 4.5 - Additional Information for details. [l] determined by ITC (see Figure 4.20 in Section 4.5 - Additional Information for details). [m] CB7 (2 µM), nandrolone (2 µM). [n] dye (2 µM). [o] see ref.[75] [p] dye (50 µM). [q] dye (40 µM) likely associative mechanism also present, see text. [r] BC (50 µM) or MDAP (25 µM) in sodium phosphate buffer (50 mM). [s] MDAP as dye. [t] calculated using the formula presented in ref.[176]. [u] in phosphate buffered saline (PBS). [v] warfarin as dye. Determination of kinetic parameters of CB6•MBA and CB8•ferrocenyl methanol can be found in Section 4.5 - Additional Information (Figure 4.21).

The kinetic rate constants that were obtained through the use of the presented methods (Table 4.2) along with the reported literature data (see Table 4.5 in Section 4.5 - Additional Information) were converted to Gibb's activation energies by Eyring's equation (see Eq.1.7-Eq.1.8 in the General Introduction - Section 1.2.2). The calculated Gibb's activation energies for all the systems investigated can be found in See Table 4.5 in Section 4.5 - Additional Information. In addition, Gibb's free energies for the formation of the complex (ΔG_a) were calculated (see Eq. 1.3 in the General Introduction - Section 1.2.2) from the available thermodynamic binding affinities (see Table 4.5 in Section 4.5 - Additional Information for the data). A correlation plot was then obtained for Gibb's free energy (ΔG_a) of complex formation versus Gibb's energy of activation ($\Delta G^{\#}$) for complexation ($\Delta G^{\#}_{in}$) and decomplexation ($\Delta G^{\#}_{out}$) to get detailed insights into the host-guest binding event. The correlation plot displayed in Figure 4.11 shows a clear decoupling of the thermodynamic and kinetic features for the CB*n*-guest, and HSA-guest complexes investigated. A first assessment demonstrates that increased thermodynamic stability is not always correlated to increased kinetic inertness of the CB*n*-guest complexes. In addition, the correlation plot gives insights into how kinetics can be affected by the geometry of host-guest complexes in the case of CB*n* systems. It can be concluded that the smaller the portal size of the CB*n* host, the higher will be Gibb's energy of activation for complexation and decomplexation as the guest molecules will face a barrier from the smaller portal size to enter/exit the CBn cavity. A more detailed analysis of this correlation plot will be possible once more kinetic data is available, thereby motivating a future in-depth analysis of these host-guest inclusion complexes.

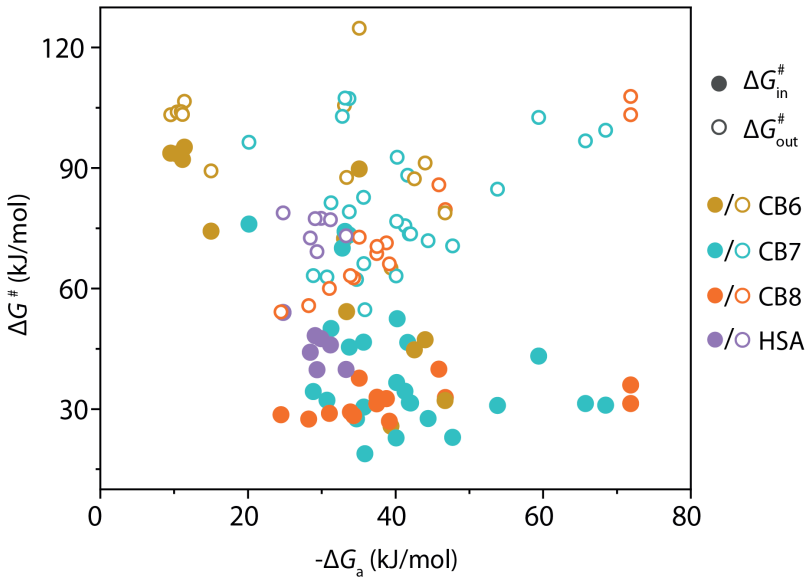

Figure 4.11: Correlation plot of Gibb's free energy (ΔG_a) of complex formation versus Gibb's energy of activation ($\Delta G^{\#}$) for complexation ($\Delta G^{\#}_{in}$) and decomplexation ($\Delta G^{\#}_{out}$). Values were calculated from acquired and literature data for CB*n* (CB6-CB8) and HSA guest complexes (see Table 4.5 in Section 4.5 - Additional Information).

4.2.3. Kinetic selectivity of molecular recognition for analyte identification and quantification

Analyte identification and quantification are essential for practical sensing applications. Several supramolecular hosts and receptor molecules, for *e.g.*, cucurbit[*n*]urils have been reported to bind a wide range of biologically relevant analytes with high binding affinities.[38,55,72,90] However, a lack of thermodynamic selectivity in the case of CB*n* and other macrocyclic hosts due to similar binding affinities for many bioorganic compounds (see Figure 4.12) have limited their immediate practical utility for selective sensing applications in complex media such as biofluids containing potential interferents.

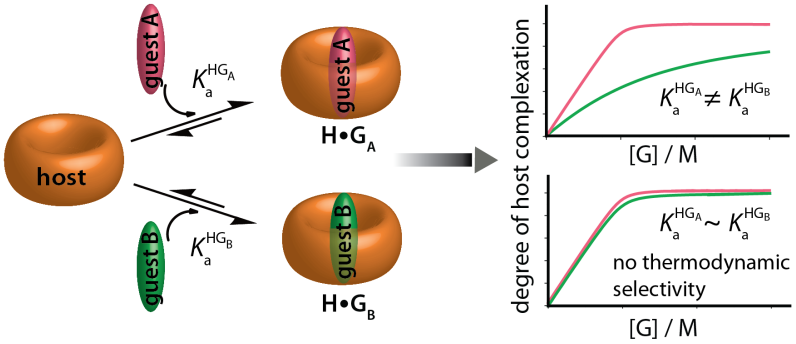

Figure 4.12: Schematic representation for the complexation of two guest molecules, guest A (G_A) and guest B (G_B), possessing binding affinities that are different ($K_a^{HG_A} \neq K_a^{HG_B}$) and similar ($K_a^{HG_A} \sim K_a^{HG_B}$) with the host molecule (H). The degree of complexation depicts a lack of thermodynamic selectivity for the latter case, preventing analyte identification and quantification.

In this section, the kinetic selectivity of supramolecular host-guest interactions is evaluated for selective analyte sensing, even in systems exhibiting poor thermodynamic selectivity. The newly developed competitive approaches described in the previous section were adopted for kinetic investigations and to achieve both analyte identification and quantification (see Figure 4.13a and 4.13b). Three representative structurally closely related steroids, testosterone, progesterone, and nandrolone, were chosen as the analytes of interest (see Figure 4.2c). The CB8 macrocyclic host (see Figure 4.2a) exhibits extraordinary binding affinities for these steroids but possesses very similar K_a^{HG} values indicating a lack a thermodynamic selectivity.[75]

The kinetic complexation (k_{in}^{HG}) and decomplexation (k_{out}^{HG}) rate constants of the three CB8•steroid complexes were explored through the time-resolved competitive approach. Figure 4.14b displays the kinetic trace recorded upon spiked addition of MPCP to a spectroscopically silent 1 µM CB8•steroid solution in water. A *kin*GDA^{PFO} analysis was utilized here, which facilitated a quick assessment of the k_{out}^{HG} values by fitting the kinetic traces recorded by a simple exponential decay function. The obtained k_{out}^{HG} and k_{in}^{HG} values are listed in Table 4.3.

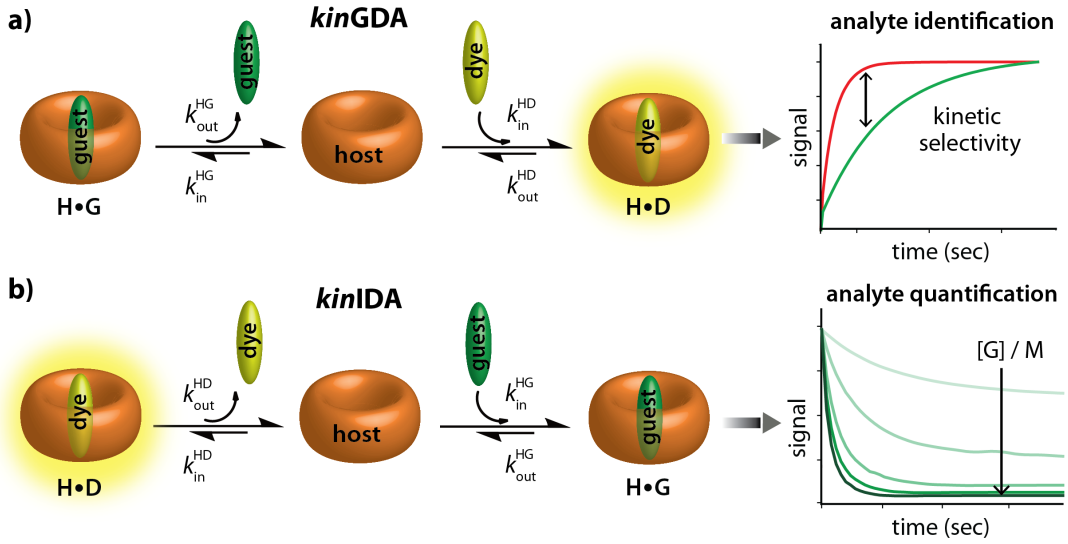

Figure 4.13: Working principle of earlier introduced supramolecular competitive (a) kinetic guest displacement assay (*kin*GDA) and (b) kinetic indicator displacement assay (*kin*IDA) consisting of a host (H), guest (G), and indicator dye (D) for the determination of kinetic rate constants (k_{in}^{HG} and k_{out}^{HG}) of H•G complexes. For a practical assay, a pseudo-first-order *kin*GDA (*kin*GDA^{PFO}) can be used for analyte identification in the first step, followed by a *kin*IDA for analyte quantification.

The kinetic and thermodynamic parameters as shown in Table 4.3 were used to obtain the simulated kinetic traces for CB8•steroid upon addition of MPCP according to the mathematical equations for a *kin*GDA binding model (Eq. 4.6 - Eq. 4.14) and is shown in Figure 4.14a. The simulated results are in good agreement with the experimental *kin*GDA^{PFO} traces obtained (see Figure 4.14 and Figure 4.22a in Section 4.5 - Additional Information for the overlaid experimental and simulated spectra after normalization). Thus, such simulations are a practical, informative tool and when combined with experimental data helps to differentiate several analytes in unknown samples and mixtures.

A significant kinetic selectivity (see Figure 4.14 and Table 4.3) was observed for CB8 binding to all three steroids, testosterone, progesterone, and nandrolone. For instance, CB8 exhibits a thermodynamic selectivity factor ($= K_a^{CB8•Testosterone}/K_a^{CB8•Progesterone}$) of 1.2 for testosterone over progesterone, while the kinetics traces recorded showed a three times higher selectivity with a kinetic selectivity factor ($= k_{out}^{CB8•Progesterone}/k_{out}^{CB8•Testosterone}$) of 3.4. Hence, this showcase depicts a situation where investigations into the binding kinetics aid in analyte differentiation even in the absence of thermodynamic selectivity.

The kinetic investigations were also carried out for a mixture of two steroids as guests to evaluate the practical applicability of the kinetic method for analyte differentiation in mixtures. Figure 4.15 displays the *kin*GDA^{PFO} traces recorded for a solution containing CB8 and an

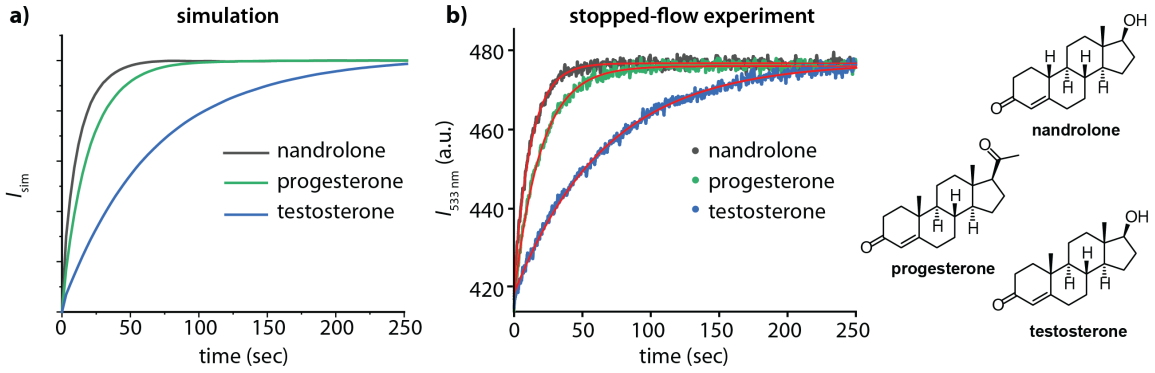

Figure 4.14: (a) Simulated *kin*GDA curve and (b) experimental *kin*GDA^{PFO} curve determined by fluorescence intensity variations (λ_{exc} = 376 nm, λ_{ems} = 533 nm) of CB8•testosterone (1 µM, blue line), CB8•progesterone (1 µM, green line) and CB8•nandrolone (1 µM, black line) host•guest complex upon spiked addition of MPCP dye (50 µM) in water at 25 °C. The red line depicts the fitted data following the *kin*GDA^{PFO} binding model (Eq.4.22). The k_{out}^{HG} and k_{in}^{HG} rate constants for the CB8•steroid binding interaction hence obtained is given in Table 4.3 and were used as input parameters in the *kin*GDA binding model (Eq. 4.14) to obtain the simulations.

Table 4.3: Experimental kinetic complexation (k_{in}^{HG}) and decomplexation (k_{out}^{HG}) rate constants for CB8•steroid complexes determined by *kin*GDA^{PFO} in water.

host•guest[a]	K_a^{HG}[b]/ M^{-1}	k_{in}^{HG}[c]/ M^{-1} s^{-1}	k_{out}^{HG}[c]/ s^{-1}
CB8•testosterone	1.1×10^8	$1.6(\pm 0.1) \times 10^6$	$1.5(\pm 0.1) \times 10^{-2}$
CB8•progesterone	9.3×10^7	$4.8(\pm 0.2) \times 10^6$	$5.1(\pm 0.2) \times 10^{-2}$
CB8•nandrolone	2.1×10^7	$1.7(\pm 0.1) \times 10^6$	$8.1(\pm 0.1) \times 10^{-2}$

If not stated differently, all experiments were conducted in deionized water at 25 °C. [a] See Figure 4.12b and Figure 4.13c-4.13d for chemical structures. CB8 and steroids are present at a concentration of 1 µM each. MPCP (50 µM) was used as the indicator dye. For the kinetic and thermodynamic parameters of the CB8•MPCP host-dye complex, see Table 4.1 [b] ref.[75] [c] Errors (StDev) from triplicate experiments are ≤20% (also taking into account estimated errors reported in K_a^{HG} values[75], which are used in calculating the k_{in}^{HG} values)

equimolar mixture of two steroids as guests, followed by a spiked addition of MPCP. The kinetics traces so acquired were initially compared to the *kin*GDA^{PFO} traces recorded for the individual steroids as guests, which gave an initial indication of the components of the mixture (Figure 4.15a and 4.15b). Additional information was gained by fitting the kinetic traces to a bi-exponential decay function (Eq. 4.23) to yield the decomplexation rate constants ($k_{out}^{HG_A}$) and($k_{out}^{HG_B}$) for the two guests with CB8 (see Figure 4.15c and 4.15d), which were then compared to the previously obtained kinetic parameters listed in Table 4.3. The simulated *kin*GDA curves can be obtained for assay containing a mixture of two guests following the mathematical equations Eq.4.24 to Eq.4.34. Figure 4.16 displays the simulated kinetic traces for CB8 with a mixture comprising varying concentrations of testosterone and progesterone as guests, followed by the addition of MPCP dye. The kinetic and thermodynamic parameters listed in Table 4.3 were used as input parameters for the simulations. Comparing the experimental *kin*GDA^{PFO} traces obtained in Figure 4.15a for the mixture to the simulated results enabled clearly

differentiating the components of the mixture along with calculating the concentration ratio of one steroid over the other in the mixture (see Figure 4.16).

$$I_t = I^{eq\cdot} + A_1 e^{-k_{\text{out}}^{\text{HG}_\text{A}} \cdot t} + A_2 e^{-k_{\text{out}}^{\text{HG}_\text{B}} \cdot t} \quad \text{Eq. 4.23}$$

Parameters for Eq. 4.23 were assigned as follows: $k_{\text{out}}^{\text{HG}_\text{A}}$ and $k_{\text{out}}^{\text{HG}_\text{B}}$ – rate constant for the dissociation of the host-guest-A (HG_A) and host-guest-B (HG_B) complex, respectively (decomplexation), $I^{eq\cdot}$– signal offset (at equilibration of HD), A– amplitude, I_t – observable signal as a function of time.

*kin*GDA (with two guests)

$$\mathrm{HG_A + D \rightleftarrows HD + G_A} \qquad \mathrm{HG_B + D \rightleftarrows HD + G_B} \quad \text{Eq. 4.24}$$

$$\mathrm{H + G_A \underset{k_{\text{out}}^{\text{HG}_\text{A}}}{\overset{k_{\text{in}}^{\text{HG}_\text{A}}}{\rightleftarrows}} HG_A} \qquad \mathrm{H + G_B \underset{k_{\text{out}}^{\text{HG}_\text{B}}}{\overset{k_{\text{in}}^{\text{HG}_\text{B}}}{\rightleftarrows}} HG_B} \quad \text{Eq. 4.25}$$

$$\mathrm{H + D \underset{k_{\text{out}}^{\text{HD}}}{\overset{k_{\text{in}}^{\text{HD}}}{\rightleftarrows}} HD} \quad \text{Eq. 4.26}$$

$$\frac{\mathrm{d[HD]}_t}{\mathrm{d}t} = k_{\text{in}}^{\text{HD}} \cdot [\mathrm{H}]_t[\mathrm{D}]_t - k_{\text{out}}^{\text{HD}} \cdot [\mathrm{HD}]_t \quad \text{Eq. 4.27}$$

$$\frac{\mathrm{d[D]}_t}{\mathrm{d}t} = -k_{\text{in}}^{\text{HD}} \cdot [\mathrm{H}]_t[\mathrm{D}]_t + k_{\text{out}}^{\text{HD}} \cdot [\mathrm{HD}]_t \quad \text{Eq. 4.28}$$

$$\frac{\mathrm{d[HG_A]}_t}{\mathrm{d}t} = k_{\text{in}}^{\text{HG}_\text{A}} \cdot [\mathrm{H}]_t[\mathrm{G_A}]_t - k_{\text{out}}^{\text{HG}_\text{A}} \cdot [\mathrm{HG_A}]_t \quad \text{Eq. 4.29}$$

$$\frac{\mathrm{d[G_A]}_t}{\mathrm{d}t} = -k_{\text{in}}^{\text{HG}_\text{A}} \cdot [\mathrm{H}]_t[\mathrm{G_A}]_t + k_{\text{out}}^{\text{HG}_\text{A}} \cdot [\mathrm{HG_A}]_t \quad \text{Eq. 4.30}$$

$$\frac{\mathrm{d[HG_B]}_t}{\mathrm{d}t} = k_{\text{in}}^{\text{HG}_\text{B}} \cdot [\mathrm{H}]_t[\mathrm{G_B}]_t - k_{\text{out}}^{\text{HG}_\text{B}} \cdot [\mathrm{HG_B}]_t \quad \text{Eq. 4.31}$$

$$\frac{\mathrm{d[G_B]}_t}{\mathrm{d}t} = -k_{\text{in}}^{\text{HG}_\text{B}} \cdot [\mathrm{H}]_t[\mathrm{G_B}]_t + k_{\text{out}}^{\text{HG}_\text{B}} \cdot [\mathrm{HG_B}]_t \quad \text{Eq. 4.32}$$

$$\frac{\mathrm{d[H]}_t}{\mathrm{d}t} = -k_{\text{in}}^{\text{HD}} \cdot [\mathrm{H}]_t[\mathrm{D}]_t + k_{\text{out}}^{\text{HD}} \cdot [\mathrm{HD}]_t - k_{\text{in}}^{\text{HG}_\text{A}} \cdot [\mathrm{H}]_t[\mathrm{G_A}]_t + k_{\text{out}}^{\text{HG}_\text{A}} \cdot [\mathrm{HG}_A]_t - k_{\text{in}}^{\text{HG}_\text{B}} \cdot [\mathrm{H}]_t[\mathrm{G}_B]_t + k_{\text{out}}^{\text{HG}_\text{B}} \cdot [\mathrm{HG}_B]_t \quad \text{Eq. 4.33}$$

$$I_t = I^0 + I^{\text{HD}} \cdot [\mathrm{HD}]_t + I^{\text{D}} \cdot [\mathrm{D}]_t \quad \text{Eq. 4.34}$$

Parameters for Eq. 4.24 to Eq. 4.34 were assigned as follows: $[\mathrm{H}]_t$ – host concentration at time t, $[\mathrm{D}]_t$ – dye concentration at time t, $[\mathrm{G_A}]_t$ – concentration of guest-A at time t, $[\mathrm{G_A}]_t$ – concentration of guest-A at time t, $[\mathrm{G_B}]_t$ – concentration of guest-B at time t, $[\mathrm{HD}]_t$ – host-dye concentration at time t, $[\mathrm{HG_A}]_t$ – host-guest-A concentration at time t, $[\mathrm{HG_B}]_t$ – host-guest B concentration at time t $k_{\text{in}}^{\text{HD}}$ – rate constant for the association of the host-dye (HD) complex (complexation), $k_{\text{out}}^{\text{HD}}$ – rate constant for the dissociation of the host-dye (HD) complex (decomplexation), $k_{\text{in}}^{\text{HG}_\text{A}}$ – rate constant for the association of the host-guest-A (HG_A) complex (complexation), $k_{\text{in}}^{\text{HG}_\text{B}}$ – rate constant for the association of the host-guest-B (HG_B) complex (complexation), $k_{\text{out}}^{\text{HG}_\text{A}}$ – rate constant for the dissociation of the host-guest-A (HG_A) complex (decomplexation), $k_{\text{out}}^{\text{HG}_\text{B}}$ – rate constant for the dissociation of the host-guest-B (HG_B) complex (decomplexation), I^0– background signal, I^{HD}– constant proportional to the fluorescence efficiency of host-dye (HD) complex at the monitoring wavelength, I^{D}– constant proportional to the fluorescence efficiency of free dye (D) at the monitoring wavelength, I_t – observable signal as a function of time.

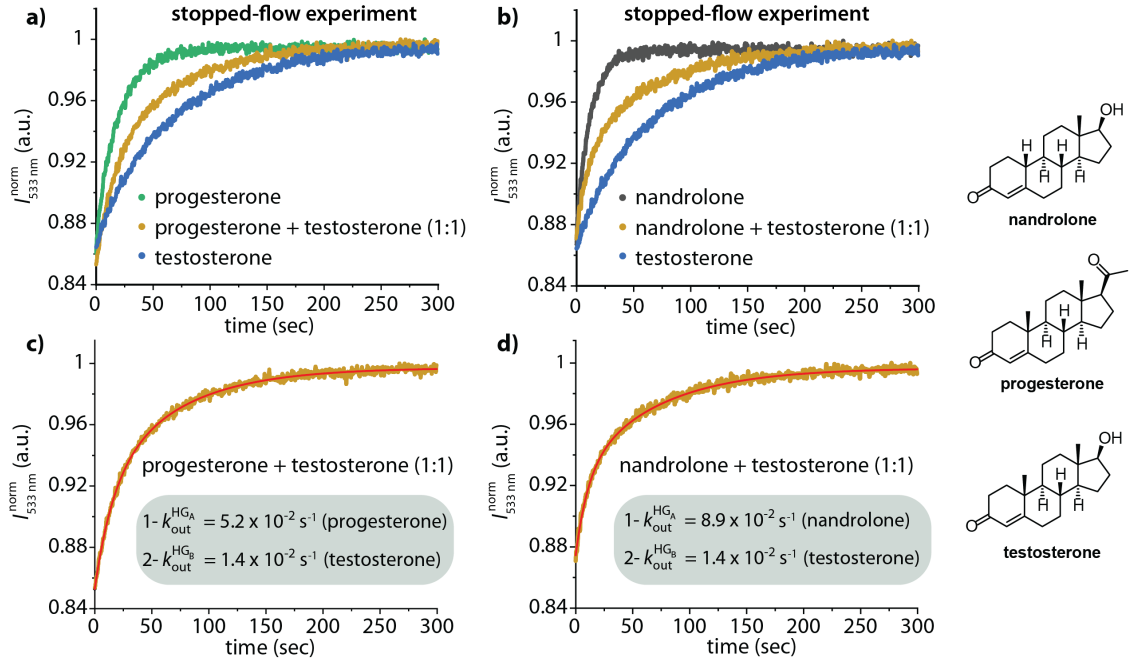

Figure 4.15: Experimental *kin*GDA^{PFO} curve determined by fluorescence intensity variations (λ_{exc} = 376 nm, λ_{ems} = 533 nm) for a mixture of two steroids as guests (yellow line) in case of (a) CB8 (1 µM), testosterone (0.5 µM) and progesterone (0.5 µM) and (b) CB8 (1 µM), testosterone (0.5 µM) and nandrolone (0.5 µM) upon spiked addition of MPCP (50 µM) in water at 25 °C. The *kin*GDA^{PFO} traces recorded for the individual steroids as guests as shown in Figure 4.14b is given for a visual comparison in (a) and (b). The red solid line in graphs (c) and (d) depicts the fitted data following a bi-exponential decay function (Eq. 4.23) for the recorded *kin*GDA^{PFO} traces containing a mixture of two steroids as guests. The $k_{out}^{HG_A}$ and $k_{out}^{HG_B}$ kinetic parameters for the two guests with CB8 as obtained from the fitted data are depicted for each case in their respective graphs.

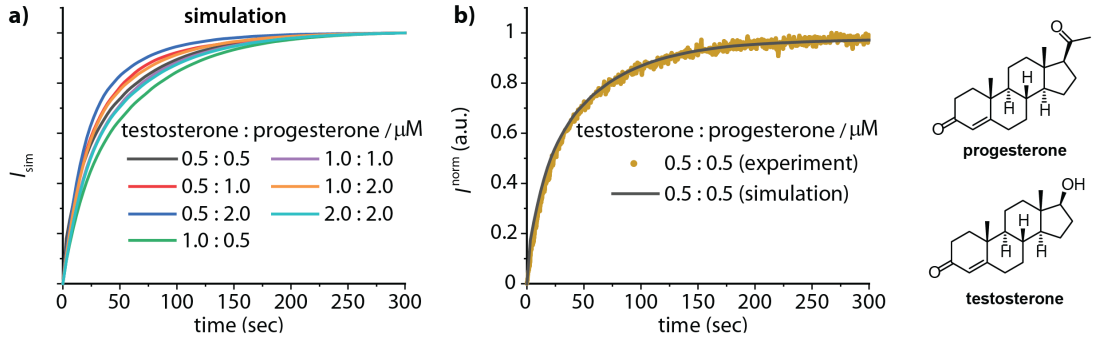

Figure 4.16: (a) Simulated *kin*GDA binding curve for a mixture of two steroids as guests in case of CB8 (1 µM) with varying concentrations of testosterone and progesterone upon spiked addition of MPCP dye (50 µM) in water. The kinetic and thermodynamic parameters listed in Table 4.3 were used as input parameters in the *kin*GDA binding model with two guests (Eq. 4.34) to obtain the simulations. (b) Comparison of the experimental *kin*GDA^{PFO} traces as obtained in Figure 4.15a for CB8 (1 µM), testosterone (0.5 µM), and progesterone (0.5 µM) upon spiked addition of MPCP (50 µM) (yellow line) to the simulated data (black solid line) at the respective concentrations show a good agreement between both results. The data were normalized to [0, 1] for the comparisons and to obtain the overlaid simulated and experimental spectra.

Accordingly, I successfully gained selectivity for analyte differentiation through insights into the kinetics of host-guest interactions. However, in a practical assay, the main target is the analyte identification and quantification once an unknown sample with an unknown concentration is provided. Ideally, in a *kin*GDA^{PFO} method, the kinetic traces should be

independent of the guest concentration (Figure 4.13a). Thereby, the recorded traces should overlay regardless of the guest concentration in the sample, excluding any concentration-induced changes in the binding mechanisms. This is advantageous for analyte identification in a sample with an unknown guest concentration. Figure 4.17a represents the simulated kinetic traces according to the *kin*GDA binding model (Eq. 4.14) for CB8 at different concentrations of nandrolone as guest, followed by spiked addition of MPCP dye. The kinetic and thermodynamic parameters listed in Table 4.3 were used as input parameters for the simulations. Under *kin*GDA^{PFO} conditions, the simulated curves showed the analyte concentration independence on the kinetic traces recorded with time. The assay was also conducted experimentally upon varying the nandrolone concentration in the sample (Figure 4.17b). The experimental results are in good match with the simulations, thereby providing a reliable method for analyte identification. This approach was also evaluated when we had a mixture of two steroids as guests. Here as well, the simulated kinetic traces were independent of the steroid concentration in the mixture, and the recorded traces overlaid at a given concentration ratio of one steroid over the other in the mixture (see Figure 4.16a for the simulated results). However, a multicomponent mixture analysis will require more complex calculations and has not been attempted in the course of this study.

Once the analyte in the sample has been identified, the next approach is a quantification step where the concentration of the analyte in the media needs to be evaluated. A competitive *kin*IDA (Figure 4.13b) approach was utilized here to achieve this. To carry out a *kin*IDA analysis for nandrolone as the guest molecule of interest, CB7 was used as the host with BC as the indicator dye.

Figure 4.17d displays the kinetic traces recorded upon the addition of the CB7•BC reporter pair to solutions containing varying concentrations of nandrolone. Significant changes in the recorded kinetic traces were observed upon increasing the nandrolone concentration. The kinetic traces were fitted according to *kin*IDA binding model (Eq. 4.14) and the kinetic parameters obtained are listed in Table 4.4. The parameters listed in Table 4.4 were utilized to obtain the simulated kinetic traces (see Figure 4.17c) according to mathematical equations for a *kin*IDA model (Eq. 4.6 - Eq. 4.14). The experimental results were in good agreement with the simulated data (see Figure 4.17c and 4.17d and Figure 4.22b in Section 4.5 - Additional Information for the overlaid experimental and simulated spectra after normalization) and is therefore a useful, informative tool to quantify the amount of analytes in unknown samples.

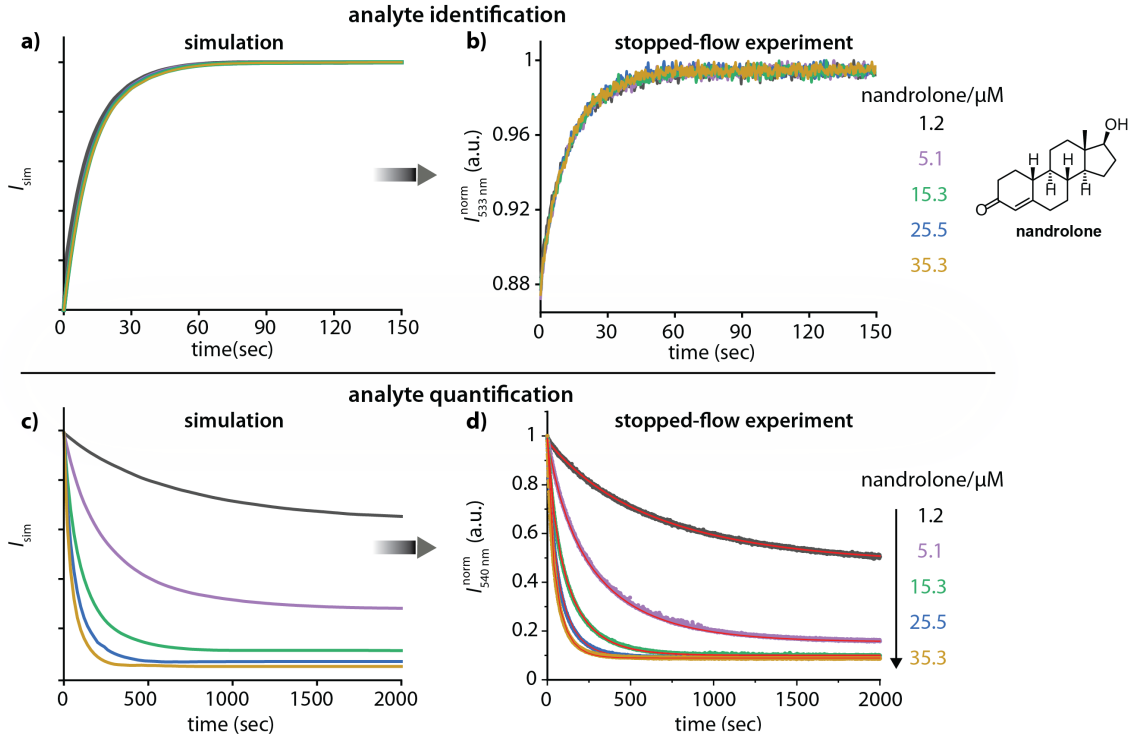

Figure 4.17: (a) Simulated *kin*GDA curve and (b) experimental *kin*GDA^{PFO} curve determined by fluorescence intensity variations (λ_{exc} = 376 nm, λ_{ems} = 533 nm) upon varying analyte concentrations for CB8 (1 µM) and nandrolone (1.2 – 35.3 µM) host-guest complex upon spiked addition of MPCP dye (50 µM) in water. (c) Simulated *kin*IDA curve and (d) experimental *kin*IDA curve determined by fluorescence intensity variations (λ_{exc} = 462 nm, λ_{ems} = 540 nm) upon varying analyte concentrations for nandrolone (1.2 – 35.3 µM) upon addition of CB7 (1 µM) and BC (1 µM) host-dye complex in water. The red line in (d) depicts the fitted data following the *kin*IDA binding model (Eq.4.14). The kinetic rate constants (k_{in}^{HG} and k_{out}^{HG}) for the CB7•nandrolone binding interaction hence obtained is given in Table 4.4 and were used as input parameters in the *kin*IDA binding model (Eq. 4.14) in order to obtain the simulations in (c).

Table 4.4: Experimental kinetic complexation (k_{in}^{HG}) and decomplexation (k_{out}^{HG}) rate constants for CB7⊃Nan complex at varying Nan concentrations determined by kinIDA in water.

host•dye[a]	**[nandrolone][b] / µM**	k_{in}^{HG} [c]/ M^{-1} s^{-1}	k_{out}^{HG} [c]/ s^{-1}
CB7•BC	1.2	4.3(± 0.3) ×10^3	3.8(± 0.2) ×10^{-4}
(1 µM)	5.1	5.5(± 0.3) ×10^3	4.9(± 0.2) ×10^{-4}
	15.3	6.0(± 0.4) ×10^3	5.4(± 0.2) ×10^{-4}
	25.5	6.5(± 0.3) ×10^3	5.8(± 0.2) ×10^{-4}
	35.3	6.8(± 0.3) ×10^3	6.1(± 0.2) ×10^{-4}

If not stated differently, all experiments were conducted in deionized water at 25 °C [a] See Figure 4.13c-4.13d for chemical structures. For the kinetic and thermodynamic parameters of CB7•BC host-dye complex, see Table 4.1. [b] See Figure 4.12b for chemical structures. CB7•Nan K_a^{HG}= 1.12 x 10^7 M^{-1}.[75] [c] Errors (StDev) from triplicate experiments are ≤20%.

Thus, once a pre-library with the necessary kinetic information and simulations is obtained, one may achieve analyte identification and quantification by comparing experimental data to simulations.

4.3. Conclusion

In conclusion, three new time-resolved competitive approaches, *kin*IDA, *kin*GDA, and *kin*GDA^{PFO,} were developed for the kinetic assessments of spectroscopically silent supramolecular host-guest complexes through a fluorescence-based assay. The methods allowed the determination of kinetic rate constants of several host-guest and protein-ligand pairs as representative examples. The extension to other hosts and supramolecular systems that bind guest molecules, *e.g.,* cages, will be interesting. Hopefully, these methods will find use in the supramolecular and protein community due to their ease and scope. The combined information from the obtained kinetic parameters along with the available thermodynamic literature data allows to gain a full picture of supramolecular systems and will therefore bring new insights into supramolecular-, bio- and materials chemistry.

In addition, focus on the kinetics of host-guest binding interactions helped achieve selective analyte sensing with notable kinetic selectivity for the analytes, even for systems lacking a thermodynamic selectivity. Consequently, not only the Gibbs free energy but also the activation energy of complex formation plays a major role in sensing applications. Both analyte identification and quantification were achieved by combining the *kin*GDA^{PFO} and *kin*IDA methods. The technique can also be, in principle, applied in the case of mixtures. However, detailed investigations need to be done for multi-component mixtures analysis. Hence, the new kinetic method is a nice addition to existing sensing concepts, reducing the requirement to synthesize selective chemosensors. Investigations into the kinetics of protein-protein and protein-ligand interactions by surface plasmon resonance method have already been proven helpful for understanding the molecular basis of such events.[369-371] Hence, the future design of selective chemosensors with combined thermodynamic and kinetic investigations will help realize real-world sensing applications in biofluids.

4.4. Experimental details

4.4.1. Materials

All solvents were used as received from Aldrich or Fluka without further purification. All chemicals were purchased and used as received unless stated otherwise. CB8 was synthesized according to literature procedures[244] and was also purchased from Strem or Sigma. CB7[372,373], MPCP[152], and MDAP[246,247] were synthesized according to literature procedures. Changming Hu and Dr. Laura Grimm from the research group of Dr. Frank Biedermann carried out the

synthesis of the host CB7 and the dye MDAP, respectively. Yichuan Wang from the research group of Prof. Stefan Bräse carried out the synthesis of the dye MPCP.

4.4.2. Instrumentation

Absorption spectra were measured on a Jasco V-730 double-beam UV–VIS spectrophotometer and baseline corrected. Steady-state emission spectra and time-resolved emission profiles were recorded on a Jasco FP-8300 fluorescence spectrometer equipped with a 150 W xenon arc lamp, single-grating excitation, and emission monochromators. Emission and excitation spectra were corrected for source intensity (lamp and grating) and the emission spectral response (detector and grating) by standard correction curves. All experiments were carried out at 25 °C by using a water thermostated cell holder STR-812, while the cuvettes were equipped with a stirrer allowing rapid mixing. Stopped-flow experiments were carried out on a Jasco FP-8300 fluorescence spectrometer equipped with a thermostated (25 °C) SFA-20 stopped-flow accessory from TgK Scientific Limited. For measurements conducted in water, deionized water was used in all cases. For spectroscopy analysis in cuvettes, UV plastic cuvettes with a light path of 10 mm and dimensions of 10x10 mm from Brand with a spectroscopic cut-off at 230 nm were utilized. The ITC experiments were carried out in deionized water at 25ºC on a Microcal PEAQ-ITC from Malvern.

The differential equations describing the kinetic process described in the chapter have been solved numerically with Wolfram Mathematica 11/12. A best practice guide on conducting a *kin*GDA, *kin*GDA^{PFO,} and *kin*IDA can be found in the Addition Information. Unless stated otherwise, I^{norm} represents the normalized signal obtained upon dividing the data by the maximum value.

4.4.3. Sample Preparation

All stock solutions, unless stated otherwise, were prepared in deionized water and kept in the fridge at +8 °C for storage. Owing to the low solubility of the steroids, testosterone (114 μM)[75] and progesterone (33 μM)[75] in water, their respective stock solutions were prepared in ethanol and then diluted in the host-containing water for the *kin*GDA and *kin*GDA^{PFO} measurements. The stock solutions prepared in ethanol were stored in the freezer at −20ºC. Nandrolone has a solubility of 810 μM[75] in water, and hence the stock solution was prepared in water. The concentration of MPCP, BC, and MDAP stock solutions were determined accurately by using their molar extinction coefficients (MPCP[152]: 7112 $M^{-1}cm^{-1}$ at 335 nm, BC[374]: 22300 $M^{-1}cm^{-1}$ at 344 nm, MDAP[201]: 7800 $M^{-1}cm^{-1}$ at 393 nm) by UV-Vis absorption titration measurements

in water. For compounds featuring unreported molar extinction coefficient, the stock solutions were prepared by weighing in the required amount of the pure sample to attain the desired concentration. The concentration of CB8 stock solution was determined by fluorescence titration against a known concentration of MPCP dye by exciting the sample at 368 nm and collecting the emission intensity at 531 nm in water. The concentration of CB7 stock solution was determined by fluorescence titration against a known concentration of MDAP dye by exciting the sample at 339 nm and collecting the emission intensity at 454 nm in water. The concentration of CB6 stock solution was determined by fluorescence titration against a known concentration of DSMI dye by exciting the sample at 450 nm and collecting the emission intensity at 575 nm in water.

4.5. Additional Information

Best Practice Guide for *kin*GDA and *kin*GDA^{PFO} and *kin*IDA

1. Gather information on solubility of host and guest in the solvent of interest.
2. Estimate binding constant and kinetic rate constants of host-guest complex, *e.g.*, by searching for related host-guest pairs on www.suprabank.org, www.supramolecular.org, or in literature reviews or articles.
3. Calculate which concentration of host and guest are needed to reach a sufficient degree of complexation of the host (ideally ≥ 50%). A software package is available on GitHub: https://github.com/ASDSE/thermosimfit/zipball/master for simulations. Excess of guest is permitted for *kin*GDA and *kin*IDA. If the required guest concentration is within the solubility window, continue with step 5.
4. If the required guest concentration is outside the solubility window, attempt to solubilize the guest in a solution of the host (sonication can help), followed by filtration/centrifugation and concentration determination of the host and guest concentration (*e.g.*, by NMR, UV-Vis, HPLC, etc.)
5. Simulate *kin*GDA by using Eq. 4.14 and adjust the indicator concentration and the host-guest concentration while maintaining the degree of host-complexation sufficiently high. (A software package, https://github.com/ASDSE/kineticsimfit/zipball/master is available on GitHub: for simulations.) Consider the solubility limit of the indicator. Ideally, dyes that show strong emission changes or distinct absorbance spectra upon host binding are chosen.

6. Simulate the *kin*DBA (without guest) and *kin*GDA (with guest) for comparison. The *kin*GDA and *kin*DBA kinetic traces should look sufficiently distinct. If not, choose different concentrations or a different indicator dye.
7. Perform the *kin*GDA with the conditions derived from the simulations by rapidly mixing the pre-equilibrated H•G solution with the dye solution at a controlled temperature. Practically, the equilibration time should be ≥ 100 ms for conventional stopped-flow setups. However, if equilibration times are ≥ 1 min, manual mixing may be used.
8. Fit the recorded *kin*GDA traces by using equations Eq. 4.14 utilizing the predetermined parameters: $K_a^{HD}, k_{in}^{HD}, k_{out}^{HD}$ and the exact concentrations as an input. Utilizing $k_{in}^{HG} = k_{out}^{HG} \cdot K_a^{HG}$ as an input will increase the goodness of the fit. (A software package is available as https://github.com/ASDSE/kineticsimfit/zipball/master on GitHub: for fitting.) The signal factors I^{HD} and I^{D} may be varied, but their ratio should stay close to the expected value from the host-dye titration experiment. From the fitting, the host-guest kinetic rate constants $k_{in}^{HG}, k_{out}^{HG}$ can be extracted. Analogously, this procedure can be applied to the akin method of *kin*IDA.
9. For *kin*GDA^{PFO}, perform steps 1 – 7, but with a large excess of dye. Fit the acquired kinetic traces to Eq. 4.22 to obtain k_{out}^{HG}. Subsequently, k_{in}^{HG} can be derived by using the relation $k_{in}^{HG} = k_{out}^{HG} \cdot K_a^{HG}$.

Additional data

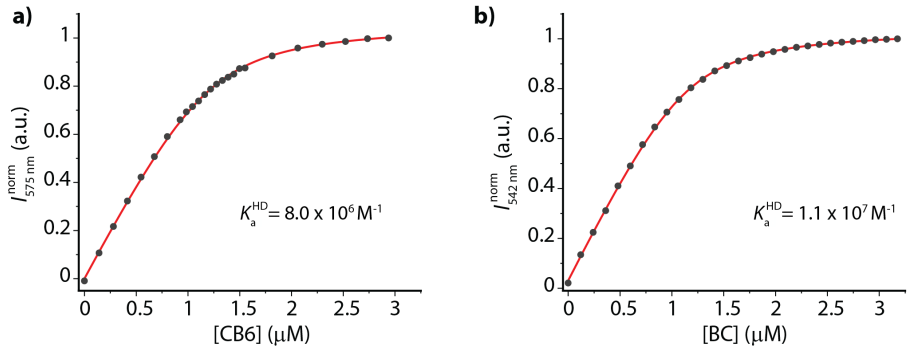

Figure 4.18: Representative DBA binding isotherm determined by fluorescence intensity variations (λ_{exc} = 519 nm, λ_{ems} = 575 nm) of DSMI (1.21 µM) and CB6 (0 – 2.94 µM) in water at 25 °C. (b) Representative DBA binding isotherm determined by fluorescence intensity variations (λ_{exc} = 440 nm, λ_{ems} = 542 nm) of desalted CB7 (1.15 µM) and BC (0-3.2 µM) in water at 25 °C. Acquired data is depicted as gray dots and fitted data as red line.

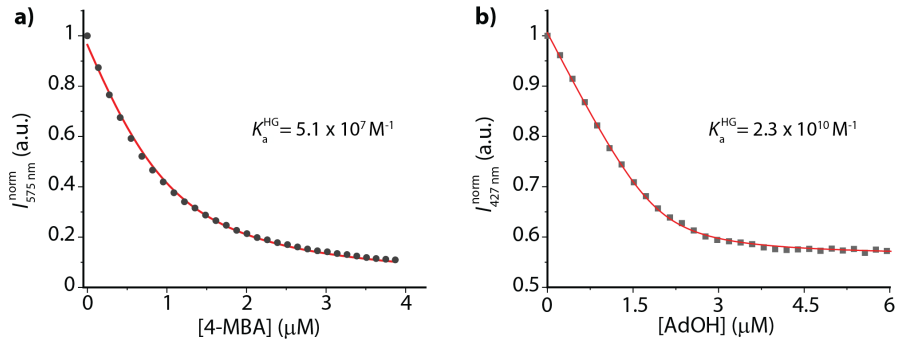

Figure 4.19: Representative IDA binding isotherm determined by fluorescence intensity variations (λ_{exc} = 519 nm, λ_{ems} = 575 nm) of DSMI (2.11 μM), CB6 (1.03 μM) and 4-MBA (0-3.87 μM) in water (3.87 μM HCl) at pH 7 at 25 °C. (b) Representative IDA binding isotherm determined by fluorescence intensity variations (λ_{exc} = 378 nm, λ_{ems} = 427.5 nm) of MDAP (3.0 μM), desalted CB7 (2.0 μM), and AdOH (0-6 μM) in water at 25 °C Acquired data is depicted as gray dots and fitted data as red line.

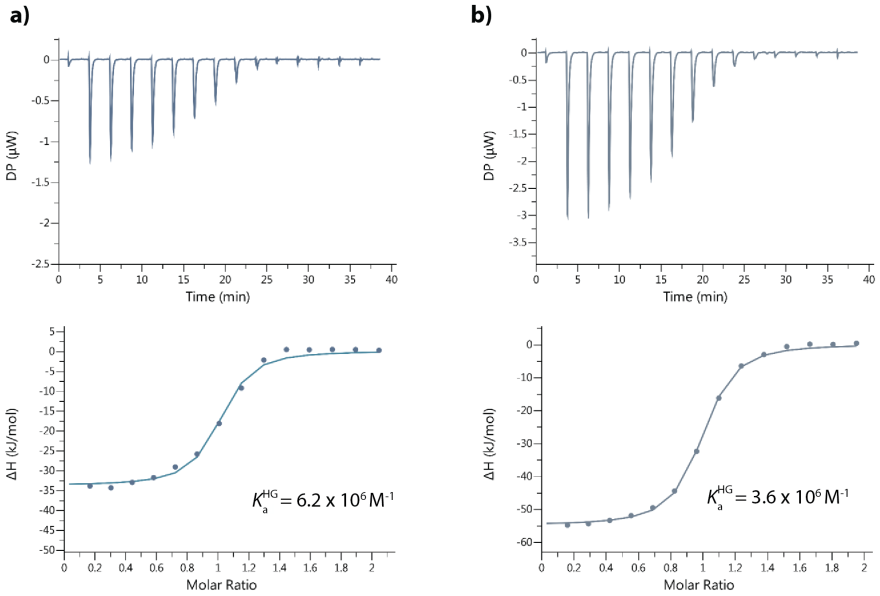

Figure 4.20: (a) Representative ITC isotherms of desalted CB8 (16 μM) and adamantanol (0-40 μM) in water at 25 °C. (b) Representative ITC isotherms of desalted CB8 (26 μM) and ferrocenyl methanol (0-60 μM) in water at 25 °C.

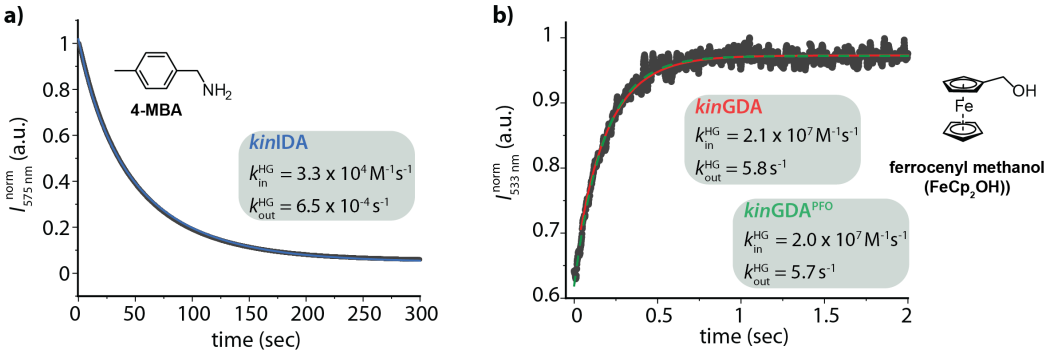

Figure 4.21: (a) Representative *kin*IDA curve determined by fluorescence intensity variations (λ_{exc} = 519 nm, λ_{ems} = 575 nm) of DSMI (2.08 μM), CB6 (1.05 μM), and 4-MBA (8.23 μM) in water (8.23 μM HCl) at pH 7 at 25 °C. Acquired data is depicted as gray dots and fitted data following the competitive binding model (Eq. 4.14) as blue line. (b) Representative *kin*GDA curve determined by fluorescence intensity variations (λ_{exc} = 366 nm, λ_{ems} = 533 nm) of MPCP (5.25 μM), ferrocenyl methanol (0.8 μM) and desalted CB8 (0.56 μM) in water at 25 °C. Acquired data is depicted as gray dots and fitted data following the competitive binding model (Eq. 4.14) as red line and following the pseudo-first order model (Eq. 4.22) as green line.

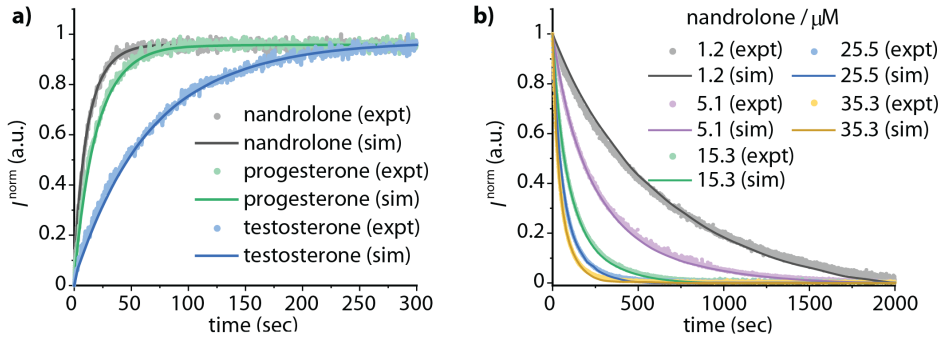

Figure 4.22: (a) Comparison of the experimental *kin*GDA^{PFO} traces (dotted line, expt) to the simulated data (solid line, sim) for CB8•testosterone (1 µM, blue line), CB8•progesterone (1 µM, green line) and CB8•nandrolone (1 µM, black line) host•guest complex upon spiked addition of MPCP dye (50 µM) in water at 25 °C. (b) Comparison of the experimental *kin*IDA traces (dotted line, expt) to the simulated data (solid line, sim) upon varying analyte concentrations for nandrolone (1.2 – 35.3 µM) upon addition of CB7 (1 µM) and BC (1 µM) host-dye complex in water. The data were normalized to [0, 1] for the comparisons and to obtain the overlaid simulated and experimental spectra.

Table 4.5: Data used for correlation analysis in Figure 4.11. If not stated differently, values were acquired by me by fluorescence titration and listed in Table 4.2.

host	guest	T / °C	logK_a	k_{in}^{HG} / M^{-1} s^{-1}	k_{out}^{HG} / s^{-1}	ΔG / kJ mol^{-1}	$\Delta G_{in}^{\#}$ / kJ mol^{-1}	$\Delta G_{out}^{\#}$ / / kJ mol^{-1}
CB6	DSMI	25	6.90	2.0×10^{8}	2.44×10^{1}	-39.4	25.7	65.1
CB6	4-MBA[a]	25	7.71	3.3×10^{4}	6.49×10^{-4}	-44.0	47.2	91.2
CB6	cyclobutylmethylamine[375]	40	5.57	5.9×10^{3}	1.6×10^{-2}	-33.4	54.2	87.6
CB6	cyclopentylmethylamine[375]	40	5.52	5.5	1.6×10^{-5}	-33.1	72.4	105.6
CB6	cyclohexylmethylamine[375]	40	1.90	8.8×10^{-4}	1.1×10^{-5}	-11.4	95.1	106.6
CB6	4-MBA[b][162]	40	2.51	2.7	$8.5 \cdot 10^{-3}$	-15.0	74.2	89.2
CB6	cyclohexylmethylamine Na^{+}[162]	25	1.67	2.4×10^{-4}	5.1×10^{-6}	-9.5	93.7	103.2
CB6	cyclohexylmethylamine K^{+}[162]	25	1.83	2.6×10^{-4}	3.9×10^{-6}	-10.4	93.5	103.9
CB6	cyclohexylmethylamine Rb^{+}[162]	25	1.92	3.2×10^{-4}	3.8×10^{-6}	-11.0	93.0	104.0
CB6	cyclohexylmethylamine Cs^{+}[162]	25	1.95	4.5×10^{-4}	5.0×10^{-6}	-11.2	92.1	103.3
CB6	1,4-diaminocyclohexane[363]	25	6.15	1.2×10^{-3}	8.5×10^{-10}	-35.1	89.7	124.8
CB6	N-butyladamantan-1-aminium[363]	25	7.30	4.4×10^{4}	2.2×10^{-3}	-41.7	46.5	88.2
CB7	nandrolone	25	7.05	4.1×10^{3}	3.6×10^{-4}	-40.2	52.4	92.7
CB7	estradiol	25	6.25	4.2×10^{4}	2.0×10^{-2}	-36.1	46.6	82.7
CB7	BC	25	7.23	6.0×10^{6}	3.5×10^{-1}	-41.3	34.4	75.6
CB7	cholesterol	25	5.91	7.0×10^{4}	8.7×10^{-2}	-33.7	45.4	79.1
CB7	MDAP	25	9.43	2.4×10^{7}	9.0×10^{-3}	-53.8	30.9	84.7
CB7	(+)-fenchone[376]	25	7.46	$3.2 \cdot \times 10^{4}$	3.2×10^{-3}	-42.6	44.7	87.3
CB7	norcamphor[376]	25	8.18	1.5×10^{7}	9.8×10^{-2}	-46.7	32.1	78.8
CB7	flavopereirine perchlorate[165]	25	7.79	9.0×10^{7}	1.6	-44.4	27.6	71.9
CB7	BC[45]	10	7.72	8.8×10^{6}	1.6×10^{-1}	-41.9	31.6	73.5
CB7	BC[45]	25	7.37	1.9×10^{7}	8.1×10^{-1}	-42.1	31.5	73.5
CB7	((trimethylamino)methyl) ferrocene[377]	25	11.52	2.0×10^{7}	7.0×10^{-5}	-65.8	31.3	96.7
CB7	R-(+)-2-naphthyl-1-ethylammonium cation[318]	25	7.03	6.3×10^{8}	5.5×10^{1}	-40.1	22.8	63.1
CB7	N-butyladamantan-1-aminium[363]	25	12.00	2.4×10^{7}	2.4×10^{-5}	-68.5	30.9	99.4
CB7	1,4-diaminocyclohexane[363]	25	8.36	6.0×10^{8}	2.7	-47.7	22.9	70.6

CB7	6-methoxy-1-methylquinolinium[378]	24	6.30	3.0×10^{9}	1.5×10^{3}	-35.8	18.9	54.7
CB7	bis(3,5-dimethoxybenzyl)-4,4′-bipyridinium[379]	25	>3.53	3.0×10^{-1}	8.0×10^{-5}	<-20.2	76.0	96.4
CB7	bis(3,5-diethoxybenzyl)-4,4′-bipyridinium[379]	25	>5.9	9.0×10^{-1}	1.0×10^{-6}	< -33.7	73.3	107.3
CB7	3′,4′,7-trimethoxyflavylium ion[380]	20	6.19	7.7×10^{7}	5.0×10^{1}	-34.7	27.5	62.2
CB7	2-aminoanthracenium cation[381]	20	6.36	2.3×10^{7}	1.0×10^{1}	-35.7	30.4	66.1
CB7	1-tri(ethylene glycol)-1'-methyl-m-xylyl-4,4'-bipyridinium[382]	25	5.06	6.0×10^{6}	5.3×10^{1}	-28.9	34.3	63.2
CB7	1,1'-(1,4-phenylenebis(methylene)) bis(pyridin-1-ium-4-carboxylate[383]	25	5.81	6.2×10^{-1}	9.6×10^{-7}	-33.2	74.2	107.4
CB7	1,1'-(1,4-phenylenebis(methylene)) bis(pyridin-1-ium-3-carboxylate[383]	25	5.75	3.4	6.0×10^{-6}	-32.8	70.0	102.8
CB7	N-phenyl-2-naphthyl ammonium cation[166]	20	5.48	1.2×10^{7}	3.87×10^{1}	-30.7	32.1	62.8
CB7	1,1'-bis(5-carboxypentyl)-[4,4'-bipyridine]-1,1'-diium[384]	20	5.57	7.5×10^{3}	2.0×10^{-2}	-31.3	50.0	81.3
CB7[c]	BC	25	7.03	2.5×10^{6}	2.3×10^{-1}	-40.1	36.5	76.7
CB7[c]	AdOH	25	10.41	1.7×10^{5}	6.6×10^{-6}	-59.4	43.2	102.6
CB8	testosterone	25	8.04	6.4×10^{5}	5.8×10^{-3}	-45.9	39.9	85.8
CB8	nandrolone	25	8.19	1.1×10^{7}	7.1×10^{-2}	-46.8	32.8	79.6
CB8	prednisolone	25	6.15	1.6×10^{6}	1.1	-35.1	37.7	72.8
CB8	MPCP	25	12.59	1.2×10^{7}	3×10^{-6}	-71.9	32.6	104.5
CB8	BC[169]	10	7.23	6.4×10^{7}	3.8	-39.2	26.9	66.1
CB8[c]	MPCP	25	12.59	2.0×10^{7}	5.1×10^{-6}	-71.9	31.3	103.2
CB8[c]	$FeCp_2OH$	25	6.56	2.1×10^{7}	5.8	-37.5	31.3	68.7
CB8[c]	AdOH	25	6.79	1.2×10^{7}	1.97	-38.8	32.6	71.3
CB8•BC	BC[169]	10	6.92	5.0×10^{6}	6.0×10^{-1}	-37.5	32.9	70.4
CB8•MV	1-Naphthylamine-PEG[164]	5	4.60	2.5×10^{7}	3.9×10^{2}	-24.5	28.6	54.2
CB8•MV	2-Naphthylamine-PEG[164]	5	≥5.30	4.0×10^{7}	$\leq 2.0 \times 10^{2}$	≤-28.2	27.5	55.7
CB8•MV	Anthracene-PEG[164]	5	≥6.45	2.8×10^{7}	$\leq 1.0 \times 10^{1}$	≤-34.3	28.3	62.6
CB8•MV	fluorene-PEG[164]	5	≥6.45	2.8×10^{7}	$\leq 1.0 \times 10^{1}$	≤-34.3	28.3	62.6
CB8•MV	Dibenzofuran-PEG[164]	5	5.83	2.2×10^{7}	3.2×10^{1}	-31.1	28.9	59.9
CB8•MV	Pyrene-PEG[164]	5	6.36	1.9×10^{7}	8.0	-33.9	29.2	63.2
HSA	PBZ	25	5.83	6.6×10^{5}	9.7×10^{-1}	-33.3	39.8	73.1
HSA	warfarin	25	5.15	6.7×10^{5}	4.8	-29.4	39.8	69.1
HSA	tolbutamide[385]	37	5.04	6.5×10^{4}	5.9×10^{-1}	-29.9	47.5	77.4
HSA	acetohexamide[385]	37	5.26	1.2×10^{5}	6.7×10^{-1}	-31.2	45.9	77.1
HSA	verapamil[385]	37	4.18	5.3×10^{3}	3.5×10^{-1}	-24.8	54.0	78.8
HSA	gliclazide[385]	37	4.90	4.9×10^{4}	6.1×10^{-1}	-29.1	48.2	77.3
HSA	chlorpromazine[385]	37	4.79	2.5×10^{5}	3.96	-28.5	44.1	72.5

[a] measured in water by fluorescence-based *kin*GDA. [b] measured in D_2O : formic acid (1:1) mixture by NMR. [c] desalted CB7/CB8.

Chapter 5

5 Pillar[*n*]arene-based fluorescence turn-on chemosensor for the selective detection of biogenic polyamines in saline media and biofluids

5.1. Introduction

Biogenic polyamines, such as spermine, spermidine, and cadaverine (see Figure 5.2a), are naturally occurring organic molecules that are produced by the decarboxylation of amino acids and found in the cells and body fluids of eukaryotes.[386-389] They play a significant role in the human body, as they are involved in several biological functions, including cell growth and proliferation, neuron regulation, immune response, etc.[389-393] At optimum concentration levels, polyamines reduce the risk of many cardiovascular diseases and exhibit anti-aging properties.[389,394,395] At the same time, altered polyamine levels in the body are often associated with several diseases, including Alzheimer's and Parkinson's disease, stroke, heart failure, and cancer.[389,395-399] For instance, elevated levels of polyamines were found in the urine, saliva, and blood serum of cancer patients and thus, serve as useful diagnostic markers for early-stage disease detection and to monitor the effectiveness of therapy.[393,400-404] Hence, it maybe beneficial to regularly monitor and maintain the level of polyamines in readily accessible biofluid samples. Current methods for polyamine detection in biological samples primarily rely on capillary electrophoresis and chromatographic methods, including high-performance liquid chromatography (HPLC) and gas chromatography (GC).[405-408] Although these techniques are very precise, they are time-consuming, require laborious sample pre-treatment, relatively long analysis times, expensive and complex equipment, and considerable skill. Thereby, the development of rapid, cost-efficient, and widely applicable methods for polyamine detection with satisfactory sensitivity and selectivity is of great importance.

Fluorescence-based sensing assays are highly desirable due to their technical simplicity, low cost, and real-time detection of analytes with high sensitivity and selectivity.[16,118] Consequently, these assays can be used in high-throughput screening (HTS) to achieve a large-scale analysis of samples.[118] The past few years have seen an increase in the number of reported fluorescent chemosensors and nanoparticle-based probes for the purpose of polyamine detection.[351,409-415] A few notable examples include the use of a negatively charged dye-embedded micelle for the charge-mediated recognition of polycationic polyamines resulting in a fluorescence "turn-off" signal,[409,410] analyte-directed formation of emissive

excimers of a sulfonated probe in the presence of polyamines[411] and fluorescence-mediated host-guest recognition interactions.[351,412,413] However, the functionality of these reported fluorescent chemosensors was evaluated in deionized water or low-salt buffers, and not assessed in real biofluids such as human urine, containing high millimolar salt concentrations.[351,409-413] BODIPY-functionalized gold nanoparticles were reported for polyamine detection through electrostatic interactions of the negatively charged nanoparticle with polyamines resulting in displacement of cationic dye.[414] Recently, a reactive probe based on agarose-coumarin hydrogel was introduced to detect spermine and spermidine in aqueous buffers, and biofluids spiked with high concentrations of polyamines.[415] Unfortunately, these nanoparticle-based systems suffer from various limitations interfering with their practical utility for sensing applications in real biofluid samples. For instance, at high salt concentrations found in biofluids, these systems can suffer from undesirable cation-exchange reactions and interferences on the charge-mediated recognition process between the negatively charged chemosensor and the polycationic polyamines (see Figure 5.1).[351,409,410,412,413] As a result, the established systems become dysfunctional in biologically relevant media such as PBS, urine or saliva that contain high millimolar salt concentrations. Besides, the sensing assay require long reaction times.[412,416] Importantly, the previously reported fluorescent chemosensors for polyamines suffer from strong interferences from other biomolecules in the media such as amino acids and other biogenic amines, proteins and nucleobases, and hence, lack selectivity for the polyamines of interest.[417,418] This makes it difficult to detect and distinguish polyamines in the media due to the lack of a selective signal output. Furthermore, the reported reactive probes for the detection of spermine in spiked biofluids show a limit of detection much higher than what is needed for a practical assay.[415] Overall, so far available chemosensors and probes cannot be used to regularly monitor variations in polyamine levels in biofluids.

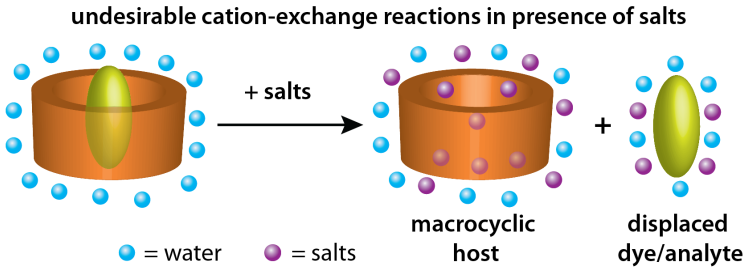

Figure 5.1: Schematic representation of the cation-exchange reaction when the known chemosensors become dysfunctional in biologically relevant media such as PBS or urine. At high salt concentrations, the signaling binding pockets of the receptor host molecule are occupied by salts and are no longer available for the detection of relevant analytes. Moreover, chemosensors self-assembled from a receptor host and dye molecule decomposes at high salt concentrations when the dye displaced from the host cavity by the salts.

Isaacs and co-workers recently reported a new class of water-soluble macrocyclic sulfonated pillar[*n*]arene host, Pillar[*n*]MaxQ (P[*n*]AS, *n* = 5-7), where the negatively charged receptor possesses ultratight binding affinities for analytes containing quaternary ammonium ions in aqueous media.[90] P[*n*]AS therefore serves as a prime candidate for the construction of fluorescent chemosensors for the detection of biogenic polyamines, where the expected high binding affinity of the host for polycationic polyamines will prohibit any salt interferences on the charge-mediated recognition event and cation-exchange reactions for sensing studies in biofluids with high millimolar salt concentrations (Figure 5.2c and 5.2d). The P[*n*]AS host molecule itself is non-chromophoric and needs to be used in combination with indicator dyes to furnish a fluorescent chemosensor.

In my investigations, I employed a novel self-assembled host-dye chemosensing ensemble composed of sulfonated pillar[*n*]arene host, P5AS (see Figure 5.2b), in combination with dicationic diazapyrenium based indicator dyes (see Figure 5.2b) to achieve the selective fluorescence-based detection of biogenic polyamines at concentration levels suitable for biomedical applications in saline media and biofluids. The relatively strong binding affinity of the introduced indicator dyes with the host ensures the stability of the self-assembled chemosensor even at high salt concentrations (see Figure 5.2c). Furthermore, the polyamine sensing is achieved *via* the emission turn-on upon displacement of the dye from the host cavity by the stronger binding polyamine upon adding the self-assembled chemosensor into polyamine sample media (Figure 5.2c). The chapter focuses on systematic investigations into the development of the self-assembled host-dye fluorescent chemosensor, the binding studies of biogenic polyamines with the chemosensor, and the stability and functionality assessments of the chemosensor for selective polyamine detection in saline and biologically relevant media. Finally, the practical applicability of the new chemosensor were evaluated in human urine and saliva samples at practically relevant polyamine levels.

5.2. Results and Discussion

5.2.1. Design and preparation of a fluorescent chemosensing ensemble based on Pillar[5]MaxQ and dicationic indicator dye

The sulfonated pillar[*n*]arene-based molecular container, Pillar[5]MaxQ (P5AS) (see Figure 5.2b), was prepared from the parent hydroxylated pillararene, P5A, by reacting with pyridine·SO_3 in pyridine at 90 °C.[90]

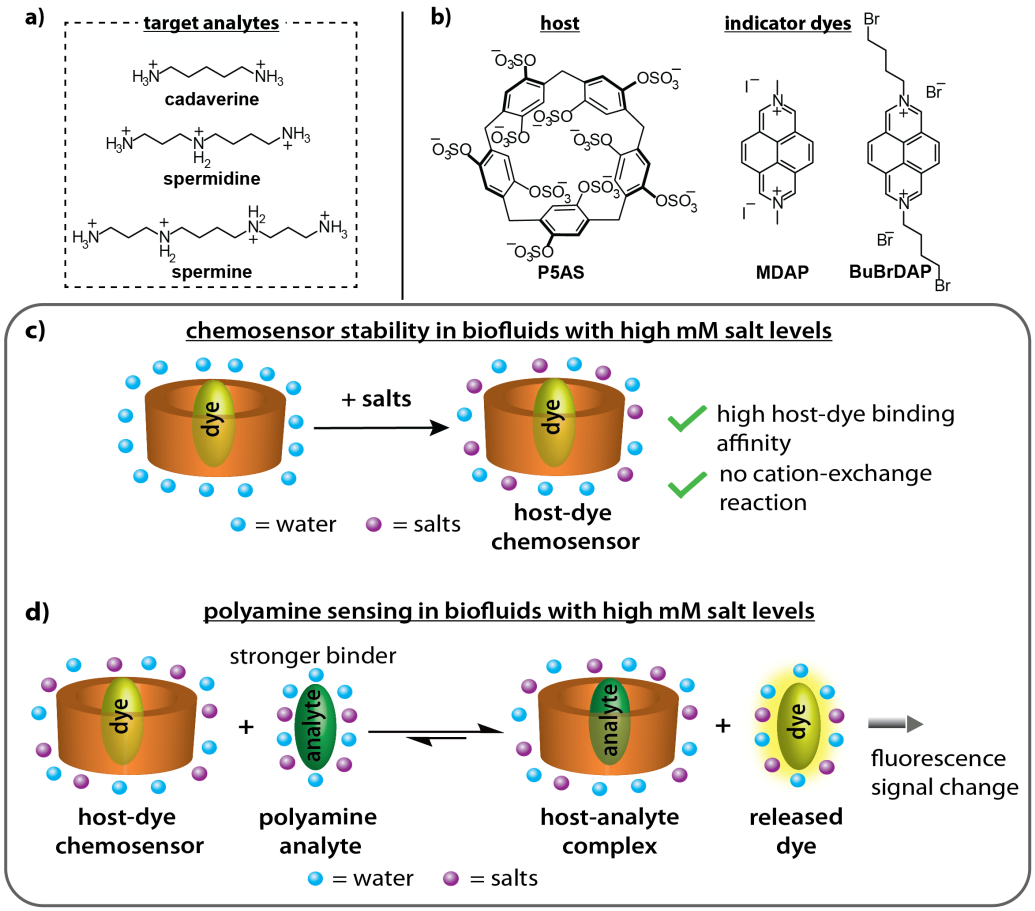

Figure 5.2: Chemical structure of (a) polyamine target analytes and (b) the host molecule, P5AS, and the indicator dye molecules, MDAP and BuBrDAP, utilized to achieve the self-assembled host-dye fluorescent chemosensor. (b) The strong binding affinity between the dye and the host in the self-assembled host-dye chemosensor prohibits cation-exchange reactions at high salt concentrations. The dye remains inside the host, ensuring the stability of the chemosensor ensemble. (b) Schematic representation of the sensing assay, where the addition of the self-assembled host-dye chemosensor into biofluids containing polyamines results in the displacement of the dye from the host by the stronger binding polyamine, which is accompanied by a fluorescence signal change.

The P5AS host is reported to exhibit superior binding affinity and selectivity toward guests containing quaternary ammonium ions, where electrostatic effects and hydrophobic forces mainly drive the binding.[90] A high negative charge density packed into a small volume near the portals of P5AS supplements the electrostatic contribution to the binding.[90] P5AS forms 1:1 host-guest complexes with cationic guests such as aliphatic amines and displays increasing binding affinity with an increase in the number of quaternary ammonium ions in the guest (owing to the electrostatic interactions in the recognition process) and the guest length (presumably due to the increased hydrophobicity and better size matching).[90] The features mentioned above, in addition to the high inherent aqueous solubility of P5AS (100 mM),[90] make it a promising host class for selective polyamine sensing applications. The P5AS host molecule itself is non-chromophoric and hence, needs to be used in combination with indicator dyes to furnish fluorescent chemosensing ensemble. The indicator dye was chosen so that it displays good aqueous solubility and strong binding affinity with the host molecule to prevent the

dissociation of the self-assembled host-dye chemosensor at high salt concentrations. A dicationic diazapyrenium-based dye, MDAP (Figure 5.2b), with two quaternary ammonium groups, was utilized as a first choice. A simple mixing of the host and dye solutions resulted in the self-assembled P5AS•MDAP host-dye fluorescent chemosensor, where the binding was instantaneous (see below). The following section describes the characterization of the chemosensor complex and its stability evaluation in saline and biologically relevant media.

5.2.1.1. NMR investigation of chemosensor complex formation

Figure 5.3 shows the ^{1}H NMR spectra recorded for MDAP, P5AS, 1:1 mixture of MDAP and P5AS in D_2O. The substantial upfield shifting observed in Figure 5.3c for the resonances of indicator dye MDAP upon addition of P5AS confirms its encapsulation by the host and the formation of self-assembled P5AS•MDAP chemosensor. Following this, the NMR spectrum was recorded after adding the polycationic polyamine spermine to the P5AS•MDAP chemosensor in D_2O (Figure 5.3d). On addition of 1 equivalent of spermine, the resonances for the indicator dye MDAP shifted back towards those of the free dye, indicating the complete displacement of the dye from P5AS by the stronger binding analyte spermine. At the same time several peaks emerged in the aliphatic region that can be assigned to bound and unbound spermine.

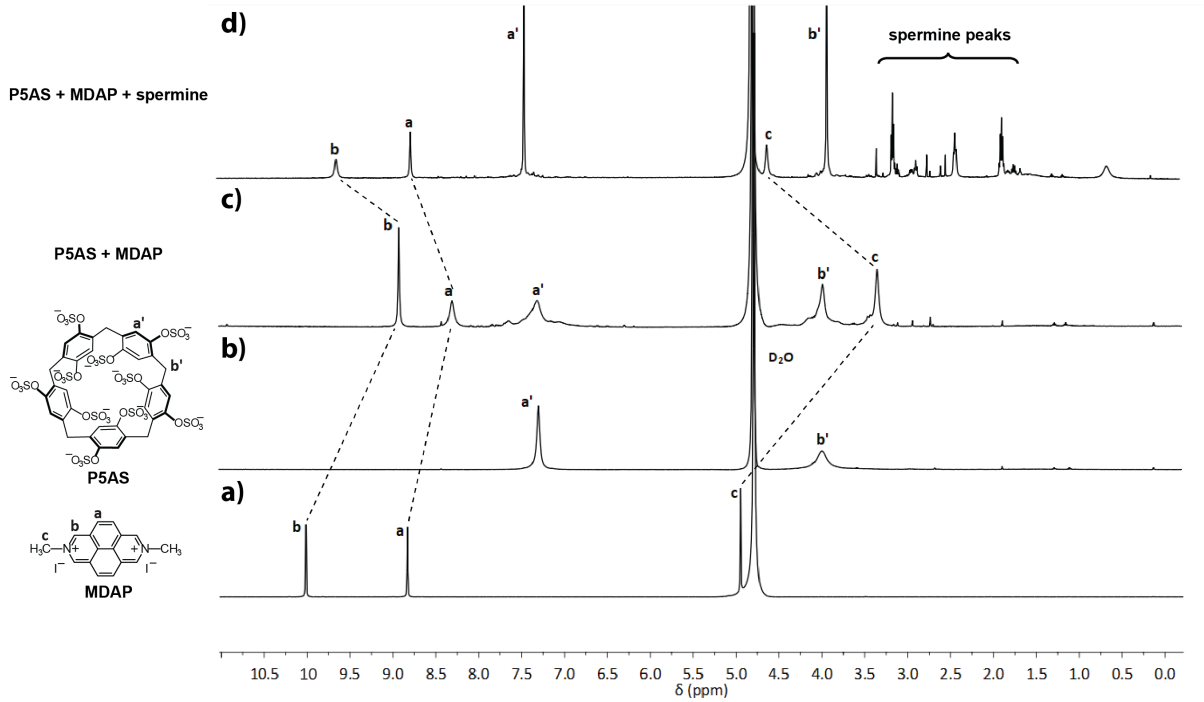

Figure 5.3: ^{1}H NMR spectra (500 MHz, D_2O, 298K) recorded for solution of (a) MDAP (1 mM), (b) P5AS (1 mM), (c) a mixture of MDAP (1 mM) and P5AS (1 mM) and (d) a mixture of MDAP (1 mM), P5AS (1 mM) and spermine (1 mM) (bottom to top).

5.2.1.2. Photophysical characterization of chemosensor and stability assessments in saline and biologically relevant media

The photophysical properties of the new self-assembled P5AS•MDAP chemosensor were investigated by UV-Vis absorption and fluorescence spectroscopy measurements. 1X phosphate-buffered saline (1X PBS) with a salt composition (137 mM NaCl, 2.7 mM KCl, 10 mM Na_2HPO_4, and 1.8 mM KH_2PO_4) comparable to that found in biofluids was chosen as the buffer for the studies. The indicator dye MDAP absorbs in the near-UV to visible wavelength range with absorption bands in the 300-450 nm region in 1X PBS (Figure 5.4a). The addition of P5AS to MDAP solution in 1X PBS resulted in an indicative 7 nm bathochromic shift of the peak maxima at 333 nm of the dye absorption to 341 nm (Figure 5.4a). This observation, in analogy to literature reports for pillar[*n*]arene-dye complexes,[419] further confirmed the formation of the self-assembled P5AS•MDAP chemosensor. The fluorescence emission spectra of MDAP showed strong emission in the 400-500 nm region with a maximum at 423 nm upon excitation at 336 nm in 1X PBS (Figure 5.4b). The addition of P5AS to MDAP was accompanied by a strong quenching in the dye emission (Figure 5.4b). Figure 5.4c shows the kinetic traces recorded by monitoring the fluorescence emission intensity at 423 nm on adding

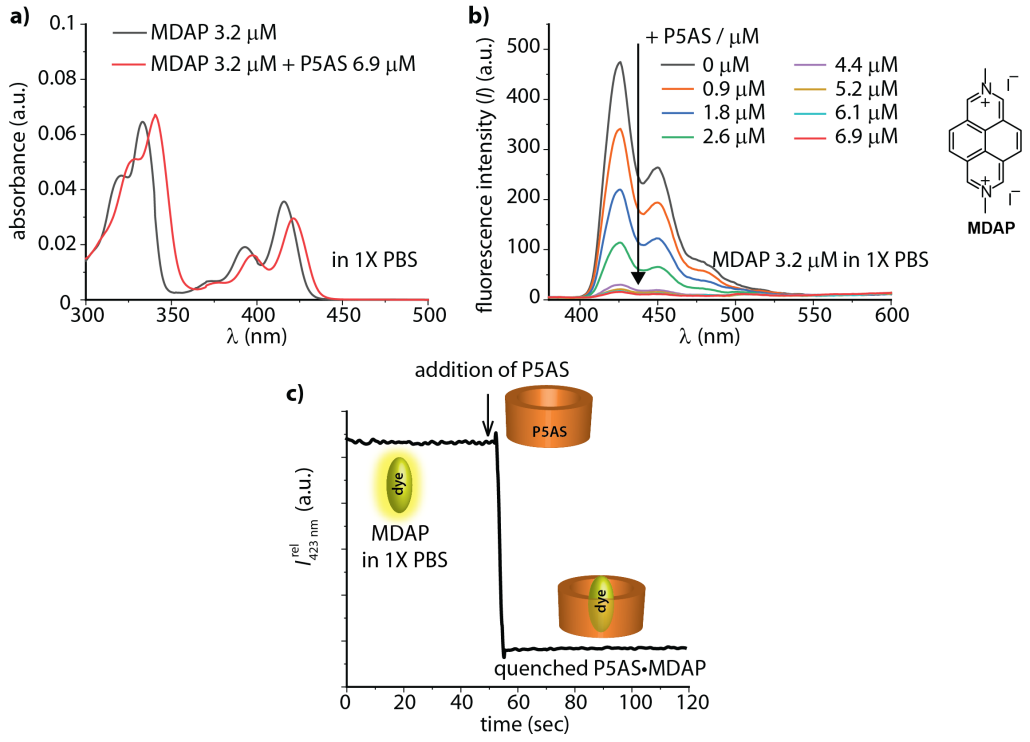

Figure 5.4: (a) Absorbance and (b) fluorescence emission spectra (λ_{exc} = 336 nm) of MDAP (3.2 μM) before and after addition of P5AS (0-6.9 μM) in 1X PBS. (c) Relative fluorescence emission intensity changes with time at 423nm (λ_{exc} = 336 nm) of MDAP (3.1 μM) in 1X PBS upon addition of P5AS (3.1 μM), resulting in the instantaneous formation of the fluorescence quenched P5AS•MDAP self-assembled chemosensor within a few milliseconds.

1 equivalent of P5AS to MDAP. The binding is instantaneous, resulting in the fluorescence quenched chemosensor within a few milliseconds.

Potential applications of the new P5AS•MDAP chemosensor require stability of the self-assembled system in complex biological fluids, such as urine, blood, and saliva containing high salt concentrations (*e.g.,* 51 -190 mM Na^+ in urine[420] and 130 -144 mM Na^+ in plasma[421] for healthy humans). Previous reports have shown that the binding affinity of many host•dye complexes significantly decreases in the presence of salts, as competitive binding of metal ions to the receptor host molecule occurs,[162,176,422,423] which reduces their practicality. Consequently, the stability of the P5AS•MDAP chemosensor in the presence of salts was evaluated by monitoring the binding affinity of the complex in saline buffers with varying salt compositions, such as 50 mM sodium phosphate buffer (Na-PB), 1X PBS, and 10X PBS (10 times concentrated as 1X PBS). In addition, the stability was also investigated in synthetic urine (surine), a non-biological urine sample with constituents that mimic human urine (often used as a negative urine control). Figure 5.5 displays the fluorescence emission-based binding curve monitored at 423 nm upon titration of P5AS to MDAP in 50 mM Na-PB, 1X PBS, 10X PBS, and surine, followed by fitting the data to a thermodynamic DBA model (see Eq.1.9-1.13 in General Introduction - Section 1.2.2) to obtain the respective binding constants (summarized in Table 5.1). A strong quenching in the dye emission was observed on addition of P5AS to MDAP

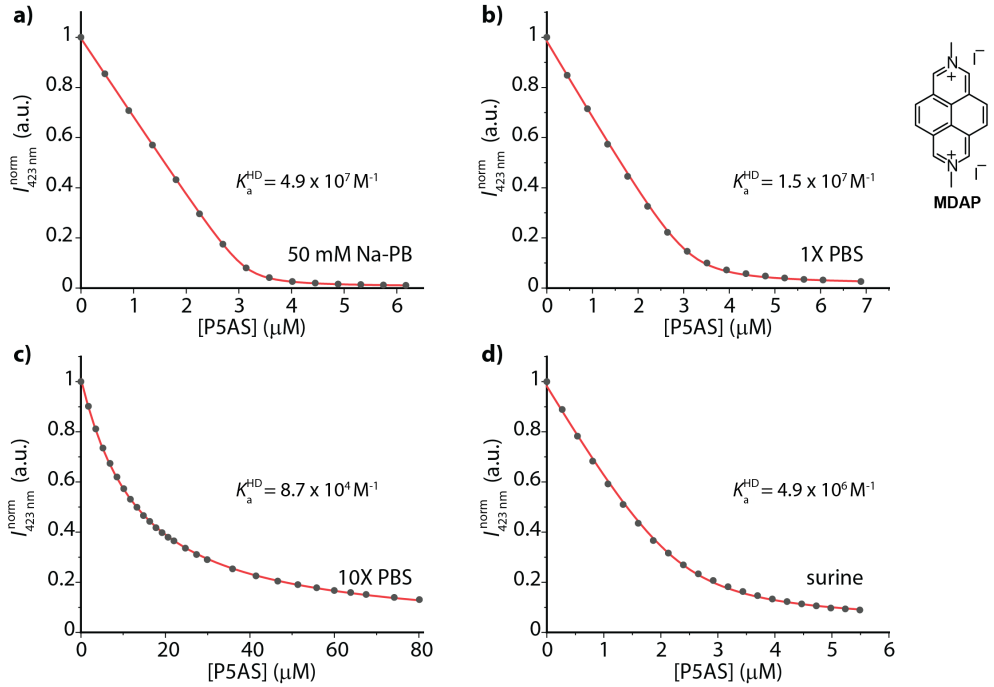

Figure 5.5: Normalized fluorescence emission intensity at 423 nm (λ_{exc} = 336 nm) of the indicator dye MDAP (3.1 μM) in (a) 50 mM sodium phosphate buffer (Na-PB), (b) 1X PBS, (c) 10X PBS and (d) surine (MDAP at 2.3 μM) upon stepwise addition of P5AS. The acquired data is depicted as grey dots, and the fitted data according to the thermodynamic DBA model as the red line. The binding constant obtained in each case is shown in their respective graphs.

Table 5.1: The binding constant (K_a^{HD}) for host-dye self-assembled P5AS•MDAP complex determined by fluorescence titration experiments at 25°C and fitting the data to a thermodynamic DBA model.

host	dye	medium[a]	K_a^{HD}[b]/ M^{-1}
P5AS	MDAP	50 mM Na-PB	$(4.9 \pm 0.1) \times 10^7$
		1X PBS	$(1.5 \pm 0.3) \times 10^7$
		10X PBS	$(8.7 \pm 0.1) \times 10^4$
		surine	$(4.9 \pm 0.4) \times 10^6$

[a] 1X PBS has a salt composition of 137 mM NaCl, 2.7 mM KCl, 10 mM Na_2HPO_4 and 1.8 mM KH_2PO_4. 10X PBS has a salt composition of 1.37 M NaCl, 27 mM KCl, 100 mM Na_2HPO_4, and 18 mM KH_2PO_4. [b] mean and standard deviation in parenthesis of at least 3 independent measurements.

in all cases studied, indicating that the P5AS•MDAP complex formed in all saline media tested. The binding constants listed in Table 5.1 show a relatively high binding affinity of MDAP with P5AS in both saline buffers (1.3 x 10^7 M^{-1} in 1X PBS) and biorelevant media (4.9 x 10^6 M^{-1} in surine). The P5AS•MDAP complex formation occurs even in the presence of 1.37 M NaCl with a binding constant of 8.7 x 10^4 M^{-1}, as observed in 10X PBS. These high binding affinities ensured the stability of the chemosensor even at high salt concentrations.

5.2.2. Binding studies of chemosensor with biogenic polyamines through fluorescence-based assays

5.2.2.1. Evaluation of binding kinetics

Figure 5.6 shows the kinetic traces recorded by monitoring the fluorescence emission intensity at 423 nm on the addition of the polyamine spermine to a solution of the fluorescence quenched P5AS•MDAP chemosensor in 1X PBS. A strong enhancement in the fluorescence signal was

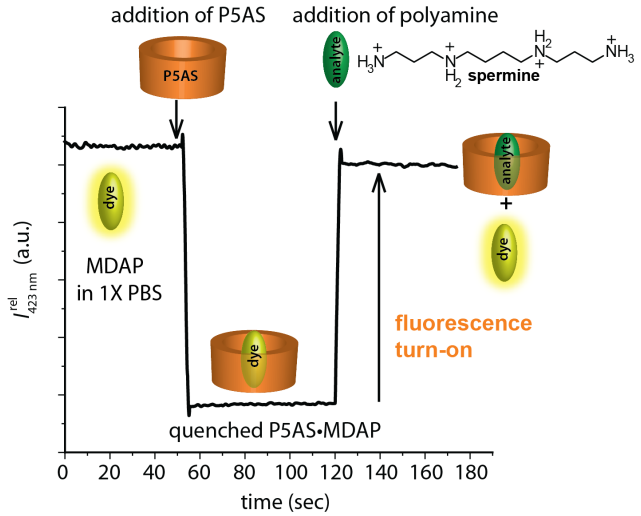

Figure 5.6: Relative fluorescence intensity changes with time at 423 nm (λ_{exc} = 336 nm) of MDAP (3.1 µM) in 1X PBS upon addition of P5AS (3.1 µM), resulting in the instantaneous formation of the fluorescence quenched P5AS•MDAP chemosensor. The addition of the stronger binder spermine (5.1 µM) to the media results in the displacement of MDAP from the host and a fluorescence signal "turn-on" achieved within a few milliseconds.

observed within a few milliseconds following the addition of spermine, indicating the displacement of the dye MDAP from P5AS by the stronger binding analyte spermine, resulting in a fluorescence "turn–on" signal. The kinetic traces recorded showed a rapid response of the P5AS•MDAP chemosensor to the presence of polyamines (Figure 5.6), enabling a broad analysis of samples with relatively short assay times. This is an important asset of the developed chemosensor-based assay compared to the conventional time-consuming HPLC-based detection methods.

5.2.2.2. Evaluation of binding affinities

The host-guest binding affinity of P5AS with biogenic polyamines, spermine, spermidine, and cadaverine was investigated through fluorescence displacement titrations based on the competitive displacement of the indicator dye MDAP from P5AS by the polyamine guest. Figure 5.7a displays the fluorescence emission intensity monitored at 423 nm upon stepwise addition of different polyamines to the P5AS•MDAP chemosensor in 1X PBS. The competitively binding guests resulted in the displacement of MDAP from P5AS in all three cases studied, accompanied by a strong fluorescence enhancement.

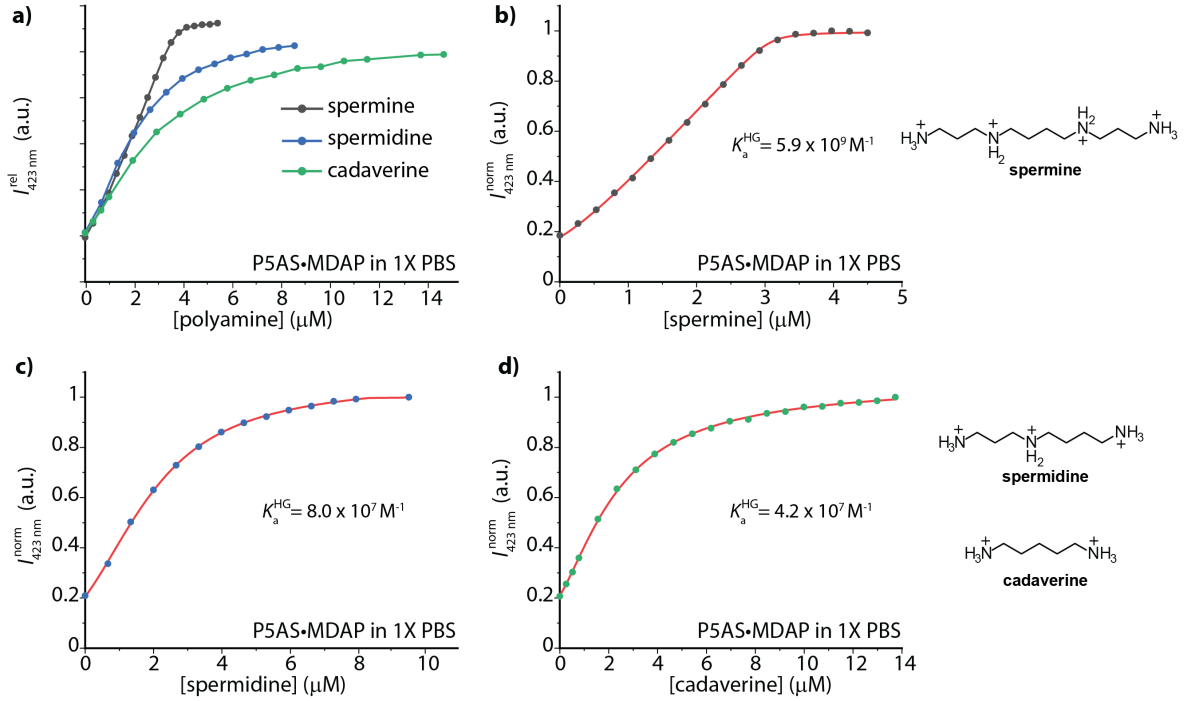

Figure 5.7: (a) Relative fluorescence emission intensity at 423 nm (λ_{exc} = 336 nm) of P5AS (3.1 μM) and MDAP (3.3 μM) upon stepwise addition of different polyamines, spermine, spermidine, or cadaverine in 1X PBS. (b-d) shows the fitted data as red line according to the competitive thermodynamic IDA model to obtain the host-guest binding affinities in the case of (b) spermine, (c) spermidine, and (d) cadaverine. The binding constant obtained in each case is shown in their respective graphs. Note: the individual data points in (a) were connected by line segments to guide the eye and do not represent fitting curves.

The binding curve was fitted following a competitive thermodynamic IDA model (see Eq.1.14-1.20 in General Introduction - Section 1.2.2) to obtain the binding constants of the analyzed polyamines with P5AS (Figure 5.7b-Figure 5.7d). The fitted details are summarized in Table 5.2.

Table 5.2: The host-guest binding constants (K_a^{HG}) for P5AS with polyamines determined by fluorescence dye displacement titration experiments (MDAP as dye) at 25ºC and fitting the data to a thermodynamic competitive IDA model.

host	guest	medium[a]	K_a^{HG}[b] / M^{-1}
P5AS	spermine	50 mM Na-PB	$(8.1 \pm 1.3) \times 10^9$
		1X PBS	$(5.9 \pm 0.5) \times 10^9$
		10X PBS	$(7.9 \pm 0.5) \times 10^5$
	spermidine	50 mM Na-PB	$(1.2 \pm 0.1) \times 10^8$
		1X PBS	$(7.9 \pm 0.6) \times 10^7$
	cadaverine	50 mM Na-PB	$(8.4 \pm 0.1) \times 10^7$
		1X PBS	$(4.2 \pm 0.1) \times 10^7$
		10X PBS	$(1.6 \pm 0.1) \times 10^5$

[a] 1X PBS has a salt composition of 137 mM NaCl, 2.7 mM KCl, 10 mM Na_2HPO_4 and 1.8 mM KH_2PO_4. 10X PBS has a salt composition of 1.37 M NaCl, 27 mM KCl, 100 mM Na_2HPO_4, and 18 mM KH_2PO_4. [b] mean and standard deviation in parenthesis of at least 3 independent measurements.

Spermine is the strongest binder to the host P5AS amongst the three biogenic polyamines studied, with a binding affinity of 5.9 x 10^9 M^{-1} in 1X PBS. This is followed by spermidine and cadaverine with a binding affinity of 8.0 x 10^7 M^{-1} and 4.2 x 10^7 M^{-1}, respectively in 1X PBS. These observed high binding affinities of P5AS with polyamines at high salt concentrations excludes any salt interferences on the recognition event. The binding affinity of P5AS with polyamines was also investigated in 50 mM Na-PB and 10X PBS similarly (see Table 5.2 and Figure 5.20– Figure 5.21 in Section 5.5 - Additional Information). Polyamines detection was possible even at the high salt concentrations (1.37 M NaCl) found in 10X PBS (Figure 5.21 in Section 5.5 - Additional Information). All three biogenic polyamines investigated showed a higher binding affinity for P5AS than the indicator dye MDAP (Table 5.1 and Table 5.2). Hence for sensing applications in biofluids, all the three polyamines, spermine, spermidine, and cadaverine, present in the sample media will result in the displacement of the dye on the addition of P5AS•MDAP chemosensor to the sample with a fluorescence "turn-on" signal output, whereas other weaker binding analytes, such as amino acids, cannot displace the dye. Therefore, P5AS•MDAP is suitable for the selective detection of the combined polyamine levels in biofluids.

5.2.3. Polyamine distinction through indicator dye modifications in the chemosensor

Chemosensors selective for individual polyamines are necessary to monitor their independent physiological effects in the body and devise personalized medicine strategies. With the utilized self-assembled host-dye chemosensor, fluorescence-based sensing of polyamines is achieved *via* the competition of the dye and the polyamine for the P5AS host. Consequently, the binding affinity of the host P5AS with the used indicator dye is crucial in determining and tuning the selectivity of the sensor for the polyamine of interest. Hence, new indicator dyes were tested to evaluate the selectivity of the obtained P5AS•dye chemosensor for different polyamines. A new dicationic diazapyrenium dye derivative with alkyl side chains, BuBrDAP (see Figure 5.2b and Section 5.5 - Additional Information for synthetic details), was developed, which displayed similar photophysical properties as MDAP, with absorption bands in the 300-450 nm region and strong emission in the 400-500 nm region with maxima at 423 nm in 1X PBS (Figure 5.8). The addition of P5AS to BuBrDAP in 1X PBS resulted in a 4 nm bathochromic shift at 334 nm of the dye absorption, accompanied by a strong quenching in the dye emission (Figure 5.8). In analogy to the previous system, this observation confirmed the formation of the self-assembled P5AS•BuBrDAP chemosensor. Here again, the binding of P5AS to BuBrDAP was instantaneous, resulting in the fluorescence quenched chemosensor within a few milliseconds.

Importantly, BuBrDAP displayed a stronger binding affinity for P5AS than MDAP. The fluorescence emission-based binding curve monitored at 423 nm upon titration of P5AS to BuBrDAP in 1X PBS displayed a steep curve (see Figure 5.9a), and a lower limit of the binding constant with a value >3.8 x 10^8 M^{-1} was obtained upon fitting the data to a thermodynamic DBA model (see Eq.1.9-1.13 in General Introduction - Section 1.2.2). As a result, to obtain the actual value of the binding constant, a competitive binding model was utilized, which followed the stepwise addition of the competitor, spermine, to P5AS•BuBrDAP in 1X PBS.

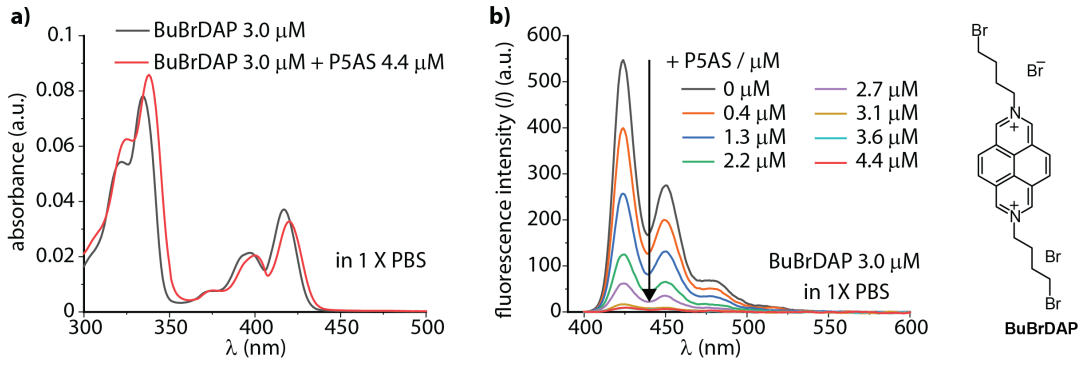

Figure 5.8: (a) Absorbance and (b) fluorescence emission spectra (λ_{exc} = 335 nm) of BuBrDAP (3.0 µM) before and after addition of P5AS (0-4.4 µM) in 1X PBS.

Figure 5.9b displays the fluorescence emission intensity monitored at 423 nm upon increasing addition of spermine to P5AS•BuBrDAP in 1X PBS, which resulted in the displacement of BuBrDAP from P5AS, accompanied by a strong fluorescence enhancement. The binding curve was fitted following a competitive thermodynamic IDA model (see Eq.1.14-1.20 in General Introduction - Section 1.2.2). The binding constant of P5AS with spermine reported in Table 5.2 was used as an input parameter in the fitting to obtain the binding constant of P5AS with BuBrDAP. BuBrDAP binds to the host P5AS with a binding constant of 2.1 x 10^9 M^{-1} in 1X PBS (see Figure 5.9b), that means, 10^2 times stronger to the host P5AS than MDAP. Additionally, the binding was also assessed in surine. The fluorescence emission-based binding curve at 423 nm on titration of P5AS to BuBrDAP in surine was not as steep as observed in 1X PBS, and the acquired data was fittable by a thermodynamic DBA model (see Eq.1.9-1.13 in General Introduction - Section 1.2.2) to obtain a binding constant of 4.5 x 10^8 M^{-1} for P5AS with BuBrDAP in surine (Figure 5.9c).

On comparing the binding affinities listed in Table 5.2 and Table 5.3 for the polyamines with P5AS versus the indicator dye BuBrDAP with P5AS in 1X PBS, it was explicit that amongst the three biogenic polyamines, only spermine has a stronger binding affinity for the host P5AS

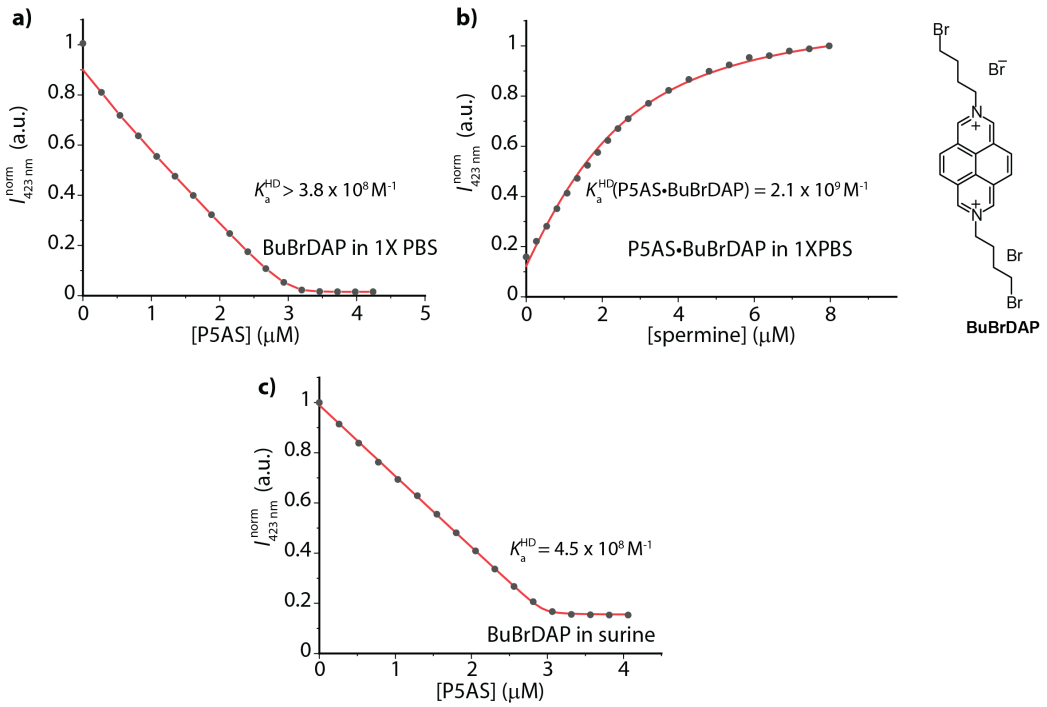

Figure 5.9: (a) Normalized fluorescence emission intensity at 423 nm (λ_{exc} = 335 nm) of (a) the indicator dye BuBrDAP (3.0 μM) in 1X PBS upon stepwise addition of P5AS, (b) P5AS (3.1 μM) and BuBrDAP (3.3 μM) in 1X PBS upon stepwise addition of spermine, and (c) the indicator dye BuBrDAP (3.0 μM) in surine upon stepwise addition of P5AS. The acquired data is depicted as grey dots, and the fitted data according to the thermodynamic DBA model as the red line in (a) and (c) and the thermodynamic competitive IDA model as the red line in (b). The binding constant obtained in each case is shown in their respective graphs.

Table 5.3: The binding constant (K_a^{HD}) for host-dye self-assembled P5AS•BuBrDAP complex determined by fluorescence titration experiments at 25°C and fitting the data to a thermodynamic DBA or a competitive IDA model.

host	dye	medium[a]	K_a^{HD}[b] / M^{-1}
P5AS	BuBrDAP	1X PBS[c]	$(2.1 \pm 0.4) \times 10^9$
		surine[d]	$(4.5 \pm 1.3) \times 10^8$

[a] 1X PBS has a salt composition of 137 mM NaCl, 2.7 mM KCl, 10 mM Na_2HPO_4 and 1.8 mM KH_2PO_4. [b] mean and standard deviation in parenthesis of at least 3 independent measurements. [c] determined by IDA with spermine as a competitor. [d] determined by DBA.

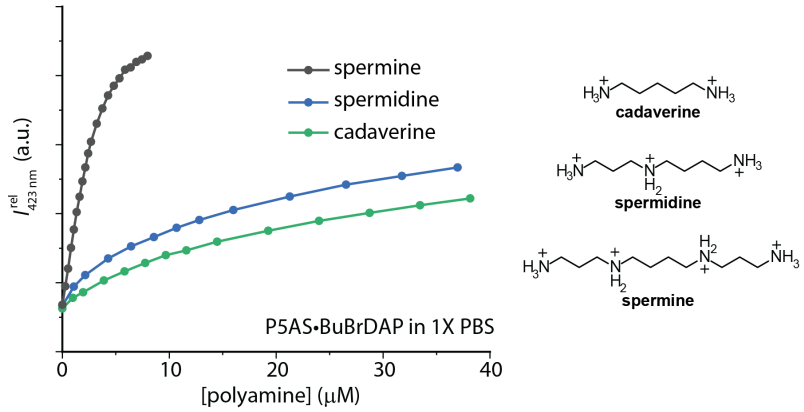

Figure 5.10: (a) Relative fluorescence emission intensity at 423 nm (λ_{exc} = 335 nm) of P5AS (3.1 μM) and BuBrDAP (3.3 μM) upon stepwise addition of different polyamines, spermine, spermidine or cadaverine in 1X PBS. Note: the individual data points were connected by line segments to guide the eye and do not represent fitting curves.

than the indicator dye BuBrDAP, and can hence displace the dye from the host in the self-assembled host-dye chemosensor in the sensing assay. On the other hand, other lower binding polyamines, spermidine, and cadaverine cannot displace the dye unless when present in a high concentration over the P5AS•BuBrDAP in the media. This was confirmed by monitoring the fluorescence emission intensity at 423 nm upon stepwise addition of different polyamines to the P5AS•BuBrDAP chemosensor in 1X PBS (Figure 5.10). As can be seen in Figure 5.10, P5AS•BuBrDAP was selective for spermine detection with a strong fluorescence signal enhancement, while a high excess concentration of spermidine or cadaverine was required to obtain a slight signal enhancement under the same conditions tested. Thus, P5AS•BuBrDAP can be utilized for the selective detection of spermine in biofluids.

5.2.4. Functionality evaluation of designed chemosensors for polyamine sensing with a fluorescence turn-on response

The functionality of the chemosensors, P5AS•MDAP and P5AS•BuBrDAP, were evaluated in biofluids for the selective sensing of polyamines with a fluorescence "turn-on" signal output. Hence, a new method was devised using the developed chemosensors to detect and analyze the

polyamine levels present in biofluids. In short, the fluorescence quenched host-dye chemosensor, P5AS•MDAP or P5AS•BuBrDAP, was titrated to the biofluid sample. The increasing addition of the chemosensor will result in the displacement of the indicator dye from the host by the stronger binding polyamines present in the media, resulting in a fluorescence "turn-on" signal arising from the free dye released into the media. However, once the host has complexed all the polyamines in the media, a further increase in the concentration of the fluorescence quenched host-dye chemosensor will result in no significant further fluorescence enhancement. Hence the different polyamine concentration levels in biofluids can be analyzed through their distinct fluorescence "turn–on" signal outputs. See Figure 5.11 for a schematic representation of the sensing assay in biofluids and a simulation of trends in fluorescence intensity with the increasing addition of chemosensor.

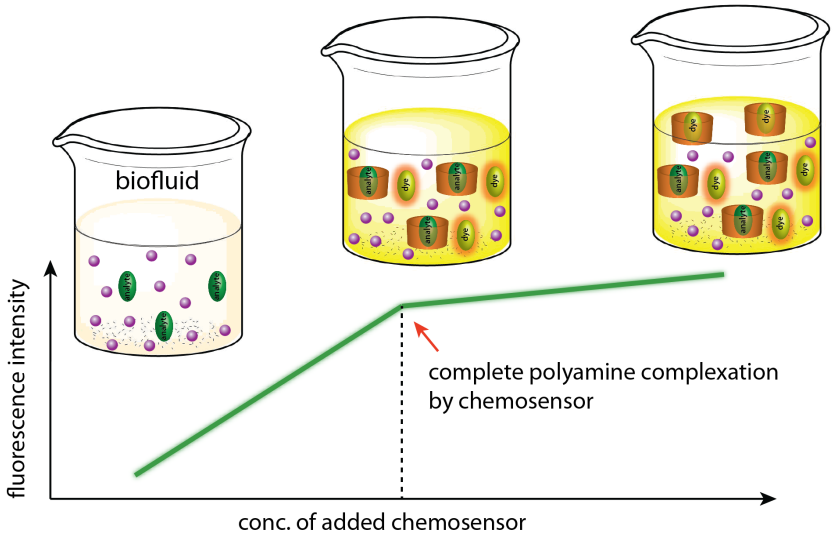

Figure 5.11: Schematic representation of polyamine detection with the self-assembled host-dye chemosensor in biofluids and simulation of the trends in fluorescent intensity with increasing addition of the chemosensor

5.2.4.1. Preliminary tests in artificial urine (surine) and neurobasal medium

Prior to measurements in real biofluids, the performance of the chemosensor-based sensing assay was evaluated in artificial urine (surine). To mimic urine samples, several surine samples spiked with individual polyamines (spermine, spermidine, or cadaverine) or polyamine mixtures were utilized. The P5AS•MDAP and P5AS•BuBrDAP chemosensor stock solutions were freshly prepared in 1X PBS by simply mixing the P5AS and the respective indicator dye solutions for each case study. The titration of the P5AS•MDAP chemosensor to surine resulted in a significant fluorescence "turn-on" signal when monitored at 423 nm for samples spiked with individual polyamines and polyamine mixture when compared to the background signal observed from the chemosensor in the absence of any polyamines in surine (Figure 5.12c). See

Figure 5.12a and 5.12b for absorption and emission spectra of P5AS•MDAP in the absence and presence of spermine in surine. On titration of P5AS•BuBrDAP chemosensor, a significant fluorescence "turn-on" signal when monitored at 423 nm was observed only for surine samples spiked with spermine. In contrast, other polyamines, such as cadaverine or spermidine, in the sample did not result in a significant fluorescence enhancement when compared to the background signal observed in the absence of any polyamines in surine (Figure 5.13c). See Figure 5.13a and 5.13b for absorption and emission spectra of P5AS•BuBrDAP in the absence and presence of spermine in surine. The polyamine putrescine was also evaluated here and gave no fluorescence signal change compared to the background chemosensor emission in surine (Figure 5.12c and Figure 5.13c). This indicated that putrescine could not displace the dye from the host in the self-assembled chemosensor and hence, will not interfere in the sensing assay.

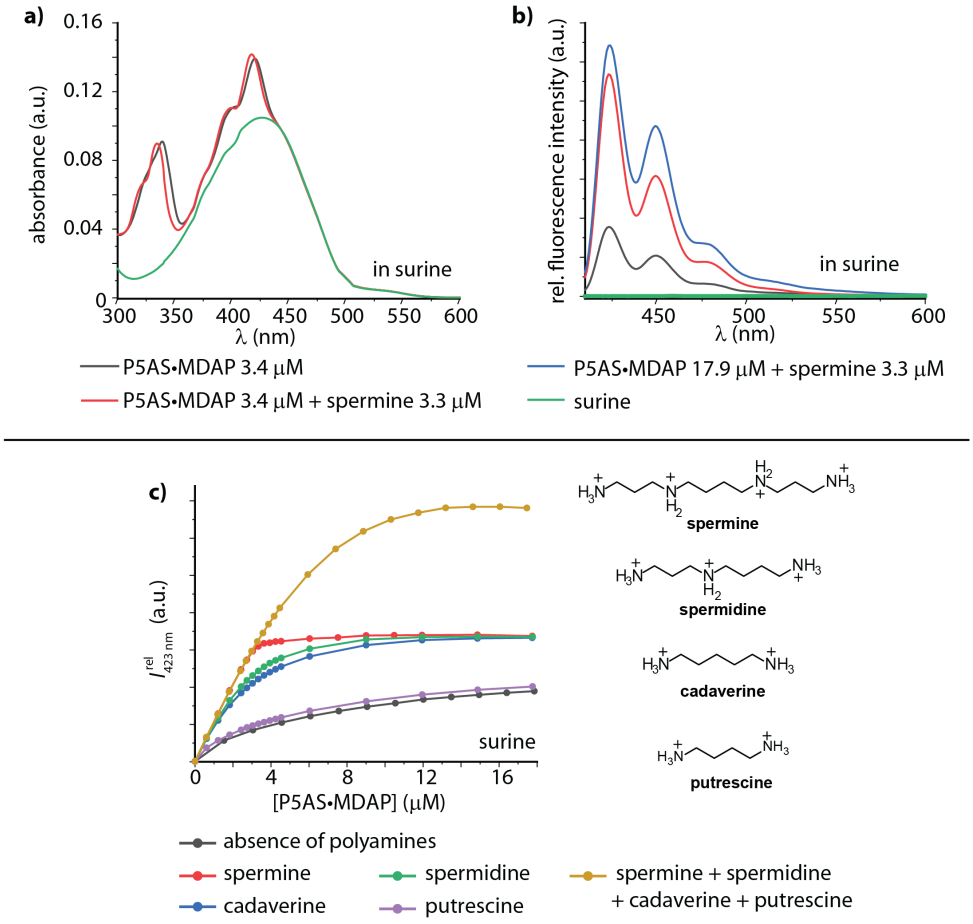

Figure 5.12: (a) Absorbance and (b) fluorescence emission spectra (λ_{exc} = 397 nm) of surine samples containing (P5AS•MDAP (3.4 μM) (black line), P5AS•MDAP (3.4 μM) in the presence of spermine (3.3 μM) (red line), and excess P5AS•MDAP (17.9 μM) in the presence of spermine (3.3 μM) (blue line). The green line represents the absorbance and emission spectra of surine alone.(c) The relative fluorescence emission intensity changes monitored at 423 nm upon addition of P5AS•MDAP and chemosensor to a solution of surine spiked with spermine (3.3 μM, red line), spermidine (3.3 μM, green line), cadaverine (3.3 μM, blue line), putrescine (3.3 μM, purple line) and a mixture of all four polyamines (each at 3.3 μM, yellow line) (λ_{exc} = 397 nm). The black line represents the fluorescence intensity from the chemosensor alone in the absence of any polyamines in surine.

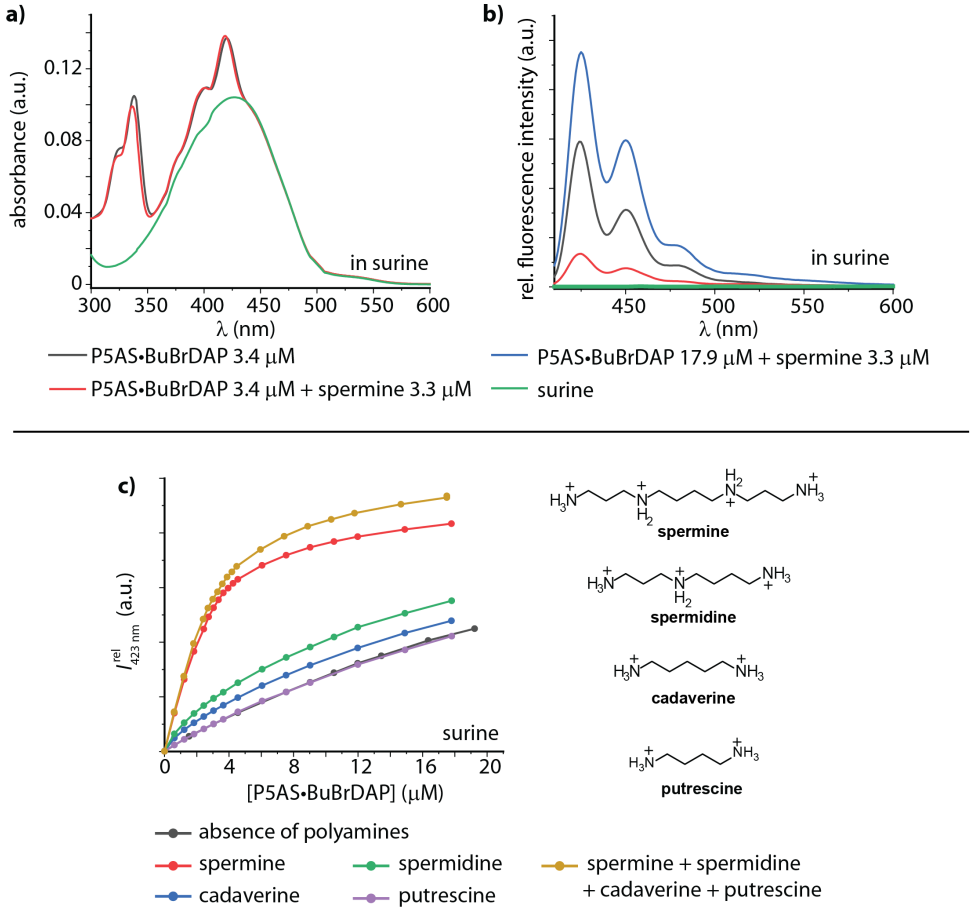

Figure 5.13: (a) Absorbance and (b) fluorescence emission spectra (λ_{exc} = 400 nm) of surine samples containing P5AS•BuBrDAP (3.4 μM) (black line), P5AS•BuBrDAP (3.4 μM) in the presence of spermine (3.3 μM) (red line), and excess P5AS•BuBrDAP (17.9 μM) in the presence of spermine (3.3 μM) (blue line). The green line represents the absorbance and emission spectra of surine alone. (c) The relative fluorescence emission intensity changes monitored at 423 nm upon addition of P5AS•BuBrDAP chemosensor to a solution of surine spiked with spermine (3.3 μM, red line), spermidine (3.3 μM, green line), cadaverine (3.3 μM, blue line), putrescine (3.3 μM, purple line) and a mixture of all four polyamines (each at 3.3 μM, yellow line) (λ_{exc} = 400 nm). The black line represents the fluorescence intensity from the chemosensor alone in the absence of any polyamines in surine.

Moreover, it was also possible to distinguish the different concentrations of spermine in surine upon addition of the chemosensor (*e.g.,* P5AS•MDAP) to the samples through the distinct fluorescence "turn-on" signal output (Figure 5.14). Additionally, the sensing assay exhibited a significant sensitivity, and detection of spermine levels down to 1 μM was possible (Figure 5.14). A slight reduction in the fluorescence intensity for the experiment carried out at 6.8 μM spermine on increasing addition of the chemosensor after all the polyamines in the media have been complexed by the host, can be due to the interaction of the free dye in the media with the added chemosensor (for *e.g.*, in Figure 5.14).

Several reports have shown elevated polyamine levels in the urine of cancer patients, which can be used as diagnostic markers for early-stage cancer detection and to evaluate the responsiveness of patients to cancer therapy.[400,424-427] Hence, the polyamine levels in the urine

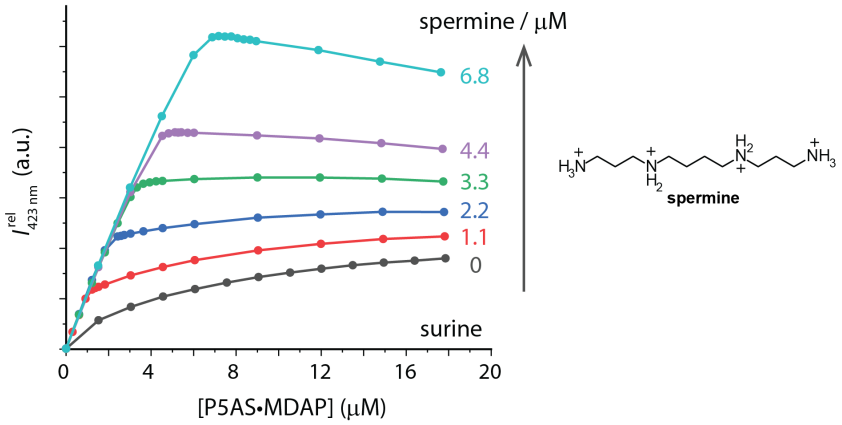

Figure 5.14: The relative fluorescence emission intensity changes monitored at 423 nm (λ_{exc} = 397 nm) upon addition of P5AS•MDAP chemosensor to a solution of surine with varying concentrations of spermine (0-6.8 µM), resulting in distinguishable fluorescence "turn-on" signal outputs.

of healthy individuals and cancer patients were simulated in surine from data collected from literature reports[400,424-427], and the utility of the developed chemosensors to distinguish between healthy and diseased samples were tested. In essence, surine was spiked with 8.8 µM spermine, 10.7 µM spermidine, 17.1 µM cadaverine, and 15.5 µM putrescine to simulate urine of healthy individuals and with 46.6 µM spermine, 25.3 µM spermidine, 62.2 µM cadaverine, and 59.5 µM putrescine to simulate urine of cancer patients. The samples were then diluted 8 times with surine (having no polyamines added) to avoid signal saturation and inner filter effects on the addition of chemosensor. As a result, the concentrations for analysis were 1.1 µM spermine, 1.3 µM spermidine, 2.1 µM cadaverine, and 1.9 µM putrescine in surine corresponding to healthy individuals, and 5.8 µM spermine, 3.2 µM spermidine, 7.8 µM cadaverine, and 7.4 µM putrescine in surine corresponding to cancer patients. Titration of the chemosensors, P5AS•MDAP and P5AS•BuBrDAP, to both the surine samples showed clearly distinguishable fluorescence "turn-on" signal outputs when monitored at 423 nm for healthy and diseased samples (Figure 5.15a and Figure 5.15b). Hence, the functionality assessments of the chemosensors in surine showed promising results for their practical applications for polyamine detection in real urine samples.

Apart from surine, the functionality of the chemosensors was also evaluated in more complex biorelevant media, such as neurobasal™ medium, which consists of 37 different components, including amino acids, vitamins, and inorganic salts (see Figure 5.16 and Figure 5.17). This is also an interesting media for polyamine sensing studies as reports have shown increased levels of polyamines in the cerebrospinal fluid for human brain tumors.[428] The neurobasal™ medium does not contain any polyamines and was hence spiked with spermine prior to conducting the sensing assay with the developed chemosensors.

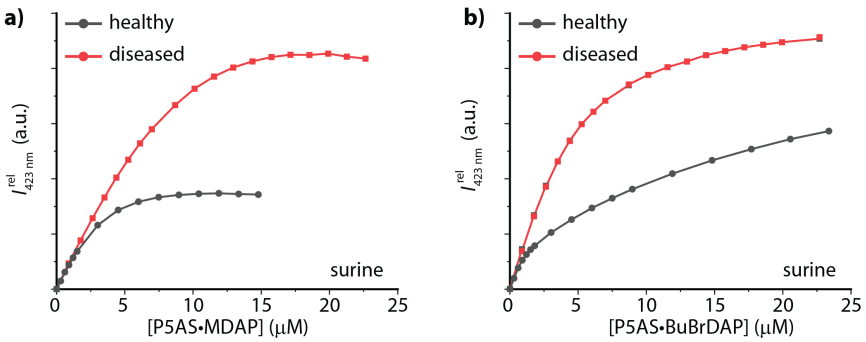

Figure 5.15: Relative fluorescence emission intensity changes at 423 nm on the addition of (a) P5AS•MDAP and (b) P5AS•BuBrDAP chemosensor to surine samples with a simulated concentration of polyamines corresponding to the urine of healthy individuals (1.1 μM spermine, 1.3 μM spermidine, 2.1 μM cadaverine, and 1.9 μM putrescine) and urine of cancer patients (5.8 μM spermine, 3.2 μM spermidine, 7.8 μM cadaverine, and 7.4 μM putrescine). (λ_{exc} = 397 nm for P5AS•MDAP and 405 nm for P5AS•BuBrDAP)

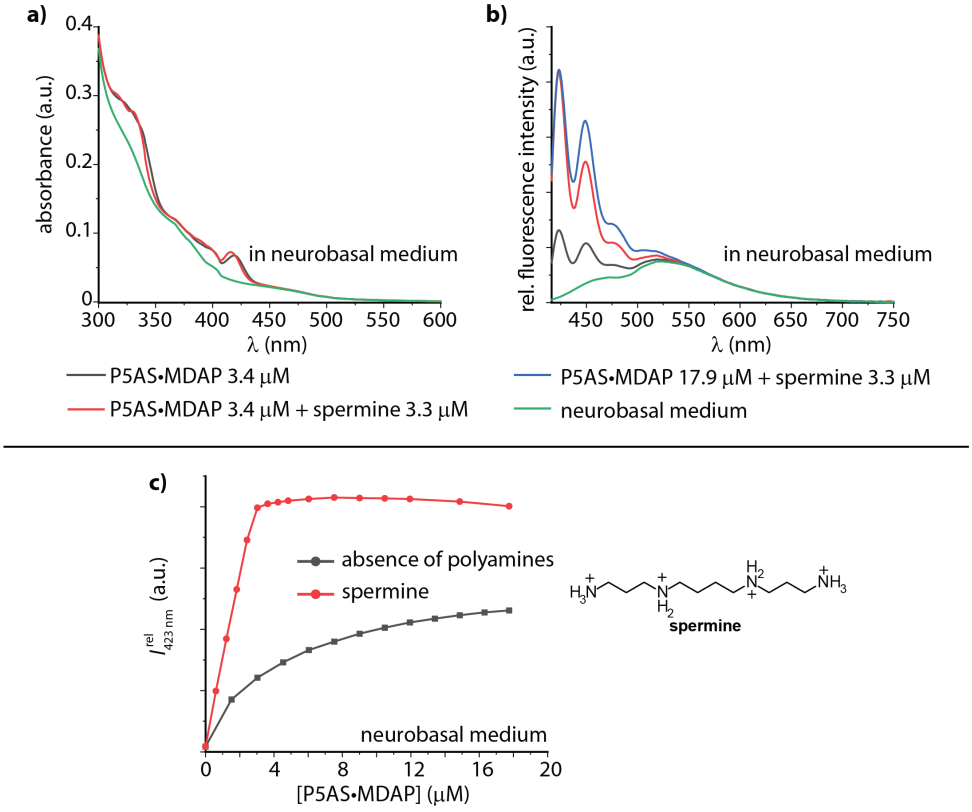

Figure 5.16: (a) Absorbance and (b) fluorescence emission spectra (λ_{exc} = 406 nm) of neurobasal™ medium containing P5AS•MDAP (3.4 μM) (black line), P5AS•MDAP (3.4 μM) in the presence of spermine (3.3 μM) (red line), and excess P5AS•MDAP (17.9 μM) in the presence of spermine (3.3 μM) (blue line). The green line represents the absorbance and emission spectra of neurobasal™ medium alone. (c) The relative fluorescence emission intensity changes monitored at 423 nm (λ_{exc} = 406 nm) upon addition of P5AS•MDAP chemosensor to a solution of neurobasal™ medium spiked with spermine (3.3 μM, red line). The black line represents the fluorescence intensity from the chemosensor alone in the absence of any polyamines in neurobasal™ medium.

The addition of the chemosensors, P5AS•MDAP and P5AS•BuBrDAP (freshly prepared in 1X PBS) to neurobasal™ medium containing spermine resulted in strong fluorescence "turn-on" signal when monitored at 423 nm (Figure 5.16c and Figure 5.17c). See Figure 5.16a-b and Figure 5.17a-b for absorption and emission spectra of P5AS•MDAP and P5AS•BuBrDAP in the absence and presence of spermine in neurobasal™ medium, respectively. This confirmed functionality of the chemosensors in neurobasal™ medium and demonstrated a selective detection of polyamines in the absence of any significant matrix interferences from other biomolecules (amino acids, vitamins, salts, etc.) in the media.

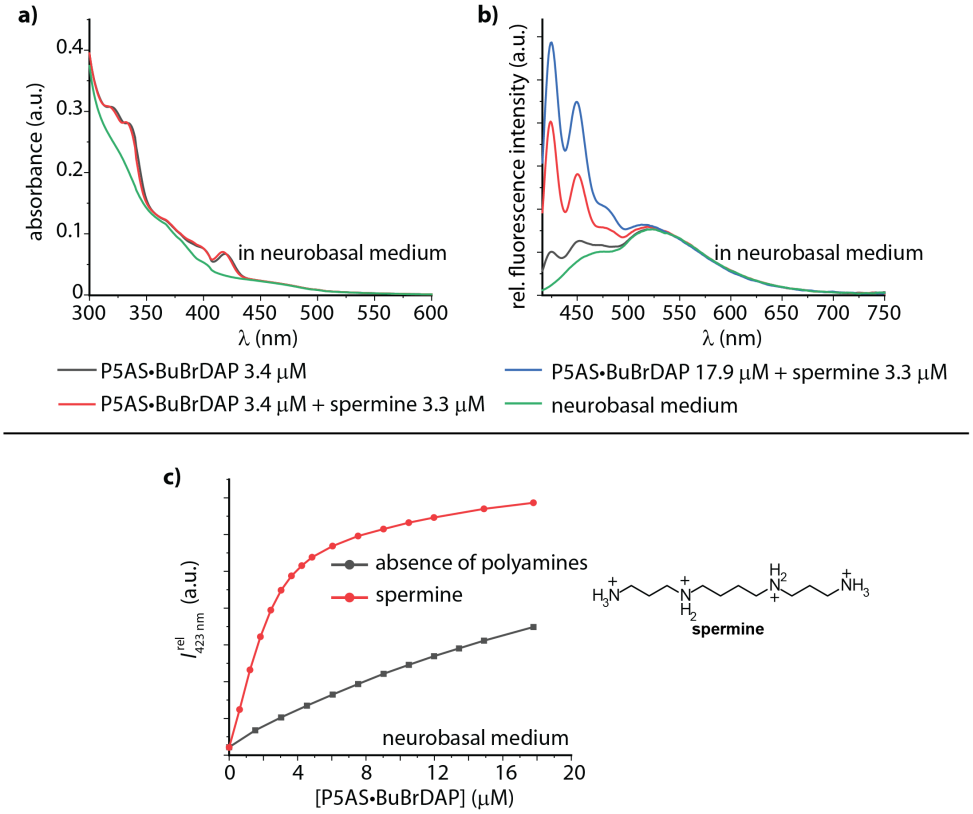

Figure 5.17: (a) Absorbance and (b) fluorescence emission spectra (λ_{exc} = 406 nm) of neurobasal™ medium containing P5AS•BuBrDAP (3.4 μM) (black line), P5AS•BuBrDAP (3.4 μM) in the presence of spermine (3.3 μM) (red line), and excess P5AS•BuBrDAP (17.9 μM) in the presence of spermine (3.3 μM) (blue line). The green line represents the absorbance and emission spectra of neurobasal™ medium alone. (c) The relative fluorescence emission intensity changes monitored at 423 nm (λ_{exc} = 406 nm) upon addition of P5AS•BuBrDAP chemosensor to a solution of neurobasal™ medium spiked with spermine (3.3 μM, red line). The black line represents the fluorescence intensity from the chemosensor alone in the absence of any polyamines in neurobasal™ medium.

5.2.4.2. Selective polyamine sensing in biofluids: human urine and saliva

Having promising results in surine, the designed chemosensors, P5AS•MDAP and P5AS•BuBrDAP, were utilized for the detection of biogenic polyamines present in human urine. For most analyte detection studies in biofluids, the analysis of urine samples is often preferred due to several advantages such as its ready availability, ease of obtaining, being non-invasive, and

often contains higher concentrations of biorelevant analytes than other biofluids such as blood.[429-432] For the chemosensor-based polyamine detection studies, spot urine samples were collected from four healthy adult volunteers (the first urine of the day was omitted) and used as such without any pre-treatment or pH adjustment. Urine samples have strong absorption and fluorescence background signal arising from various other metabolites present in urine[431] that absorb/emit light (see Figure 5.22 in Section 5.5 - Additional Information). Hence, two solutions were adopted to keep the urine fluorescence background signal to a minimum and not interfere with the sensing assay. Firstly, dilution of the urine sample before the measurement, and secondly, exciting the sample where the absorbance from urine is minimum, helped reduce the strong urine fluorescence background signal (see Figure 5.22 in Section 5.5 - Additional Information). Thus, the collected urine samples from four healthy individuals were diluted two times (2x) with 1X PBS prior to the measurements. In order to mimic urine samples from disease patients (*e.g.,* cancer patients) featuring elevated polyamine levels, the 2x diluted urine samples from four healthy individuals were spiked with individual polyamines (spermine, spermidine, or cadaverine) or polyamine mixtures. The assay was conducted in a microwell plate, and the fluorescence signal changes on the addition of the P5AS•MDAP or P5AS•BuBrDAP chemosensor (freshly prepared in 1X PBS) to urine samples were followed by monitoring the emission intensity at 423 nm on exciting the sample at 406 nm (Figure 5.18). Prior to the addition of the chemosensor in the sensing assay, the urine fluorescence background signal from each sample was recorded and later subtracted from the signal intensity observed on the addition of the chemosensor. Selective detection of biogenic polyamines, spermine, spermidine, and cadaverine in human urine was achieved on addition of P5AS•MDAP chemosensor, marked by a strong fluorescence "turn-on" signal (Figure 5.18a). In addition, it was possible to clearly distinguish between healthy urine samples and urine samples spiked with elevated polyamine levels in all cases studied through their distinct fluorescence "turn-on" signal outputs (Figure 5.18a). The addition of P5AS•BuBrDAP chemosensor to urine samples resulted in selective spermine detection, and a clear distinction between the signal outputs between healthy and urine samples spiked with elevated polyamines levels was observed only for samples spiked with spermine (Figure 5.18b). No distinction was possible for samples spiked with spermidine or cadaverine alone (Figure 5.18b).

The detection of biogenic polyamines was also conducted in human saliva through the fluorescence-based assay utilizing P5AS•MDAP and P5AS•BuBrDAP chemosensor. Thus, a saliva sample was collected from a healthy adult volunteer and later spiked with individual polyamines (spermine, spermidine, or cadaverine) or polyamine mixtures to mimic the saliva samples from disease patients (*e.g.,* cancer patients) featuring elevated polyamine levels.

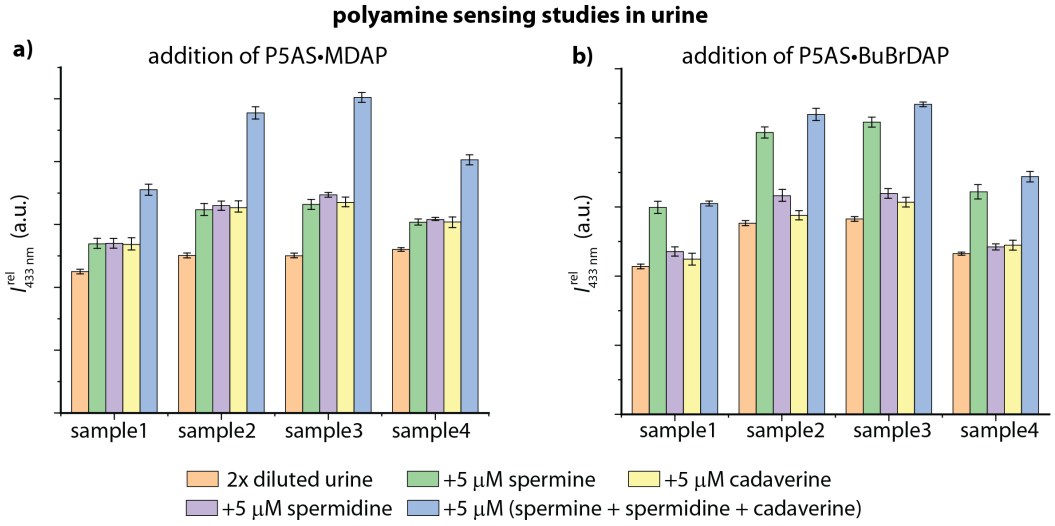

Figure 5.18: Relative fluorescence emission intensity changes monitored at 433 nm (λ_{exc} = 406 nm) on the addition of (a) P5AS•MDAP chemosensor (21.6 μM) and (b) P5AS•BuBrDAP chemosensor (21.6 μM) to human urine samples (diluted 2 times with 1X PBS) collected from 4 healthy individuals (sample1-sample4) and later spiked with several polyamines (at 5 μM) and polyamine mixtures (each at 5 μM) in order to simulate urine from disease patients (microplate assay). The vertical error bars in the bar graph represent the standard deviation in the collected fluorescence intensity from four repetitions. The urine fluorescence background signal was subtracted from the fluorescence signal intensity obtained following the addition of the chemosensor in all cases studied.

The saliva sample displayed only minimal fluorescence background signal compared to urine and hence, was utilized undiluted for the measurements. The fluorescence emission intensity monitored at 423 nm on exciting the sample at 406 nm showed clearly distinguishable fluorescence "turn-on" signal outputs on the addition of P5AS•MDAP chemosensor for healthy saliva samples and saliva samples spiked with elevated polyamines levels in all cases studied (Figure 5.19a). In contrast, only saliva samples spiked with spermine gave distinct fluorescence "turn-on" signal outputs from the healthy saliva sample on the addition of P5AS•BuBrDAP chemosensor (Figure 5.19b).

The biogenic polyamine sensing studies conducted in human urine and saliva confirmed that P5AS•MDAP can be used to selectively detect the combined polyamine levels in biofluids and distinguish between healthy and elevated polyamine levels. This may become advantageous for early disease detection, such as in cancer or Alzheimer's patients, marked by a spike in the combined polyamine levels in biofluids. Moreover, with the P5AS•BuBrDAP chemosensor, selective spermine detection and the distinction between healthy and elevated spermine levels in biofluids is possible, which is helpful in monitoring its individual physiological effects in the body.

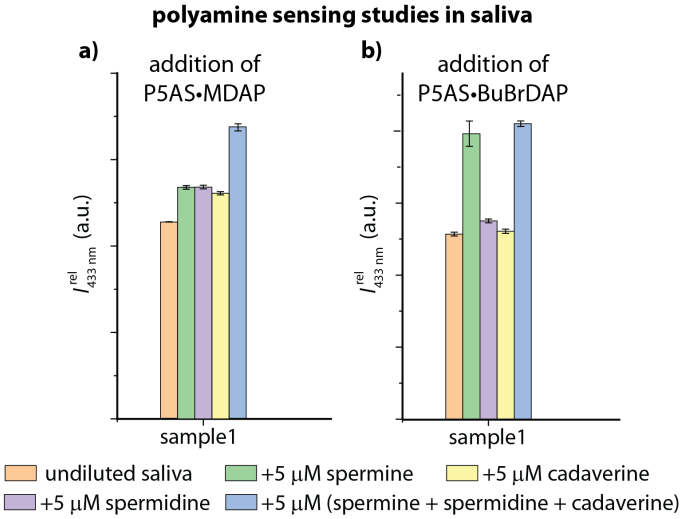

Figure 5.19: Relative fluorescence emission intensity changes monitored at 433 nm (λ_{exc} = 406 nm) on the addition of (a) P5AS•MDAP chemosensor (21.6 μM) and (b) P5AS•BuBrDAP chemosensor (21.6 μM) to human saliva samples (undiluted) collected from a healthy individual (sample1) and later spiked with several polyamines (at 5 μM) and polyamine mixtures (each at 5 μM) in order to stimulate saliva from disease patients (microplate assay). The vertical error bars in the bar graph represent the standard deviation in the collected fluorescence emission intensity from four repetitions. The saliva fluorescence background signal was subtracted from the fluorescence signal intensity obtained following the addition of the chemosensor in all cases studied.

To further establish the practical applicability of the developed chemosensor-based sensing assay and its medical diagnostic applications, human urine and saliva samples collected from a group of actual disease patients, for *e.g.*, suffering from cancer, needs to be compared to a group of healthy individuals to carry out a statistical verification of the procedure. In addition, a comparison of the determined polyamine levels through the chemosensor-based fluorescence assay with concentration values obtained in specialized laboratories with certified polyamine tests will enable an accurate determination of the polyamine concentrations in the sample and hence, provide further validation of the chemosensor assay for future applications. A cooperation project with Dr. Michael Kiehntopf at the Institut für Klinische Chemie und Laboratoriumsdiagnostik, Jena is proposed for the mentioned studies.

Likewise, the design of new P5AS•dye chemosensors with distinct fluorescence response features towards the presence of polyamines will open up opportunities for numerous sensing applications. The P5AS•dye combinations can then be employed for differential sensing and unique identification of polyamines through their fluorescence response pattern and mathematical treatment of the measured data by principal component analysis (PCA).[75]

5.3. Conclusion

In conclusion, two novel self-assembled host-dye chemosensors from pillar[*n*]arene-based host (P5AS) in combination with tailor-made dicationic indicator dyes (MDAP or BuBrDAP) were developed for the fluorescence-based detection of biogenic polyamines in saline buffers and biofluids. The very high binding affinity of P5AS•MDAP and P5AS•BuBrDAP chemosensor in saline and biorelevant media with high millimolar salt concentrations ensured the stability of the chemosensor for their practical applications in biofluids. Polyamine sensing was achieved by the competitive displacement of the indicator dye from the host by the stronger binding polyamines in the sample media, resulting in a fluorescence "turn-on" signal within a few milliseconds. Furthermore, the high binding affinity of the host for polyamines excluded salt interferences on the sensing assay. Functionality evaluation of the chemosensors in artificial urine (surine) and later in human urine and saliva samples displayed a selective detection of the combined polyamine levels in biofluids by P5AS•MDAP chemosensor and a selective spermine detection by P5AS•BuBrDAP chemosensor with significant sensitivity (detection down to 1 μM of spermine). The binding affinity of the indicator dye for the host can be used to tune the selectivity of the chemosensor for different polyamines of interest. Additionally, lower affinity analytes, including salts and other biomolecules in the media, cannot displace the dye from the host and hence do not interfere in the sensing assay, making selective polyamine detection feasible. Importantly, it was possible to distinguish between healthy and elevated levels of polyamines (*e.g.*, as present in cancer patients) in human urine and saliva samples through the distinct fluorescence "turn-on" signal outputs obtained on the addition of the chemosensor. Hence, the newly developed fluorescent chemosensors for polyamines, on account of their simplicity, cost-effectiveness, and fast detection capabilities, will assist the future development of rapid diagnostic tests for home-use and point-of-care applications.

5.4. Experimental details

5.4.1. Materials

All solvents were used as received from Aldrich or Fluka without further purification. All chemicals were purchased and used as received unless stated otherwise. The host P5AS[90] and indicator dye MDAP[246,247] were synthesized according to literature procedures. The indicator dye BuBrDAP was synthesized according to procedures described in Section 5.5 - Additional Information. Dr. Pronay Kumar Biswas and Dr. Laura Grimm from the research group of Dr. Frank Biedermann carried out the synthesis of the host P5AS and the indicator dyes, MDAP and BuBrDAP, respectively. The stock solutions of 1X PBS (137 mM NaCl, 2.7 mM KCl,

10 mM Na_2HPO_4 and 1.8 mM KH_2PO_4) and 10X PBS (1.37 M NaCl, 27 mM KCl, 100 mM Na_2HPO_4 and 18 mM KH_2PO_4) were prepared from Gibco™ PBS tablets by dissolving a tablet in 500 mL or 50 mL of distilled water, respectively. The pH was 7.45 and required no adjustment. The 50 mM sodium phosphate buffer (Na-PB) was prepared from 28.9 mM sodium phosphate dibasic heptahydrate and 21.1 mM sodium phosphate dibasic heptahydrate, and the pH was adjusted to 7.0 using 1 M HCl or 1 M NaOH. Surine was purchased from Cerilliant and used as received. The neurobasal™ medium (minus phenol red) was purchased from Thermo Fisher Scientific and used as received.

5.4.2. Instrumentation

Absorption spectra were measured on a Jasco V-730 double-beam UV–VIS spectrophotometer and baseline corrected. Steady-state emission spectra and time-resolved emission profiles were recorded on a Jasco FP-8300 fluorescence spectrometer equipped with a 150 W xenon arc lamp, single-grating excitation, and emission monochromators. Emission and excitation spectra were corrected for source intensity (lamp and grating) and the emission spectral response (detector and grating) by standard correction curves. All experiments were carried out at 25 °C by using a water thermostated cell holder STR-812, while the cuvettes were equipped with a stirrer allowing rapid mixing. For spectroscopy analysis in cuvettes, UV plastic cuvettes with a light path of 10 mm and dimensions of 10x10 mm from Brand with a spectroscopic cut-off at 230 nm were utilized.

Microplate assays were performed on EnSight™ multimode plate reader by Perkin Elmer equipped with fluorescence intensity detection with monochromator (top- and bottom-reading) as well as filter- and monochromator-based absorbance detection with the temperature control unit of the plate reader set at 25 °C. All measurements were conducted in black opaque OptiPlate-96 polystyrene microplates supplied by Perkin Elmer.

The NMR spectra of the compounds described herein were recorded on a Bruker Avance 500 at 500 MHz for ^{1}H NMR and 126 MHz for ^{13}C NMR. The NMR spectra were recorded at room temperature in deuterated solvents acquired from Eurisotop. The chemical shift δ is displayed in parts per million [ppm] and the references used were the ^{1}H and ^{13}C peaks of the solvents themselves. For the characterization of centrosymmetric signals, the signals median point was chosen, for multiplets the signal range. The multiplicities of the signals were abbreviated as follows: s = singlet, d = doublet, t = triplet, quart = quartet, quin = quintet, m = multiplet. All coupling constants (*J*) are stated as modulus in Hertz (Hz). Signals of the ^{13}C spectrum were assigned with the help of distortionless enhancement by polarization transfer spectra (DEPT)

and stated as follows: DEPT: "+" = primary or secondary carbon atoms (positive DEPT-signal), "–" = secondary carbon atoms (negative DEPT-signal), Cq = quaternary carbon atoms (no DEPT-signal).

Electrospray ionization mass spectrometry (ESI-MS) experiments were carried out on a Bruker MicroTOF Q (208 - 320 Vac, 50/60 Hz, 1800 VA) mass spectrometer equipped with an Online NanoElectrospray ion source. The spectra were interpreted by molecular peaks $[M]^{n+}$, peaks of protonated molecules $[M+H]^{n+}$, and characteristic fragment peaks and indicated with their mass-to-charge ratio (m/z). Solvents used were H_2O, MeOH, and DMSO.

5.4.3. Sample Preparation

For measurements in 50 mM sodium phosphate buffer, 1X or 10X PBS, the host P5AS and indicator dye, MDAP and BuBrDAP, stock solutions were prepared in the respective solvents. For functionality evaluation studies in surine, neurobasal™ medium, human urine, and saliva, the chemosensor, P5AS•MDAP and P5AS•BuBrDAP, stock solutions were freshly prepared in 1X PBS and titrated to the respective medium. The polyamine (spermine, spermidine, cadaverine, and putrescine) stock solutions were prepared in deionized water and then diluted in the respective solvent/media for the measurements. All stock solutions were kept in the fridge at +8 °C for storage. The concentration of MDAP and BuBrDAP stock solutions were determined accurately by using their molar extinction coefficients (MDAP[201]: 7800 $M^{-1}cm^{-1}$ at 393 nm, BuBrDAP: 7453 $M^{-1}cm^{-1}$ at 393 nm in water) by UV-Vis absorption titration measurements in water. For polyamines, the stock solutions were prepared by weighing in the required amount of the pure sample to attain the desired concentration. The concentration of the P5AS stock solution was determined by fluorescence titration against a known concentration of MDAP dye by exciting the sample at 336 nm and collecting the emission intensity at 423 nm in the respective solvent used to prepare the stock solutions.

Urine samples (spot urine) were collected from healthy voluntary donors spontaneously during the day (morning urine was not used) and used without any pre-treatment steps except for dilution. Saliva samples were collected from healthy voluntary donors spontaneously during the day and used without any pre-treatment steps. Urine/saliva samples were stored in aliquots at –20 °C. For measurements, samples were defrosted and stored at +4 °C and used within 3 - 4 days. Before analysis, samples were incubated at room temperature for 30 minutes. Dilutions were done with 1X PBS for urine samples.

5.5. Additional Information

- **Synthesis of BuBrDAP indicator dye**

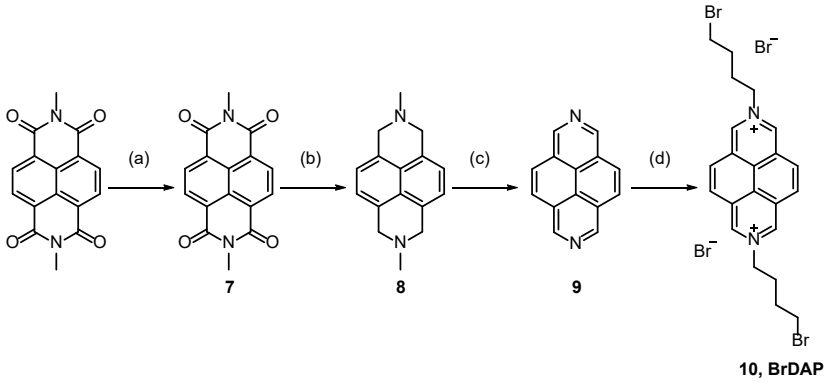

Scheme 5.1: Synthetic route of BuBrDAP. (a) methylamine, 40% aq., 130 °C, 3 h, 70%. (b) $AlCl_3$, $LiAlH_4$, THF, 70 °C, 4 h, 39%. (c) selenium, no solvent, 265 °C, 4 h, 300 °C, 1 h, 63%. (d) 1,4-dibromobutane, DMF, 85 °C, 1 d, 75%. This synthesis was carried out by Dr. Laura Grimm from the research group of Dr. Frank Biedermann.

2,7-dimethylbenzo[*lmn*][3,8]phenanthroline-1,3,6,8(2H,7H)-tetraone[433] (7)

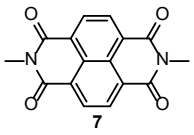

A two-neck flask with a reflux condenser was filled with aqueous methylamine (40 wt%, 120 mL, 1.39 mol, 74.5 eq). To this solution, 1,4,5,8-naphthalenetetracarboxylic dianhydride (5.00 g, 18.6 mmol, 1.0 eq) was added slowly, and the orange reaction mixture was refluxed for 3 h. After cooling to room temperature, the precipitate was collected by filtration, washed with copious amounts of methanol, and dried *in vacuo*. The product (**7**) was isolated as a nude-colored solid with a yield of 70% (3.50 g, 13.1 mmol).

^{1}H NMR (500 MHz, $CDCl_3$, 298 K): δ (ppm) = 8.78 (s, 4H, H-Ar), 3.61 (s, 6H, CH_3). – ^{13}C NMR (126 MHz, $CDCl_3$, 298 K): δ (ppm) = 163.1 (C_q), 131.0 (CH), 126.6 (CH), 27.5 (CH_3).

2,7-dimethyl-1,2,3,6,7,8-hexahydrobenzo[*lmn*][3,8]phenanthroline[434] (8)

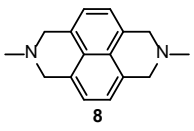

In a 500 ml two-neck flask, anhydrous $AlCl_3$ (3.27 g, 24.6 mmol, 2.3 eq) was dissolved in 200 ml dry THF. To the stirring solution, $LiAlH_4$ (2.40 g, 74.0 mmol, 7.1 eq) was added carefully in small portions under ice-bath cooling. Next, **7** (3.10 g, 10.5 mmol, 1.0 eq) was added in portions, and the red reaction mixture was heated to reflux. After 4h, the reaction mixture turned green and was cooled to room temperature. Subsequently, the reaction mixture was quenched with 400 mL of ice water. The brown precipitate was filtered off and dried under reduced pressure. The solid was extracted

with 1.5 L chloroform in a Soxhlet extractor for 5 h. The extract was evaporated, and a brown-green solid was obtained. Product (**8**) was isolated with a yield of 39% (970 mg, 4.08 mmol). ^{1}H NMR (500 MHz, $CDCl_3$, 298 K): δ (ppm) = 7.18 (s, 4H, H-Ar), 3.99 (s, 8H, CH_2), 2.61 (s, 6H, CH_3). – ^{13}C NMR (126 MHz, $CDCl_3$, 298 K): δ (ppm) = 128.4 (C_q), 126.3 (CH), 125.3 (C_q), 54.1 (CH_2), 34.1 (CH_3).

Benzo[*lmn*][3,8]phenanthroline // 2,7-diazapyrene[434] (9)

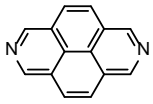

9

In a 250 ml flask, selenium (5.00 g, 64.5 mmol, 20.0 eq) and **8** (770 mg, 3.23 mmol, 1.0 eq) were stirred at 265 °C for 4 h. Next, the black viscous mixture was heated to 300 °C for 1 h. After cooling to room temperature, the reaction flask was boiled four times with 1 M aqueous HCl for 10 min. After each boiling, the black solid was filtered off the acidic solution yielding a red filtrate. The filtrates were combined, and the addition of 5 M NaOH aq. caused the precipitation of a yellow powder. The precipitate was filtered off, washed with water, and dried *in vacuo*. The product (**9**) was isolated as a yellow solid with a yield of 63% (414 mg, 2.03 mmol).

^{1}H NMR (500 MHz, MeOD–*d*3, 298 K): δ (ppm) = 9.53 (s, 4H, H-Ar), 8.39 (s, 4H, CH_2). – ^{13}C NMR (126 MHz, MeOD–*d*3, 298 K): δ (ppm) = 146.0 (CH), 128.0 (CH), 127.8 (C_q), 127.5 (C_q).

2,7-bis(4-bromobutyl)benzo[*lmn*][3,8]phenanthroline-2,7-diium dibromide // 2,7-bis(4-bromobutyl)diazapyrenium (BuBrDAP, 10)

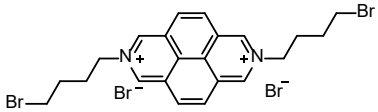

10
BrDAP

Under nitrogen atmosphere, **9** (25.0 mg, 122 µmol, 1.0 eq) was dissolved in 11 mL dry DMF. 1,4-Dibromobutane (1.09 mL, 1.98 g, 9.15 mmol, 75.0 eq) was added, and the reaction solution was stirred at 85 °C for 20 h. The yellow precipitate was filtered off, washed with DMF, and dried under reduced pressure. Product (**10**) was isolated as a yellow solid with a yield of 75% (53.4 mg, 90.1 µmol).

^{1}H NMR (500 MHz, D_2O, 298 K): δ (ppm) = 10.12 (s, 4H, H-Ar), 8.86 (s, 4H, H-Ar), 5.24 (t, ^{3}J = 7.5 Hz, 4H, CH_2), 3.57 (t, ^{3}J = 6.4 Hz, 1H, CH_2), 2.46 (quin, ^{3}J = 7.5 Hz, 4H, CH_2), 2.04 (quin, ^{3}J = 7.5 Hz, 4H, CH_2). – ^{13}C NMR (126 MHz, D_2O, 298 K): δ (ppm) = 141.1 (CH), 130.0 (C_q), 129.9 (CH), 127.0 (C_q), 62.9 (CH_2), 33.0 (CH_2), 30.1 (CH_2), 28.5 (CH_2). – ESI-MS (pos., H_2O): m/z calc. for $C_{22}H_{24}N_2Br_{22}^{+}$ ($[M]^{2+}$) 238.0137, found 238.0220.

Additional data

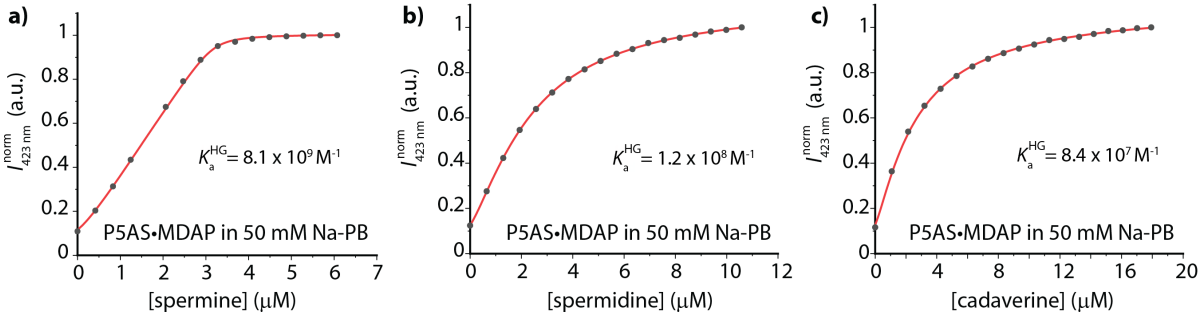

Figure 5.20: (a) Normalized fluorescence emission intensity at 423 nm (λ_{exc} = 336 nm) of P5AS (3.2 μM) and MDAP (3.3 μM) upon stepwise addition of (a) spermine, (b) spermidine, and (c) cadaverine in 50 mM sodium phosphate buffer (50 mM Na-PB). The acquired data is depicted as grey dots, and the fitted data following the competitive thermodynamic IDA model as red line. The binding constant obtained in each case is shown in their respective graphs.

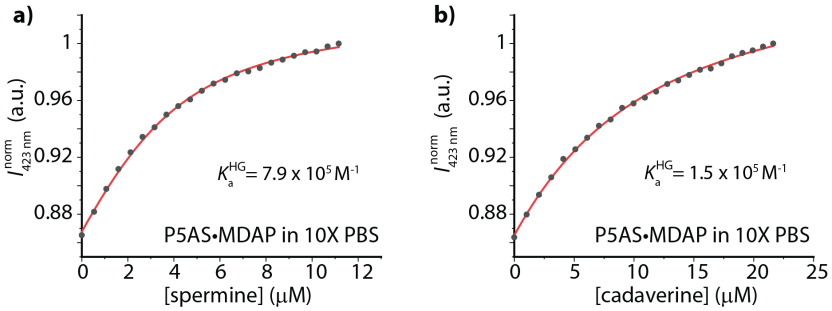

Figure 5.21: (a) Normalized fluorescence emission intensity at 423 nm (λ_{exc} = 336 nm) of P5AS (3.1 μM) and MDAP (3.3 μM) upon stepwise addition of (a) spermine and (b) cadaverine in 10X PBS. The acquired data is depicted as grey dots, and the fitted data following the competitive thermodynamic IDA model as red line. The binding constant obtained in each case is shown in their respective graphs.

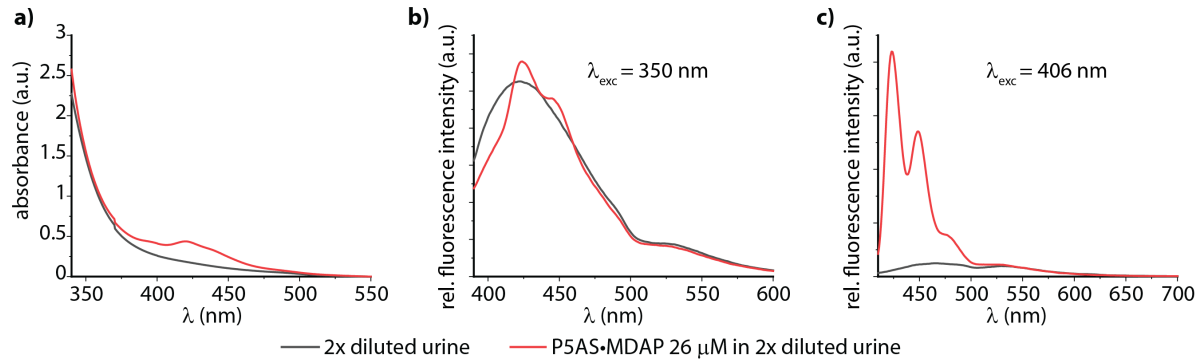

Figure 5.22: (a) Absorbance spectra of urine (diluted 2 times with 1X PBS) in the absence and presence of P5AS•MDAP (36 μM) chemosensor. (a) Fluorescence emission spectra of urine (diluted 2 times with 1X PBS) in the absence and presence of P5AS•MDAP (36 μM) chemosensor upon exciting the sample at (a) 350 nm and (b) 406 nm. Dilution of the urine sample and exciting the sample where the self-absorption from urine is minimum helped reduce the strong urine fluorescence background signal.

List of abbreviations

ECD	electronic circular dichroism
FDCD	fluorescence-detected circular dichroism
ΔF	differential circularly polarized fluorescence excitation
LD	linear dichroism
FDLD	fluorescence-detected linear dichroism
LB	linear birefringence
CPL	circularly polarized luminescence
H	host
G	guest
D	(indicator) dye
GDA	guest displacement assay
*kin*GDA	kinetic GDA
*kin*GDA^{PFO}	pseudo-first order *kin*GDA
IDA	indicator displacement assay
*kin*IDA	kinetic IDA
CB6	cucurbit[6]uril
CB7	cucurbit[7]uril
CB8	cucurbit[8]uril
acyclic CB*n*	acyclic cucurbit[*n*]uril
MT	endo-functionalized molecular tube
P5AS	pillar[5]MaxQ
HSA	human serum albumin (fatty acid free)
MDPP	2,9-dimethyldiazaperoperylenium dication
MDAP	2,7-dimethyldiazapyrenium dication
BuBrDAP	2,7-bis(4-bromobutyl)diazapyrenium dication
(R_p)-MPCP	(R_p)-*N*-methyl-4-pyridinylium[2.2]paracyclophane
(S_p)-MPCP	(S_p)-*N*-methyl-4-pyridinylium[2.2]paracyclophane
(S_p)-MVCP	(*E*)-4-((S_P)-4-vinyl[2.2]paracyclophane)-1-methyl pyridin-1-ium
DSMI	*trans*-4-[4-(dimethylamino)styryl]-1-methylpyridinium iodide
BC	berberine chloride
L-Phe-L-Ala	L-phenylalanyl-L-alanine

L-Phe-Gly	L-phenylalanylglycine
L-Phe-L-Val	L-phenylalanyl-L-valine
L-Ala-L-Phe	L-alanyl-L-phenylalanine
D-Phe	D-phenylalanine
L-Phe	L-phenylalanine
L-Trp-NH_2	L-tryptophanamide hydrochloride
L-Trp-OMe	L-tryptophan methyl ester hydrochloride
D-Trp-OMe	D-tryptophan methyl ester hydrochloride
D-Trp	D-tryptophan
L-Trp	L-tryptophan
L-Arg	L-arginine hydrochloride
D-Arg	D-arginine hydrochloride
L-Lys	L-lysine hydrochloride
Ac-L-Arg-OMe	N-acetyl-L-arginine methyl ester hydrochloride
Ac-L-Lys-OMe	N-acetyl-L-lysine methyl ester hydrochloride
PPO	1-phenylpropylene oxide
4-MBA	4-methylbenzylamine hydrochloride
AdOH	1-adamantanol
$FeCp_2OH$	ferrocenyl methanol
PBZ	phenylbutazone
PB	sodium phosphate buffer
PBS	phosphate buffered saline
HS	human blood serum
DC	direct current
PMT	photomultiplier tube
HT	high tension voltage
BW	bandwidth
Acc	accumulations
LP-Filter	long-pass filter
D.I.T	digital integration time
$t_{measure}$	measuring time
ΔF corr.	HT Voltage corrected ΔF
V	volts

h	hours
λ	wavelength
λ_{obs}	monitoring wavelength
λ_{exc}	excitation wavelength
λ_{ems}	emission wavelength
ε	molar extinction coefficient
$\Delta\varepsilon$	molar circular dichroism
T	temperature
S.D	standard deviation
I	observable signal (fluorescence intensity)
I^{norm}	normalized signal (fluorescence intensity)
I_{sim}	simulated signal (fluorescence intensity)
NMR	nuclear magnetic resonance
DEPT	distortionless enhancement by polarization transfer
DOSY	diffusion-ordered spectroscopy
ITC	isothermal titration calorimetry
ESI-MS	electrospray ionization mass spectrometry
HPLC	high performance liquid chromatography
HPLC-MS	high performance liquid chromatography-mass spectrometry
DLS	dynamic light scattering
RI	refractive index
ee	enantiomeric excess

References

1. J. Krämer, R. Kang, L. M. Grimm, L. De Cola, P. Picchetti and F. Biedermann, *Chem. Rev.*, **2022**, 122, 3459-3636.
2. S. P. Usha, H. Manoharan, R. Deshmukh, R. Álvarez-Diduk, E. Calucho, V. V. R. Sai and A. Merkoçi, *Chem. Soc. Rev.*, **2021**, 50, 13012-13089.
3. W. Li, L. Wang, T. Sun, H. Tang, B. Bui, D. Cao, R. Wang and W. Chen, *Commun. Biol.*, **2021**, 4, 803.
4. D. Ma, G. Hettiarachchi, D. Nguyen, B. Zhang, J. B. Wittenberg, P. Y. Zavalij, V. Briken and L. Isaacs, *Nat. Chem.*, **2012**, 4, 503-510.
5. Y. Zhou, Z. Xu and J. Yoon, *Chem. Soc. Rev.*, **2011**, 40, 2222-2235.
6. S. Kubik, in *Supramolecular Chemistry: From Concepts to Applications*, De Gruyter, **2020**, *Chapter 3 - Understanding molecular recognition*, 37-100.
7. G. Li, in *Nano-Inspired Biosensors for Protein Assay with Clinical Applications*, Elsevier, **2019**, *Part II: Molecular Recognition in Protein Assay*, 113-114.
8. S. H. Gellman, *Chem. Rev.*, **1997**, 97, 1231-1232.
9. H.-X. Zhou and X. Pang, *Chem. Rev.*, **2018**, 118, 1691-1741.
10. D. Corrada, G. Morra and G. Colombo, *J. Phys. Chem. B*, **2013**, 117, 535-552.
11. S. Kubik, *Supramolecular Chemistry: From Concepts to Applications*, De Gruyter, **2020**.
12. T. Nakamura, Y. Kaneko, E. Nishibori and T. Nabeshima, *Nat. Commun.*, **2017**, 8, 129.
13. S. J. Barrow, S. Kasera, M. J. Rowland, J. del Barrio and O. A. Scherman, *Chem. Rev.*, **2015**, 115, 12320-12406.
14. X. Ma and Y. Zhao, *Chem. Rev.*, **2015**, 115, 7794-7839.
15. F. G. Bănică, *Chemical Sensors and Biosensors*, John Wiley & Sons, **2012**.
16. D. Wu, A. C. Sedgwick, T. Gunnlaugsson, E. U. Akkaya, J. Yoon and T. D. James, *Chem. Soc. Rev.*, **2017**, 46, 7105-7123.
17. S. M. Borisov and O. S. Wolfbeis, *Chem. Rev.*, **2008**, 108, 423-461.
18. M. A. Morales and J. M. Halpern, *Bioconjugate Chem.*, **2018**, 29, 3231-3239.
19. J. d. D. Habimana, J. Ji and X. Sun, *Anal. Lett.*, **2018**, 51, 2933-2966.
20. L. C. Clark Jr and C. Lyons, *Ann. N.Y. Acad. Sci.*, **1962**, 102, 29-45.
21. C. I. L. Justino, A. C. Freitas, R. Pereira, A. C. Duarte and T. A. P. Rocha Santos, *TrAC, Trends Anal. Chem.*, **2015**, 68, 2-17.
22. N. J. Ronkainen, H. B. Halsall and W. R. Heineman, *Chem. Soc. Rev.*, **2010**, 39, 1747-1763.
23. G. Rocchitta, A. Spanu, S. Babudieri, G. Latte, G. Madeddu, G. Galleri, S. Nuvoli, P. Bagella, M. I. Demartis, V. Fiore, R. Manetti and P. A. Serra, *Sensors*, **2016**, 16, 780.
24. H. Liu, J. Ge, E. Ma and L. Yang, in *Biomaterials in Translational Medicine*, Academic Press, **2019**, *Chapter 10 - Advanced biomaterials for biosensor and theranostics*, 213-255.
25. S. Sharma, H. Byrne and Richard J. O'Kennedy, *Essays Biochem.*, **2016**, 60, 9-18.

26. J. M. Fowler, D. K. Y. Wong, H. B. Halsall and W. R. Heineman, in *Electrochemical Sensors, Biosensors and their Biomedical Applications*, Academic Press, **2008**, *Chapter 5 - Recent developments in electrochemical immunoassays and immunosensors*, 115-143.

27. M. S. Wilson, *Anal. Chem.*, **2005**, 77, 1496-1502.

28. M. Hasanzadeh, N. Shadjou, M. Eskandani, M. de la Guardia and E. Omidinia, *TrAC, Trends Anal. Chem.*, **2013**, 49, 20-30.

29. W. Liang, Y. Li, B. Zhang, Z. Zhang, A. Chen, D. Qi, W. Yi and C. Hu, *Biosens. Bioelectron.*, **2012**, 31, 480-485.

30. E. Miller and H. D. Sikes, *Nanobiomedicine*, **2015**, 6.

31. A. Liu, K. Wang, S. Weng, Y. Lei, L. Lin, W. Chen, X. Lin and Y. Chen, *TrAC, Trends Anal. Chem.*, **2012**, 37, 101-111.

32. H. Yoo, H. Jo and S. S. Oh, *Mater. Adv.*, **2020**, 1, 2663-2687.

33. W. Zhou, P.-J. Jimmy Huang, J. Ding and J. Liu, *Analyst*, **2014**, 139, 2627-2640.

34. M. A. Beatty and F. Hof, *Chem. Soc. Rev.*, **2021**, 50, 4812-4832.

35. E. M. Peck and B. D. Smith, in *Synthetic Receptors for Biomolecules: Design Principles and Applications*, The Royal Society of Chemistry, **2015**, *Chapter 1 - Applications of Synthetic Receptors for Biomolecules*, 1-38.

36. H.-J. Schneider, *Angew. Chem. Int. Ed.*, **2009**, 48, 3924-3977.

37. B. Smith, *Synthetic Receptors for Biomolecules: Design Principles and Applications*, The Royal Society of Chemistry, **2015**.

38. F. Biedermann, in *Supramolecular Chemistry in Water*, Wiley-VCH, **2019**, *Chapter 2 - Water-Compatible Host Systems*, 35-77.

39. B. Zhang and L. Isaacs, *J. Med. Chem.*, **2014**, 57, 9554-9563.

40. J.-F. Chen, Q. Lin, Y.-M. Zhang, H. Yao and T.-B. Wei, *Chem. Commun.*, **2017**, 53, 13296-13311.

41. C. Jiang, Z. Song, L. Yu, S. Ye and H. He, *TrAC, Trends Anal. Chem.*, **2020**, 133, 116086.

42. Z. Tang and C.-e. A. Chang, *J. Chem. Theory Comput.*, **2018**, 14, 303-318.

43. C. Bohne, *Chem. Soc. Rev.*, **2014**, 43, 4037-4050.

44. S. Kubik, in *Supramolecular Chemistry: From Concepts to Applications*, De Gruyter, **2020**, *Chapter 2 - Analyzing complex formation*, 7-36.

45. Z. Miskolczy and L. Biczók, *J. Phys. Chem. B*, **2014**, 118, 2499-2505.

46. G. V. Oshovsky, D. N. Reinhoudt and W. Verboom, *Angew. Chem. Int. Ed.*, **2007**, 46, 2366-2393.

47. H.-J. Schneider and A. K. Yatsimirsky, *Chem. Soc. Rev.*, **2008**, 37, 263-277.

48. L. Avram, A. D. Wishard, B. C. Gibb and A. Bar-Shir, *Angew. Chem. Int. Ed.*, **2017**, 56, 15314-15318.

49. P. C. Weber, J. J. Wendoloski, M. W. Pantoliano and F. R. Salemme, *J. Am. Chem. Soc.*, **1992**, 114, 3197-3200.

50. K. N. Houk, A. G. Leach, S. P. Kim and X. Zhang, *Angew. Chem. Int. Ed.*, **2003**, 42, 4872-4897.

51. T. Young, R. Abel, B. Kim, B. J. Berne and R. A. Friesner, *Proc. Natl. Acad. Sci.*, **2007**, 104, 808-813.

52. F. Biedermann, W. M. Nau and H.-J. Schneider, *Angew. Chem. Int. Ed.*, **2014**, 53, 11158-11171.

53. Z. Huang, K. Qin, G. Deng, G. Wu, Y. Bai, J.-F. Xu, Z. Wang, Z. Yu, O. A. Scherman and X. Zhang, *Langmuir*, **2016**, 32, 12352-12360.

54. W. M. Nau, M. Florea and K. I. Assaf, *Isr. J. Chem.*, **2011**, 51, 559-577.

55. J. Murray, K. Kim, T. Ogoshi, W. Yao and B. C. Gibb, *Chem. Soc. Rev.*, **2017**, 46, 2479-2496.

56. G. W. Gokel, W. M. Leevy and M. E. Weber, *Chem. Rev.*, **2004**, 104, 2723-2750.

57. G. Crini, *Chem. Rev.*, **2014**, 114, 10940-10975.

58. M. V. Rekharsky and Y. Inoue, *Chem. Rev.*, **1998**, 98, 1875-1918.

59. M. V. Rekharsky and Y. Inoue, *J. Am. Chem. Soc.*, **2002**, 124, 813-826.

60. T. Irie and K. Uekama, *Adv. Drug Deliv. Rev.*, **1999**, 36, 101-123.

61. A. V. Eliseev and H.-J. Schneider, *J. Am. Chem. Soc.*, **1994**, 116, 6081-6088.

62. T. Kraus, M. Buděšínský and J. Závada, *J. Org, Chem*, **2001**, 66, 4595-4600.

63. A. Bom, O. Epemolu, F. Hope, S. Rutherford and K. Thomson, *Curr. Opin. Pharmacol.*, **2007**, 7, 298-302.

64. M. E. Davis and M. E. Brewster, *Nat. Rev. Drug Discov.*, **2004**, 3, 1023-1035.

65. S. B. Nimse and T. Kim, *Chem. Soc. Rev.*, **2013**, 42, 366-386.

66. D.-S. Guo and Y. Liu, *Acc. Chem. Res.*, **2014**, 47, 1925-1934.

67. G. Arena, A. Pappalardo, S. Pappalardo, G. Gattuso, A. Notti, M. F. Parisi, I. Pisagatti and C. Sgarlata, *J. Therm. Anal. Calorim.*, **2015**, 121, 1073-1079.

68. G. Gattuso, A. Notti, S. Pappalardo, M. F. Parisi and I. Pisagatti, *Supramol. Chem.*, **2014**, 26, 597-600.

69. D.-S. Guo, L.-H. Wang and Y. Liu, *J. Org. Chem.*, **2007**, 72, 7775-7778.

70. G. Ghale, A. G. Lanctôt, H. T. Kreissl, M. H. Jacob, H. Weingart, M. Winterhalter and W. M. Nau, *Angew. Chem. Int. Ed.*, **2014**, 53, 2762-2765.

71. H.-W. Tian, Y.-X. Chang, X.-Y. Hu, M. R. Shah, H.-B. Li and D.-S. Guo, *Nanoscale*, **2021**, 13, 15362-15368.

72. S. Sinn and F. Biedermann, *Isr. J. Chem.*, **2018**, 58, 357-412.

73. K. I. Assaf and W. M. Nau, *Chem. Soc. Rev.*, **2015**, 44, 394-418.

74. J. W. Lee, S. Samal, N. Selvapalam, H.-J. Kim and K. Kim, *Acc. Chem. Res.*, **2003**, 36, 621-630.

75. A. I. Lazar, F. Biedermann, K. R. Mustafina, K. I. Assaf, A. Hennig and W. M. Nau, *J. Am. Chem. Soc.*, **2016**, 138, 13022-13029.

76. L. Cao, M. Šekutor, P. Y. Zavalij, K. Mlinarić-Majerski, R. Glaser and L. Isaacs, *Angew. Chem. Int. Ed.*, **2014**, 53, 988-993.

77. N. Dong, J. He, T. Li, A. Peralta, M. R. Avei, M. Ma and A. E. Kaifer, *J. Org. Chem.*, **2018**, 83, 5467-5473.

78. K. Kim, N. Selvapalam, Y. H. Ko, K. M. Park, D. Kim and J. Kim, *Chem. Soc. Rev.*, **2007**, 36, 267-279.

79. T. Minami, N. A. Esipenko, A. Akdeniz, B. Zhang, L. Isaacs and P. Anzenbacher, *J. Am. Chem. Soc.*, **2013**, 135, 15238-15243.

80. A. T. Bockus, L. C. Smith, A. G. Grice, O. A. Ali, C. C. Young, W. Mobley, A. Leek, J. L. Roberts, B. Vinciguerra, L. Isaacs and A. R. Urbach, *J. Am. Chem. Soc.*, **2016**, 138, 16549-16552.

81. J. M. Chinai, A. B. Taylor, L. M. Ryno, N. D. Hargreaves, C. A. Morris, P. J. Hart and A. R. Urbach, *J. Am. Chem. Soc.*, **2011**, 133, 8810-8813.

82. S. K. Samanta, D. Moncelet, V. Briken and L. Isaacs, *J. Am. Chem. Soc.*, **2016**, 138, 14488-14496.

83. T. Ogoshi, S. Kanai, S. Fujinami, T.-a. Yamagishi and Y. Nakamoto, *J. Am. Chem. Soc.*, **2008**, 130, 5022-5023.

84. M. Xue, Y. Yang, X. Chi, Z. Zhang and F. Huang, *Acc. Chem. Res.*, **2012**, 45, 1294-1308.

85. T. Ogoshi, T.-a. Yamagishi and Y. Nakamoto, *Chem. Rev.*, **2016**, 116, 7937-8002.

86. N. L. Strutt, H. Zhang, S. T. Schneebeli and J. F. Stoddart, *Acc. Chem. Res.*, **2014**, 47, 2631-2642.

87. P. J. Cragg and K. Sharma, *Chem. Soc. Rev.*, **2012**, 41, 597-607.

88. C. Li, J. Ma, L. Zhao, Y. Zhang, Y. Yu, X. Shu, J. Li and X. Jia, *Chem. Commun.*, **2013**, 49, 1924-1926.

89. G. Yu, M. Xue, Z. Zhang, J. Li, C. Han and F. Huang, *J. Am. Chem. Soc.*, **2012**, 134, 13248-13251.

90. W. Xue, P. Y. Zavalij and L. Isaacs, *Angew. Chem. Int. Ed.*, **2020**, 59, 13313-13319.

91. Z. Z. C. Han, X. Chi, M. Zhang, G. Yu, F. Huang, *Acta Chim. Sinica*, **2012**, 70, 1775-1778.

92. G. Yu, K. Jie and F. Huang, *Chem. Rev.*, **2015**, 115, 7240-7303.

93. H. Zhang, X. Ma, K. T. Nguyen and Y. Zhao, *ACS Nano*, **2013**, 7, 7853-7863.

94. N. J. Wheate, K.-A. Dickson, R. R. Kim, A. Nematollahi, R. B. Macquart, V. Kayser, G. Yu, W. B. Church and D. J. Marsh, *J. Pharm. Sci.*, **2016**, 105, 3615-3625.

95. G.-B. Huang, S.-H. Wang, H. Ke, L.-P. Yang and W. Jiang, *J. Am. Chem. Soc.*, **2016**, 138, 14550-14553.

96. L.-L. Wang, Z. Chen, W.-E. Liu, H. Ke, S.-H. Wang and W. Jiang, *J. Am. Chem. Soc.*, **2017**, 139, 8436-8439.

97. L.-P. Yang, X. Wang, H. Yao and W. Jiang, *Acc. Chem. Res.*, **2020**, 53, 198-208.

98. Y.-L. Ma, M. Quan, X.-L. Lin, Q. Cheng, H. Yao, X.-R. Yang, M.-S. Li, W.-E. Liu, L.-M. Bai, R. Wang and W. Jiang, *CCS Chem.*, **2021**, 3, 1078-1092.

99. X. Huang, X. Wang, M. Quan, H. Yao, H. Ke and W. Jiang, *Angew. Chem. Int. Ed.*, **2021**, 60, 1929-1935.

100. M. Fokkens, T. Schrader and F.-G. Klärner, *J. Am. Chem. Soc.*, **2005**, 127, 14415-14421.

101. F.-G. Klärner and T. Schrader, *Acc. Chem. Res.*, **2013**, 46, 967-978.

102. T. Schrader, G. Bitan and F.-G. Klärner, *Chem. Commun.*, **2016**, 52, 11318-11334.

103. S. Dutt, C. Wilch, T. Gersthagen, P. Talbiersky, K. Bravo-Rodriguez, M. Hanni, E. Sánchez-García, C. Ochsenfeld, F.-G. Klärner and T. Schrader, *J. Org, Chem*, **2013**, 78, 6721-6734.

104. T. Weil, R. Groß, A. Röcker, K. Bravo-Rodriguez, C. Heid, A. Sowislok, M.-H. Le, N. Erwin, M. Dwivedi, S. M. Bart, P. Bates, L. Wettstein, J. A. Müller, M. Harms, K. Sparrer, Y. B. Ruiz-Blanco, C. M. Stürzel, J. von Einem, S. Lippold, C. Read, P. Walther, M. Hebel, F. Kreppel, F.-G. Klärner, G. Bitan, M. Ehrmann, T. Weil, R. Winter, T. Schrader, J. Shorter, E. Sanchez-Garcia and J. Münch, *J. Am. Chem. Soc.*, **2020**, 142, 17024-17038.

105. M.-H. Le, E. S. Taghuo K and T. Schrader, *Chem. Commun.*, **2022**, 58, 2954-2966.

106. S. Ganapati and L. Isaacs, *Isr. J. Chem.*, **2018**, 58, 250-263.

107. D. Ma, B. Zhang, U. Hoffmann, M. G. Sundrup, M. Eikermann and L. Isaacs, *Angew. Chem. Int. Ed.*, **2012**, 51, 11358-11362.

108. S. A. Zebaze Ndendjio and L. Isaacs, *Supramol. Chem.*, **2019**, 31, 432-441.

109. D. Ma, P. Y. Zavalij and L. Isaacs, *J. Org, Chem*, **2010**, 75, 4786-4795.

110. T. Minami, N. A. Esipenko, B. Zhang, L. Isaacs and P. Anzenbacher, *Chem. Commun.*, **2014**, 50, 61-63.

111. S. Ganapati, S. D. Grabitz, S. Murkli, F. Scheffenbichler, M. I. Rudolph, P. Y. Zavalij, M. Eikermann and L. Isaacs, *ChemBioChem*, **2017**, 18, 1583-1588.

112. B. Wang and E. V. Anslyn, *Chemosensors*, John Wilet & Sons, Inc., **2011**.

113. L. You, D. Zha and E. V. Anslyn, *Chem. Rev.*, **2015**, 115, 7840-7892.

114. R. M. Duke, E. B. Veale, F. M. Pfeffer, P. E. Kruger and T. Gunnlaugsson, *Chem. Soc. Rev.*, **2010**, 39, 3936-3953.

115. Y. Zhang, Q. Li, J. Guo, Y. Li, Q. Yang and J. Du, *RSC Adv.*, **2015**, 5, 66674-66680.

116. V. Yrjänä, I. Saar, M. Ilisson, S. A. Kadam, I. Leito and J. Bobacka, *Chemosensors*, **2021**, 9.

117. M. A. Hortalá, L. Fabbrizzi, N. Marcotte, F. Stomeo and A. Taglietti, *J. Am. Chem. Soc.*, **2003**, 125, 20-21.

118. A. P. Demchenko, in *Introduction to Fluorescence Sensing*, Springer International Publishing, **2020**, *Chapter 1 - Principles and Techniques in Chemical and Biological Sensing*, 1-29.

119. J. R. Lakowicz, in *Principles of Fluorescence Spectroscopy*, Springer US, **2006**, *Chapter 1 - Introduction to Fluorescence*, 1-26.

120. B. Valeur and M. N. Berberan-Santos, in *Molecular Fluorescence: Principles and Applications*, John Wiley & Sons, Inc., **2012**, *Chapter 3 - Characteristics of Fluorescence Emission*, 53-74.

121. R. Parkesh, E. B. Veale and T. Gunnlaugsson, in *Chemosensors*, John Wiley & Sons, Inc., **2011**, *Chapter 12 - Fluorescent Detection Principles and Strategies*, 229-252.

122. A. P. Demchenko, in *Introduction to Fluorescence Sensing*, Springer International Publishing, **2020**, *Chapter 3 - Fluorescence Detection in Sensor Technologies*, 55-110.

123. B. Valeur and M. N. Berberan-Santos, in *Molecular Fluorescence: Principles and Applications*, John Wiley & Sons, Inc., **2012**, *Chapter 2 - Absorption of Ultraviolet, Visible, and Near-Infrared Radiation*, 31-51.

124. M. Kasha, *Discuss. Faraday Soc.*, **1950**, 9, 14-19.

125. J. V. Caspar and T. J. Meyer, *J. Phys. Chem.*, **1983**, 87, 952-957.

126. R. Englman and J. Jortner, *Mol. Phys.*, **1970**, 18, 145-164.

127. T. L. Mako, J. M. Racicot and M. Levine, *Chem. Rev.*, **2019**, 119, 322-477.

128. G. Ghale and W. M. Nau, *Acc. Chem. Res.*, **2014**, 47, 2150-2159.

129. H. Ikeda, *J. Incl. Phenom. Macrocycl. Chem.*, **2017**, 89, 71-75.

130. R. Kumar, A. Sharma, H. Singh, P. Suating, H. S. Kim, K. Sunwoo, I. Shim, B. C. Gibb and J. S. Kim, *Chem. Rev.*, **2019**, 119, 9657-9721.

131. S. Murkli, J. Klemm, D. King, P. Y. Zavalij and L. Isaacs, *Chem. Eur. J.*, **2020**, 26, 15249-15258.

132. J. Mohanty, K. Jagtap, A. K. Ray, W. M. Nau and H. Pal, *ChemPhysChem*, **2010**, 11, 3333-3338.

133. W. M. Nau and J. Mohanty, *Int. J. Photoenergy*, **2005**, 7, 568352.

134. R. N. Dsouza, U. Pischel and W. M. Nau, *Chem. Rev.*, **2011**, 111, 7941-7980.

135. A. L. Koner and W. M. Nau, *Supramol. Chem.*, **2007**, 19, 55-66.

136. G. H. Aryal, L. Huang and K. W. Hunter, *RSC Adv.*, **2016**, 6, 82566-82570.

137. F. Biedermann, E. Elmalem, I. Ghosh, W. M. Nau and O. A. Scherman, *Angew. Chem. Int. Ed.*, **2012**, 51, 7739-7743.

138. T. Minami, N. A. Esipenko, B. Zhang, M. E. Kozelkova, L. Isaacs, R. Nishiyabu, Y. Kubo and P. Anzenbacher, *J. Am. Chem. Soc.*, **2012**, 134, 20021-20024.

139. C. Hu, L. Grimm, A. Prabodh, A. Baksi, A. Siennicka, P. A. Levkin, M. M. Kappes and F. Biedermann, *Chem. Sci.*, **2020**, 11, 11142-11153.

140. D. Lucas, T. Minami, G. Iannuzzi, L. Cao, J. B. Wittenberg, P. Anzenbacher and L. Isaacs, *J. Am. Chem. Soc.*, **2011**, 133, 17966-17976.

141. L. You and E. V. Anslyn, in *Supramolecular Chemistry*, John Wiley & Sons, Ltd., **2012**, *Competition Experiments*.

142. Y. Zhou, L. Gao, X. Tong, Q. Li, Y. Fei, Y. Yu, T. Ye, X.-S. Zhou and Y. Shao, *Anal. Chem.*, **2018**, 90, 13183-13187.

143. X. Wang, L. Cohen, J. Wang and D. R. Walt, *J. Am. Chem. Soc.*, **2018**, 140, 18132-18139.

144. A. C. Sedgwick, J. T. Brewster, T. Wu, X. Feng, S. D. Bull, X. Qian, J. L. Sessler, T. D. James, E. V. Anslyn and X. Sun, *Chem. Soc. Rev.*, **2021**, 50, 9-38.

145. I. A. Rather and R. Ali, *Org. Biomol. Chem.*, **2021**, 19, 5926-5981.

146. G. Ghale, V. Ramalingam, A. R. Urbach and W. M. Nau, *J. Am. Chem. Soc.*, **2011**, 133, 7528-7535.

147. A. Norouzy, Z. Azizi and W. M. Nau, *Angew. Chem. Int. Ed.*, **2015**, 54, 792-795.

148. Z. Zheng, W.-C. Geng, J. Gao, Y.-Y. Wang, H. Sun and D.-S. Guo, *Chem. Sci.*, **2018**, 9, 2087-2091.

149. L. Zhu, Z. Zhao, X. Zhang, H. Zhang, F. Liang and S. Liu, *Molecules*, **2018**, 23.

150. S. Välimäki, N. K. Beyeh, V. Linko, R. H. A. Ras and M. A. Kostiainen, *Nanoscale*, **2018**, 10, 14022-14030.

151. A. Paudics, M. Kubinyi, I. Bitter and M. Bojtár, *RSC Adv.*, **2019**, 9, 16856-16862.

152. S. Sinn, E. Spuling, S. Bräse and F. Biedermann, *Chem. Sci.*, **2019**, 10, 6584-6593.

153. S. A. Minaker, K. D. Daze, M. C. F. Ma and F. Hof, *J. Am. Chem. Soc.*, **2012**, 134, 11674-11680.

154. S. Sinn, J. Krämer and F. Biedermann, *Chem. Commun.*, **2020**, 56, 6620-6623.

155. P. Anzenbacher Jr. and M. A. Palacios, in *Chemosensors*, John Wiley & Sons, Inc., **2011**, *Chapter 17 - Array-Based Sensors*, 345-368.

156. F. Biedermann, D. Hathazi and W. M. Nau, *Chem. Commun.*, **2015**, 51, 4977-4980.

157. H.-J. Kim, J. Heo, W. S. Jeon, E. Lee, J. Kim, S. Sakamoto, K. Yamaguchi and K. Kim, *Angew. Chem. Int. Ed.*, **2001**, 40, 1526-1529.

158. F. Biedermann and O. A. Scherman, *J. Phys. Chem. B*, **2012**, 116, 2842-2849.

159. V. Sindelar, M. A. Cejas, F. M. Raymo, W. Chen, S. E. Parker and A. E. Kaifer, *Chem. Eur. J.*, **2005**, 11, 7054-7059.

160. F. Biedermann, U. Rauwald, M. Cziferszky, K. A. Williams, L. D. Gann, B. Y. Guo, A. R. Urbach, C. W. Bielawski and O. A. Scherman, *Chem. Eur. J.*, **2010**, 16, 13716-13722.

161. P. Thordarson, *Chem. Soc. Rev.*, **2011**, 40, 1305-1323.

162. C. Márquez, R. R. Hudgins and W. M. Nau, *J. Am. Chem. Soc.*, **2004**, 126, 5806-5816.

163. E. Masson, M. Raeisi and K. Kotturi, *Isr. J. Chem.*, **2018**, 58, 413-434.

164. E. A. Appel, F. Biedermann, D. Hoogland, J. del Barrio, M. D. Driscoll, S. Hay, D. J. Wales and O. A. Scherman, *J. Am. Chem. Soc.*, **2017**, 139, 12985-12993.

165. Z. Miskolczy, L. Biczók and I. Jablonkai, *Phys. Chem. Chem. Phys.*, **2017**, 19, 766-773.

166. S. S. Thomas, H. Tang and C. Bohne, *J. Am. Chem. Soc.*, **2019**, 141, 9645-9654.

167. A. Hennig, H. Bakirci and W. M. Nau, *Nat. Methods*, **2007**, 4, 629-632.

168. W. M. Nau, G. Ghale, A. Hennig, H. Bakirci and D. M. Bailey, *J. Am. Chem. Soc.*, **2009**, 131, 11558-11570.

169. Z. Miskolczy and L. Biczók, *Phys. Chem. Chem. Phys.*, **2014**, 16, 20147-20156.

170. M. Megyesi, L. Biczók and I. Jablonkai, *J. Phys. Chem. C*, **2008**, 112, 3410-3416.

171. P. Montes-Navajas, A. Corma and H. Garcia, *ChemPhysChem*, **2008**, 9, 713-720.

172. S. Stewart, M. A. Ivy and E. V. Anslyn, *Chem. Soc. Rev.*, **2014**, 43, 70-84.

173. F. Biedermann and W. M. Nau, *Angew. Chem. Int. Ed.*, **2014**, 53, 5694-5699.

174. S. Kasera, Z. Walsh, J. del Barrio and O. A. Scherman, *Supramol. Chem.*, **2014**, 26, 280-285.

175. V. Rekharsky Mikhail, T. Mori, C. Yang, H. Ko Young, N. Selvapalam, H. Kim, D. Sobransingh, E. Kaifer Angel, S. Liu, L. Isaacs, W. Chen, S. Moghaddam, K. Gilson Michael, K. Kim and Y. Inoue, *Proc. Natl. Acad. Sci.*, **2007**, 104, 20737-20742.

176. S. Zhang, L. Grimm, Z. Miskolczy, L. Biczók, F. Biedermann and W. M. Nau, *Chem. Commun.*, **2019**, 55, 14131-14134.

177. W. Sliwa and T. Girek, *J. Incl. Phenom. Macrocycl. Chem.*, **2010**, 66, 15-41.

178. R. Ludwig and N. T. K. Dzung, *Sensors*, **2002**, 2, 397-416.

179. Suprabank, Biedermann Labs, (accessed 02-02-2022, DOI: www.suprabank.org).

180. M. Inaki, J. Liu and K. Matsuno, *Philos. Trans. R. Soc. Lond., B, Biol. Sci.*, **2016**, 371, 20150403.

181. G. P. Moss, *Pure Appl. Chem.*, **1996**, 68, 2193-2222.

182. R. S. Cahn, C. Ingold and V. Prelog, *Angew. Chem. Int. Ed. Engl.*, **1966**, 5, 385-415.

183. V. Prelog and G. Helmchen, *Angew. Chem. Int. Ed. Engl.*, **1982**, 21, 567-583.

184. G. P. Moss, *Pure Appl. Chem.*, **1996**, 68, 2193-2222.

185. D. G. Blackmond, *Cold Spring Harb. Perspect. Biol.*, **2010**, 2, a002147-a002147.

186. M. Somagoni Jagan, M. Eaga Chandra and Y. Madhsudan Rao, *Int. J. Pharm. Sci. Nanotech.*, **1970**, 1.

187. F. Saito and P. R. Schreiner, *Eur. J. Org. Chem.*, **2020**, 2020, 6328-6339.

188. A. Ozcelik, R. Pereira-Cameselle, N. Poklar Ulrih, A. G. Petrovic and J. L. Alonso-Gómez, *Sensors*, **2020**, 20.

189. H. Eyring, H.-C. Liu and D. Caldwell, *Chem. Rev.*, **1968**, 68, 525-540.

190. N. Berova, L. D. Bari and G. Pescitelli, *Chem. Soc. Rev.*, **2007**, 36, 914-931.

191. G. Pescitelli, L. Di Bari and N. Berova, *Chem. Soc. Rev.*, **2011**, 40, 4603-4625.

192. N. Berova, K. Nakanishi and R. W. Woody, *Circular Dichroism: Principles and Applications*, Wiley-VCH, **2000**.

193. N. Berova and K. Nakanishi, in *Circular Dichroism: Principles and Applications*, Wiley-VCH, **2000**, *Chapter 12 - Exciton Chirality Method: Principles and Application*, 337-382.

194. N. Harada and K. Nakanishi, *Circular dichroic spectroscopy : exciton coupling in organic stereochemistry*, Oxford University Press, **1983**.

195. E. Castiglioni, S. Abbate, F. Lebon and G. Longhi, *Methods Appl. Fluoresc.*, **2014**, 2, 024006.

196. D. H. Turner, I. Tinoco and M. Maestre, *J. Am. Chem. Soc.*, **1974**, 96, 4340-4342.

197. I. Tinoco and D. H. Turner, *J. Am. Chem. Soc.*, **1976**, 98, 6453-6456.

198. J.-G. Dong, A. Wada, T. Takakuwa, K. Nakanishi and N. Berova, *J. Am. Chem. Soc.*, **1997**, 119, 12024-12025.

199. K. Tanaka, G. Pescitelli, K. Nakanishi and N. Berova, *Monatsh. Chem.*, **2005**, 136, 367-395.

200. M. Quan, X.-Y. Pang and W. Jiang, *Angew. Chem. Int. Ed.*, **2022**, e202201258.

201. A. Prabodh, D. Bauer, S. Kubik, P. Rebmann, F. G. Klärner, T. Schrader, L. Delarue Bizzini, M. Mayor and F. Biedermann, *Chem. Commun.*, **2020**, 56, 4652-4655.

202. X. Huang, K. Nakanishi and N. Berova, *Chirality*, **2000**, 12, 237-255.

203. G. Pescitelli, S. Gabriel, Y. Wang, J. Fleischhauer, R. W. Woody and N. Berova, *J. Am. Chem. Soc.*, **2003**, 125, 7613-7628.

204. G. Pescitelli, *Chirality*, **2022**, 34, 333-363.

205. G. A. Hembury, V. V. Borovkov and Y. Inoue, *Chem. Rev.*, **2008**, 108, 1-73.

206. Z. Chen, Q. Wang, X. Wu, Z. Li and Y.-B. Jiang, *Chem. Soc. Rev.*, **2015**, 44, 4249-4263.

207. N. Berova, G. Pescitelli, A. G. Petrovic and G. Proni, *Chem. Commun.*, **2009**, DOI: 10.1039/B909582A, 5958-5980.

208. L. You, G. Pescitelli, E. V. Anslyn and L. Di Bari, *J. Am. Chem. Soc.*, **2012**, 134, 7117-7125.

209. S. J. Wezenberg, G. Salassa, E. C. Escudero-Adán, J. Benet-Buchholz and A. W. Kleij, *Angew. Chem. Int. Ed.*, **2011**, 50, 713-716.

210. C. Wolf and K. W. Bentley, *Chem. Soc. Rev.*, **2013**, 42, 5408-5424.

211. G. Proni, G. Pescitelli, X. Huang, K. Nakanishi and N. Berova, *J. Am. Chem. Soc.*, **2003**, 125, 12914-12927.

212. H. Tsukube and S. Shinoda, *Chem. Rev.*, **2002**, 102, 2389-2404.

213. K. W. Bentley, P. Zhang and C. Wolf, *Sci. Adv.*, **2016**, 2, e1501162.

214. S. L. Pilicer, P. R. Bakhshi, K. W. Bentley and C. Wolf, *J. Am. Chem. Soc.*, **2017**, 139, 1758-1761.

215. Z. A. De los Santos and C. Wolf, *J. Am. Chem. Soc.*, **2016**, 138, 13517-13520.

216. C. Ni, D. Zha, H. Ye, Y. Hai, Y. Zhou, E. V. Anslyn and L. You, *Angew. Chem. Int. Ed.*, **2018**, 57, 1300-1305.

217. J.-B. Xiong, H.-T. Feng, J.-P. Sun, W.-Z. Xie, D. Yang, M. Liu and Y.-S. Zheng, *J. Am. Chem. Soc.*, **2016**, 138, 11469-11472.

218. X. Liang, W. Liang, P. Jin, H. Wang, W. Wu and C. Yang, *Chemosensors*, **2021**, 9.

219. J. Monod, J. Wyman and J.-P. Changeux, *J. Mol. Biol.*, **1965**, 12, 88-118.

220. L.-P. Yang, L. Zhang, M. Quan, J. S. Ward, Y.-L. Ma, H. Zhou, K. Rissanen and W. Jiang, *Nat. Commun.*, **2020**, 11, 2740.

221. Y. Chen, L. Fu, B. Sun, C. Qian, R. Wang, J. Jiang, C. Lin, J. Ma and L. Wang, *Org. Lett.*, **2020**, 22, 2266-2270.

222. Y. Chen, L. Fu, B. Sun, C. Qian, S. Pangannaya, H. Zhu, J. Ma, J. Jiang, Z. Ni, R. Wang, X. Lu and L. Wang, *Chem. Eur. J.*, **2021**, 27, 5890-5896.

223. D. E. Koshland, *Proc. Natl. Acad. Sci.*, **1958**, 44, 98-104.

224. L.-L. Wang, M. Quan, T.-L. Yang, Z. Chen and W. Jiang, *Angew. Chem. Int. Ed.*, **2020**, 59, 23817-23824.

225. P. Metola, E. V. Anslyn, T. D. James and S. D. Bull, *Chem. Sci.*, **2012**, 3, 156-161.

226. J. Podlech, S. C. Fleck, M. Metzler, J. Bürck and A. S. Ulrich, *Chem. Eur. J.*, **2014**, 20, 11463-11470.

227. J. Bürck, P. Wadhwani, S. Fanghänel and A. S. Ulrich, *Acc. Chem. Res.*, **2016**, 49, 184-192.

228. M. Sapotta, P. Spenst, C. R. Saha-Möller and F. Würthner, *Org. Chem. Front.*, **2019**, 6, 892-899.

229. L.-J. Chen, H.-B. Yang and M. Shionoya, *Chem. Soc. Rev.*, **2017**, 46, 2555-2576.

230. L. You, J. S. Berman and E. V. Anslyn, *Nat. Chem.*, **2011**, 3, 943-948.

231. K. W. Bentley, Y. G. Nam, J. M. Murphy and C. Wolf, *J. Am. Chem. Soc.*, **2013**, 135, 18052-18055.

232. H. Gholami, M. Anyika, J. Zhang, C. Vasileiou and B. Borhan, *Chem. Eur. J.*, **2016**, 22, 9235-9239.

233. M. Inouye, M. Waki and H. Abe, *J. Am. Chem. Soc.*, **2004**, 126, 2022-2027.

234. M. Anyika, H. Gholami, K. D. Ashtekar, R. Acho and B. Borhan, *J. Am. Chem. Soc.*, **2014**, 136, 550-553.

235. T. Morozumi and S. Shinkai, *J. Chem. Soc., Chem. Commun.*, **1994**, DOI: 10.1039/C39940001219, 1219-1220.

236. L. Vial, M. Dumartin, M. Donnier-Maréchal, F. Perret, J.-P. Francoia and J. Leclaire, *Chem. Commun.*, **2016**, 52, 14219-14221.

237. H. Goto, Y. Furusho and E. Yashima, *Chem. Commun.*, **2009**, DOI: 10.1039/B900113A, 1650-1652.

238. S. He, F. Biedermann, N. Vankova, L. Zhechkov, T. Heine, R. E. Hoffman, A. De Simone, T. T. Duignan and W. M. Nau, *Nat. Chem.*, **2018**, 10, 1252-1257.

239. D. Bauer, B. Andrae, P. Gaß, D. Trenz, S. Becker and S. Kubik, *Org. Chem. Front.*, **2019**, 6, 1555-1560.

240. Y. Yokoyama, H. Hikawa and Y. Murakami, *J. Chem. Soc., Perkin Trans. 1*, **2001**, 1431-1434.

241. L. Delarue Bizzini, T. Müntener, D. Häussinger, M. Neuburger and M. Mayor, *Chem. Commun.*, **2017**, 53, 11399-11402.

242. L. Delarue Bizzini, T. Bürgi and M. Mayor, *Helv. Chim. Acta*, **2020**, 103, e2000019.

243. D. Bier, R. Rose, K. Bravo-Rodriguez, M. Bartel, J. M. Ramirez-Anguita, S. Dutt, C. Wilch, F.-G. Klärner, E. Sanchez-Garcia, T. Schrader and C. Ottmann, *Nat. Chem.*, **2013**, 5, 234-239.

244. J. Kim, I.-S. Jung, S.-Y. Kim, E. Lee, J.-K. Kang, S. Sakamoto, K. Yamaguchi and K. Kim, *J. Am. Chem. Soc.*, **2000**, 122, 540-541.

245. A. N. Basuray, H.-P. Jacquot de Rouville, K. J. Hartlieb, T. Kikuchi, N. L. Strutt, C. J. Bruns, M. W. Ambrogio, A.-J. Avestro, S. T. Schneebeli, A. C. Fahrenbach and J. F. Stoddart, *Angew. Chem. Int. Ed.*, **2012**, 51, 11872-11877.

246. M. A. Cejas and F. M. Raymo, *Langmuir*, **2005**, 21, 5795-5802.

247. A. J. Blacker, J. Jazwinski and J.-M. Lehn, *Helv. Chim. Acta*, **1987**, 70, 1-12.

248. PhotoChemCAD, (accessed 01-11-2019, DOI: https://omlc.org/spectra/PhotochemCAD).

249. A. Prabodh, Y. Wang, S. Sinn, P. Albertini, C. Spies, E. Spuling, L.-P. Yang, W. Jiang, S. Bräse and F. Biedermann, *Chem. Sci.*, **2021**, 12, 9420-9431.

250. M. Liu, L. Zhang and T. Wang, *Chem. Rev.*, **2015**, 115, 7304-7397.

251. Y. Li, C. Liu, X. Bai, F. Tian, G. Hu and J. Sun, *Angew. Chem. Int. Ed.*, **2020**, 59, 3486-3490.

252. X. Li and B. Borhan, *J. Am. Chem. Soc.*, **2008**, 130, 16126-16127.

253. X. Li, C. E. Burrell, R. J. Staples and B. Borhan, *J. Am. Chem. Soc.*, **2012**, 134, 9026-9029.

254. M. Tanasova, M. Anyika and B. Borhan, *Angew. Chem. Int. Ed.*, **2015**, 54, 4274-4278.

255. H. H. Jo, X. Gao, L. You, E. V. Anslyn and M. J. Krische, *Chem. Sci.*, **2015**, 6, 6747-6753.

256. C.-Y. Lin, M. W. Giuliano, B. D. Ellis, S. J. Miller and E. V. Anslyn, *Chem. Sci.*, **2016**, 7, 4085-4090.

257. L. A. Joyce, M. S. Maynor, J. M. Dragna, G. M. da Cruz, V. M. Lynch, J. W. Canary and E. V. Anslyn, *J. Am. Chem. Soc.*, **2011**, 133, 13746-13752.

258. A. E. Holmes, D. Das and J. W. Canary, *J. Am. Chem. Soc.*, **2007**, 129, 1506-1507.

259. J. Zhang, A. E. Holmes, A. Sharma, N. R. Brooks, R. S. Rarig, J. Zubieta and J. W. Canary, *Chirality*, **2003**, 15, 180-189.

260. M. J. Kim, Y. R. Choi, H.-G. Jeon, P. Kang, M.-G. Choi and K.-S. Jeong, *Chem. Commun.*, **2013**, 49, 11412-11414.

261. E. Badetti, K. Wurst, G. Licini and C. Zonta, *Chem. Eur. J.*, **2016**, 22, 6515-6518.

262. S. Superchi, R. Bisaccia, D. Casarini, A. Laurita and C. Rosini, *J. Am. Chem. Soc.*, **2006**, 128, 6893-6902.

263. Circular Dichroism Spectroscopy, (accessed 01-04-2020, DOI: http://www.cryst.bbk.ac.uk/PPS2/course/section8/ss-960531_21.html).

264. N. J. Greenfield, *Anal. Biochem.*, **1996**, 235, 1-10.

265. T. Nehira, C. A. Parish, S. Jockusch, N. J. Turro, K. Nakanishi and N. Berova, *J. Am. Chem. Soc.*, **1999**, 121, 8681-8691.

266. N. Sharma, E. Spuling, Cornelia M. Mattern, W. Li, O. Fuhr, Y. Tsuchiya, C. Adachi, S. Bräse, I. D. W. Samuel and E. Zysman-Colman, *Chem. Sci.*, **2019**, 10, 6689-6696.

267. K. Dhbaibi, L. Favereau, M. Srebro-Hooper, M. Jean, N. Vanthuyne, F. Zinna, B. Jamoussi, L. Di Bari, J. Autschbach and J. Crassous, *Chem. Sci.*, **2018**, 9, 735-742.

268. R. Carr, N. H. Evans and D. Parker, *Chem. Soc. Rev.*, **2012**, 41, 7673-7686.

269. J. Yuasa, T. Ohno, H. Tsumatori, R. Shiba, H. Kamikubo, M. Kataoka, Y. Hasegawa and T. Kawai, *Chem. Commun.*, **2013**, 49, 4604-4606.

270. E. M. Sánchez-Carnerero, A. R. Agarrabeitia, F. Moreno, B. L. Maroto, G. Muller, M. J. Ortiz and S. de la Moya, *Chem. Eur. J.*, **2015**, 21, 13488-13500.

271. E. W. Lobenstine, W. C. Schaefer and D. H. Turner, *J. Am. Chem. Soc.*, **1981**, 103, 4936-4940.

272. S. Park, K. Ajtai and T. P. Burghardt, *Biophys. Chem.*, **1996**, 63, 67-80.

273. K. Muto, R. Yoshida, R. Yashida, T. Ishii and T. Handa, *J. Am. Chem. Soc.*, **1986**, 108, 6416-6417.

274. J. P. Riehl and G. Muller, in *Comprehensive Chiroptical Spectroscopy*, Wiley, **2011**, *Chapter 3 - Circularly Polarized Luminescence Spectroscopy and Emission-Detected Circular Dichroism*, 65-90.

275. T. Smidlehner, I. Piantanida and G. Pescitelli, *Beilstein J. Org. Chem.*, **2018**, 14, 84-105.

276. G. Longhi, E. Castiglioni, J. Koshoubu, G. Mazzeo and S. Abbate, *Chirality*, **2016**, 28, 696-707.

277. T. R. Schulte, J. J. Holstein, L. Krause, R. Michel, D. Stalke, E. Sakuda, K. Umakoshi, G. Longhi, S. Abbate and G. H. Clever, *J. Am. Chem. Soc.*, **2017**, 139, 6863-6866.

278. K. Watanabe, K. Muto and T. Ishii, *Biospectroscopy*, **1997**, 3, 103-111.

279. S. Egusa, M. Sisido and Y. Imanishi, *Macromolecules*, **1985**, 18, 882-889.

280. D. Banerjee and S. K. Pal, *Langmuir*, **2008**, 24, 8163-8168.

281. F. Meadows, N. Narayanan and G. Patonay, *Talanta*, **2000**, 50, 1149-1155.

282. T. Nehira, K. Ishihara, K. Matsuo, S. Izumi, T. Yamazaki and A. Ishida, *Anal. Biochem.*, **2012**, 430, 179-184.

283. M. L. Lamos, E. W. Lobenstine and D. H. Turner, *J. Am. Chem. Soc.*, **1986**, 108, 4278-4284.

284. C. Reich and I. Tinoco Jr., *Biopolymers*, **1980**, 19, 833-848.

285. Web of Science, (accessed 07-08-2020, DOI: https://apps.webofknowledge.com/WOS_GeneralSearch_input.do?product=WOS&search_mode=GeneralSearch&SID=F6WjmQzAP1oOGUb5aI6&preferencesSaved=).

286. R. Hofsäß, S. Sinn, F. Biedermann and H.-A. Wagenknecht, *Chem. Eur. J.*, **2018**, 24, 16257-16261.

287. Z. Dai, G. Proni, D. Mancheno, S. Karimi, N. Berova and J. W. Canary, *J. Am. Chem. Soc.*, **2004**, 126, 11760-11761.

288. D. M. Bailey, A. Hennig, V. D. Uzunova and W. M. Nau, *Chem. Eur. J.*, **2008**, 14, 6069-6077.

289. A. C. Bhasikuttan, H. Pal and J. Mohanty, *Chem. Commun.*, **2011**, 47, 9959-9971.

290. L.-M. Bai, H. Zhou, W.-E. Liu, H. Chai, L.-P. Yang, W. Yan, W. Zhang, H.-H. Yang and W. Jiang, *Chem. Commun.*, **2019**, 55, 3128-3131.

291. M. I. Childers, J. M. Longo, N. J. Van Zee, A. M. LaPointe and G. W. Coates, *Chem. Rev.*, **2014**, 114, 8129-8152.

292. E. N. Jacobsen, *Acc. Chem. Res.*, **2000**, 33, 421-431.

293. C. J. Thibodeaux, W.-c. Chang and H.-w. Liu, *Chem. Rev.*, **2012**, 112, 1681-1709.

294. R. E. Parker and N. S. Isaacs, *Chem. Rev.*, **1959**, 59, 737-799.

295. S. Bonollo, D. Lanari and L. Vaccaro, *Eur. J. Org. Chem.*, **2011**, 2011, 2587-2598.

296. J. Jiao, G. R. Douglas, J. D. Gingerich and L. M. Soper, *Mutat. Res. - Fundam. Mol. Mech. Mutagen.*, **1996**, 372, 141-145.

297. M. E. T. Dollé, H.-J. Martus, M. Novak, N. J. van Orsouw and J. Vijg, *Mutagenesis*, **1999**, 14, 287-293.

298. H. Yao, H. Ke, X. Zhang, S.-J. Pan, M.-S. Li, L.-P. Yang, G. Schreckenbach and W. Jiang, *J. Am. Chem. Soc.*, **2018**, 140, 13466-13477.

299. B. Ehrenberg and I. Z. Steinberg, *J. Am. Chem. Soc.*, **1976**, 98, 1293-1295.

300. I. Tinoco, B. Ehrenberg and I. Z. Steinberg, *J. Chem. Phys.*, **1977**, 66, 916-920.

301. D. M. Jameson and J. A. Ross, *Chem. Rev.*, **2010**, 110, 2685-2708.

302. M. R. Hicks, J. Kowałski and A. Rodger, *Chem. Soc. Rev.*, **2010**, 39, 3380-3393.

303. M. Hirschmann, C. Merten and C. M. Thiele, *Soft Matter*, **2021**, 17, 2849-2856.

304. A. E. Tudose, I. Dumitrascu, L. Dumitrascu, D. G. Dimitriu and D. O. Dorohoi, *AIP Conf. Proc.*, **2017**, 1796, 030007.

305. A. M. Wemyss, K. Razmkhah, N. P. Chmel and A. Rodger, *Analyst*, **2018**, 143, 5805-5811.

306. T. Nehira, K. Tanaka, T. Takakuwa, C. Ohshima, H. Masago, G. Pescitelli, A. Wada and N. Berova, *Appl. Spectrosc.*, **2005**, 59, 121-125.

307. S. Mondal, S. Ghosh and S. P. Moulik, *J. Photochem. Photobiol.*, **2016**, 158, 212-218.

308. W. I. Goldburg, *Am. J. Phys.*, **1999**, 67, 1152-1160.

309. Polydispersity – what does it mean for DLS and chromatography?, (accessed 11-05-2020, DOI: https://www.materials-talks.com/polydispersity-what-does-it-mean-for-dls-and-chromatography/).

310. S. M. Patil, D. A. Keire and K. Chen, *The AAPS journal*, **2017**, 19, 1760-1766.

311. C. N. Pace, F. Vajdos, L. Fee, G. Grimsley and T. Gray, *Protein Sci.*, **1995**, 4, 2411-2423.

312. E. W. Lobenstine and D. H. Turner, *J. Am. Chem. Soc.*, **1979**, 101, 2205-2207.

313. E. W. Lobenstine and D. H. Turner, *J. Am. Chem. Soc.*, **1980**, 102, 7786-7787.

314. Circular Dichroism Spectrometer J-1000 Series, (accessed 20-04-2020, DOI: https://www.jasco.de/uploads/files/J-1000-Series-Brochure.pdf).

315. T. W. Bell and N. M. Hext, *Chem. Soc. Rev.*, **2004**, 33, 589-598.

316. J. Wu, W. Liu, J. Ge, H. Zhang and P. Wang, *Chem. Soc. Rev.*, **2011**, 40, 3483-3495.

317. R. N. Dsouza, A. Hennig and W. M. Nau, *Chem. Eur. J.*, **2012**, 18, 3444-3459.

318. H. Tang, D. Fuentealba, Y. H. Ko, N. Selvapalam, K. Kim and C. Bohne, *J. Am. Chem. Soc.*, **2011**, 133, 20623-20633.

319. E. A. Appel, J. del Barrio, X. J. Loh and O. A. Scherman, *Chem. Soc. Rev.*, **2012**, 41, 6195-6214.

320. H. Adams, F. J. Carver, C. A. Hunter, J. C. Morales and E. M. Seward, *Angew. Chem. Int. Ed.*, **1996**, 35, 1542-1544.

321. I. K. Mati and S. L. Cockroft, *Chem. Soc. Rev.*, **2010**, 39, 4195-4205.

322. E. Persch, O. Dumele and F. Diederich, *Angew. Chem. Int. Ed.*, **2015**, 54, 3290-3327.

323. F. Biedermann and H.-J. Schneider, *Chem. Rev.*, **2016**, 116, 5216-5300.

324. J. Řezáč and P. Hobza, *Chem. Rev.*, **2016**, 116, 5038-5071.

325. D.-S. Guo, V. D. Uzunova, K. I. Assaf, A. I. Lazar, Y. Liu and W. M. Nau, *Supramol. Chem.*, **2016**, 28, 384-395.

326. K. I. Assaf and W. M. Nau, *Angew. Chem. Int. Ed.*, **2018**, 57, 13968-13981.

327. F. Hof, S. L. Craig, C. Nuckolls and J. J. Rebek, *Angew. Chem. Int. Ed.*, **2002**, 41, 1488-1508.

328. E. C. Hulme and M. A. Trevethick, *Br. J. Pharmacol.*, **2010**, 161, 1219-1237.

329. H.-J. Schneider and A. Yatsimirsky, *Principles and methods in supramolecular chemistry*, Wiley, **2000**.

330. X. Yan, F. Wang, B. Zheng and F. Huang, *Chem. Soc. Rev.*, **2012**, 41, 6042-6065.

331. H. J. Motulsky and L. C. Mahan, *Mol. Pharmacol.*, **1984**, 25, 1.

332. R. Casasnovas, V. Limongelli, P. Tiwary, P. Carloni and M. Parrinello, *J. Am. Chem. Soc.*, **2017**, 139, 4780-4788.

333. M. Bernetti, A. Cavalli and L. Mollica, *MedChemComm*, **2017**, 8, 534-550.

334. P. J. Tonge, *ACS Infectious Diseases*, **2019**, 5, 796-808.

335. D. C. Swinney, *Curr. Opin. Drug Discovery Dev.*, **2009**, 12, 31-39.

336. R. Zhang and F. Monsma, *Curr. Opin. Drug Discovery Dev.*, **2009**, 12, 488-496.

337. D. Guo, T. Mulder-Krieger, A. P. Ijzerman and L. H. Heitman, *Br. J. Pharmacol.*, **2012**, 166, 1846-1859.

338. D. A. Sykes, M. R. Dowling and S. J. Charlton, *Mol. Pharmacol.*, **2009**, 76, 543.

339. G. Ashkenasy, T. M. Hermans, S. Otto and A. F. Taylor, *Chem. Soc. Rev.*, **2017**, 46, 2543-2554.

340. J. H. van Esch, R. Klajn and S. Otto, *Chem. Soc. Rev.*, **2017**, 46, 5474-5475.

341. S. Borsley, J. A. Cooper, P. J. Lusby and S. L. Cockroft, *Chem. Eur. J.*, **2018**, 24, 4542-4546.

342. T. Rama, E. M. López-Vidal, M. D. García, C. Peinador and J. M. Quintela, *Chem. Eur. J.*, **2015**, 21, 9482-9487.

343. T. J. Williams, A. D. Kershaw, V. Li and X. Wu, *J. Chem. Educ.*, **2011**, 88, 665-669.

344. J. S. Mugridge, R. G. Bergman and K. N. Raymond, *Angew. Chem. Int. Ed.*, **2010**, 49, 3635-3637.

345. J. S. Mugridge, R. G. Bergman and K. N. Raymond, *J. Am. Chem. Soc.*, **2012**, 134, 2057-2066.

346. A. Wu and L. Isaacs, *J. Am. Chem. Soc.*, **2003**, 125, 4831-4835.

347. D. J. Cram and G. M. Lein, *J. Am. Chem. Soc.*, **1985**, 107, 3657-3668.

348. F. Biedermann, M. Vendruscolo, O. A. Scherman, A. De Simone and W. M. Nau, *J. Am. Chem. Soc.*, **2013**, 135, 14879-14888.

349. S. Liu, C. Ruspic, P. Mukhopadhyay, S. Chakrabarti, P. Y. Zavalij and L. Isaacs, *J. Am. Chem. Soc.*, **2005**, 127, 15959-15967.

350. S. Lim, Y. Kuang and H. A. M. Ardoña, *Front. Chem.*, **2021**, 9.

351. C. Zhong, C. Hu, R. Kumar, V. Trouillet, F. Biedermann and M. Hirtz, *ACS Appl. Nano Mater.*, **2021**, 4, 4676-4687.

352. A. Stahl, A. I. Lazar, V. N. Muchemu, W. M. Nau, M. S. Ullrich and A. Hennig, *Anal. Bioanal. Chem.*, **2017**, 409, 6485-6494.

353. Y.-C. Liu, W. M. Nau and A. Hennig, *Chem. Commun.*, **2019**, 55, 14123-14126.

354. E. Karnas, S. K. Kim, K. A. Johnson, J. L. Sessler, K. Ohkubo and S. Fukuzumi, *J. Am. Chem. Soc.*, **2010**, 132, 16617-16622.

355. X. Zheng, C. Bi, Z. Li, M. Podariu and D. S. Hage, *J. Pharm. Biomed.*, **2015**, 113, 163-180.

356. M. Nilam, P. Gribbon, J. Reinshagen, K. Cordts, E. Schwedhelm, W. M. Nau and A. Hennig, *SLAS Discovery*, **2017**, 22, 906-914.

357. V. Sindelar, M. A. Cejas, F. M. Raymo and A. E. Kaifer, *New J. Chem.*, **2005**, 29, 280-282.

358. Å. Frostell-Karlsson, A. Remaeus, H. Roos, K. Andersson, P. Borg, M. Hämäläinen and R. Karlsson, *J. Med. Chem.*, **2000**, 43, 1986-1992.

359. V. Maes, Y. Engelborghs, J. Hoebeke, Y. Maras and A. Vercruysse, *Mol. Pharmacol.*, **1982**, 21, 100.

360. I. Petitpas, A. A. Bhattacharya, S. Twine, M. East and S. Curry, *J. Biol. Chem.*, **2001**, 276, 22804-22809.

361. M. Wiemann and P. Jonkheijm, *Isr. J. Chem.*, **2018**, 58, 314-325.

362. K. Kim, J. Murray, N. Selvapalam, Y. H. Ko and I. Hwang, in *Cucurbiturils Chemistry, Supramolecular Chemistry and Applications*, World Scientific Publishing Co, **2018**, *Chapter 3 - Host–Guest Chemistry of Cucurbit[n]urils*, 31-55.

363. P. Mukhopadhyay, P. Y. Zavalij and L. Isaacs, *J. Am. Chem. Soc.*, **2006**, 128, 14093-14102.

364. Z. Miskolczy, M. Megyesi, L. Biczók, A. Prabodh and F. Biedermann, *Chem. Eur. J.*, **2020**, 26, 7433-7441.

365. M. V. Rekharsky, Y. H. Ko, N. Selvapalam, K. Kim and Y. Inoue, *Supramol. Chem.*, **2007**, 19, 39-46.

366. A. L. Koner, C. Márquez, M. H. Dickman and W. M. Nau, *Angew. Chem. Int. Ed.*, **2011**, 50, 545-548.

367. L. M. Grimm, S. Spicher, B. Tkachenko, P. R. Schreiner, S. Grimme and F. Biedermann, *Chem. Eur. J.*, **2022**, e202200529.

368. S. Moghaddam, C. Yang, M. Rekharsky, Y. H. Ko, K. Kim, Y. Inoue and M. K. Gilson, *J. Am. Chem. Soc.*, **2011**, 133, 3570-3581.

369. P. Zhang, G. Ma, W. Dong, Z. Wan, S. Wang and N. Tao, *Nat. Methods*, **2020**, 17, 1010-1017.

370. F. Domenici, M. Frasconi, F. Mazzei, G. D'Orazi, A. R. Bizzarri and S. Cannistraro, *J. Mol. Recognit.*, **2011**, 24, 707-714.

371. D. J. Oshannessy, M. Brighamburke, K. K. Soneson, P. Hensley and I. Brooks, *Anal. Biochem.*, **1993**, 212, 457-468.

372. C. Marquez, H. Fang and W. M. Nau, *IEEE Trans. Nanobiosci.*, **2004**, 3, 39-45.

373. D. Jiao and O. A. Scherman, *Green Chem.*, **2012**, 14, 2445-2449.

374. K. Bhadra and G. S. Kumar, *Biochim. Biophys. Acta. Gen Subj.*, **2011**, 1810, 485-496.

375. C. Marquez and W. M. Nau, *Angew. Chem. Int. Ed.*, **2001**, 40, 3155-3160.

376. A. Prabodh, S. Sinn, L. Grimm, Z. Miskolczy, M. Megyesi, L. Biczók, S. Bräse and F. Biedermann, *Chem. Commun.*, **2020**, 56, 12327-12330.

377. M. H. Tootoonchi, S. Yi and A. E. Kaifer, *J. Am. Chem. Soc.*, **2013**, 135, 10804-10809.

378. Z. Miskolczy, J. G. Harangozó, L. Biczók, V. Wintgens, C. Lorthioir and C. Amiel, *Photochem. Photobiol. Sci.*, **2014**, 13, 499-508.

379. S. Senler, B. Cheng and A. E. Kaifer, *Org. Lett.*, **2014**, 16, 5834-5837.

380. B. Held, H. Tang, P. Natarajan, C. P. da Silva, V. de Oliveira Silva, C. Bohne and F. H. Quina, *Photochem. Photobiol. Sci.*, **2016**, 15, 752-757.

381. S. S. Thomas and C. Bohne, *Faraday Discuss.*, **2015**, 185, 381-398.

382. J. Kalmár, S. B. Ellis, M. T. Ashby and R. L. Halterman, *Org. Lett.*, **2012**, 14, 3248-3251.

383. I. Neira, M. D. García, C. Peinador and A. E. Kaifer, *J. Org, Chem*, **2019**, 84, 2325-2329.

384. A. E. Kaifer, W. Li, S. Silvi and V. Sindelar, *Chem. Commun.*, **2012**, 48, 6693-6695.

385. X. Zheng, Z. Li, M. I. Podariu and D. S. Hage, *Anal. Chem.*, **2014**, 86, 6454-6460.

386. E. Agostinelli, M. P. M. Marques, R. Calheiros, F. P. S. C. Gil, G. Tempera, N. Viceconte, V. Battaglia, S. Grancara and A. Toninello, *Amino Acids*, **2010**, 38, 393-403.

387. E. Larqué, M. Sabater-Molina and S. Zamora, *Nutrition*, **2007**, 23, 87-95.

388. K. Igarashi and K. Kashiwagi, *Int. J. Biochem. Cell Biol.*, **2010**, 42, 39-51.

389. F. Madeo, T. Eisenberg, F. Pietrocola and G. Kroemer, *Science*, **2018**, 359, eaan2788.

390. A. E. Pegg, *IUBMB Life*, **2009**, 61, 880-894.

391. S. Mandal, A. Mandal, E. Johansson Hans, V. Orjalo Arturo and H. Park Myung, *Proc. Natl. Acad. Sci.*, **2013**, 110, 2169-2174.

392. N. de Vera, E. Martínez and C. Sanfeliu, *J. Neurosci. Res.*, **2008**, 86, 861-872.

393. R. A. Casero, T. Murray Stewart and A. E. Pegg, *Nat. Rev. Cancer*, **2018**, 18, 681-695.

394. N. A. Sagar, S. Tarafdar, S. Agarwal, A. Tarafdar and S. Sharma, *Medical Sciences*, **2021**, 9.

395. N. Minois, D. Carmona-Gutierrez and F. Madeo, *Aging*, **2011**, 3, 716-732.

396. C. Gomes-Trolin, I. Nygren, S. M. Aquilonius and H. Askmark, *Exp. Neurol.*, **2002**, 177, 515-520.

397. H. Tomitori, T. Usui, N. Saeki, S. Ueda, H. Kase, K. Nishimura, K. Kashiwagi and K. Igarashi, *Stroke*, **2005**, 36, 2609-2613.

398. E. W. Gerner and F. L. Meyskens, *Nat. Rev. Cancer*, **2004**, 4, 781-792.

399. L. D. Morrison and S. J. Kish, *Neurosci. Lett.*, **1995**, 197, 5-8.

400. D. H. Russell, *Nature New Biol.*, **1971**, 233, 144-145.

401. T. Thomas and T. J. Thomas, *J. Cell. Mol. Med.*, **2003**, 7, 113-126.

402. C. Lo, Y.-L. Hsu, C.-N. Cheng, C.-H. Lin, H.-C. Kuo, C.-S. Huang and C.-H. Kuo, *J. Proteome Res.*, **2020**, 19, 4061-4070.

403. Y. Asai, T. Itoi, M. Sugimoto, A. Sofuni, T. Tsuchiya, R. Tanaka, R. Tonozuka, M. Honjo, S. Mukai, M. Fujita, K. Yamamoto, Y. Matsunami, T. Kurosawa, Y. Nagakawa, M. Kaneko, S. Ota, S. Kawachi, M. Shimazu, T. Soga, M. Tomita and M. Sunamura, *Cancers*, **2018**, 10.

404. K. Igarashi, S. Ota, M. Kaneko, A. Hirayama, M. Enomoto, K. Katumata, M. Sugimoto and T. Soga, *J. Chromatogr. A*, **2021**, 1652, 462355.

405. M. Y. Khuhawar and G. A. Qureshi, *J. Chromatogr. B Biomed. Appl.*, **2001**, 764, 385-407.

406. Z. Dai, Z. Wu, J. Wang, X. Wang, S. Jia, F. W. Bazer and G. Wu, *Amino Acids*, **2014**, 46, 1557-1564.

407. Y. Ma, G. Liu, M. Du and I. Stayton, *Electrophoresis*, **2004**, 25, 1473-1484.

408. M. Niitsu, K. Samejima, S. Matsuzaki and K. Hamana, *J. Chromatogr. A*, **1993**, 641, 115-123.

409. Z. Köstereli and K. Severin, *Chem. Commun.*, **2012**, 48, 5841-5843.

410. J. Tu, S. Sun and Y. Xu, *Chem. Commun.*, **2016**, 52, 1040-1043.

411. T.-I. Kim and Y. Kim, *Chem. Commun.*, **2016**, 52, 10648-10651.

412. A. D'Urso, G. Brancatelli, N. Hickey, E. Farnetti, R. De Zorzi, C. Bonaccorso, R. Purrello and S. Geremia, *Supramol. Chem.*, **2016**, 28, 499-505.

413. C. P. Carvalho, R. Ferreira, J. P. Da Silva and U. Pischel, *Supramol. Chem.*, **2013**, 25, 92-100.

414. T.-I. Kim, J. Park and Y. Kim, *Chem. Eur. J.*, **2011**, 17, 11978-11982.

415. R. R. Nair, S. Debnath, S. Das, P. Wakchaure, B. Ganguly and P. B. Chatterjee, *ACS Appl. Bio Mater.*, **2019**, 2, 2374-2387.

416. B. Lee, R. Scopelliti and K. Severin, *Chem. Commun.*, **2011**, 47, 9639-9641.

417. K. Liu, Y. Yao, Y. Kang, Y. Liu, Y. Han, Y. Wang, Z. Li and X. Zhang, *Sci. Rep.*, **2013**, 3, 2372.

418. M. Ikeda, T. Yoshii, T. Matsui, T. Tanida, H. Komatsu and I. Hamachi, *J. Am. Chem. Soc.*, **2011**, 133, 1670-1673.

419. Q. Duan, Y. Xing and K. Guo, *Front. Chem.*, **2021**, 9.

420. What Is the Chemical Composition of Urine?, (accessed 25-03-2022, DOI: https://www.thoughtco.com/the-chemical-composition-of-urine-603883).

421. H. A. Krebs, *Annu. Rev. Biochem*, **1950**, 19, 409-430.

422. W. Ong and A. E. Kaifer, *J. Org, Chem*, **2004**, 69, 1383-1385.

423. V. Francisco, A. Piñeiro, W. M. Nau and L. García-Río, *Chem. Eur. J.*, **2013**, 19, 17809-17820.

424. D. H. Russell, C. C. Levy, S. C. Schimpff and I. A. Hawk, *Cancer Res.*, **1971**, 31, 1555-1558.

425. X. Jiang, *Biomed. Chromatogr.*, **1990**, 4, 73-77.

426. R. Liu, Y. Jia, W. Cheng, J. Ling, L. Liu, K. Bi and Q. Li, *Talanta*, **2011**, 83, 751-756.

427. S. Antoniello, M. Auletta, P. Magri and F. Pardo, *Int. J. Biol. Markers*, **1998**, 13, 92-97.

428. J. P. Moulinoux, V. Quemener, M. Le Calve, M. Chatel and F. Darcel, *J. Neuro-Oncol.*, **1984**, 2, 153-158.

429. D. Ryan, K. Robards, P. D. Prenzler and M. Kendall, *Anal. Chim. Acta*, **2011**, 684, 17-29.

430. A. Zhang, H. Sun, X. Wu and X. Wang, *Clin. Chim. Acta*, **2012**, 414, 65-69.

431. S. Bouatra, F. Aziat, R. Mandal, A. C. Guo, M. R. Wilson, C. Knox, T. C. Bjorndahl, R. Krishnamurthy, F. Saleem, P. Liu, Z. T. Dame, J. Poelzer, J. Huynh, F. S. Yallou, N. Psychogios, E. Dong, R. Bogumil, C. Roehring and D. S. Wishart, *PLoS One*, **2013**, 8, e73076.

432. J. Bartel, J. Krumsiek, K. Schramm, J. Adamski, C. Gieger, C. Herder, M. Carstensen, A. Peters, W. Rathmann, M. Roden, K. Strauch, K. Suhre, G. Kastenmüller, H. Prokisch and F. J. Theis, *PLoS Genet*, **2015**, 11, e1005274.

433. P. J. Stang, D. H. Cao, S. Saito and A. M. Arif, *J. Am. Chem. Soc.*, **1995**, 117, 6273-6283.

434. S. Hünig, J. Groβ, E. F. Lier and H. Quast, *Justus Liebigs Ann. Chem.*, **1973**, 1973, 339-358.

Patents, publications and conference contributions

Patents

European patent application 22192620.7, *Self-assembled chemosensors for detecting polyamines in physiological media and biofluids*, filed August 29, 2022 (patent pending).

Scientific publications

A. Prabodh, Y. Wang, S. Sinn, P. Albertini, C. Spies, E. Spuling, L.-P. Yang, W. Jiang, S. Bräse and F. Biedermann, Fluorescence detected circular dichroism (FDCD) for supramolecular host-guest complexes, *Chem. Sci*., **2021**, 12, 9420-9431.

A. Prabodh, S. Sinn, L. Grimm, Z. Miskolczy, M. Megyesi, L. Biczók, S. Bräse and F. Biedermann, Teaching indicators to unravel the kinetic features of host–guest inclusion complexes, *Chem. Commun.*, **2020**, 56, 12327-12330.

A. Prabodh, D. Bauer, S. Kubik, P. Rebmann, F. G. Klärner, T. Schrader, L. Delarue Bizzini, M. Mayor and F. Biedermann, Chirality sensing of terpenes, steroids, amino acids, peptides and drugs with acyclic cucurbit[*n*]urils and molecular tweezers, *Chem. Commun.*, **2020**, 56, 4652-4655.

C. Hu, L. Grimm, A. Prabodh, A. Baksi, A. Siennicka, P. A. Levkin, M. M. Kappes and F. Biedermann, Covalent cucurbit[7]uril–dye conjugates for sensing in aqueous saline media and biofluids, *Chem. Sci*., **2020**, 11, 11142-11153.

Z. Miskolczy, M. Megyesi, L. Biczók, A. Prabodh and F. Biedermann, Kinetics and mechanism of cation-Induced guest release from cucurbit[7]uril, *Chem. Eur. J*., **2020**, 26, 7433-7441.

A. Prabodh, S. Sinn, and F. Biedermann, Analyte sensing with unselectively binding synthetic receptors: Virtues of time-resolved supramolecular assays.
Manuscript submitted to Chem. Commun. (in revision).

A. Prabodh, L. Grimm, P. K. Biswas and F. Biedermann, Pillar[*n*]arene-based fluorescence turn-on chemosensor for the selective detection of biogenic polyamines in saline media and biofluids.
Manuscript in preparation.

Poster presentations

Amrutha Prabodh, Wei Jiang, Stefan Bräse and Frank Biedermann, 1st Women in Supramolecular Chemistry (WISC) workshop, 2021, Cagliari, Italy. *Fluorescence detected circular dichroism (FDCD) for supramolecular host–guest complexes.*

Amrutha Prabodh, Stephan Sinn, Stefan Bräse, Thomas Schrader and Frank Biedermann, Indo-German Workshop, 2019 on Multivalent and Adaptive Bioinspired Materials, Essen, Germany. *Fluorescence detected circular dichroism (FDCD) for supramolecular host–guest complexes – an Explorative Study*.

Acknowledgements

I would like to dedicate this section to express my sincere appreciation to all the people who helped and supported me during my Ph.D. journey.

First of all, I would like to thank my supervisor, Dr. Frank Biedermann, without whom this work would have never been possible. I am deeply indebted to Dr. Frank Biedermann for giving me the opportunity to do my Ph.D. under his guidance and in his research group. I am incredibly grateful for his continuous guidance, patience, and the time he spent with me solving numerous scientific problems. Importantly, he gave me the freedom, opportunity, and encouragement to explore new ideas, which helped me grow as an independent researcher. I would also like to express my gratitude to Prof. Dr. Pavel Levkin for accepting my application for a doctorate in his research group and thank the guidance and support he provided me.

I would like to thank all the former and present colleagues in the Biedermann group. I am extremely grateful to Dr. Stephan Sinn for his help and guidance during the initial phase of my Ph.D., for teaching me all the necessary to become a good scientist, and for constantly motivating me to figure out quality answers to complex questions. I would also like to extend my sincere thanks to Matthias Schuster, who helped me not only on a scientific level but also with several social aspects when I first joined the group. Many thanks to Dr. Laura Grimm, Dr. Pronay Kumar Biswas, Yichuan Wang, and Changming Hu for their synthesis efforts and for providing me with several compounds for my project. I thank Dr. Pierre Picchetti, Rui Kang, Joana Krämer, Nilima Manoj Kumar, Chunting Zhong, Wenjing Wang, and Patrick Gruhs for all their help and support and for sharing with me a pleasant time in the lab. I enjoyed our coffee break sessions, all the informative conversations, the fun group activities, and our cooperation as a working group.

Thanks should also go to all my collaborators who helped me fulfill my research projects. I thank Daniel Bauer, Prof. Stefan Kubik, Philipp Rebmann, Prof. Thomas Schrader, Prof. Frank Gerritt Klärner, Lorenzo Delarue Bizzini, and Prof. Marcel Mayor for providing synthetic host or guest molecules for the ECD-based analyte sensing project and for their valuable discussions in understanding the host sensing behavior. I would also like to acknowledge the valuable contribution of Paolo Albertini and Christian Spies to the FDCD project by providing insights into the spectroscopy details and performing additional measurements to explain several spectroscopic features. I also thank Liu-Pan Yang and Prof. Wei Jiang for providing the synthetic host molecule for the FDCD project and their efforts to study the system's aggregation

properties, which helped me understand the host recognition behavior. I thank Yichuan Wang and Prof. Stefan Bräse for providing me with suitable chiral indicator dyes for the project. Finally, I acknowledge Zsombor Miskolczy, Mónika Megyesi, and Prof. László Biczók for providing me with detailed insights into unravelling the kinetics features of supramolecular host-guest inclusion complexes.

During my stay at INT, I appreciated the help and support from Christine Fischer, Patricia Jäger, Heidi Hagel, Matthias Hettler, and Hartmut Speck in various administrative and official matters. In addition, Michael Birkel-Suck, Thomas Koch, Marc Schleifer, and Daniel Lerch were always very helpful with IT-related problems.

Special thanks go to the proofreaders of this thesis. I thank you for your time and constructive criticism.

Last but not least, I would like to acknowledge the Deutscher Akademischer Austauschdienst (DAAD) for funding my Ph.D. project, without which this project would not have been possible.

I cannot complete this without acknowledging my family and friends, who mean everything to me. They have constantly supported me at all stages of my life. Special thanks to my parents, Prabodh Madambath and Meena Prabodh, and my sister, Adithya Prabodh, for their love and support and believing in me all the time.